University of Bradford eThesis

MODELLING AND ANALYSIS OF COMPLEX ELECTROMAGNETIC PROBLEMS USING FDTD SUBGRIDDING IN HYBRID COMPUTATIONAL METHODS

K N RAMLI

Ph.D.

2011

MODELLING AND ANALYSIS OF COMPLEX ELECTROMAGNETIC PROBLEMS USING FDTD SUBGRIDDING IN HYBRID COMPUTATIONAL METHODS

Development of Hybridised Method of Moments, Finite-Difference Time-Domain Method and Subgridded Finite-Difference Time-Domain Method for Precise Computation of Electromagnetic Interaction with Arbitrarily Complex Geometries

KHAIRUN NIDZAM RAMLI
B.Eng., M.Eng.

Submitted for the Degree of

Doctor of Philosophy

School of Engineering, Design and Technology

University of Bradford

2011

Abstract

MODELLING AND ANALYSIS OF COMPLEX ELECTROMAGNETIC PROBLEMS USING FDTD SUBGRIDDING IN HYBRID COMPUTATIONAL METHODS

Development of Hybridised Method of Moments, Finite-Difference Time-Domain Method and Subgridded Finite-Difference Time-Domain Method for Precise Computation of Electromagnetic Interaction with Arbitrarily Complex Geometries

Keywords
Computational Electromagnetics; Method of Moments (MoM); Finite-Difference Time-Domain (FDTD); Quasi-static method; Hybrid computational method; Subgridding; Principle of equivalent sources; Perfectly Matched Layer (PML); Antennas.

The main objective of this research is to model and analyse complex electromagnetic problems by means of a new hybridised computational technique combining the frequency domain Method of Moments (MoM), Finite-Difference Time-Domain (FDTD) method and a subgridded Finite-Difference Time-Domain (SGFDTD) method. This facilitates a significant advance in the ability to predict electromagnetic absorption in inhomogeneous, anisotropic and lossy dielectric materials irradiated by geometrically intricate sources. The Method of Moments modelling employed a two-dimensional electric surface patch integral formulation solved by independent linear basis function methods in the circumferential and axial directions of the antenna wires. A similar orthogonal basis function is used on the end surface and appropriate attachments with the wire surface are employed to satisfy the requirements of current continuity. The surface current distributions on structures which may include closely spaced parallel wires, such as dipoles, loops and helical antennas are computed. The results are found to be stable and showed good agreement with less comprehensive earlier work by others.

The work also investigated the interaction between overhead high voltage transmission lines and underground utility pipelines using the FDTD technique for the whole structure, combined with a subgridding method at points of interest, particularly the pipeline. The induced fields above the pipeline are investigated and analysed.

FDTD is based on the solution of Maxwell's equations in differential form. It is very useful for modelling complex, inhomogeneous structures. Problems arise when open-region geometries are modelled. However, the Perfectly Matched Layer (PML) concept has been employed to circumvent this difficulty. The establishment of edge elements has greatly improved the performance of this method and the computational burden due to huge numbers of time steps, in the order of tens of millions, has been eased to tens of thousands by employing quasi-static methods.

This thesis also illustrates the principle of the equivalent surface boundary employed close to the antenna for MoM-FDTD-SGFDTD hybridisation. It depicts the advantage of using hybrid techniques due to their ability to analyse a system of multiple discrete regions by employing the principle of equivalent sources to excite the coupling surfaces. The method has been applied for modelling human body interaction with a short range RFID antenna to investigate and analyse the near field and far field radiation pattern for which the cumulative distribution function of antenna radiation efficiency is presented. The field distributions of the simulated structures show reasonable and stable results at 900 MHz. This method facilitates deeper investigation of the phenomena in the interaction between electromagnetic fields and human tissues.

Table of Contents

Chapter 1: Introduction

Chapter 2: FDTD Technique for Field Truncation

Chapter 3: Surface Kernel Solution of the Method of Moments

Chapter 4: Quasi-Static Finite-Difference Time-Domain Subgridding Technique

Chapter 5: Interaction of EM Fields to the Human Body Using Hybrid Computational Method

Chapter 6: Conclusion and Recommendation for Further Work

Appendix

Acknowledgements

My sincere recognition goes first of all to **Prof. R. A. Abd-Alhameed** and **Prof. P. S. Excell** for their invaluable advices and constructive criticism throughout the completion of this thesis. They have been generous in their time and always a source of ingenuity to me. I have been deeply impressed by their ability to respond to various work and non-work related state of affairs with sensitivity and understanding. I am indebted to **Dr. D. T. W. Liang**, **Dr. C. H. See** and **Mr. M. B. Child** for their constructive help throughout critical discussions and helpful comments they have provided pertinent to my research work.

I wish to convey my deepest thanks to my father, **Ramli Bandahara** and my mother, **Noorsah Ismail** for their endless support throughout my life and for providing me the chance to reach this far with my studies. I thank them for having faith in me and always inspiring me through calls. In particular, the financial support from **Ministry of Higher Education Malaysia** and my employer, **Universiti Tun Hussein Onn Malaysia (UTHM)** is gratefully acknowledged. I am sure that I have missed people in the list. However, their help was really appreciated and acknowledged.

Lastly, and by no means least, I am grateful for the love and advocate of my wife, **Roziyana Omar** and my children, **Zaki Irfan Khairun Nidzam** and **Zakwan Hazim Khairun Nidzam** for their sacrifice during this often difficult effort and for their endless support towards my career.

Acronyms

1-D	One-dimension
2-D	Two-dimension
3-D	Three-dimension
3G	Third Generation
ABC	Absorbing Boundary Condition
AC	Alternating Current
ADI-FDTD	Alternating Direction Implicit Finite-Difference Time-Domain
BAN	Body Area Networks
CDF	Cumulative Distribution Function
CFL	Courant-Friedrich-Levy
DC	Direct Current
DOP	Direction of Propagation
EMC	Electromagnetic Compatibility
FDTD	Finite-Difference Time-Domain
FEM	Finite-Element Method
FSS	Frequency Selective Surface
GA	Genetic Algorithm
GTD	Geometrical Theory of Diffraction
HF	High Frequency
HSG	Huygens Subgridding
IFA	Incident-field Array
MIMO	Miltiple Input Multiple Output
MoM	Method of Moment
MRI	Magnetic Resonance Imaging
MSMoM	Multistructure Method of Moment
MTR	Multitemporal Resolution
NAG	Numerical Algorithms Group
NMHA	Normal Mode Helical Antenna
OHTL	Overhead High Voltage Transmission Lines
PBG	Photonic Bandgap
PDF	Probability Density Function
PEC	Perfect Electric Conductor
PEE	Partial Eigenfunction Expansion
PML	Perfectly Matched Layer
Q-factor	Quality Factor
RCS	Radar Cross Section
RF	Radio Frequency
RFID	Radio Frequency Identification

RSS	Received Signal Strength
SAR	Specific Absorption Rate
SGFDTD	Subgridded Finite-Difference Time-Domain
TE	Transverse Electric
TE_z	Transverse electric relative to the z-direction (only H_z, E_x, and E_y fields are present)
TEM	Transverse Electromagnetic
TM	Transverse Magnetic
TM_z	Transverse magnetic relative to the z-direction (only E_z, H_x, and H_y fields are present)
UMTS	Universal Mobile Telecommunications System
UTD	Uniform Geometrical Theory of Diffraction
UWB	Ultra Wideband
VIE	Volume Integral Equation
VHF	Very High Frequency
WBSN	Wireless Body Sensor Network
WLAN	Wireless Local Area Network

Symbols

E	Electric field intensity
H	Magnetic field intensity
B	Magnetic flux density
D	Electric flux density
σ^*	Magnetic resistivity
σ	Electric conductivity
μ	Magnetic permeability
ε	Electric permittivity
I_j	Basis function for surface current
$\mathbf{J}_j$	Surface current
$\mathbf{E}_i$	Incident electric field strength
L	Integro-differential operator
A	Vector potentials
ϕ	Scalar potentials
$\mathbf{W}_m$	Testing functions
Z	Impedance matrix
V	Excitation vector
$g(R)$	Free-space Green function
R	Distance between observation and source points on wire surface
A	Radius of helix wire
B	Radius of helix wire
P	Pitch distance between helix wire turns
α	Azimuth angle of circumferential cross-section wire
δ	Pitch angle
γ	Axial length of curvilinear patch
$\hat{a}_\gamma$	Unit vector in axial surfaces of wire antenna
$\hat{a}_{cs}$	Unit vector in circumferential surfaces of wire antenna
$\hat{a}_r$	Unit vectors in radial directions on the end surface of wire antenna
$\hat{a}_{ce}$	Unit vectors in circumferential directions on the end surface of wire antenna
$f(\gamma)$	Triangular basis functions into the axial direction
$P_{absorbed}$	Absorbed power
$P_{radiated}$	Radiated power

List of Tables

List of Figures

Chapter 1

Introduction

1.1 Background and Motivations

Over the past years, a number of numerical and analytical approaches to Maxwell's time-dependent curl equations were broadly used with the increases in computer memory capacity and relentless advances in computational imitating efficiency. Consequently, the demand for efficient field modelling tools in electromagnetic scattering problems is ceaselessly expanding. In general, computational electromagnetic techniques have been applied to vast areas including the study of the radiation, scattering and penetration of electromagnetic wave with 3-D objects, in problems related to telecommunication, electromagnetic compatibility (EMC), microwave devices, waveguide structures and medical diagnosis.

Apparently, many considerations need to be taken into account when deciding to choose the most suitable numerical technique in order to solve a specific problem. Some of the main factors include the geometry of the scattering and radiating objects, computer requirements, the domain of interest whether time-domain or frequency-domain, and the absorbing boundary conditions (ABC). The material characteristics and its geometry play important roles in choosing the approach used to mathematically model the properties of the electromagnetic interaction. In biomedical application for instance, the object is inhomogeneous, anisotropy, penetrable body which cannot be easily included in the formulations. However, the ability of FDTD algorithm to simulate and investigate the inhomogeneous, anisotropy media makes it very useful and effective technique thus far. Typically, there are two main categories of numerical algorithms approaches applied by researches. They are namely the frequency-domain integral formulation using the Method of Moments (MoM), and the time-domain differential formulation by means of the Finite-Difference Time-Domain (FDTD) method and the Finite Element Method (FEM). Integro-differential equation method is generally global in nature so that the initial and boundary conditions must be imposed as the algorithm continues. In contrast, differential-equation technique is typically local in nature so that the initial and boundary conditions are both directly included in the computational algorithm. The former technique usually postulates extensive analytical pre-processing whereas the later demands negligible analytical pre-processing. The methods mentioned above can be applied to certain specific geometries of concern. Consequently, the differential-equation formulations are increasingly well-known due to the fact that it can solve any type of geometries in the problem space of the computational domain.

1.2 Development History of FDTD

First introduced by Yee in 1966 [1], FDTD is widely used to solve electromagnetic scattering problems due to its muscular characteristics including:

- Simplicity: The second-order accurate central finite-difference approximations for spatial and temporal derivatives of the electric and magnetic vector field components is directly used to solve Maxwell's equations explicitly in the absence of linear algebra.

- Fidelity: Wideband and narrowband applications can be easily implemented by applying different type of time pulse shape such as Gaussian and sinusoidal wave respectively.
- Robustness: Numerical dispersions in FDTD computations can be enclosed to model very large variety of electromagnetic scattering problems accurately. Furthermore, the FDTD algorithm can be easily implemented on parallel computers for faster simulation time.
- Effectiveness: Problems involving nonlinear media can be inherently alleviated in a straightforward manner in the time-domain compared with those in the frequency-domain technique.
- Versatility: It can intrinsically be used to model inhomogeneous, anisotropy materials such as biological tissues, geophysical strata and shielding metal structures.

Generally, the algorithm used by Yee was described by the electric field component which was spatially and temporally offset from the magnetic field component to acquire the update equations. These equations were used in a leap-frog manner to propagate the electric and magnetic fields ahead in time. The equations provide the present fields in terms of the past fields all over the computational domain. After Yee’s publication, the approach was widely used with different endeavour [2-6].

The boundaries of the computational domain in FDTD need to be carefully treated when simulating problems in open regions. Spurious reflections will generally occur from the termination of the grid. The problem can be solved by means of the well known method called the absorbing boundary condition (ABC). It is generally meant to absorb any outgoing propagating waves without ideally producing spurious reflections. The ABCs was first proposed in 1971 by Merewether [7] to solve the open region difficulties. The development chronicle to magnify the practicability study of the technique was continued in the literature by [8-12] which were based of nonmaterial type. In contrast, Berenger presented a new idea in 1994 called the perfectly matched layer (PML) ABC which was based on material category [13]. The state of the art of Berenger's PML contributes to notably better precision when compared to the other ABCs in the written works [14, 15] for broad assortment of applications.

The main handicap of FDTD lies in the truth that only consistent grids can be used. Accordingly, the geometry resemblance in FDTD is restricted to staircase-shaped boundaries which lead to a large number of computer memory requirements and the CPU time particularly when dealing with curvature geometries with fine features [16]. The total number of cells in the computational domain grows significantly due to a global fine mesh. Another FDTD weakness is the presence of error due to numerical dispersion [17, 18]. In this case, many scientists were prompted to examine the subgridding scheme as an approach to parry the problem. A variety of methods have been proposed to boost the efficiency of FDTD technique such as non-uniform meshing [19], sub-cellular technique [20], non-orthogonal meshing [21], alternative direction implicit (ADI) method [22-24], higher-order technique [25, 26], hybrid method [27-29] and subgridding method [30-34]. In FDTD subgridding technique, the smaller size components in a structure is filled with fine grids and the remaining of the space is represented by coarse grids. The fields on the boundary between coarse and fine grids are basically unknown in nature. They are predicted by using spatial and temporal interpolations. The regions of the coarse and fine grids are computed by the FDTD method and are kept in time step which satisfy the Courant stability condition. Consequently, the stable subgridding algorithm can refine the mesh locally. Hence, the accuracy of the solution can be improved without increasing the computational efforts significantly.

1.3 Development History of MoM

The MoM is basically a general procedure for solving linear equations. The “moments” in its name is due to the process of taking moments by multiplying the suitable weighting functions and integrating. In other words, it is essentially the technique of weighted residuals applicable for solving both the differential and integral equations. The advantages of MoM are accuracy, versatility and the potential to compute the near and far zone parameters. Furthermore, the method proved its ability to solve real complex antenna geometry in both frequency and time domain. The use of MoM and related matrix methods has become widespread in electromagnetic areas since the published paper of Richmond in 1965 [35] by generating a system of linear equations for the unknown current density and enforcing the boundary conditions at discrete points in the scattering body. Afterwards, he developed a point-matching solution for scattering by conducting bodies of arbitrary shape [36]. In 1967, Harrington documented the mathematical concept of MoM by which the functional equations of the field theory were reduced to matrix equations [37]. Later, he published a book on MoM which was a step forward towards the development of the numerical techniques [38].

The prime drawback of using MoM lies beneath its rectangular and triangular basis function. Their usage to examine the problem of electromagnetic scattering by dielectric objects with high dielectric constant leads to spurious charges. This problem was alleviated by means of solenoidal basis function [39, 40]. Wilton and Govind [41] made an effort to circumvent the error currents and anomaly behaviour of the solution near the edges by means of triangle expansion functions with suitable singular pulses at the edges.

The MoM has been favourably employed in variety of electromagnetic applications such as scattering problems [42-45], synthesis of slotted waveguide array antenna [46], field analysis in circular-loop antenna [47, 48], the solution for patch antenna using volume integral equation (VIE) [49], VHF propagation modelling [50] and microwave tomography system [51].

1.4 State of the Art of the Original Contribution

The dominant focus of the research work is the modelling and analysis of the complex electromagnetic problems by means of subgridded FDTD (SGFDTD) scheme to be employed in several applications. In order to achieve the research goal, the basic idea is to use the hybridisation of SGFDTD with MoM in which the tools for electromagnetic field modelling problems can be designed with more accuracy and efficiency. The surface kernel solution of MoM technique is derived. The method is used to predict the surface current distributions on structures with closely spaced parallel wires, such as dipoles, loops and helical antennas. Next, the present work is devoted to mathematical modelling and implementing SGFDTD in 2-D Cartesian coordinate keeping minimum reflection at the boundary. This method is applied to the interaction between overhead transmission lines to the underground pipeline for validation purposes. The SGFDTD formulation is then embedded inside the hybrid MoM-FDTD method. The full code with the adaptation of subgridding inside the hybrid MoM-FDTD design problems is written in Fortran 90 as a platform. The hybridisation of MoM-FDTD-SGFDTD code is used to analyse and investigate the applications in electromagnetic problems for validation such as the interaction between EM fields to the human body.

1.5 Overview of the Thesis

Chapter 1 postulates historical background and literature survey of FDTD and MoM techniques used to solve electromagnetic scattering issues. It should be noted that a more detailed review of existing literature is reported at the beginning of each chapter with separate references at the end.

Chapter 2 unfolds the theoretical concept of FDTD principles including the derivation of the magnetic and electric field update equations, parameters that control the stability and accuracy, plane wave source modelling concept by applying the equivalent surface, and finally the implementation of Berenger’s PML absorbing boundary condition.

Chapter 3 presents the surface kernel solution of the Method of Moments. The surface current distributions on structures with closely spaced parallel wires, such as dipoles, loops and helical antennas, are computed by using the method of moments with a general surface patch formulation. The modelling method employed a two-dimensional electric surface patch integral equation formulation solved by independent piecewise-linear basis function methods in the circumferential and axial directions of the wire.

Chapter 4 explains the modelling and analysis of quasi-static FDTD subgridding technique in two-dimensional approach. The method has been applied to model biological cell with floquet theorem. The interaction between overhead transmission lines and underground pipeline at power-line frequency is also modelled for validation. FDTD technique is used for the whole structure spatial problem combined with subgrid method at the pipeline. The soil in the common corridor has been designed as arbitrarily inhomogeneous.

Chapter 5 describes the hybridisation MoM-FDTD-SGFDTD computational method. The modelling on multiple-region hybrid techniques with frequency-domain MoM and time-domain FDTD and subgridding are suggested and investigated. The method is validated for near field and far field applications particularly on the interaction between electromagnetic fields and human body in which the RFID antenna is located and moved at several positions in front and back of inhomogeneous human body model.

Chapter 6 summarises the overall conclusions and recommendations for further work on related topics.

1.6 References

[1] K. S. Yee, "Numerical solution of initial boundary value problems involving Maxwell's equations in isotropic media," *IEEE Transactions on Antennas and Propagation,* vol. AP-14, pp. 302-307, 1966.

[2] A. Taflove and M. E. Brodwin, "Numerical solution of steady-state electromagnetic scattering problems using the time-dependent maxwell's equations," *IEEE Transactions on Microwave Theory and Techniques*, vol. 23, pp. 623-630, 1975.

[3] A. Taflove and M. E. Brodwin, "Computation of the electromagnetic fields and induced temperatures within a model of the microwave-irradiated human eye," *IEEE Transactions on Microwave Theory and Techniques*, vol. 23, pp. 888-896, 1975.

[4] R. Holland, "THREDE: A free-field EMP coupling and scattering code," *IEEE Transactions on Nuclear Science,* vol. NS-24, pp. 2416-2421, 1977.

[5] K. S. Kunz and K. M. Lee, "A three-dimensional finite-difference solution of the external response of an aircraft to a complex transient EM environment: Part I-The method and its implementation," *IEEE Transactions on Electromagnetic Compatibility,* vol. EMC-20, pp. 328-333, 1978.

[6] A. Taflove, "Application of the finite-difference time-domain method to sinusoidal steady-state electromagnetic-penetration problems," *IEEE Transactions on Electromagnetic Compatibility,* vol. EMC-22, pp. 191-202, 1980.

[7] D. E. Merewether, "Transient currents induced on a metallic body of revolution by an electromagnetic pulse," *IEEE Transactions on Electromagnetic Compatibility,* vol. EMC-13, pp. 41-44, 1971.

[8] B. Engquist and A. Majda, "Absorbing boundary conditions for numerical simulation of waves," *Applied Mathematical Sciences*, vol. 74, pp. 1765-1766, 1977.

[9] G. Mur, "Absorbing boundary conditions for the finite-difference approximation of the time-domain electromagnetic-field equations," *IEEE Transactions on Electromagnetic Compatibility*, vol. EMC-23, pp. 377-382, 1981.

[10] Z. P. Liao, H. L. Wong, B. P. Yang, and Y. F. Yuan, "A transmitting boundary for transient wave analysis," *Scientia Sinica (Series A)*, vol. XXVII, pp. 1063-1076, 1984.

[11] R. G. Keys, "Absorbing boundary conditions for acoustic media," *Geophysics*, vol. 50, pp. 892-902, 1985.

[12] R. L. Higdon, "Absorbing boundary conditions for difference approximations to the multi-dimensional wave equation," *Mathematics of Computation*, vol. 47, pp. 437-459, 1986.

[13] J. P. Berenger, "A perfectly matched layer for the absorption of electromagnetic waves," *Journal of Computational Physics*, vol. 114, pp. 185-200, 1994.

[14] D. T. Prescott and N. V. Shuley, "Reflection analysis of FDTD boundary conditions - Part I: Time-space absorbing boundaries," *IEEE Transactions on Microwave Theory and Techniques*, vol. 45, pp. 1162-1170, 1997.

[15] D. T. Prescott and N. V. Shuley, "Reflection analysis of FDTD boundary conditions - Part II: Berenger’s PML absorbing layers," *IEEE Transactions on Microwave Theory and Techniques*, vol. 45, pp. 1171-1178, 1997.

[16] A. Akyurtlu, D. H. Werner, V. Veremey, D. J. Steich, and K. Aydin, "Staircasing errors in FDTD at an air-dielectric interface," *IEEE Microwave and Guided Wave Letters*, vol. 9, pp. 444-446, 1999.

[17] J. B. Schneider and C. L. Wagner, "FDTD dispersion revisited: Faster-than-light propagation," *IEEE Microwave and Guided Wave Letters*, vol. 9, pp. 54-56, 1999.

[18] J. Represa, C. Pereira, M. Panizo, and F. Tadeo, "A simple demonstration of numerical dispersion under FDTD," *IEEE Transactions on Education*, vol. 40, pp. 98-102, 1997.

[19] R. Wu, G. Benqing, and Y. Shiming, "An improved method in FDTD simulation to reduce reflection from non-uniform mesh," *3rd International Conference on Microwave and Millimeter Wave Technology Proceedings*, pp. 646-649, 2002.

[20] S. Kapoor, "Sub-cellular technique for finite-difference time-domain method," *IEEE Transactions on Microwave Theory and Techniques*, vol. 45, pp. 673-677, 1997.

[21] P. Thoma and T. Weiland, "Numerical stability of finite difference time domain methods," *IEEE Transactions on Magnetics*, vol. 34, pp. 2740-2743, 1998.

[22] T. Namiki, "A new FDTD algorithm based on alternating-direction implicit method," *IEEE Transactions on Microwave Theory and Techniques*, vol. 47, pp. 2003-2007, 1999.

[23] F. H. Zheng, Z. Z. Chen, and J. Z. Zhang, "Toward the development of a three-dimensional unconditionally stable finite-difference time-domain method," *IEEE Transactions on Microwave Theory and Techniques*, vol. 48, pp. 1550-1558, 2000.

[24] B. K. Huang, Y. S. Jiang, and W. B. Wang, "A hybrid 2-D ADI-FDTD subgridding scheme," *IEEE International Symposium on Antennas, Propagation and EM Theory Proceedings*, pp. 707-710, 2003.

[25] M. F. Hadi and M. P. May, "A modified FDTD (2,4) scheme for modeling electrically large structures with high-phase accuracy," *IEEE Transactions on Antennas and Propagation*, vol. 45, pp. 254-264, 1997.

[26] Z. H. Shao, Z. X. Shen, Q. Y. He, and G. W. Wei, "A generalized higher order finite-difference time-domain method and its application in guided-wave problems," *IEEE Transactions on Microwave Theory and Techniques*, vol. 51, pp. 856-861, 2003.

[27] G. Cerri, P. Russo, A. Schiavoni, G. Tribellini, and P. Bielli, "MoM-FDTD hybrid technique for analysing scattering problems," *Electronic Letters*, vol. 34, pp. 438-440, 1998.

[28] A. Monorchio and R. Mittra, "A hybrid finite-element finite-difference time-domain (FE/FDTD) technique for solving complex electromagnetic problems," *IEEE Microwave and Guided Wave Letters*, vol. 8, pp. 93-95, 1998.

[29] N. V. Venkatarayalu, Y. B. Gan, R. Lee, and L. W. Li, "Antenna modeling using stable hybrid FETD-FDTD method," *Proceedings of 2007 International Symposium on Antennas and Propagation, Honolulu, USA*, pp. 3736-3739, 2007.

[30] S. S. Zivanovic, K. S. Yee, and K. K. Mei, "A subgridding method for the time-domain finite-difference method to solve Maxwell's equations," *IEEE Transactions on Microwave Theory and Techniques*, vol. 39, pp. 471-479, 1991.

[31] P. Thoma and T. Weiland, "A consistent subgridding scheme for the finite difference time domain method," *International Journal of Numerical Modelling-Electronic Networks Devices and Fields*, vol. 9, pp. 359-374, 1996.

[32] S. Chaillou, J. Wiart, and W. Tabbara, "A subgridding scheme based on mesh nesting for the FDTD method," *Microwave and Optical Technology Letters*, vol. 22, pp. 211-214, 1999.

[33] S. M. Wang, F. L. Teixeira, R. Lee, and J. F. Lee, "Optimization of subgridding schemes for FDTD," *IEEE Microwave and Wireless Components Letters*, vol. 12, pp. 223-225, 2002.

[34] K. Xiao, D. J. Pommerenke, and J. L. Drewniak, "A three-dimensional FDTD subgridding algorithm based on interpolation of current density," *IEEE International Symposium on Electromagnetic Compatibility*, vol. 1, pp. 118-123, 2004.

[35] J. H. Richmond, "Digital computer solutions of the rigorous equations for scattering problems," *Proceedings of the IEEE*, vol. 53, pp. 796- 804, 1965.

[36] J. H. Richmond, "A wire-grid model for scattering by conducting bodies," *IEEE Transactions on Antennas and Propagation*, vol. 14, pp. 782-786, 1966.

[37] R. F. Harrington, "Matrix methods for field problems," *Proceedings of the IEEE*, vol. 55, pp. 136-149, 1967.

[38] R. F. Harrington, *Field computation by moment methods*. New York: The Macmillan Co., 1968.

[39] L. Mendes and S. Antenor, "A tridimensional solenoidal basis function to analyze 3D scattering of homogeneous dielectrics using the method of moments," *SBMO/IEEE MTT-S International Microwave and Optoelectronics Conference Proceedings*, vol. 2, pp. 897-900, 1995.

[40] S. Antenor and L. Mendes, "Method of moments with solenoidal basis functions: an approach to analyze the scattering by inhomogeneous dielectrics," *Third International Conference on Computation in Electromagnetics (Conf. Publ. No. 420)*, pp. 318-321, 1996.

[41] D. Wilton and S. Govind, "Incorporation of edge conditions in moment method solutions," *IEEE Transactions on Antennas and Propagation*, vol. 25, pp. 845-850, 1977.

[42] N. C. Albertsen, J. E. Hansen, and N. E. Jensen, "Computation of radiation from wire antennas on conducting bodies," *IEEE Transactions on Antennas and Propagation*, vol. 22, pp. 200-206, 1974.

[43] E. H. Newman and D. M. Pozar, "Electromagnetic modeling of composite wire and surface geometries," *IEEE Transactions on Antennas and Propagation*, vol. 26, pp. 784-789, 1978.

[44] M. E. Peters and E. H. Newman, "Method of moments analysis of anisotropic artificial media composed of dielectric wire objects," *IEEE Transactions on Microwave Theory and Techniques*, vol. 43, pp. 2023-2027, 1995.

[45] S. M. Rao, D. R. Wilton, and A. W. Glisson, "Electromagnetic scattering by surfaces of arbitrary shape," *IEEE Transactions on Antennas and Propagation*, vol. 30, pp. 409-418, 1982.

[46] A. J. Sangster and A. H. I. McCormick, "Theoretical design/synthesis of slotted waveguide arrays," *IEE Proceedings Microwaves, Antennas and Propagation*, vol. 136, pp. 39-46, 1989.

[47] L. W. Li, C. P. Lim, and M. K. Leong, "Method of moments analysis of electrically large circular-loop antennas: non-uniform currents," *IEEE Antennas and Propagation Society International Symposium*, vol. 4, pp. 2542-2545, 1999.

[48] L. W. Li, M. S. Yeo, and M. K. Leong, "Method of moments analysis of EM fields in a multilayered spheroid radiated by a thin circular loop antenna," *IEEE Transactions on Antennas and Propagation*, vol. 52, pp. 2391-2402, 2004.

[49] S. N. Makarov, S. D. Kulkarni, A. G. Marut, and L. C. Kempel, "Method of moments solution for a printed patch/slot antenna on a thin finite dielectric substrate using the volume integral equation," *IEEE Transactions on Antennas and Propagation*, vol. 54, pp. 1174-1184, 2006.

[50] J. T. Johnson, R. T. Shin, J. C. Eidson, L. Tsang, and J. A. Kong, "A method of moments model for VHF propagation," *Antennas and Propagation Society International Symposium*, vol. 1, pp. 362-365, 1997.

[51] J. L. Hu, Z. P. Wu, H. McCann, L. E. Davis, and C. G. Xie, "Quasi-three-dimensional method of moments for analyzing electromagnetic wave scattering in microwave tomography systems," *IEEE Sensors Journal*, vol. 5, pp. 216-223, 2005.

Chapter 2

FDTD Technique for Field Truncation

2.1 Introduction

Over the past few years, finite-difference time-domain (FDTD) method [1] have become increasingly prevalent in the computational electromagnetic problems due to its simplicity, efficiency, robustness and versatility scheme for highly complex configuration in the computational domain. Generally, FDTD technique is the most well-known numerical method for the solution of problems in electromagnetic simulation ranging from RF to optical frequencies. It is considered to be one of the most powerful numerical techniques for solving partial differential equations of any kind. In addition, it can be utilized to solve the spatial as well as the temporal distributions of electric and magnetic fields in various media. In principle, FDTD is a method that divides the solution domain into finite discrete points and then replaces the partial differential equation with a set of difference equations. It has successfully been applied to many problems of propagation, radiation and scattering of electromagnetic waves such as antenna, radar, wireless communication system, high speed electronic, photonic, radiography, x-ray crystallography, bio-electromagnetic and geophysical imaging. A good measure of its success lies in the fact that thousand of papers on the subject have been published in journals and international symposium, apart from the books and tutorials devoted to it. Moreover, much specific and general purpose commercial software is available on the market which further extends its appeal globally. Furthermore, three books are used as the main references to the recent FDTD research written by Taflove and Hagness [1], Taflove [2] and Kunz and Luebbers [3].

2.2 FDTD Updating Stencils

A pioneering way of describing the electromagnetic phenomena was introduced by James Clerk Maxwell in 1865 [4]. Later in 1873, he published an article called "Treatise on Electricity and Magnetism" in which the discoveries of Coulomb, Oersted, Ampere and Faraday were united into four refined constructed mathematical equations known as Maxwell's equations. The differential time domain Maxwell's equations in a linear medium are given by:

$$\frac{\partial B}{\partial t} = -\nabla \times E - J_m \tag{2.1}$$

$$\frac{\partial D}{\partial t} = \nabla \times H - J_e \tag{2.2}$$

B is the magnetic flux density in Wb/m^2, D is the electric flux density in C/m^2, E is the electric field in V/m and H is the magnetic field in A/m. J_m is the magnetic current density in V/m^2 and is defined to relate any magnetic loss to the field. J_e is the electric current density in A/m^2 and is defined to relate any electric loss to the field. J_m and J_e are respectively given by:

$$J_m = \sigma^* \times H \tag{2.3}$$

$$J_e = \sigma \times E \tag{2.4}$$

σ^* is magnetic resistivity in Ω/m and σ is the electric conductivity in S/m. In materials with field-independent, direction-independent and frequency-independent electric and magnetic properties, the following proportions apply:

$$B = \mu \times H \tag{2.5}$$

$$D = \varepsilon \times E \tag{2.6}$$

μ is the magnetic permeability in H/m and ε is the electric permittivity in F/m. Inserting (2.3) and (2.5) to (2.1) and dividing by μ gives:

$$\frac{\partial H}{\partial t} = \frac{1}{\mu}\left(-\nabla \times E - \sigma^* H\right) \tag{2.7}$$

$\sigma^* H$ is the magnetic losses which may exist inside the medium. Inserting (2.4) and (2.6) to (2.2) and dividing by ε gives:

$$\frac{\partial E}{\partial t} = \frac{1}{\varepsilon}\left(\nabla \times H - \sigma E\right) \tag{2.8}$$

σE is the electric losses which may exist inside the medium. In Cartesian coordinates, equations (2.7) and (2.8) yield the following six scalar equations:

$$\frac{\partial H_x}{\partial t} = \frac{1}{\mu}\left(\frac{\partial E_y}{\partial z} - \frac{\partial E_z}{\partial y} - \sigma^* H_x\right) \tag{2.9}$$

$$\frac{\partial H_y}{\partial t} = \frac{1}{\mu}\left(\frac{\partial E_z}{\partial x} - \frac{\partial E_x}{\partial z} - \sigma^* H_y\right) \tag{2.10}$$

$$\frac{\partial H_z}{\partial t} = \frac{1}{\mu}\left(\frac{\partial E_x}{\partial y} - \frac{\partial E_y}{\partial x} - \sigma^* H_z\right) \tag{2.11}$$

$$\frac{\partial E_x}{\partial t} = \frac{1}{\varepsilon}\left(\frac{\partial H_z}{\partial y} - \frac{\partial H_y}{\partial z} - \sigma E_x\right) \tag{2.12}$$

$$\frac{\partial E_y}{\partial t} = \frac{1}{\varepsilon}\left(\frac{\partial H_x}{\partial z} - \frac{\partial H_z}{\partial x} - \sigma E_y\right) \tag{2.13}$$

$$\frac{\partial E_z}{\partial t} = \frac{1}{\varepsilon}\left(\frac{\partial H_y}{\partial x} - \frac{\partial H_x}{\partial y} - \sigma E_z\right) \tag{2.14}$$

A space point in a rectangular grid is defined from Yee's original notation [5] as:

$$(i, j, k) = (i\Delta x, j\Delta y, k\Delta z) \tag{2.15}$$

Let *F* denote any function of discrete space and time given by:

$$F(i\Delta x, j\Delta y, k\Delta z, n\Delta t) \equiv F^n_{i,j,k} \tag{2.16}$$

Δx, Δy and Δz are the grid space increments in *x, y* and *z* directions respectively, and Δt is the time increment. Using a central finite-difference approximation, space and time derivatives of *F* can be written as:

$$\frac{\partial F}{\partial x} = \frac{F^n_{i+1/2,j,k} - F^n_{i-1/2,j,k}}{\Delta x} + O(\Delta x)^2 \tag{2.17}$$

$$\frac{\partial F}{\partial t} = \frac{F^{n+1/2}_{i,j,k} - F^{n-1/2}_{i,j,k}}{\Delta t} + O(\Delta t)^2 \tag{2.18}$$

In equation (2.17), $O(\Delta x)^2$ is the error term that represents all the remaining terms in a Taylor series expansion. It is known as a central finite difference scheme in space with second-order accuracy. Similarly, (2.18) is second-order accurate in time. Applying Yee's finite-difference scheme to (2.9) gives:

$$\frac{H_x\Big|_{i,j,k}^{n+1/2}-H_x\Big|_{i,j,k}^{n-1/2}}{\Delta t}=\frac{1}{\mu_{i,j,k}}\left(\begin{array}{l}\dfrac{E_y\Big|_{i,j,k+1/2}^{n}-E_y\Big|_{i,j,k-1/2}^{n}}{\Delta z}- \\ \dfrac{E_z\Big|_{i,j+1/2,k}^{n}-E_z\Big|_{i,j-1/2,k}^{n}}{\Delta y}-\sigma_{i,j,k}^{*}H_x\Big|_{i,j,k}^{n}\end{array}\right) \tag{2.19}$$

The $H_x\big|_{i,j,k}^{n}$ field component in (2.19) is evaluated at time step *n*. However, the value of $H_x\big|_{i,j,k}^{n}$ at time step *n* is not available and hence the following interpolated approximation is used:

$$H_x\Big|_{i,j,k}^{n}=\frac{H_x\Big|_{i,j,k}^{n+1/2}+H_x\Big|_{i,j,k}^{n-1/2}}{2} \tag{2.20}$$

By substituting equation (2.20) in (2.19), leaving $H_x\big|_{i,j,k}^{n+1/2}$ on the left hand side and passing the all remaining terms to the right, assuming cubical FDTD cells are used, the finite difference updating equation for the magnetic and electric field components can be derived as:

$$H_x\Big|_{i,j,k}^{n+1/2}=D_{a,H_x}\Big|_{i,j,k}H_x\Big|_{i,j,k}^{n-1/2}+D_{b,H_x}\Big|_{i,j,k}\left(\begin{array}{l}E_y\Big|_{i,j,k+1/2}^{n}-E_y\Big|_{i,j,k-1/2}^{n} \\ +E_z\Big|_{i,j-1/2,k}^{n}-E_z\Big|_{i,j+1/2,k}^{n}\end{array}\right) \tag{2.21}$$

$$H_y\Big|_{i,j,k}^{n+1/2}=D_{a,H_y}\Big|_{i,j,k}H_y\Big|_{i,j,k}^{n-1/2}+D_{b,H_y}\Big|_{i,j,k}\left(\begin{array}{l}E_z\Big|_{i+1/2,j,k}^{n}-E_z\Big|_{i-1/2,j,k}^{n} \\ +E_x\Big|_{i,j,k-1/2}^{n}-E_x\Big|_{i,j,k+1/2}^{n}\end{array}\right) \tag{2.22}$$

$$H_z\Big|_{i,j,k}^{n+1/2} = D_{a,H_z}\Big|_{i,j,k} H_z\Big|_{i,j,k}^{n-1/2} + D_{b,H_z}\Big|_{i,j,k}\begin{pmatrix} E_x\big|_{i,j+1/2,k}^{n} - E_x\big|_{i,j-1/2,k}^{n} \\ + E_y\big|_{i-1/2,j,k}^{n} - E_y\big|_{i+1/2,j,k}^{n} \end{pmatrix} \tag{2.23}$$

$$E_x\Big|_{i,j,k}^{n+1} = C_{a,E_x}\Big|_{i,j,k} E_x\Big|_{i,j,k}^{n} + C_{b,E_x}\Big|_{i,j,k}\begin{pmatrix} H_z\big|_{i,j+1/2,k}^{n+1/2} - H_z\big|_{i,j-1/2,k}^{n+1/2} \\ + H_y\big|_{i,j,k-1/2}^{n+1/2} - H_y\big|_{i,j,k+1/2}^{n+1/2} \end{pmatrix} \tag{2.24}$$

$$E_y\Big|_{i,j,k}^{n+1} = C_{a,E_y}\Big|_{i,j,k} E_y\Big|_{i,j,k}^{n} + C_{b,E_y}\Big|_{i,j,k}\begin{pmatrix} H_x\big|_{i,j,k+1/2}^{n+1/2} - H_x\big|_{i,j,k-1/2}^{n+1/2} \\ + H_z\big|_{i-1/2,j,k}^{n+1/2} - H_z\big|_{i+1/2,j,k}^{n+1/2} \end{pmatrix} \tag{2.25}$$

$$E_z\Big|_{i,j,k}^{n+1} = C_{a,E_z}\Big|_{i,j,k} E_z\Big|_{i,j,k}^{n} + C_{b,E_z}\Big|_{i,j,k}\begin{pmatrix} H_y\big|_{i+1/2,j,k}^{n+1/2} - H_y\big|_{i-1/2,j,k}^{n+1/2} \\ + H_x\big|_{i,j-1/2,k}^{n+1/2} - H_x\big|_{i,j+1/2,k}^{n+1/2} \end{pmatrix} \tag{2.26}$$

It can be seen that the coefficients on the left hand side are referred to as Yee's updating coefficients. The electric field coefficients are given by:

$$C_a\Big|_{i,j,k} = \left(1 - \frac{\sigma_{i,j,k}\Delta t}{2\varepsilon_{i,j,k}}\right) \Bigg/ \left(1 + \frac{\sigma_{i,j,k}\Delta t}{2\varepsilon_{i,j,k}}\right) \tag{2.27}$$

$$C_{b_p}\Big|_{i,j,k} = \left(\frac{\Delta t}{\varepsilon_{i,j,k}\Delta_p}\right) \Bigg/ \left(1 + \frac{\sigma_{i,j,k}\Delta t}{2\varepsilon_{i,j,k}}\right) \tag{2.28}$$

The magnetic updating coefficients can be written as:

$$D_a\Big|_{i,j,k} = \left(1 - \frac{\sigma^*_{i,j,k}\Delta t}{2\mu_{i,j,k}}\right) \Bigg/ \left(1 + \frac{\sigma^*_{i,j,k}\Delta t}{2\mu_{i,j,k}}\right) \tag{2.29}$$

$$D_{b_p}\Big|_{i,j,k} = \left(\frac{\Delta t}{\mu_{i,j,k}\Delta_p}\right) \Bigg/ \left(1 + \frac{\sigma^*_{i,j,k}\Delta t}{2\mu_{i,j,k}}\right) \tag{2.30}$$

The subscript p can be x, y or z and Δ_p is the cell size in the p-direction. Assuming the structure under investigation contains different types of material such as dielectric or magnetic, electric and magnetic field updating coefficients can be easily calculated from equations (2.27) to (2.30) before the FDTD time stepping algorithm starts. The orientation of the fields in Figure 2.1 is known as the FDTD lattice or Yee cell. The magnetic and electric fields are located on the faces and the edges of the cube respectively. Each electric field vector component is surrounded by four circulating magnetic field vector components and vice versa. Both the electric and magnetic field vector components are located half a cell from each other. In addition, this arrangement permits easy implementations of the central finite difference approximations and the integral form of the Faraday's law and the Ampere's law. The system of difference equations is solved at the nodes. Figure 2.2 illustrates the typical relationship between field components within a quarter of a cell and on a plane distinctly helpful when handling boundary conditions of a closed region.

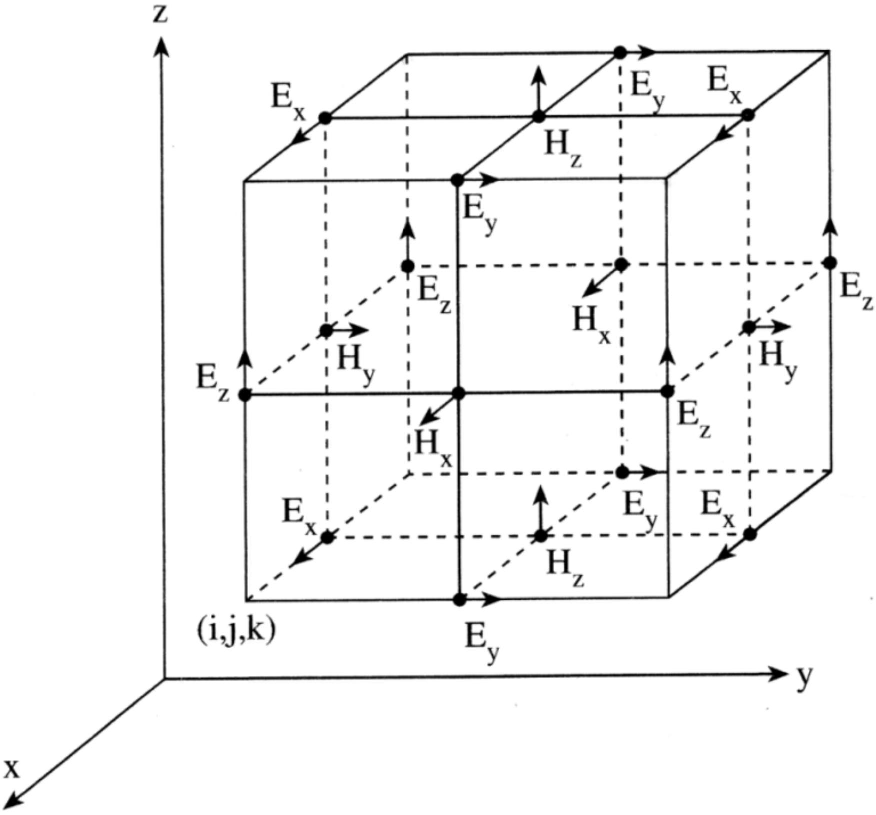

Figure 2.1: The electric and magnetic field components distribution on the FDTD lattice [6].

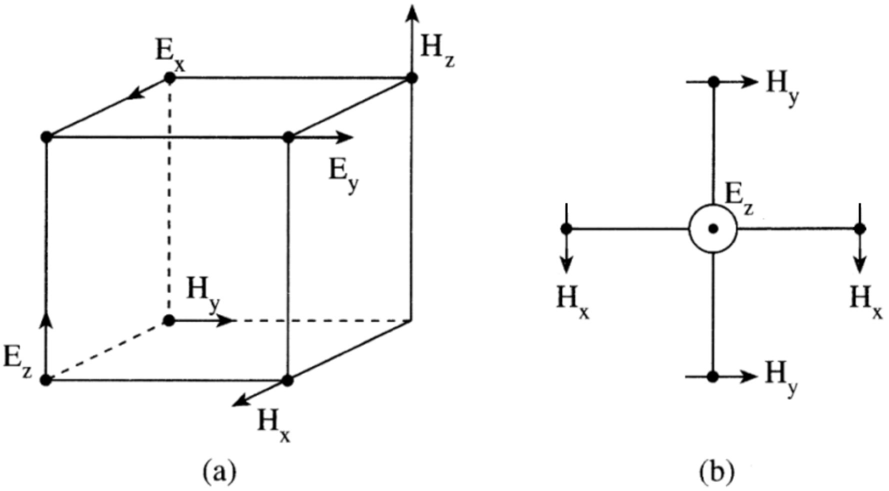

Figure 2.2: Relationship between field components: (a) within a quarter of a unit cell, (b) on a plane [6].

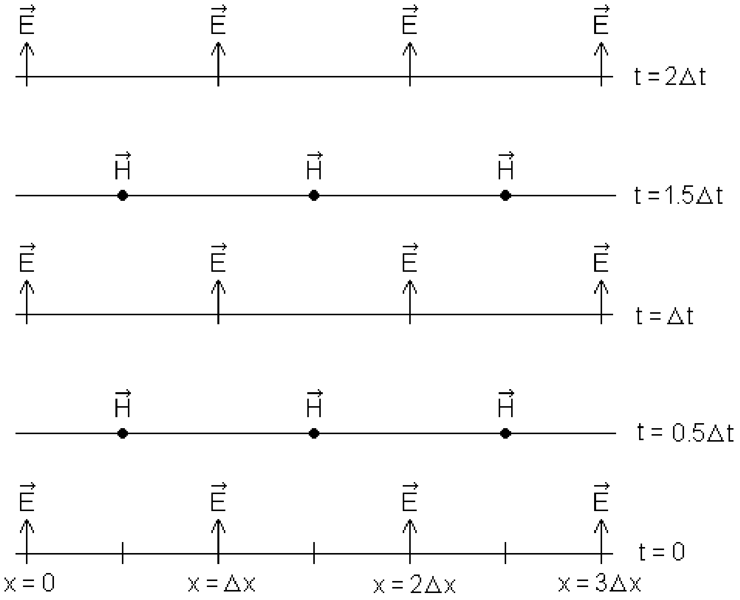

Figure 2.3: Space-time chart of the Yee algorithm in a leapfrog arrangement [1].

The field quantities are solved with a leapfrog arrangement where a half time step separates the solutions of the electric and magnetic fields as shown in Figure 2.3. The time-stepping of the FDTD algorithm is continued until the desired late time pulse response or steady state behaviour is reached. Figure 2.4 depicts the time-stepping FDTD algorithms flow chart. Apparently, a suitable size of the time step should be chosen properly to avoid the late time instability of the algorithms, after determining the spatial resolution based on the geometrical features and the operating frequency. It can be seen that a leapfrog arrangement between the electric and magnetic field vector components is used to implement the time step of the FDTD algorithm. The grids of the electric and magnetic fields are displaced half a cell between them indicating that the computer must work through them in turn.

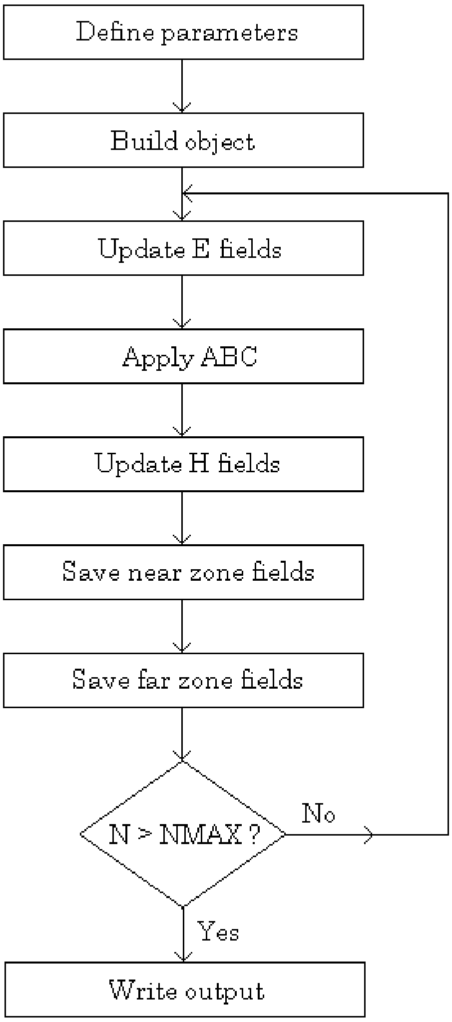

Figure 2.4: The flow chart of the time stepping FDTD algorithm [3].

2.3 Numerical Dispersion and Stability

The accuracy and stability of FDTD method is controlled by two significant parameters namely the space resolution Δx, Δy, Δz and the time resolution Δt. Waves of different frequencies will propagate at slightly different speeds through the grid due to the approximations inherent in FDTD. As a result, the grid dispersion error will occur in the FDTD. The difference in the propagation speed also depends on the direction of propagation relative to the grid. Hence, the grid dispersion error must be reduced to an acceptable level to increase the accuracy and stability of the results. To ensure the FDTD numerical accuracy, the spatial increment h used in the simulation is required to be small enough compared to the wavelength. Usually, h is less than or equal to $\lambda_{min}/10$, where λ_{min} is the shortest wavelength at the frequency of computation. The numerical grid produces a certain amount of numerical dispersion error, when the grid size and the angle of propagating wave are increased as illustrated in Figure 2.5. Numerical dispersion is observed to be approximately 1% when the cell size is exactly $\lambda/10$.

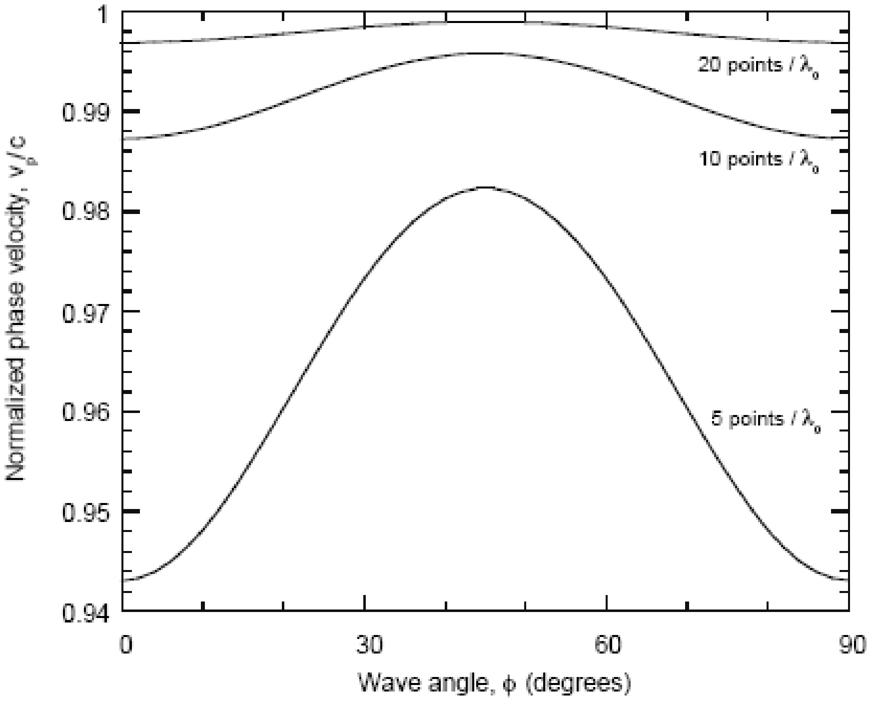

Figure 2.5: Variation of the numerical phase velocity with wave propagation angle in two-dimensional FDTD grid [1].

The time increment Δt must satisfy the CFL criterion [1, 3] to ensure the stability of the computation process, which sets the relation between the time and space resolution for three-dimensional FDTD given by:

$$v_{\max}\Delta t \leq \frac{1}{c\sqrt{\frac{1}{(\Delta x)^2}+\frac{1}{(\Delta y)^2}+\frac{1}{(\Delta z)^2}}} \tag{2.31}$$

v_{max} is the maximum phase velocity of the propagating wave in any material in the model. For the three-dimensional cubic cell space lattice with $\Delta x = \Delta y = \Delta z = h$ in a d-dimensional spatially homogeneous FDTD grid, the time step is bounded by:

$$\Delta t \leq \frac{h}{v_{\max}\sqrt{d}} \tag{2.32}$$

d is the number of the space dimensions (d = 1, 2 or 3). The time step should be chosen as large as possible to minimise the burden on the computer run time requirement. Smaller time step will give more accurate result with longer simulation run time. The time resolution value of $h/(2v_{max})$ is always conceived in many FDTD codes to compromise the accuracy and stability of FDTD simulation whilst the CFL criterion is satisfied.

2.4 Incident Wave Source Conditions

An electromagnetic wave excitation will be introduced into the FDTD lattice for modelling the scattering problem. This can be achieved by using the electric and magnetic field vector components to realize the wave source compared to the total number of field components in the space lattice. In addition, the required computation time and resources to simulate the source is relatively small compared to the required ordinary time-stepping of the fields. As a result, the maximum algorithm efficiency is achieved. The compact electromagnetic wave sources can be classified into two general classes namely the hard source and the total/scattered field formulation for the plane wave excitation in one and three dimensional lattices.

2.4.1 Hard Source Excitation

The hard source is set up by assigning a desired time function to specific electric or magnetic field components in the FDTD lattice. In 1-D TM grid, the hard source on E_z could be established at the grid source point i_s to generate a continuous sinusoidal wave of frequency f_o which is switched on at $n = 0$. There are three common hard sources discussed here. The first type of the hard source can be expressed as [1]:

$$E_z\Big|_{i_s}^{n} = E_o \sin\left(2\pi f_o n\Delta t\right) \tag{2.33}$$

The second hard source provides a wideband Gaussian pulse with finite DC content. The pulse is centred at the time step n_o and has a $1/e$ characteristic decay of n_{decay} time steps. It is simply given by:

$$E_z\Big|_{i_s}^{n} = E_o e^{-\left((n-n_o)/n_{decay}\right)^2} \tag{2.34}$$

Equation (2.34) has a nonzero value at $n = 0$. n_o should take a value of at least $3n_{decay}$ if a smooth transition from zero into the Gaussian pulse is needed. The third hard source provides zero DC content, bandpass Gaussian pulse with Fourier spectrum symmetrical about f_o. The pulse is centred at the time step n_o and has a $1/e$ characteristic decay of n_{decay} time steps. It is expressed as:

$$E_z\Big|_{i_s}^{n} = E_0 e^{-\left(\left(n-n_0\right)/n_{decay}\right)^2} \sin\left[2\pi f_0\left(n-n_0\right)\Delta t\right] \qquad (2.35)$$

2.4.2 Plane-Wave Source Excitation

The plane wave source excitation model was used by Yee in 1966 [5]. An arbitrary incident plane wave is used for the excitation purposes. The incident plane wave is modelled and approximated within the FDTD space lattice. Two methods of excitation of the plane wave on the space lattice is discussed here, namely the initial condition technique and the total/scattered field formulation technique. The initial condition method was used by Yee in the implementation of the FDTD method to represent an incident plane wave with special applications in the RCS simulations. The values of electric and magnetic field vector components at the zero time step of the incident plane wave throughout the problem space are preset in sign and magnitude. As a result, this will give the desired polarisation of the incident plane wave. However, this method has a drawback due to the fact that it is a non-compact wave source. It requires a large number of additional free space cells to contain initial conditions of long duration pulses or continuous sinusoids for oblique incident angles of the propagating wave. This will unfortunately increase the size of the problem space which one must avoid. Hence, the technique is limited to special usage only. The most popular method used in many FDTD software is the total/scattered field formulation method [7, 8] due to the fact that it allows the modelling of the FDTD with long-duration pulsed or sinusoidal illuminations for arbitrary plane wave propagation directions.

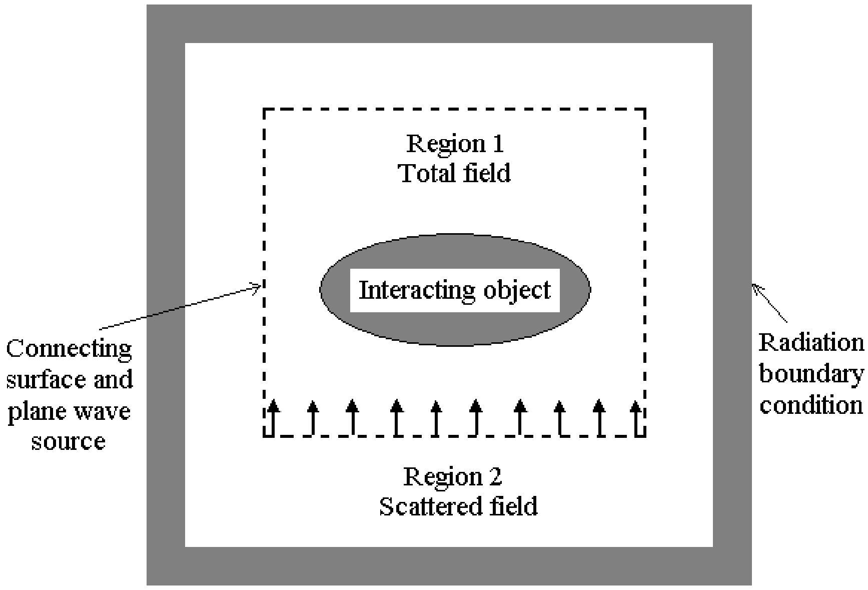

Figure 2.6: Total and scattered field zoning for a generic scattering case [1].

Figure 2.6 presents the total and scattered field zoning for a generic scattering case. Basically, it shows two distinct regions of interest namely the total field and scattered field region. Both of the regions are separated by a non-physical virtual surface applied numerically with a special treatment to include the incident wave excitation and to split the problem space into the total field and scattered field regions. As a result, the scattered field vector values can be computed in the scattered field region without the presence of the incident field. Furthermore, the arbitrary incident plane wave with different oblique incidence angles using incident-field array (IFA) excitation scheme [1] can be modelled efficiently. The IFA is generally an FDTD-based lookup table from which the incident-field values are covered on the FDTD lattice in the propagating direction.

2.4.2.1 Total/Scattered Field Formulation in 1-D

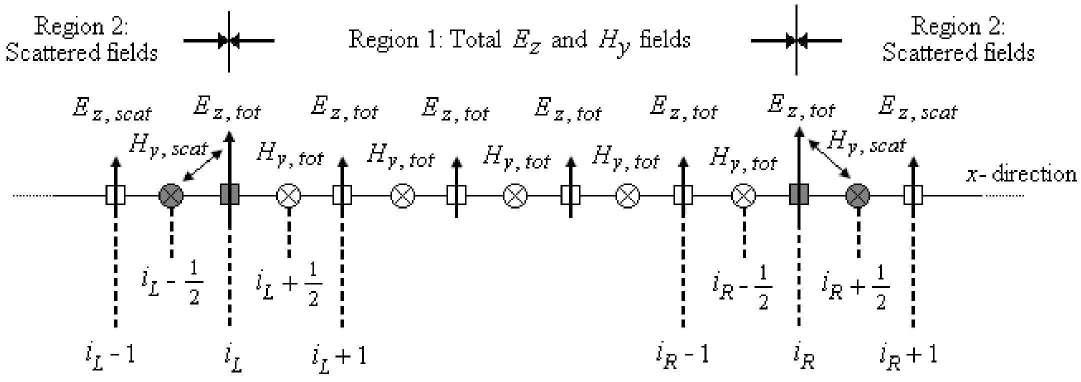

Figure 2.7: Total and scattered field components for 1-D FDTD grid.

The basic principle of the total/scattered formulation example is best illustrated by simple example of one-dimensional transverse magnetic (TM) field case, as shown in Figure 2.7 [1]. The formulation divides the x-directed array of E_z and H_y components into two regions, region 1 (total fields) and region 2 (scattered fields) by a virtual surface. At this surface interface between the two regions, there exists a special set of E and H components as depicted by the grey-coloured components. These four field components are E_z at i_L and i_R and H_y at (i_L-$^1/_2$) and (i_R+$^1/_2$). Subscripts L and R represent left and right respectively. According to Yee algorithm, these may have different types, total or scattered, respectively. The incident fields, E_{inc} and H_{inc} are known and may be calculated at the outer interface points. They are added to the regular updating equations. For example, E_z at i_L, the left interface surface, is considered to be a total field component and by applying the basic FDTD algorithm, it is updated as:

$$E_z\Big|_{tot,i_L}^{n+1} = E_z\Big|_{tot,i_L}^{n} + \frac{\Delta t}{\varepsilon_o \Delta}\left(H_y\Big|_{tot,i_L+1/2}^{n+1/2} - H_y\Big|_{scat,i_L-1/2}^{n+1/2} \right) \tag{2.36}$$

Subscripts *tot* and *scat* stand for total and scattered fields respectively. It is clear that the above equation is inconsistent, so $H_{y,tot}$ at (i_L-$^1/_2$) must be subtracted from $H_{y,tot}$ at (i_L+$^1/_2$) to advance the value of $E_{z,tot}$ at i_L. To correct this updating equation, the vector function $H_{y,inc}$ at (i_L-$^1/_2$) is added as an excitation wave source of the FDTD algorithm. The boundary E_z updating equation is given by:

$$E_z\Big|_{tot,i_L}^{n+1} = E_z\Big|_{tot,i_L}^{n} + \frac{\Delta t}{\varepsilon_o \Delta}\left(H_y\Big|_{tot,i_L+1/2}^{n+1/2} - H_y\Big|_{scat,i_L-1/2}^{n+1/2} \right) - \frac{\Delta t}{\varepsilon_o \Delta} H_y\Big|_{inc,i_L-1/2}^{n+1/2} \tag{2.37}$$

Subscript *inc* stands for incident field. The added term is assumed to be a known function such as sinusoidal wave or Gaussian pulse for plane wave representation, while the rest of the terms of the right hand side are assumed stored in computer memory from the previous updating time step. By following proper modifications of equation (2.37), the updating equations for the other three special magnetic and electric boundary field components are expressed as follows:

$$H_y\Big|_{scat,i_L-1/2}^{n+1/2} = H_y\Big|_{scat,i_L-1/2}^{n-1/2} + \frac{\Delta t}{\mu_o \Delta}\left(E_z\Big|_{tot,i_L}^{n} - E_z\Big|_{scat,i_L-1}^{n} \right) - \frac{\Delta t}{\mu_o \Delta} E_z\Big|_{inc,i_L}^{n} \tag{2.38}$$

$$E_z\Big|_{tot,i_R}^{n+1} = E_z\Big|_{tot,i_R}^{n} + \frac{\Delta t}{\varepsilon_o \Delta}\left(H_y\Big|_{scat,i_R+1/2}^{n+1/2} - H_y\Big|_{tot,i_R-1/2}^{n+1/2} \right) + \frac{\Delta t}{\varepsilon_o \Delta} H_y\Big|_{inc,i_R+1/2}^{n+1/2} \tag{2.39}$$

$$H_y\Big|_{scat,i_R+1/2}^{n+1/2} = H_y\Big|_{scat,i_R+1/2}^{n-1/2} + \frac{\Delta t}{\mu_o \Delta}\left(E_z\Big|_{scat,i_R+1}^{n} - E_z\Big|_{tot,i_R}^{n} \right) + \frac{\Delta t}{\mu_o \Delta} E_z\Big|_{inc,i_R}^{n} \tag{2.40}$$

Equations (2.38)-(2.40) are the one-dimensional total/scattered field FDTD formulations to generate the equivalent effects of the plane wave at one surface interface. The same principle can be extended to 2-D and 3-D scattering problems.

2.4.2.2 Total/Scattered Field Formulation in 3-D

In general, the equivalence principle surface implementation in FDTD code is employed with electric and magnetic field nodes are located at half a cell apart between each other. In three-dimensional case, the interface of the total and the scattered field zone is constituted by six flat planes to form a closed rectangular box as depicted in Figure 2.8. Furthermore, each face of the rectangular box consists of two tangential electric and magnetic fields in a closed surface.

The notation used by Taflove in [1] is used in order to simplify the equations. Equations from (2.21) to (2.26) are used as the basis of the updating equations. A cubic-cell space lattice is assumed for simplicity.

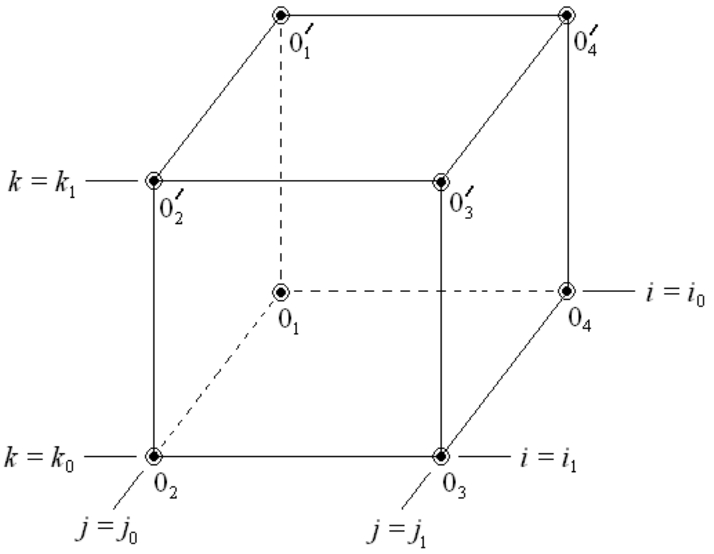

Figure 2.8: Coordinate origins for the calculation of incident field.

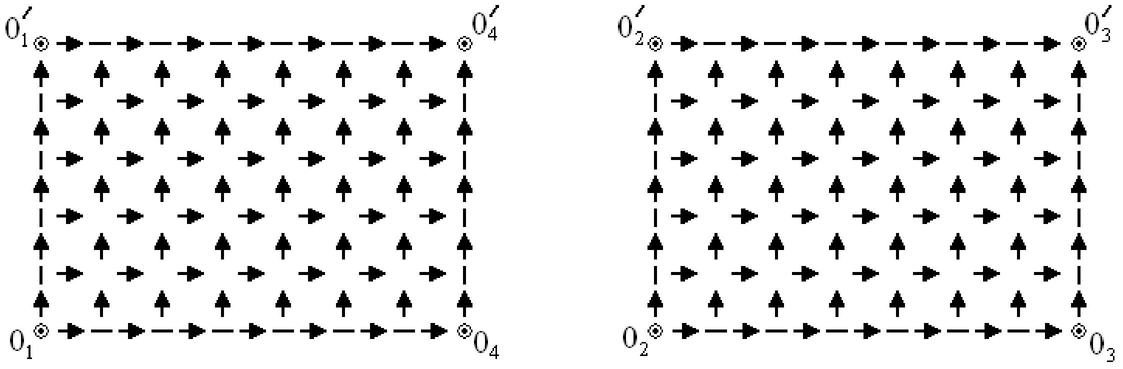

Figure 2.9: Location of E_y(→) and E_z(↑) components in planes $i = i_o$ and $i = i_1$.

The E_y and E_z components can be determined from Figure 2.9. E_y ($i = i_o$; $j = j_o + ½, \ldots, j_1 - ½$; $k = k_o, \ldots, k_1$) is given by:

$$E_y\Big|_{i_0,j,k}^{n+1} = \{E_y\Big|_{i_0,j,k}^{n+1}\}_{(2.25)} + C_{b,E_y}\Big|_{i_0,j,k} H_{z,inc}\Big|_{i_0-1/2,j,k}^{n+1/2} \qquad (2.41)$$

E_z ($i = i_o$; $j = j_o, \ldots, j_1$; $k = k_o + ½, \ldots, k_1 - ½$) is given by:

$$E_z\Big|_{i_0,j,k}^{n+1} = \{E_z\Big|_{i_0,j,k}^{n+1}\}_{(2.26)} - C_{b,E_z}\Big|_{i_0,j,k} H_{y,inc}\Big|_{i_0-1/2,j,k}^{n+1/2} \qquad (2.42)$$

E_y ($i = i_1$; $j = j_o + ½, \ldots, j_1 - ½$; $k = k_o, \ldots, k_1$) is given by:

$$E_y\Big|_{i_1,j,k}^{n+1} = \{E_y\Big|_{i_1,j,k}^{n+1}\}_{(2.25)} - C_{b,E_y}\Big|_{i_1,j,k} H_{z,inc}\Big|_{i_1+1/2,j,k}^{n+1/2} \qquad (2.43)$$

E_z ($i = i_1$; $j = j_o, \ldots, j_1$; $k = k_o + ½, \ldots, k_1 - ½$) is given by:

$$E_z\Big|_{i_1,j,k}^{n+1} = \{E_z\Big|_{i_1,j,k}^{n+1}\}_{(2.26)} + C_{b,E_z}\Big|_{i_1,j,k} H_{y,inc}\Big|_{i_1+1/2,j,k}^{n+1/2} \qquad (2.44)$$

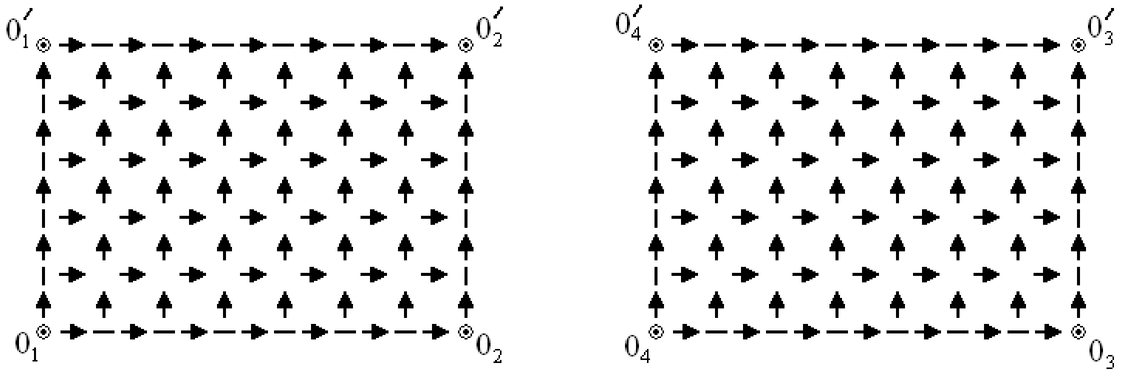

Figure 2.10: Location of E_x(→) and E_z(↑) components in planes $j = j_o$ and $j = j_1$.

The E_x and E_z components can be determined from Figure 2.10. E_x ($i = i_o + ½, \ldots, i_1 - ½$; $j = j_o$; $k = k_o, \ldots, k_1$) is given by:

$$E_x\Big|_{i,j_0,k}^{n+1} = \{E_x\Big|_{i,j_0,k}^{n+1}\}_{(2.24)} - C_{b,E_x}\Big|_{i,j_0,k} H_{z,inc}\Big|_{i,j_0-1/2,k}^{n+1/2} \qquad (2.45)$$

E_z ($i = i_o, \ldots, i_1; j = j_o; k = k_o + ½, \ldots, k_1 - ½$) is given by:

$$E_z\Big|^{n+1}_{i,j_0,k} = \{E_z\Big|^{n+1}_{i,j_0,k}\}_{(2.26)} + C_{b,E_z}\Big|_{i,j_0,k} H_{x,inc}\Big|^{n+1/2}_{i,j_0-1/2,k} \tag{2.46}$$

E_x ($i = i_o + ½, \ldots, i_1 - ½; j = j_1; k = k_o, \ldots, k_1$) is given by:

$$E_x\Big|^{n+1}_{i,j_1,k} = \{E_x\Big|^{n+1}_{i,j_1,k}\}_{(2.24)} + C_{b,E_x}\Big|_{i,j_1,k} H_{z,inc}\Big|^{n+1/2}_{i,j_1+1/2,k} \tag{2.47}$$

E_z ($i = i_o, \ldots, i_1; j = j_1; k = k_o + ½, \ldots, k_1 - ½$) is given by:

$$E_z\Big|^{n+1}_{i,j_1,k} = \{E_z\Big|^{n+1}_{i,j_1,k}\}_{(2.26)} - C_{b,E_z}\Big|_{i,j_1,k} H_{x,inc}\Big|^{n+1/2}_{i,j_1+1/2,k} \tag{2.48}$$

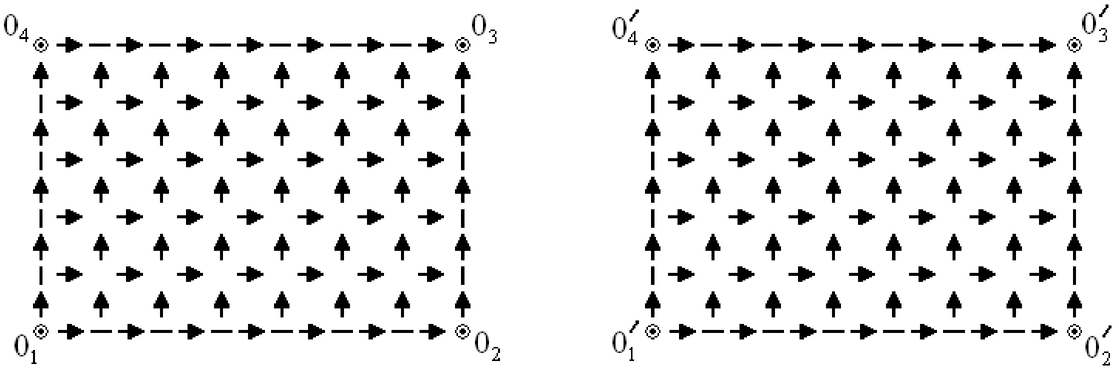

Figure 2.11: Location of E_x(→) and E_y(↑) components in planes $k = k_o$ and $k = k_1$.

The E_x and E_y components can be determined from Figure 2.11. E_x ($i = i_o + ½, \ldots, i_1 - ½$; $j = j_o, \ldots, j_1; k = k_o$) is given by:

$$E_x\Big|_{i,j,k_0}^{n+1} = \{E_x\Big|_{i,j,k_0}^{n+1}\}_{(2.24)} + C_{b,E_x}\Big|_{i,j,k_0} H_{y,inc}\Big|_{i,j,k_0-1/2}^{n+1/2} \tag{2.49}$$

E_y ($i = i_o, \ldots, i_1; j = j_o + ½, \ldots, j_1 - ½; k = k_o$) is given by:

$$E_y\Big|_{i,j,k_0}^{n+1} = \{E_y\Big|_{i,j,k_0}^{n+1}\}_{(2.25)} - C_{b,E_y}\Big|_{i,j,k_0} H_{x,inc}\Big|_{i,j,k_0-1/2}^{n+1/2} \tag{2.50}$$

E_x ($i = i_o + ½, \ldots, i_1 - ½; j = j_o, \ldots, j_1; k = k_1$) is given by:

$$E_x\Big|_{i,j,k_1}^{n+1} = \{E_x\Big|_{i,j,k_1}^{n+1}\}_{(2.24)} - C_{b,E_x}\Big|_{i,j,k_1} H_{y,inc}\Big|_{i,j,k_1+1/2}^{n+1/2} \tag{2.51}$$

E_y ($i = i_o, \ldots, i_1; j = j_o + ½, \ldots, j_1 - ½; k = k_1$) is given by:

$$E_y\Big|_{i,j,k_1}^{n+1} = \{E_y\Big|_{i,j,k_1}^{n+1}\}_{(2.25)} + C_{b,E_y}\Big|_{i,j,k_1} H_{x,inc}\Big|_{i,j,k_1+1/2}^{n+1/2} \tag{2.52}$$

The consistency condition for the magnetic field components located 0.5Δ outside of each face of the total/scattered-field interface are given by analogy. The H_y and H_z components can be determined from Figure 2.9. H_y ($i = i_o - ½; j = j_o, \ldots, j_1; k = k_o + ½, \ldots, k_1 - ½$) is given by:

$$H_y\Big|_{i_0-1/2,j,k}^{n+1/2} = \{H_y\Big|_{i_0-1/2,j,k}^{n+1/2}\}_{(2.22)} - D_{b,H_y}\Big|_{i_0-1/2,j,k} E_{z,inc}\Big|_{i_0,j,k}^{n} \tag{2.53}$$

H_z ($i = i_o - ½; j = j_o + ½, \ldots, j_1 - ½; k = k_o, \ldots, k_1$) is given by:

$$H_z\Big|_{i_0-1/2,j,k}^{n+1/2} = \{H_z\Big|_{i_0-1/2,j,k}^{n+1/2}\}_{(2.23)} + D_{b,H_z}\Big|_{i_0-1/2,j,k} E_{y,inc}\Big|_{i_0,j,k}^{n} \tag{2.54}$$

H_y ($i = i_1 + ½; j = j_o, …, j_1; k = k_o + ½, …, k_1 - ½$) is given by:

$$H_y\Big|_{i_1+1/2,j,k}^{n+1/2} = \{H_y\Big|_{i_1+1/2,j,k}^{n+1/2}\}_{(2.22)} + D_{b,H_y}\Big|_{i_1+1/2,j,k} E_{z,inc}\Big|_{i_1,j,k}^{n} \tag{2.55}$$

H_z ($i = i_1 + ½; j = j_o + ½, …, j_1 - ½; k = k_o, …, k_1$) is given by:

$$H_z\Big|_{i_1+1/2,j,k}^{n+1/2} = \{H_z\Big|_{i_1+1/2,j,k}^{n+1/2}\}_{(2.23)} - D_{b,H_z}\Big|_{i_1+1/2,j,k} E_{y,inc}\Big|_{i_1,j,k}^{n} \tag{2.56}$$

The H_x and H_z components can be determined from Figure 2.10. H_x ($i = i_o, …, i_1; j = j_o - ½; k = k_o + ½, …, k_1 - ½$) is given by:

$$H_x\Big|_{i,j_0-1/2,k}^{n+1/2} = \{H_x\Big|_{i,j_0-1/2,k}^{n+1/2}\}_{(2.21)} + D_{b,H_x}\Big|_{i,j_0-1/2,k} E_{z,inc}\Big|_{i,j_0,k}^{n} \tag{2.57}$$

H_z ($i = i_o + ½, …, i_1 - ½; j = j_o - ½; k = k_o, …, k_1$) is given by:

$$H_z\Big|_{i,j_0-1/2,k}^{n+1/2} = \{H_z\Big|_{i,j_0-1/2,k}^{n+1/2}\}_{(2.23)} - D_{b,H_z}\Big|_{i,j_0-1/2,k} E_{x,inc}\Big|_{i,j_0,k}^{n} \tag{2.58}$$

H_x ($i = i_o, …, i_1; j = j_1+½; k = k_o + ½, …, k_1 - ½$) is given by:

$$H_x\Big|_{i,j_1+1/2,k}^{n+1/2} = \{H_x\Big|_{i,j_1+1/2,k}^{n+1/2}\}_{(2.21)} - D_{b,H_x}\Big|_{i,j_1+1/2,k} E_{z,inc}\Big|_{i,j_1,k}^{n} \tag{2.59}$$

H_z ($i = i_o + ½, \ldots, i_1 - ½; j = j_1+½; k = k_o, \ldots, k_1$) is given by:

$$H_z\Big|_{i,j_1+1/2,k}^{n+1/2} = \{H_z\Big|_{i,j_1+1/2,k}^{n+1/2}\}_{(2.23)} + D_{b,H_z}\Big|_{i,j_1+1/2,k} E_{x,inc}\Big|_{i,j_1,k}^{n} \tag{2.60}$$

The H_x and H_y components can be determined from Figure 2.11. H_x ($i = i_o, \ldots, i_1; j = j_o + ½, \ldots, j_1 - ½; k = k_o - ½$) is given by:

$$H_x\Big|_{i,j,k_0-1/2}^{n+1/2} = \{H_x\Big|_{i,j,k_0-1/2}^{n+1/2}\}_{(2.21)} - D_{b,H_x}\Big|_{i,j,k_0-1/2} E_{y,inc}\Big|_{i,j,k_0}^{n} \tag{2.61}$$

H_y ($i = i_o + ½, \ldots, i_1 - ½; j = j_o, \ldots, j_1; k = k_o - ½$) is given by:

$$H_y\Big|_{i,j,k_0-1/2}^{n+1/2} = \{H_y\Big|_{i,j,k_0-1/2}^{n+1/2}\}_{(2.22)} + D_{b,H_y}\Big|_{i,j,k_0-1/2} E_{x,inc}\Big|_{i,j,k_0}^{n} \tag{2.62}$$

H_x ($i = i_o, \ldots, i_1; j = j_o + ½, \ldots, j_1 - ½; k = k_1 + ½$) is given by:

$$H_x\Big|_{i,j,k_1+1/2}^{n+1/2} = \{H_x\Big|_{i,j,k_1+1/2}^{n+1/2}\}_{(2.21)} + D_{b,H_x}\Big|_{i,j,k_1+1/2} E_{y,inc}\Big|_{i,j,k_1}^{n} \tag{2.63}$$

H_y ($i = i_o + ½, \ldots, i_1 - ½; j = j_o, \ldots, j_1; k = k_1 + ½$) is given by:

$$H_y\Big|_{i,j,k_1+1/2}^{n+1/2} = \{H_y\Big|_{i,j,k_1+1/2}^{n+1/2}\}_{(2.22)} - D_{b,H_y}\Big|_{i,j,k_1+1/2} E_{x,inc}\Big|_{i,j,k_1}^{n} \qquad (2.64)$$

2.5 Absorbing Boundary Conditions (ABC)

ABC is generally one of the most critical elements in FDTD simulation and analysis for several reasons. It is introduced at the outer boundary of the FDTD lattice to limit the problem space into bounded regions and hence the electromagnetic wave interaction problems can be solved easily. It is meant to simulate the extension of the FDTD mesh to infinity. In other words, it is used to truncate the computational region at the edges of the finite FDTD mesh. The key to the success of an ABC is that it should be able to absorb the waves travelling outward from the FDTD lattice with extremely low reflection at the boundary.

There have been numerous ABC approaches [1] to effectively approximate an infinite mesh. Mur [7] used analytical ABC which provides the effective reflection at the boundary between -35 to -40 dB. Liao *et al.* [9] implemented both spatial and temporal extrapolation of the electromagnetic fields by means of Newton backward-difference polynomial. The result was 20 dB less reflective than the second order Mur. Nevertheless, the method was delicate to the frequency and direction of propagation of the incident wave [10]. Therefore, the ABC boundary must be located at large distances from the radiator and scatterer to be more efficient and effective. Mei *et al.* [11] used error cancellation procedure to improve the performance of the local ABC. However, the method had a considerable residual error due to the assumption of zero degree of the incidence wave angle. One of the most flexible and efficient methods is the perfectly matched layer (PML) developed by Berenger [12]. Though PML is perfect in theory, spurious reflection is present in the actual FDTD computation [13, 14]. The basic idea in [12] is to produce an artificial lossy medium by complex electric permittivity and magnetic permeability surrounding the FDTD problem space so that the wave will be absorbed before it hits the boundary. In addition, this technique permitted the boundary reflections below -80 dB. The PML boundary can now be placed close to the scatterer and radiator. Berenger's PML is now considered as the predominant and standard used in the most FDTD imitations [15, 16].

2.5.1 3-D Berenger′s PML

In 3-D, all six Cartesian field vector components are separated to realize the following twelve modified version of Maxwell's equations [12]:

$$\mu_o \frac{\partial H_{xy}}{\partial t} + \sigma_y^* H_{xy} = -\frac{\partial (E_{zx} + E_{zy})}{\partial y} \tag{2.65}$$

$$\mu_o \frac{\partial H_{xz}}{\partial t} + \sigma_z^* H_{xz} = \frac{\partial (E_{yx} + E_{yz})}{\partial z} \tag{2.66}$$

$$\mu_o \frac{\partial H_{yz}}{\partial t} + \sigma_z^* H_{yz} = -\frac{\partial (E_{xy} + E_{xz})}{\partial z} \tag{2.67}$$

$$\mu_o \frac{\partial H_{yx}}{\partial t} + \sigma_x^* H_{yx} = \frac{\partial (E_{zx} + E_{zy})}{\partial x} \tag{2.68}$$

$$\mu_o \frac{\partial H_{zx}}{\partial t} + \sigma_x^* H_{zx} = -\frac{\partial (E_{yx} + E_{yz})}{\partial x} \tag{2.69}$$

$$\mu_o \frac{\partial H_{zy}}{\partial t} + \sigma_y^* H_{zy} = \frac{\partial (E_{xy} + E_{xz})}{\partial y} \tag{2.70}$$

$$\varepsilon_o \frac{\partial E_{xy}}{\partial t} + \sigma_y E_{xy} = \frac{\partial (H_{zx} + H_{zy})}{\partial y} \tag{2.71}$$

$$\varepsilon_o \frac{\partial E_{xz}}{\partial t} + \sigma_z E_{xz} = -\frac{\partial (H_{yx} + H_{yz})}{\partial z} \tag{2.72}$$

$$\varepsilon_o \frac{\partial E_{yz}}{\partial t} + \sigma_z E_{yz} = \frac{\partial (H_{xy} + H_{xz})}{\partial z} \tag{2.73}$$

$$\varepsilon_o \frac{\partial E_{yx}}{\partial t} + \sigma_x E_{yx} = -\frac{\partial (H_{zx} + H_{zy})}{\partial x} \tag{2.74}$$

$$\varepsilon_o \frac{\partial E_{zx}}{\partial t} + \sigma_x E_{zx} = \frac{\partial (H_{yx} + H_{yz})}{\partial x} \tag{2.75}$$

$$\varepsilon_o \frac{\partial E_{zy}}{\partial t} + \sigma_y E_{zy} = -\frac{\partial (H_{xy} + H_{xz})}{\partial y} \tag{2.76}$$

PML matching conditions and lattice structures are basically similar to the TM case.

2.5.2 3-D PML Numerical Implementations

The standard time-stepping of the Yee algorithm cannot be used since the attenuation of the outgoing source waves in the PML layer is very fast. Consequently, an explicit exponential time step algorithm is suggested in the PML layer [17]. From equations (2.70) and (2.71), the updating H_{zy} and E_{xy} in the PML medium can both be expanded by the expressions:

$$H_{zy}\Big|_{i,j,k}^{n+1/2} = e^{-\left(\frac{\sigma^{*}_{y_{i,j,k}}\Delta t}{\mu_{i,j,k}}\right)} H_{zy}\Big|_{i,j,k}^{n-1/2} + \frac{1-e^{-\left(\frac{\sigma^{*}_{y_{i,j,k}}\Delta t}{\mu_{i,j,k}}\right)}}{\sigma^{*}_{y_{i,j,k}}\Delta_p}\begin{pmatrix} E_{xy}\Big|_{i,j+1/2,k}^{n} - E_{xy}\Big|_{i,j-1/2,k}^{n} \\ + E_{xz}\Big|_{i,j+1/2,k}^{n} - E_{xz}\Big|_{i,j-1/2,k}^{n} \end{pmatrix} \tag{2.77}$$

$$E_{xy}\Big|_{i,j,k}^{n+1} = e^{-\left(\frac{\sigma_{y_{i,j,k}}\Delta t}{\varepsilon_{i,j,k}}\right)} E_{xy}\Big|_{i,j,k}^{n} + \frac{1-e^{-\left(\frac{\sigma_{y_{i,j,k}}\Delta t}{\varepsilon_{i,j,k}}\right)}}{\sigma_{y_{i,j,k}}\Delta_p}\begin{pmatrix} H_{zx}\Big|_{i,j+1/2,k}^{n+1/2} - H_{zx}\Big|_{i,j-1/2,k}^{n+1/2} \\ + H_{zy}\Big|_{i,j+1/2,k}^{n+1/2} - H_{zy}\Big|_{i,j-1/2,k}^{n+1/2} \end{pmatrix} \tag{2.78}$$

The subscript p can be x, y or z and Δ_p is the cell size in the p-direction. In addition, the updating equation for the other ten vector field components can be derived by using the same technique. The thickness of the PML layer can be reduced to obtain the optimum profile of the conductivity by means of geometric progression [18, 19]:

$$\sigma(\rho) = \sigma_o g^{\frac{\rho}{\Delta_p}} = -\frac{\varepsilon_o c}{2\Delta_p}\frac{\ln g}{\left(g^N - 1\right)}\ln R(0) g^{\frac{\rho}{\Delta_p}} \tag{2.79}$$

N is the number of cells in the PML layer and g is the geometric progression grading factor. This is an empirical factor in a function of the number of cells in the scatterer region. Equation (2.79) shows that the conductivity increases by the factor g from one cell to the other.

2.6 Conclusion

The fundamental concepts of the FDTD computational method were briefly explained in this chapter. Some of them deal with the solution of Maxwell's equations by means of finite differences, the derivation of FDTD updating equations for electric and magnetic field vector components, and the explanation on the accuracy and stability which necessitate the FDTD computational method. In addition, the excitation source inside the FDTD lattice was also explained. The general idea of the ABC to the specific Berenger’s PML in 2-D and 3-D were well treated. Last but not least, Fortran 90 source code was written successfully in 2-D FDTD with subgridding (SGFDTD) and 3-D MoM-FDTD-SGFDTD hybrid technique for different applications in electromagnetic scattering problems.

2.7 References

[1] A. Taflove and S. C. Hagness, *Computational electrodynamics: The finite-difference time-domain method*, 3rd ed. Boston, MA: Artech House, 2005.

[2] A. Taflove, *Advances in computational electrodynamics: The finite-difference time-domain method*. Dedham, MA: Artech House, 1998.

[3] K. S. Kunz and R. J. Luebbers, *The finite difference time domain method for*

electromagnetics. Boca Raton, FL: CRC Press, 1993.

[4] J. D. Jackson, *Classical electrodynamics*, 3rd ed. New York: John Wiley & Sons Inc., 1998.

[5] K. S. Yee, "Numerical solution of initial boundary value problems involving Maxwell's equations in isotropic media," *IEEE Transactions on Antennas and Propagation*, vol. AP-14, pp. 302-307, 1966.

[6] M. N. O. Sadiku, *Numerical techniques in electromagnetics*. Boca Raton: CRC Press, 2001.

[7] G. Mur, "Absorbing boundary conditions for the finite-difference approximation of the time-domain electromagnetic-field equations," *IEEE Transactions on Electromagnetic Compatibility*, vol. EMC-23, pp. 377-382, 1981.

[8] K. Umashankar and A. Taflove, "A novel method to analyze electromagnetic scattering of complex objects," *IEEE Transactions on Electromagnetic Compatibility*, vol. EMC-24, pp. 397-405, 1982.

[9] Z. P. Liao, H. L. Wong, B. P. Yang, and Y. F. Yuan, "A transmitting boundary for transient wave analysis," *Scientia Sinica (Series A)*, vol. XXVII, pp. 1063-1076, 1984.

[10] J. Y. Fang, "Absorbing boundary conditions applied to model wave propagation in microwave integrated-circuits," *IEEE Transactions on Microwave Theory and Techniques*, vol. 42, pp. 1506-1513, 1994.

[11] K. K. Mei and J. Y. Fang, "Superabsorption - A method to improve absorbing boundary conditions," *IEEE Transactions on Antennas and Propagation*, vol. 40, pp. 1001-1010, 1992.

[12] J. P. Berenger, "A perfectly matched layer for the absorption of electromagnetic waves," *Journal of Computational Physics*, vol. 114, pp. 185-200, 1994.

[13] A. F. Oskooi, *An investigation of the perfectly matched layer for inhomogeneous media*. M. Sc. Thesis, Cambridge: Massachusetts Institute of Technology, 2008.

[14] J. P. Berenger, "Numerical reflection from FDTD-PMLs: a comparison of the split PML with the unsplit and CFS PMLs," *IEEE Transactions on Antennas and Propagation*, vol. 50, pp. 258-265, 2002.

[15] D. T. Prescott and N. V. Shuley, "Reflection analysis of FDTD boundary conditions - Part I: Time-space absorbing boundaries," *IEEE Transactions on Microwave Theory and Techniques*, vol. 45, pp. 1162-1170, 1997.

[16] D. T. Prescott and N. V. Shuley, "Reflection analysis of FDTD boundary conditions - Part II: Berenger's PML absorbing layers," *IEEE Transactions on Microwave Theory and Techniques*, vol. 45, pp. 1171-1178, 1997.

[17] R. Holland, "Finite-difference time-domain (FDTD) analysis of magnetic diffusion," *IEEE Transactions on Electromagnetic Compatibility*, vol. 36, pp. 32-39, 1994.

[18] J. P. Berenger, "Perfectly matched layer for the FDTD solution of wave-structure interaction problems," *IEEE Transactions on Antennas and Propagation*, vol. 44, pp. 110-117, 1996.

[19] J. P. Berenger, "Improved PML for the FDTD solution of wave-structure interaction problems," *IEEE Transactions on Antennas and Propagation*, vol. 45, pp. 466-473, 1997.

Chapter 3

Surface Kernel Solution of the Method of Moments

3.1 Introduction

When parallel wires are close together the surface current distribution becomes non-uniform. This effect has been investigated previously, subject to certain approximations. Smith [1, 2] and Olaofe [3] assumed that the average current flowing in a set of parallel wires was equal, which means that the cross-sectional distribution of surface current remains constant along the wires. Tulyathan and Newman [4] used a more general treatment but still neglected the possibility of a circumferential component in the surface current: it is intuitively obvious that such a component must be present when there is significant displacement current flow in the inter-wire capacitance. A more general detailed solution by Abd-Alhameed and Excell [5] included the modelling of two surface current components at any point on the wire surface, subject to certain geometry constraints. And more recently [6-8] in which two parallel dipoles and loop antennas were investigated for the existence of the non-uniform surface currents, in which the antenna power losses were fully covered in [8].

In addition, most of the methods used for analysis of wire antennas of arbitrary shape (including the possibility of closely parallel wires) assume a uniform surface current distribution across the cross section, (e.g. Djordjevic *et al.* [9], Burke and Poggio [10] and Richmond [11]). Hence, surface resistive losses and reactive effects that may be augmented by the non-uniform surface current will not be correctly predicted.

This problem is particularly significant for resonant coiled electrically-small antennas, such as the normal-mode helical antenna (NMHA), in which the surface current distribution has a critical effect on the efficiency and Q-factor. A moment-method (MoM) formulation uses two orthogonal basis functions on the surface of the wire including its ends was thus developed to investigate this problem in details. The work detailed a more generalised theory and results of the work done by the present authors [6]. It should be noted that there are more advanced commercial codes now available which, in particular, implement patch modelling more effectively (e.g. FEKO [12], CST [13], HFSS [14] and IE3D [15]).

Basically, the original motivation for this work was to assess the degree of benefit that would be obtained if an antenna of this type were to be realised in high-temperature superconductor. Electrically-small antennas have a low radiation resistance that is easily swamped by ohmic loss resistance, resulting in a low efficiency. Superconductors have the potential to remove much of the loss and hence raise the efficiency significantly. There is then the possible disadvantage that the inherent Q-factor of the antenna may become very high: whether this is a real disadvantage depends on the nature of the system into which the antenna is proposed for deployment. To quantify the reduction in loss, and hence improvement in efficiency, which might accrue from the use of superconductor, it is necessary to quantify the surface loss P_s measured in W/m^2:

$$P_s = \frac{J_s^2}{\sigma_s} \tag{3.1}$$

where J_s is the surface current density (A/m) and σ_s is the surface conductivity (Ω).The self-resonant helix had already been identified as a convenient design of electrically-small antenna in which quite interesting results were reported for example, broad band V-helical antenna [16], circular NMHA [17], double pitch NMHA [18] and multiple pitches NMHA [19], however, for realisation in high-temperature superconductor, the superconducting element may be left electrically isolated. The detailed quantification of J_s in this particularly complex case was thus the main original objective of the work. The very detailed modelling procedure that has been developed has much wider uses, particularly in the accurate modelling of normally-conducting NMHAs, which see extensive use in mobile telecommunications. Complete validation of the predictions of the procedure poses considerable difficulties, since it would require measurement of the surface current distribution on wire. This matter is an important topic for future work, but an adequate degree of validation can be claimed for the results that have been presented in this work from this type of modelling process.

3.2 Moment Method Formulation

Initially, the normal MoM approach is followed, but no attempt is made to approximate the surface current or the scattered field observation points to a single point on the wire cross-section. Instead, both are allowed to be completely general points on the wire surface and the surface current is allowed to have components both parallel to, and transverse to the wire axis. This leads to an equation of the form:

$$\sum_j I_j . L(\mathbf{J}_j) = (\mathbf{E}_i) \tag{3.2}$$

where I_j is a basis function for the surface current $\mathbf{J}_j$, $\mathbf{E}_i$ is the incident electric field strength and L is the integro-differential operator given by:

$$L(\mathbf{J}) = (j\omega\mathbf{A} + \nabla\phi)_{\text{tan}} \tag{3.3}$$

where A and ϕ are the vector and scalar potentials. If a set of testing functions $\mathbf{W}_m$ is defined, equation (3.2) may be rewritten as:

$$\sum_j I_j \left\langle \mathbf{W}_m, L(\mathbf{J}_j) \right\rangle = \left\langle \mathbf{W}_m, \mathbf{E}_i \right\rangle \qquad \mathit{for} \quad j = 1,2,\ldots N \tag{3.4}$$

where

$$\left\langle \mathbf{W}_m, L(\mathbf{J}_j) \right\rangle = \iint_s \iint_{s'} (\mathbf{W}_m . L(\mathbf{J}_j)) ds' ds = Z_{mj} \tag{3.5}$$

$$\left\langle \mathbf{W}_m, \mathbf{E}_i \right\rangle = \iint_{s'} (\mathbf{W}_m . \mathbf{E}_i) ds = V_m \tag{3.6}$$

where *ds'* and *ds* are the differential areas on the wire surface for the source and the observation points respectively, $m = 1, 2, ... N$ is the index of the testing function and Z and V are the conventional abbreviations for the interaction matrix and excitation vector terms in the Method of Moments.

3.3 Evaluation of Impedance Matrix Elements

The impedance matrix elements Z_{mj} can be written using the closed surface integral identity [20] as follows:

$$Z_{mj} = j\omega\mu \iint_s \iint_{s'} \left(\mathbf{J}_j . \mathbf{W}_m - \frac{1}{k^2} (\nabla . \mathbf{J}_j)(\nabla . \mathbf{W}_m) \right) g(R) ds' ds \tag{3.7}$$

where $g(R)$ is the free-space Green function [21-23] and is given by the expression:

$$g(R) = \frac{e^{-jkR}}{4\pi R} \tag{3.8}$$

R is the distance between the observation and source points on the wire surface.

Singular integral occurs when $R = 0$ (i.e., $g(R) \to \propto$). The coordinates for a point on the surface of the helix wire can be given by:

$$x(\phi,\alpha) = x'\cos(\phi) - y'\sin(\phi) \tag{3.9}$$

$$y(\phi,\alpha) = x'\sin(\phi) - y'\cos(\phi) \tag{3.10}$$

$$z(\phi,\alpha) = \frac{P}{2\pi}\phi + a\sin(\alpha)\cos(\delta) \tag{3.11}$$

where

$$x' = b + a\cos(\alpha) \tag{3.12}$$

$$y' = -a\sin(\alpha)\sin(\delta) \tag{3.13}$$

$$\tan(\delta) = \frac{P}{2\pi b} \tag{3.14}$$

where a is the radius of the helix wire, b is the radius of the helix, P is the pitch distance between the turns, α is the azimuth angle of the circumferential cross-section wire and δ is the pitch angle. Equations (3.12), (3.13) and (3.14) are the exact coordinates of helix geometry. Defining two orthogonal directions on the surface of the helix wire as shown in Figure 3.1, the unit vectors of the curvilinear surface patches in both directions are:

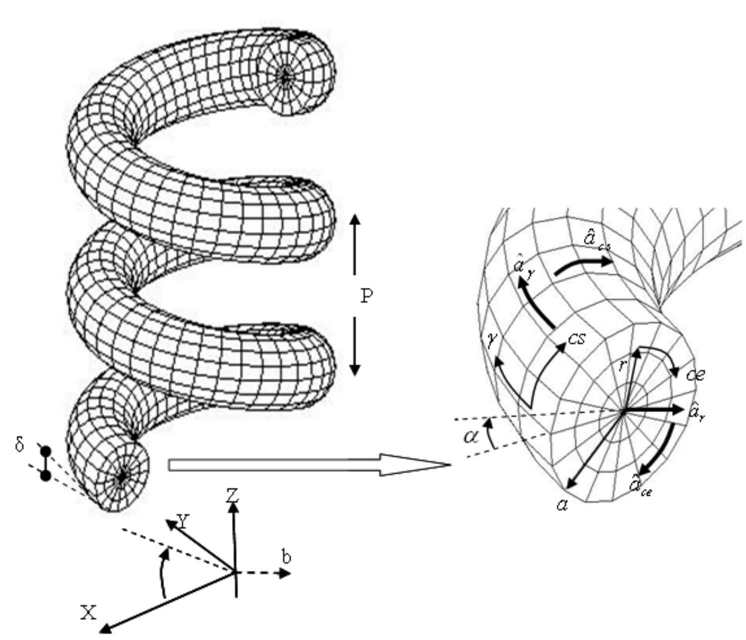

Figure 3.1: Basic geometry of the helical antenna driven by a voltage source at its centre. The directions of the orthogonal basis or test functions are shown on the right and represent the source or observations points on the wire surface and its ends.

$$\hat{a}_{\gamma} = -\sin(\phi)\cos(\delta)\hat{a}_x + \cos(\phi)\cos(\delta)\hat{a}_y + \sin(\delta)\hat{a}_z \tag{3.15}$$

$$\begin{aligned}\hat{a}_{cs} &= \left(-\sin(\alpha)\cos(\phi) + \cos(\alpha)\sin(\phi)\sin(\delta)\right)\hat{a}_x \\ &\quad - \left(\sin(\alpha)\sin(\phi) + \cos(\alpha)\cos(\phi)\sin(\delta)\right)\hat{a}_y + \cos(\alpha)\cos(\delta)\hat{a}_z\end{aligned} \tag{3.16}$$

where $\hat{a}_{\gamma}$ and $\hat{a}_{cs}$ are the unit vectors in the axial and circumferential surfaces of the wire respectively as shown in Figure 3.1. The differential lengths in both directions are:

$$d\gamma = b''d\phi \tag{3.17}$$

$$dcs = ad\alpha \tag{3.18}$$

where $d\phi$ and $d\alpha$ are the differential lengths in ϕ and α respectively, and

$$b'' = \sqrt{\left(\frac{P}{2\pi}\right)^2 + b'^2} \tag{3.19}$$

$$b'^2 = (b + a\cos(\alpha))^2 \tag{3.20}$$

The coordinates of the start surface of the helix at $\phi = 0$ is given by:

$$x(r,\alpha) = b + r\cos(\alpha) \tag{3.21}$$

$$y(r,\alpha) = -r\sin(\alpha)\sin(\delta) \tag{3.22}$$

$$z(r,\alpha) = r\sin(\alpha)\cos(\delta) \tag{3.23}$$

where $0 \le r \le a$. Hence, the unit direction vectors of the basis function on the end surface can be expressed as:

$$\hat{a}_r = \cos(\alpha)\hat{a}_x - \sin(\alpha)\sin(\delta)\hat{a}_y + \sin(\alpha)\cos(\delta)\hat{a}_z \tag{3.24}$$

$$\hat{a}_{ce} = -\sin(\alpha)\hat{a}_x - \cos(\alpha)\sin(\delta)\hat{a}_y + \cos(\alpha)\cos(\delta)\hat{a}_z \tag{3.25}$$

where $\hat{a}_r$ and $\hat{a}_{ce}$ are the unit vectors in the radial and the circumferential directions on the end surface of the wire respectively as shown in Figure 3.1. The differential area on the end surface can be given by:

$$dA_{end} = rdrd\,\alpha \tag{3.26}$$

Similarly, the unit direction vectors, coordinators and differential area on the other end of the helix wire can be defined. Now, assume the surface current density over the wire surface can be expressed by two orthogonal current components in $\hat{a}_\gamma$ and $\hat{a}_{cs}$ (similarly at the surface end directions $\hat{a}_r$ and $\hat{a}_{ce}$). Then if the surface current is expanded over the wire surface using triangular basis functions in which the divergence of the current continuity is finite [24], then as example, these functions into the axial direction can be given by:

$$f(\gamma) = \begin{cases} f^{+} = \dfrac{\gamma}{\gamma_o} \\ f^{-} = 1 - \dfrac{\gamma}{\gamma_o} \end{cases} \quad for \quad 0 \le \gamma \le \gamma_o \quad and \quad \alpha_1 \le \alpha \le \alpha_2 \tag{3.27}$$

$$f^{'}(\gamma) = f^{'\pm}(\gamma) = \pm\frac{\gamma}{\gamma_o} \quad for \quad 0 \le \gamma \le \gamma_o \quad and \quad \alpha_1 \le \alpha \le \alpha_2 \tag{3.28}$$

where $f^{'}(\gamma)$ is the differentiation of $f(\gamma)$ and γ_o is the axial length of the curvilinear patch presented in Figure 3.1 in the direction of γ for all angle values of α from α_1 to

α_2. A similar basis functions in the directions of $\hat{a}_{cs}$, $\hat{a}_r$ and $\hat{a}_{ce}$ can be given. The testing functions are chosen to be identical to the expansion basis functions (Galerkin's method) yielding a symmetric impedance matrix. Hence, by substituting equations (3.9)-(3.28) into equation (3.7), the impedance matrix elements can be found. As an example, the impedance element for basis and test function in the axial direction can be stated as follows:

$$Z_{\gamma\gamma'} = j\omega\mu\iint_{s}\iint_{s'}\left(\mathbf{\hat{a}}_{\gamma}.\mathbf{\hat{a}}_{\gamma'}f(\gamma)f(\gamma') - \frac{1}{k^2}f(\gamma)f(\gamma')\right)g(R)ds'ds \tag{3.29}$$

where

$$ds = ab''d\phi d\alpha \tag{3.30}$$

The other self and mutual impedance elements for all other basis directions can be obtained in a similar way. The magnitude of R is written as:

$$R = \sqrt{(x-x')^2 + (y-y')^2 + (z-z')^2} \tag{3.31}$$

Since x, y and z are the function of ϕ and α, then R is also a function of ϕ and α. By integrating equation (3.17), the following expression is achieved:

$$\gamma = b''\phi \tag{3.32}$$

By substituting equations (3.19) and (3.20) into equation (3.32) gives:

$$\gamma = \left(\sqrt{\left(\frac{P}{2\pi}\right)^2 + (b + a\cos(\alpha))^2} \right)\phi \tag{3.33}$$

Let say there is another axial length γ_1 of the curvilinear patch, then:

$$\gamma_1 = \left(\sqrt{\left(\frac{P}{2\pi}\right)^2 + (b + a\cos(\alpha))^2} \right)\phi_1 \tag{3.34}$$

It can be clearly seen that α remains constant along the axial length. In other words:

$$f(\gamma) = \frac{\gamma}{\gamma_1} = \frac{\phi}{\phi_1} \tag{3.35}$$

3.4 Solution for Singularity

Equation (3.29) can be rewritten as:

$$Z_{\phi\alpha\phi'\alpha'} = j\omega\mu \int\limits_{\alpha}\int\limits_{\phi}\int\limits_{\alpha'}\int\limits_{\phi'} \frac{\mathbf{H}(\phi,\alpha,\phi',\alpha')e^{-jkR(\phi,\alpha,\phi',\alpha')}}{4\pi R(\phi,\alpha,\phi',\alpha')} d\phi' d\alpha' d\phi d\alpha \tag{3.36}$$

From this equation, singularity occurs when:

$$\phi = \phi' \quad and \quad \alpha = \alpha' \tag{3.37}$$

Moreover, when the surfaces of the patches are very close in proximity to each other still there will be pseudo-singularity. The condition occurs when:

$$\phi = \phi' + \delta\phi' \quad and \quad \alpha = \alpha' + \delta\alpha' \tag{3.38}$$

In this case, equation (3.36) cannot be integrated directly due to the problem of singularity. However, the obstacle can be alleviated by means of cancellation technique [25] with the introduction of additional function (see Appendix A).

Consider a point P on a patch of helix wire as depicted in Figure 3.2. The point is considered to be anywhere on the patch which is located in proximity above the origin. It should be noted that point S is the starting point for integration process. L and W are the length and the width of the patch respectively. $\hat{a}_{\gamma}$ and $\hat{a}_{cs}$ are the unit vectors in the axial and circumferential surfaces of the wire respectively. $\hat{u}_p$ and $\hat{u}_t$ are the new unit vectors due to point P in the axial and circumferential surfaces of the wire respectively.

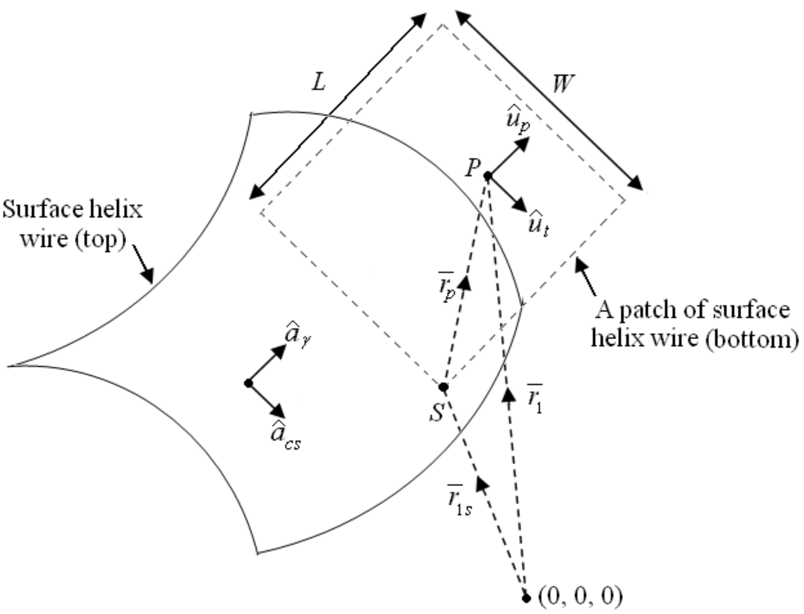

Figure 3.2: Point *P* on a patch of helix wire above the origin.

It can be shown that from Figure 3.2, the following expression can be obtained fundamentally:

$$\overline{r}_p = p\hat{u}_p + t\hat{u}_t \tag{3.39}$$

$$\overline{r}_{1s} = \overline{r}_1 - \overline{r}_p \tag{3.40}$$

By substituting equation (3.39) into equation (3.40), the following expression can be achieved:

$$\overline{r}_{1s} = \overline{r}_1 - (p\hat{u}_p + t\hat{u}_t) \tag{3.41}$$

In general, equation (3.41) is used as the starting point for integration. Equation (3.36) can thus be expanded as:

$$
\begin{aligned}
Z_{\phi\alpha\phi'\alpha'} = j\omega\mu \Bigg[& \int_{\alpha}\int_{\phi}\int_{\alpha'}\int_{\phi'} \frac{\mathbf{H}(\phi,\alpha,\phi',\alpha')e^{-jkR(\phi,\alpha,\phi',\alpha')}}{4\pi R(\phi,\alpha,\phi',\alpha')} d\phi' d\alpha' d\phi d\alpha \\
& - \int_{\alpha}\int_{\phi}\int_{p'}\int_{t'} \frac{\mathbf{J}(\phi,\alpha,p',t')e^{-jkR(\phi,\alpha,p',t')}}{4\pi R(\phi,\alpha,p',t')} dp' dt' d\phi d\alpha \Bigg] \\
& + j\omega\mu \int_{\alpha}\int_{\phi}\int_{p'}\int_{t'} \frac{\mathbf{J}(\phi,\alpha,p',t')e^{-jkR(\phi,\alpha,p',t')}}{4\pi R(\phi,\alpha,p',t')} dp' dt' d\phi d\alpha
\end{aligned}
\qquad (3.42)
$$

The above equation can be solved using numerical solution:

$$
\begin{aligned}
Z_{\phi\alpha\phi'\alpha'} = j\omega\mu \sum_{i=1}^{n_\phi}\sum_{j=1}^{n_\alpha} \Bigg[& \sum_{k=1}^{n_{\phi'}}\sum_{l=1}^{n_{\alpha'}} \left(\frac{\mathbf{H}(\phi_i,\alpha_j,\phi'_k,\alpha'_l)e^{-jkR(\phi_i,\alpha_j,\phi'_k,\alpha'_l)}}{4\pi R(\phi_i,\alpha_j,\phi'_k,\alpha'_l)} \right) w_{\alpha'_l} w_{\phi'_k} \\
& - \sum_{k=1}^{n_{p'}}\sum_{l=1}^{n_{t'}} \left(\frac{\mathbf{J}(\phi_i,\alpha_j,p'_k,t'_l)e^{-jkR(\phi_i,\alpha_j,p'_k,t'_l)}}{4\pi R(\phi_i,\alpha_j,p'_k,t'_l)} \right) \Bigg] w_{t'_l} w_{p'_k} \\
& + j\omega\mu \sum_{i=1}^{n_\phi}\sum_{j=1}^{n_\alpha} \left(\int_{p'}\int_{t'} \frac{\mathbf{J}(\phi_i,\alpha_j,p',t')e^{-jkR(\phi_i,\alpha_j,p',t')}}{4\pi R(\phi_i,\alpha_j,p',t')} dt' dp' \right) w_{\alpha_j} w_{\phi_i}
\end{aligned}
\qquad (3.43)
$$

The last term of equation (3.43) can be solved using analytical solution:

$$
I_{\phi\alpha p't'} = \int_{p'}\int_{t'} \frac{\mathbf{J}(\phi_i,\alpha_j,p',t')e^{-jkR(\phi_i,\alpha_j,p',t')}}{4\pi R(\phi_i,\alpha_j,p',t')} dt' dp' \qquad (3.44)
$$

For simplicity, the above equation can be reduced to the following format:

$$I = \int_p \int_t \frac{a_1 + a_2 t}{\sqrt{v^2 + (p + p_1)^2 + (t + t_1)^2}} dtdp \tag{3.45}$$

where a_1, a_2, v, p_1 and t_1 are constants. The analytical solution of the equation is given by the expression:

$$I = a_1 C + a_2 D + constant \tag{3.46}$$

The expression for C and D are given in the Appendix B.

3.5 Simulation and Results

Initially, simple antenna geometries such as dipole and loop antennas were investigated and discussed as special cases of more complex geometries such as the helix. The antenna geometries of the parallel dipoles and loops are shown in Figure 3.3. A similar procedure of placing orthogonal basis distribution over the wire surface and wire ends as for the dipoles are used. A computer program was written to implement the analysis given in the previous section. The surface patch subdivision was automatically generated by the program, subject to the number of the basis functions in both orthogonal directions. The impressed field E_i is modelled by a delta-function voltage source at the centre of the dipole and the helix whereas in loop it was placed at $\phi = 0°$.

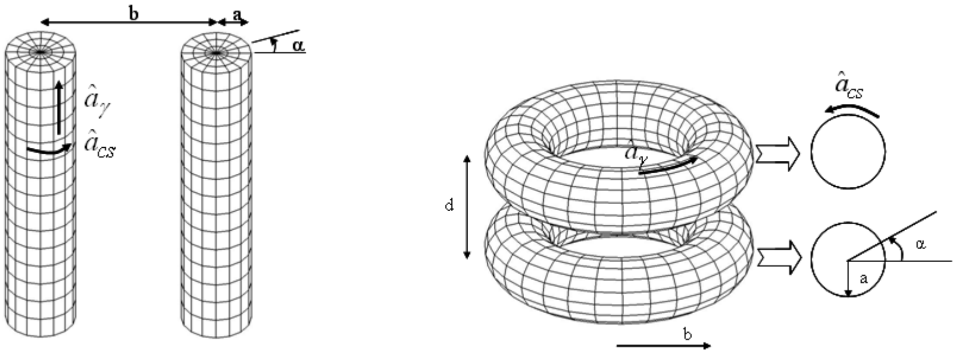

(a) (b)

Figure 3.3: The geometry models of two parallel dipoles and loop antennas including the directions of the basis or test functions used; (a) dipoles, (b) loops.

A simple axial excitation (in the γ-direction) was considered. Thus the impressed field can be given by:

$$E_i = \frac{1}{2\pi a}\delta(\gamma_c)\hat{a}_\gamma \tag{3.47}$$

where a is the radius of the wire antenna and γ_c is the half axial length of the dipole or the helix. The antenna wire for all geometries was assumed to be perfectly conducting and surrounded by free space. Several examples were used to investigate the surface current distribution of dipoles, loops and NMHA as predicted by the formulation, as follows:

The response of the input impedance of two parallel dipoles of 50 cm length and 5 mm wire radius separated by 15 mm is presented in Figure 3.4. In this example, both dipoles were centrally fed as presented in equation (3.47).

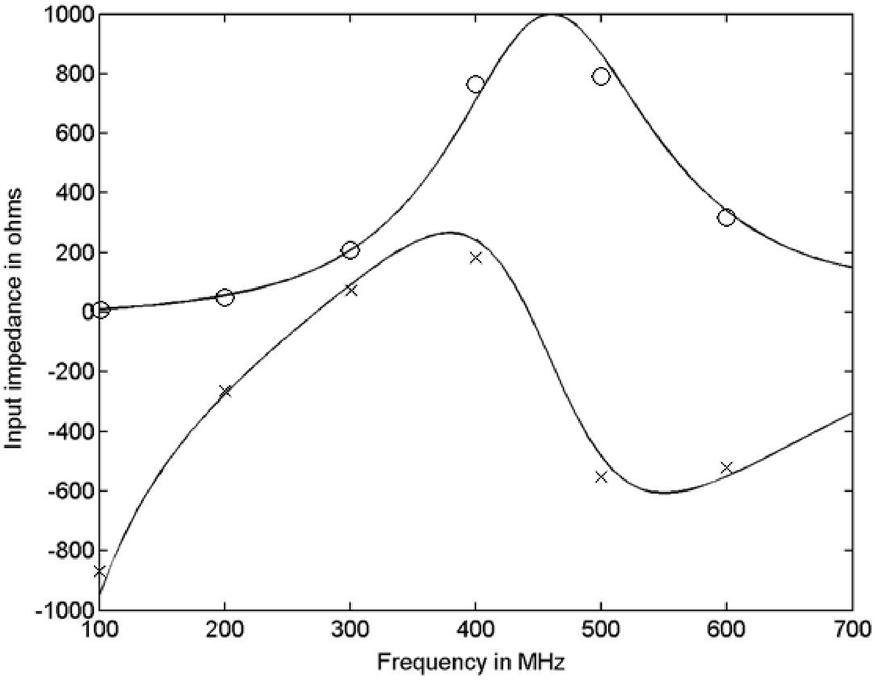

Figure 3.4: The input impedance versus frequency for two parallel dipoles separated by 15 mm; solid line: NEC [6], ('ooo' Resistance, 'xxx' Reactance present work).

The axial and circumferential lengths were subdivided by 16 curvilinear patches of equal lengths in both directions. The attachment basis modes between the wire ends and the wire surface were placed subject to the corresponding number of axial and circumferential patches used. It is found that the results agree well with those calculated using NEC [10] (extended kernel solution), although it is to be expected that the latter will be less reliable, as less detail in the behaviour of the wire is taken into account. It is worth noting that Tulyathan and Newman [4], observed this behaviour on half wavelength dipoles when they ignored the circumferential surface current component.

For the same antenna geometry, the input impedance at 300 MHz (equivalent to half wavelength dipoles and 0.005 wavelength wire radius) versus the separated distance between the dipoles is shown in Figure 3.5.

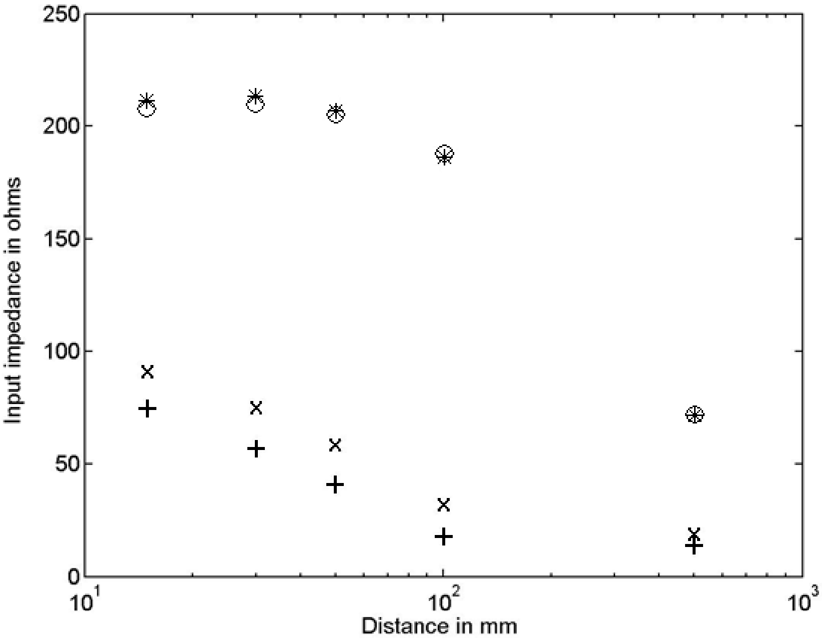

Figure 3.5: Input impedance at 300 MHz operating frequency of two parallel dipoles of 50 cm length and 5 mm wire radius versus the separated distance between them; (‘***’, ‘+++’: Present work), (‘ooo’ and ‘xxx’: NEC).

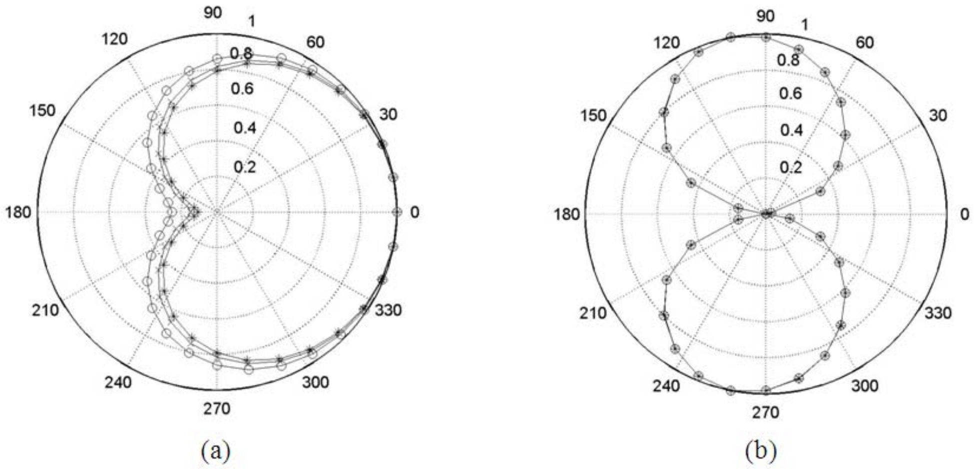

Figure 3.6: The normalised magnitudes of the axial and circumferential surface current components of the antenna geometry given in Figure 3.3 separated by 15 mm versus α at γ= 6.25 cm for axial and γ= 4.6845 cm for circumferential from the bottom of the dipoles for different operating frequencies: ‘xxx’ 100 MHz, ‘***’ 300 MHz, ‘ooo’ 500 MHz; (a) axial component, (b) circumferential component.

It is clearly seen that there is good agreement between the results of the present work and those obtained from NEC except for the reactance values for closely spaced distances. However, the methods were completely different in their numerical solutions. The normalised magnitudes of the axial and circumferential surface current components of two parallel dipoles separated by 15 mm for the same wire radius as above are shown in Figure 3.6, versus α (the azimuth of the circumferential cross-section wire) at 6.25 cm and 4.6845 cm respectively, considered from bottom of the dipoles of their local axes (equivalent to γ length measured from the bottom of the dipole), for different operating frequencies. It is very interesting to note that the non-uniform variations of these currents over different frequencies have small marginal differences. The maximum ratio of the axial component to the circumferential component was around 34:1. Similarly, these currents at 300 MHz (equivalent to half wavelength dipoles) for different separation distances are presented in Figure 3.7. It should be noted that the actual magnitudes of the circumferential component is inversely proportional to the distance between the dipoles in spite of their fixed variations shown in Figure 3.7(b). Also the axial component is still non-uniform even when the separation distance between the dipoles is 100 mm (0.1 wavelengths). The normalised surface currents for a thicker wire of radius of 10 mm (0.01 wavelengths) for the same antenna geometry versus the separation distances between the dipoles are shown in Figure 3.8. Comparing Figures 3.7(a) and 3.8(a) the non-uniform effects on the axial components can be strongly seen on the thick wires, for example at the separation distance of 100 mm. It is clear from Figures 3.4 and 3.5 that the average current along the local axis of the dipoles will be similar to that computed using NEC, thus the expected field pattern will be similar, and is not reproduced here. The ratio of the power losses predicted from the non-uniform surface current distribution to those predicted from the average (or uniform) current distribution was considered as an equivalent measure of the improvement in modelling verisimilitude when using the new method. However, since the losses are small in most cases it is possible to assume that the antenna wire is perfectly conducting and surrounded by free space; then losses can be predicted by taking them as proportional to the surface current density squared. The variation of the power loss ratio against the separated distance between two parallel half wavelength dipoles, for two wire thicknesses, is shown in Figure 3.9. It can be noticed that for high separation distances, the power loss converged to unity value as is expected. However, the variations show a significant power loss for closely spaced dipole antennas. For the following two antenna geometries we restrict our discussion on the presence of non-uniformity of the surface currents that clearly match the variations of the power loss ratios.

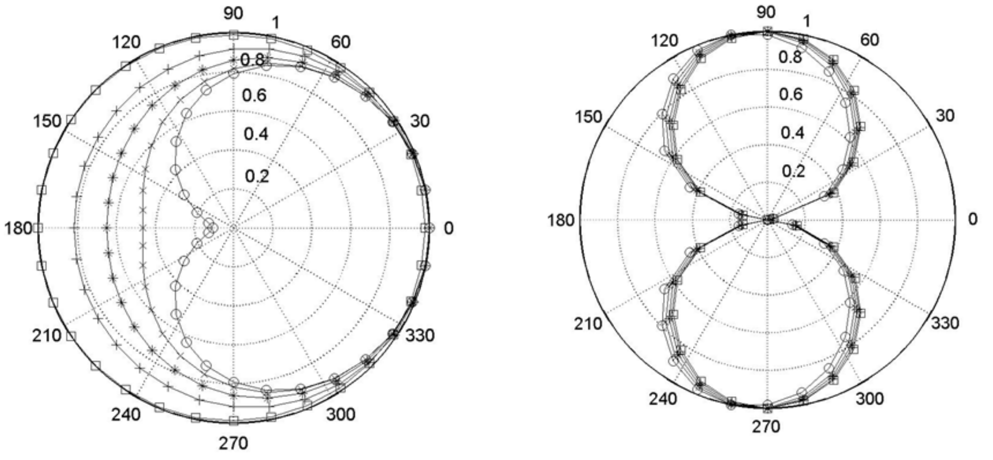

(a)

(b)

Figure 3.7: The normalised magnitudes of the axial and circumferential surface current components versus α at similar location as Figure 3.6, for different separated distances between the dipoles at 300 MHz (equivalent half wavelength dipoles with 0.005λ wire radius): (a) axial component, (b) circumferential component. ('ooo': 15 mm, 'xxx': 30 mm, '***': 50 mm, '+++': 100 mm, '□□□':500 mm).

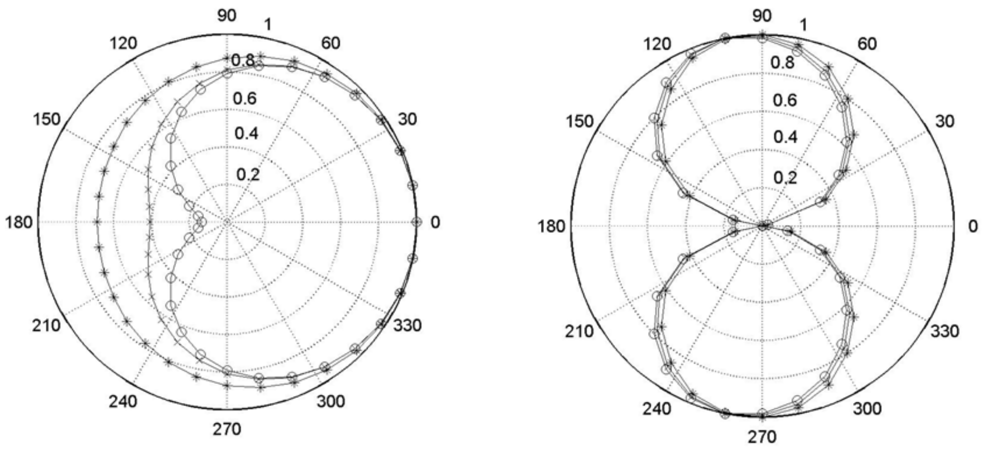

(a) (b)

Figure 3.8: The normalised magnitudes of the axial and circumferential surface current components versus α at similar locations as Figure 3.6, for different separated distances between the dipoles at 300 MHz (equivalent to half wavelength dipoles with 0.01λ wire radius): (a) axial component, (b) circumferential component. (‘ooo’: 30 mm, ‘xxx’: 50 mm, ‘***’: 100 mm).

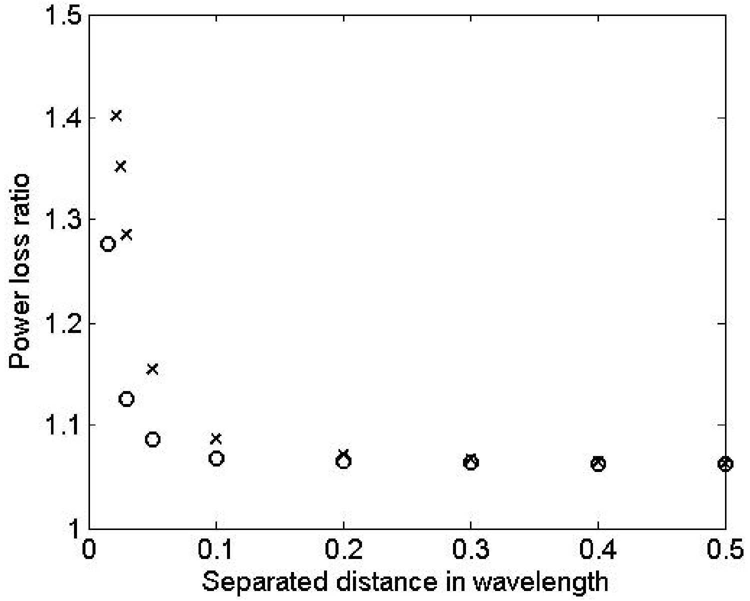

Figure 3.9: Power loss ratio of two parallel half wavelength dipoles for various separation distances; ‘ooo’: wire radius = 0.005λ, ‘xxx’: wire radius = 0.01λ.

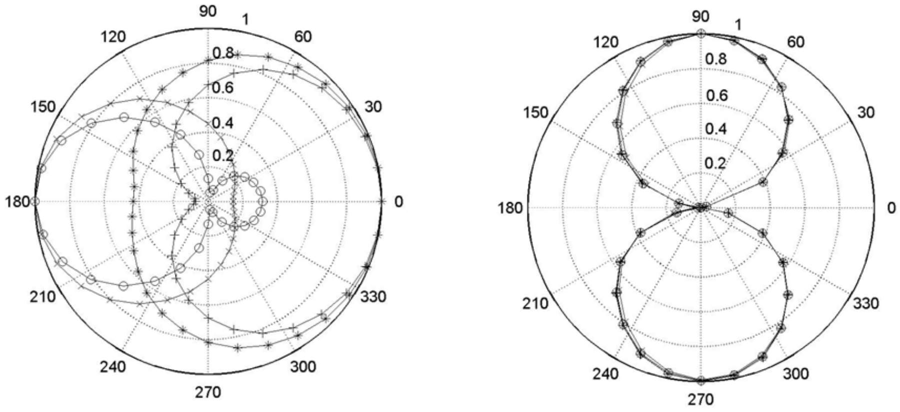

(a) (b)

Figure 3.10: The normalised magnitudes of the axial and circumferential surface current components versus α at $\phi = 0°$: axial component and $\phi = 33.75°$: circumferential component, for a single loop antenna for different operating frequencies.
The loop radius and wire radius are 3 cm and 5 mm respectively.
(a) axial component, (b) circumferential component.
('xxx': 400 MHz, 'ooo': 600 MHz, '+++': 800 MHz, '***': 900 MHz).

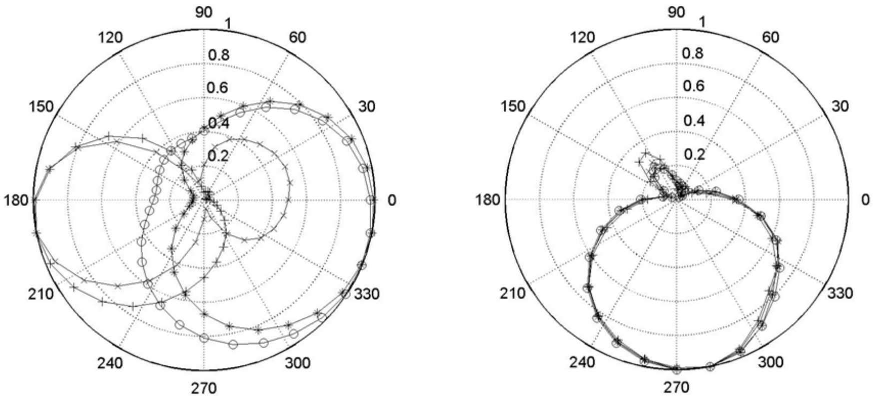

(a) (b)

Figure 3.11: The normalised magnitudes of the axial and circumferential surface current components versus α at $\phi = 0°$: axial component and $\phi = 33.75°$: circumferential component, for two parallel loops separated by 15 mm and each has a radius of 3 cm and 5 mm wire radius versus different operating frequencies.
(a) axial component, (b) circumferential component.
('+++': 400 MHz, 'xxx': 600 MHz, '***': 800 MHz, 'ooo': 900 MHz).

The normalised magnitudes of the axial and circumferential surface current components for single and two parallel loops versus α for different operating frequencies are shown in Figures 3.10 and 3.11 respectively. For both figures the loop radius and wire radius are 3 cm and 5 mm respectively. In the case of parallel loops the separation distance was selected to be 15 mm. The loops are fed by a simple delta excitation source at $\phi = 0°$. The axial component is taken at the source location whereas the circumferential is taken at $\phi = 33.75°$ (angles are simply used here to define the locations of the circumferential cross-section wire, and for this particular angle the γ length is 0.0177cm). It should be noted that the variations of the currents for two parallel loops are taken for the bottom loop as shown in Figure 3.3(b). It is clearly shown that the maximum variations of the axial currents for frequencies less that the expected parallel resonance frequency of the antenna structure are always pointed inside the loops geometries (i.e. $\alpha = 180°$). The circumferential component for the single loop antenna is similar to that computed on the two parallel dipoles, and its ratio compared to the axial component was found to be 41:1. However, the same component for two parallel loops was reduced to minimum around $\alpha = 90°$, whereas its ratio to axial component was 28:1. Moreover, the normalised magnitudes of the axial and circumferential surface current components for two half wavelength parallel loops each of radius 0.0796 wavelength and 0.013 wavelength wire radius versus α for various separation distances d are shown in Figure 3.12. The locations of these currents are similar to those taken in Figures 3.10 and 3.11. The axial component reserved its variations for most of the distances considered in this example as in the case of the single loop antenna except when at very close distance. The variations of the circumferential component was also eliminated around $\alpha = 90°$ even the separation distance was $20a$.

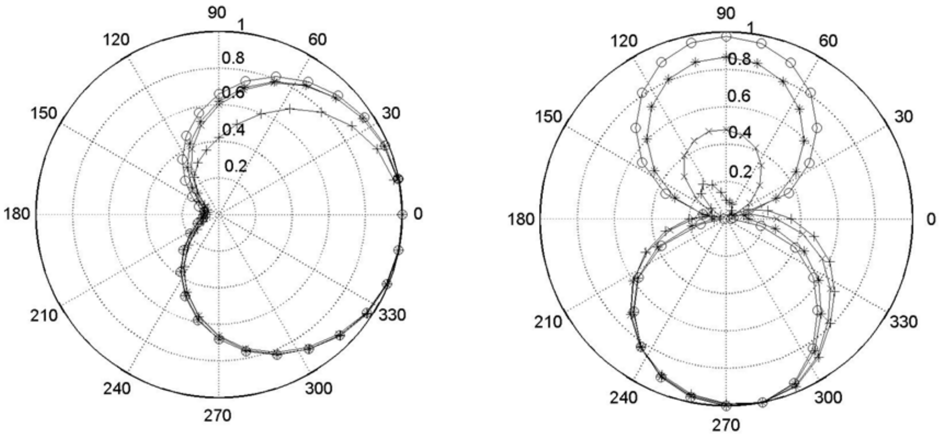

(a) (b)

Figure 3.12: The normalised magnitudes of the axial and circumferential surface current components versus α at $\phi = 0°$: axial component and $\phi = 33.75°$: circumferential component, for two half wavelength parallel loops each of radius 0.0796 wavelength and 0.013 wavelength wire radius, versus the separation distance '*d*'.
(a) axial component, (b) circumferential component.
('+++': $d = 3a$, 'xxx': $d = 6a$, '***': $d = 20a$, 'ooo': $d = 100a$).

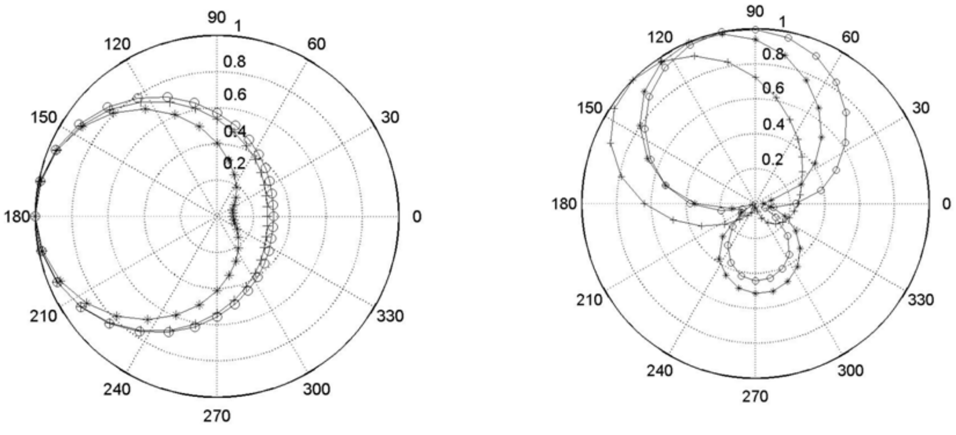

(a) (b)

Figure 3.13: The normalised magnitudes of the axial and circumferential surface current components of a half wavelength single turn helix antenna versus α at different positions from the first end of the helix. The helix radius, wire radius and pitch distance are 0.0796λ, 0.013λ and $3a$ respectively.
(a) axial component: '***':0.031λ, 'ooo':0.125λ, '+++':0.25λ
(b) circumferential component: '***':0.0156λ, 'ooo':0.109λ, '+++':0.234λ.

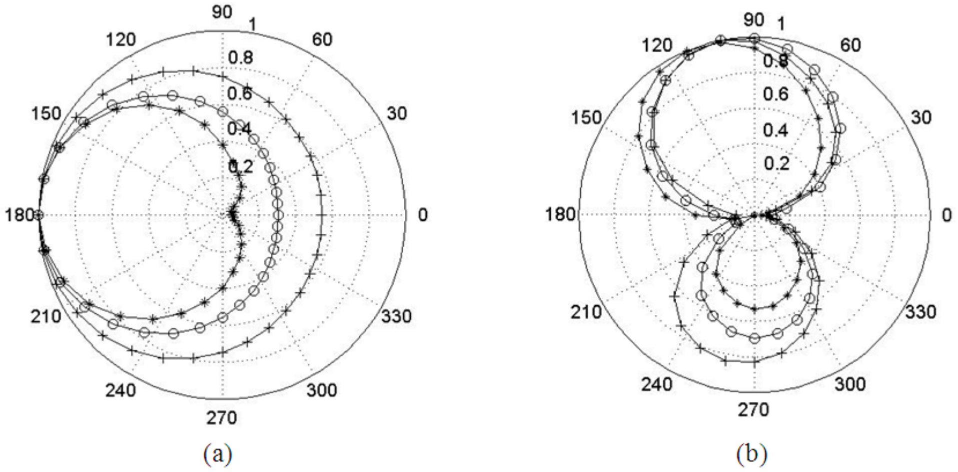

(a) (b)

Figure 3.14: The normalised magnitudes of the axial and circumferential surface current components of the same antenna geometry given in Figure 3.12, except that the operating frequency is half than that used in Figure 3.12 (i.e. operating wavelength 2λ).
(a) axial component: '***':0.031λ, 'ooo':0.125λ, '+++':0.25λ
(b) circumferential component: '***':0.0156λ, 'ooo':0.109λ, '+++':0.234λ.

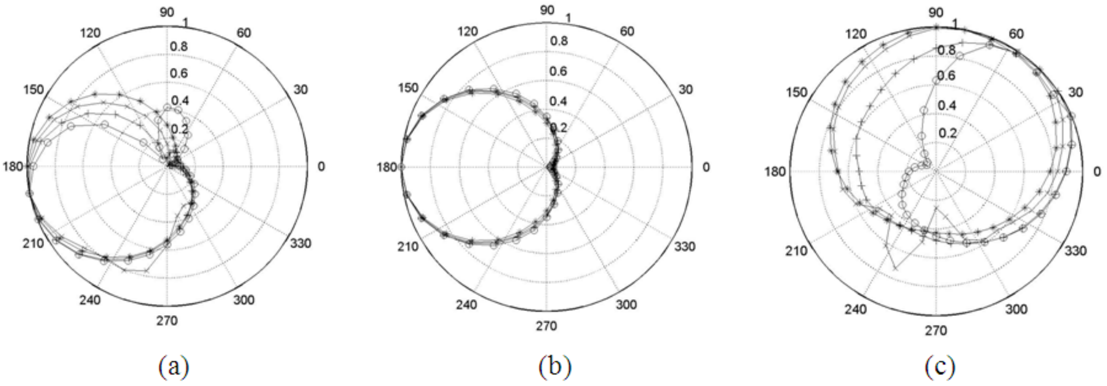

(a) (b) (c)

Figure 3.15: The normalised magnitudes of the axial and circumferential surface current components of a half wavelength two turns helix antenna versus α for different pitch distances. The helix radius and wire radius are 0.04λ and 0.006λ respectively.
('ooo': $P = 3a$, '+++': $P = 5a$, 'xxx': $P = 7a$, '***': $P = 9a$)
(a) axial component: taken at 0.031λ from the bottom end of the helix.
(b) axial component: taken at the centre of the helix.
(c) circumferential component: taken at 0.023λ from the bottom end of the helix.

The normalised magnitudes of the axial and circumferential surface current components of a half wavelength single turn helix antenna versus α at different positions from the first end of the helix are shown in Figure 3.13. The helix radius, wire radius and pitch distance are 0.0796λ, 0.013λ and $3a$ respectively. It is shown that the strong effects of the axial component were pointed inside the helix for all locations presented. These results might help to approximate the equivalent of these variations into one curve that might be taken along all the local length of the helix to assess the total loss power in the axial direction. Similar variations were observed on the circumferential component except that the strong effect has shifted from $\alpha = 90°$ to $\alpha = 135°$ for the locations presented. However, considering the strong effect locations of these currents regardless of the locations of their maxima and taking into account the similarities in these variations it may be concluded that this indicates the approximate contribution of this current to the total loss power.

However, for the same antenna geometry given in Figure 3.13, the currents were computed at half the operating frequency (i.e. operating wavelength 2λ) as shown in Figure 3.14. It is clearly shown that the strong effects of these current variations are mostly similar to that presented in Figure 3.13. Moreover, a strong correlation can be found in the variations of the circumferential currents for different locations for this example. However, a one turn helix is not sufficient to permit comment on the currents variations of a multi-turn helix antenna, thus the following examples are considered.

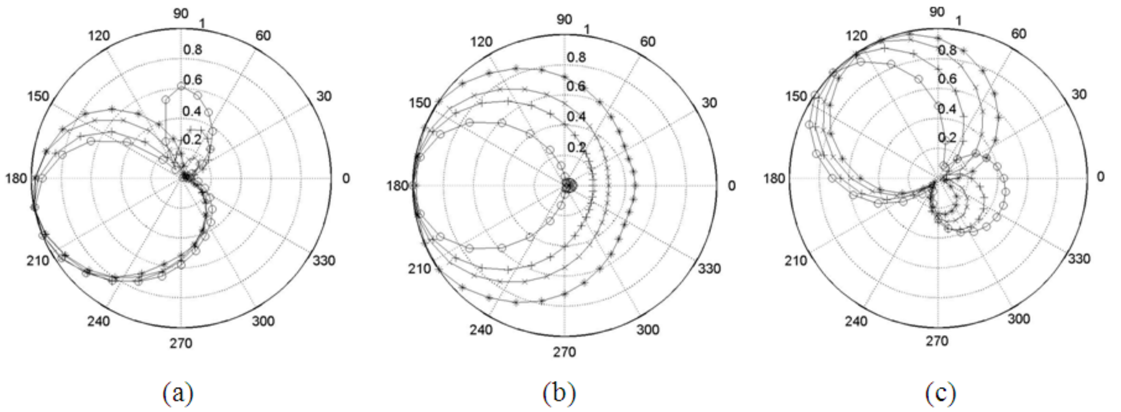

(a) (b) (c)

Figure 3.16: The normalised magnitudes of the axial and circumferential surface current components of a half wavelength three turns helix antenna versus α for different pitch distances. The helix radius and wire radius are 0.0265λ and 0.004λ respectively.
('ooo': $P = 3a$, '+++': $P = 5a$, 'xxx': $P = 7a$, '***': $P = 9a$)
(a) axial component: taken at 0.0294λ from the bottom end of the helix.
(b) axial component: taken at the centre of the helix.
(c) circumferential component: taken at 0.022λ from the bottom end of the helix.

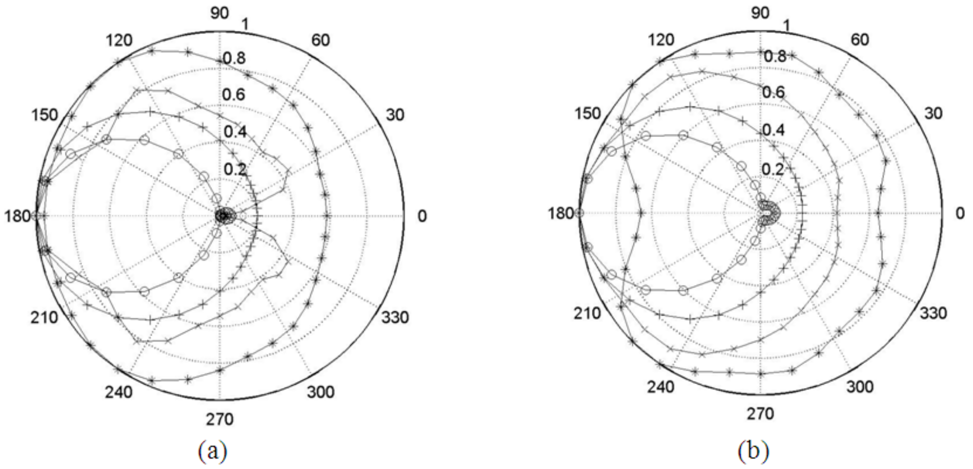

(a) (b)

Figure 3.17: The normalised magnitudes of the axial surface current components of a half wavelength four turns helix antenna versus α for different pitch distances. (a) four turns: the helix radius and wire radius are 0.02λ and 0.003λ respectively; (b) five turns: the helix radius and wire radius are 0.015λ and 0.002λ respectively;
('ooo': $P = 3a$, '+++': $P = 5a$, 'xxx': $P = 7a$, '***': $P = 9a$).

The normalised magnitudes of the axial and circumferential surface current components of a half wavelength of two, three, four and five turns helix antenna versus α for different pitch distances are shown in Figures 3.15, 3.16 and 3.17. It is very clear that the axial and circumferential components were non-uniform even if the pitch distance between the helix turns was nine times the radius of the wire. Another interesting point is that the peak values of the axial component were pointed inside the helix (i.e. around α = 180°) for all helices presented. This is clearly shown in the variations of these currents at the feed points on Figures 3.15(b), 3.16(b), 3.17(a) and 3.17(b) and the helix turns in Figures 3.15(a) (first turn) and 3.16(a) (first turn). The similarities of these variations permit the approximate calculation of the effective power loss in that particular direction. It was also observed that the maximum variations of the circumferential component on the first turn confined between α = 0° and 180° as shown in Figures 3.13(b), 3.14(b), 3.15(c) and 3.16(c). However, the maximum ratio of the axial component to the circumferential component for all pitch distances was found between 15:1 and 40:1 for all helices more than one turn.

General comments on the trend of these results are to predict the accurate or approximated equivalent power losses that are associated with non-uniform variations along the wire surfaces. Hence this will follow to affect the radiation efficiency of this kind of antennas.

3.6 Conclusion

The surface current distributions on structures with closely spaced parallel wires, such as dipoles, loops and helical antennas, can be computed by using the method of moments with a general surface patch formulation. The current distribution varies substantially from the common assumption that it is uniform around the wire cross-section. Transverse (circumferential) currents are shown to be present: they are relatively weak on thin wires (around 0.01λ wire radius) excited by axial component parallel to the local axis of the wire. The effect is still significant when the wire separation distance is relatively large.

In spite the strong variations of the axial and circumferential currents, it was found that the input impedance and the average value of the axial surface current are in reasonable good agreement with the results of thin wire codes such as NEC using an extended kernel solution. The power loss ratio resulting from use of non-uniform surface current, compared with the conventional uniform assumption of two parallel dipoles, shows a significant increase of power loss when they are closely separated. However, these current variations will dominate the radiation efficiency when predicting the accurate total power loss on these types of antennas and this can be important in some applications, e.g. highly resonant antennas and antennas realised in superconducting materials. As a matter of interest it was computed that the maximum ratio of the variations of the axial component to the circumferential component on a half wavelength helix of a few turns for different pitch distances was between 15:1 to 40:1. This behaviour is expected as the NMHA has a hybrid of dipole and loop behaviour.

The modelling method employed a two-dimensional electric surface patch integral equation formulation solved by independent piecewise-linear basis function methods in the circumferential and axial directions of the wire. A similar orthogonal basis function was used on the end surface and appropriate attachments with the wire surface were employed to satisfy the requirements of current continuity. The results were stable and showed good agreement with less comprehensive earlier work by others.

3.7 References

[1] G. Smith, "The proximity effect in systems of parallel conductors and electrically small multiturn loop antennas," *Tech. Rep. 624, Division of Engineering and Applied Physics, Harvard University, USA*, 1971.

[2] G. Smith, "The proximity effect in systems of parallel conductors," *J. Applied Physics*, vol. 43, pp. 2196-2203, 1972.

[3] G. O. Olaofe, "Scattering by two cylinders," *Radio Sci.*, vol. 5, pp. 1351-1360, 1970.

[4] P. Tulyathan and E. H. Newman, "The circumferential variation of the axial component of current in closely spaced thin-wire antennas," *IEEE Transactions on Antennas and Propagation*, vol. AP-27, pp. 46-50, 1979.

[5] R. A. Abd-Alhameed and P. S. Excell, "The complete surface current for NMHA using sinusoidal basis functions and Galerkins solution," *IEE Proc. Science, Measurement and Technology on Computational Electromagnetics*, vol. 149, pp. 272-276, 2002.

[6] R. A. Abd-Alhameed and P. S. Excell, "Surface current distribution on closely

parallel wires within antennas," *The Second European Conference on Antennas and Propagation, EuCAP 2007*, pp. 1-6, 2007.

[7] R. A. Abd-Alhameed and P. S. Excell, "Accurate power loss computation of closely spaced radiating wire elements for mobile phone MIMO application," *IEEE International Conference on Signal Processing and Communication, Dubai, United Arab Emirates*, pp. 1-4, 2007.

[8] R. A. Abd-Alhameed and P. S. Excell, "Non-uniform surface current distribution on parallel wire loop antennas using curved patches in the method of moments," *IET Science, Measurement and Technology*, vol. 2, pp. 493-498, 2008.

[9] A. R. Djordjevic, M. B. Bazdar, V. V. Petrovic, D. I. Olcan, T. K. Sarkar, and R. F. Harrington, *Analysis of wire antennas and scatterers*. Boston, USA: Artech House, 1990.

[10] G. J. Burke and A. J. Poggio, "Numerical electromagnetics code (NEC): method of moments," *US Naval Ocean Systems Centre, Rep. No. TD116*, 1981.

[11] J. H. Richmond, "Radiation and scattering by thin-wire structures in the complex frequency domain," *NASA Rept. No. CR-2396*, 1974.

[12] FEKO: EM Software and Systems S. A., (Pty) Ltd, Stellenbosch, South Africa.

[13] CST: Computer Simulation Technology Corporation, Microwave Studio, Version 5.0, German.

[14] HFSS: v. 10, Ansoft [online], www.ansoft.com.

[15] IE3D: Release 12, Zeland Software Inc., Fremont CA, USA, 2007.

[16] D. A. E. Mohamed, "Comprehensive analysis of broad band wired antennas," *National Radio Science Conference (NRSC)*, pp. 1-10, 2009.

[17] W. G. Hong, Y. Yamada, and N. Michishita, "Low profile small normal mode helical antenna achieving long communication distance," *International Workshop on Antenna Technology: Small Antennas and Novel Metamaterials (iWAT), Chiba, Japan*, pp. 167-170, 2008.

[18] H. Mimaki and H. Nakano, "Double pitch helical antenna," *IEEE Antennas and Propagation Society International Symposium*, vol. 4, pp. 2320-2323, 1998.

[19] S. Ooi, "Normal mode helical antenna broad-banding using multiple pitches," *IEEE Antennas and Propagation Society International Symposium*, vol. 1, pp. 860-863 2003.

[20] W. L. Stutzman and G. A. Thiele, *Antenna theory and design*, 2nd ed. New York: John Wiley & Sons, 1998.

[21] K. Sawaya, "Antenna design by using method of moments," *IEICE Transaction Communication*, vol. E88-B, pp. 1766-1773, 2005.

[22] R. E. Collin, *Field theory of guided waves*, 2nd ed. New York: The Institute of Electrical and Electronics Engineers Inc., 1995.

[23] A. Ishimaru, *Electromagnetic wave propagation, radiation and scattering*. Englewood Cliffs, New Jersey: Prentice Hall, 1991.

[24] M. I. Aksun and R. Mittra, "Choices of expansion and testing functions for the method of moments applied to a class of electromagnetic problems," *IEEE Transactions on Microwave Theory and Techniques*, vol. 41, pp. 503-509, 1993.

[25] M. A. Khayat and D. R. Wilton, "Numerical evaluation of singular and near-singular potential integrals," *IEEE Transactions on Antennas and Propagation*, vol. 53, pp. 3180-3190, 2005.

Chapter 4

Quasi-Static Finite-Difference Time-Domain Subgridding Technique

4.1 Introduction

The development of robust finite-difference time-domain (FDTD) method has been widely used in electromagnetic scattering problems due to its easiness and potentiality to treat complex geometry structures in the huge calculation region [1]. This method of solving Maxwell's differential equations was first proposed in two-dimensional problems [2] and then utilized in three-dimensional applications [3]. However, the standard FDTD method is incompetent if the details of the geometry need to be modelled due to a global fine mesh. As a result, the total number of cells increases dramatically. The time step must be reduced to fulfill the Courant stability condition causing the computational time to increase significantly. The discretisation of time step is crucial for accurate determination of the scheme and has to be small enough to resolve different dielectric or metal structures.

A few methods can be used to improve the efficiency of the FDTD method, such as non-uniform meshing [4], sub-cellular technique [5], non-orthogonal meshing [6] and subgridding method [7-10]. Subgridding generally involves local mesh refinement particularly inside the area or volume of interest which require more accurate discretisation. A stable subgridding algorithm can refine the mesh locally and improve the accuracy of the result without increasing the computational efforts significantly. It is hence very useful for FDTD code. Both the numerical dispersion and memory usage must be reduced but there is a trade-off between them. The accuracy of the solution can be improved by using finer grids since numerical dispersion is controlled by the size of the grid in the computational domain. However, the memory and computation requirement are increased accordingly.

An alternative approach to reduce the memory usage in the computational domain is to use FDTD subgridding scheme by controlling the distribution of the degrees-of-freedom. In FDTD subgridding method, the smaller size components in a structure is discretised by fine grids and the residual of the space is filled with coarse grids. The fields on the boundary between coarse and fine grids are coupled using spatial and temporal interpolations. The regions of the coarse and fine grids are computed by the FDTD method and are kept in time step. Many articles are published with different updating field methods at the unknown cell of the boundary by means of both interpolation and extrapolation techniques. In general, some of them are based on interpolation of current density [7], time interpolation subgridding algorithm [9], dielectric transverse capability [11] and finite element formulation [12, 13].

4.2 Quasi-Static Theorem

FDTD technique is not a practical scheme when low frequency is applied due to lengthy simulation time. The computer burden cannot be solved even for reasonable spatial resolution. For example, the spatial resolution of $\Delta x = \Delta y = \Delta z = 1$ cm is given at 50 Hz power line frequency. The duration of time step required is given from Courant stability criterion, $\Delta t = \Delta x / c\sqrt{3} = 1.92$ ns. In order to cover one complete cycle, the number of time steps needed is $N = 1/(f\Delta t) = 1.0 \times 10^7$. It needs many years to complete the simulation even when run on fast machine. However, a method known as quasi-static approximation proposed by Moerloose *et al.* [14] solve the difficulties. The formulation takes into account the wavelength which is much greater than the object of study. The primary advantage of quasi-static formulation is thus reducing the long simulation time constraint. There have been some early efforts of using quasi-static idea to study the interaction between living tissues exposed to extremely low frequency (ELF) electric fields in the published literature such as [15-17]. The basis of their research dominantly verifies the effectiveness of quasi-static scheme at very low frequency. FDTD comes into play when researches in [18-21] applied the same knowledge. In this case, the dimension of the object of study is at a fraction of the wavelength. An attempt to gain the scheme of using the same technique but at much higher frequencies of 900 MHz and 1800 MHz has been made by Emili *et al.* in 2003 [22].

The theoretical method discussed by the authors in [15-17] has been realised in the present work to approximate the quasi-static FDTD subgridding. In general, two conditions must be satisfied before applying the quasi-static formulation:

i. The size of the object is a factor of 10 or more, smaller than the wavelength.

ii. $|\sigma + j\omega\varepsilon| >> \omega\varepsilon_o$

where:

σ is the conductivity of the object (S/m)

ε is permittivity of the object (F/m)

ω is the angular frequency (measured in radians per second, with units s^{-1})

ε_o is the free space permittivity (8.85×10^{-12} F/m)

From the conditions stated above, the electric field components tangent to the surface of the structure and the internal fields are roughly zero compared to the applied field. The external electric field components can be viewed as orthogonal to the structure. From Maxwell's equation with div $D = \rho$, the boundary condition for the normal electric field components at the surface of the region of interest is given by the expression [16-18]:

$$j\omega\varepsilon_o \hat{n} \bullet \vec{E}_{air} = \left(\sigma_{tissue} + j\omega\varepsilon_{tissue}\right)\hat{n} \bullet \vec{E}_{tissue} \qquad (4.1)$$

The '•' symbol in equation (4.1) basically refers to vector dot product. From this equation with the two stated conditions satisfied, the scaling relationship can be deduced [16-18]:

$$\vec{E}_{tissue}(f)=\left(\frac{\omega}{\omega'}\right)\left[\frac{\sigma'(f')+j\omega'\varepsilon(f')}{\sigma(f)+j\omega\varepsilon(f)}\right]\vec{E}'_{tissue}(f') \tag{4.2}$$

where:

$\vec{E}_{tissue}(f)$ is the resultant internal electric field (V/m)

$\vec{E}'_{tissue}(f')$ is the scaling internal electric field (V/m)

f is the frequency of interest (Hz)

f' is the scaling frequency (Hz)

ω is the angular frequency of interest (s^{-1})

ω' is the scaling angular frequency (s^{-1})

σ is the conductivity of the object (S/m)

σ' is the scaling conductivity of the object (S/m)

Assuming that $\omega\varepsilon(f) << \sigma(f)$ and $\omega'\varepsilon'(f') << \sigma'(f')$, then equation (4.2) can be approximated as [16-18]:

$$\vec{E}_{tissue}(f)\cong\left[\frac{f\sigma'(f')}{f'\sigma(f)}\right]\vec{E}'_{tissue}(f') \tag{4.3}$$

It can be concluded that from this equation, a higher working scaling frequency f' which falls within the quasi-static region can be chosen to excite the model in order to reduce the computational burden. Hence, the scaling internal electric field which is calculated at much higher frequency can be shifted back to the actual power line frequency.

4.3 Plane Wave Solutions

This section explains Maxwell's equation solutions and derives the basis of electromagnetic wave motion in free space, lossy and lossless penetrable media [23, 24].

4.3.1 Plane Wave in Free Space

The following equations can be expressed in free space:

$$\sigma = 0, \qquad \varepsilon = \varepsilon_o, \qquad \mu = \mu_o \tag{4.4}$$

$$\alpha = 0, \qquad \beta = \omega\sqrt{\mu_o \varepsilon_o} = \frac{\omega}{c} \tag{4.5}$$

$$u = \frac{\omega}{\beta} = \frac{1}{\sqrt{\mu_o \varepsilon_o}} = c, \qquad \lambda = \frac{2\pi}{\beta} \tag{4.6}$$

$$\eta_o = \sqrt{\frac{\mu_o}{\varepsilon_o}} = 120\pi \approx 377\Omega \tag{4.7}$$

where σ is the conductivity, ε is the permittivity, ε_o is the free space permittivity, μ is the permeability, μ_o is the free space permeability, α is attenuation factor, β is phase constant, ω is the angular frequency, c is the speed of light in free space, u is the wave velocity, λ is the wavelength and η_o is the free space intrinsic impedance of the media.

4.3.2 Plane Wave in Lossy Medium

Maxwell's equations in a linear, isotropic, homogeneous, lossy dielectric medium without the presence of a source can be written in phasor form as:

$$\nabla \times E = -j\omega\mu H \tag{4.8}$$

$$\nabla \times H = (\sigma + j\omega\varepsilon)E \tag{4.9}$$

$$\nabla \cdot E = 0 \tag{4.10}$$

$$\nabla \cdot H = 0 \tag{4.11}$$

Taking the curl of both side of equation (4.8) gives:

$$\nabla \times \nabla \times E = -j\omega\mu\nabla \times H \tag{4.12}$$

Vector identity is given by:

$$\nabla \times \nabla \times A = \nabla(\nabla \cdot A) - \nabla^2 A \tag{4.13}$$

Equation (4.13) is applied to the left-hand side of equation (4.12) with both equations (4.9) and (4.10) are implemented to get the expression below:

$$\nabla^2 E - \gamma^2 E = 0 \tag{4.14}$$

$$\gamma^2 = j\omega\mu(\sigma + j\omega\varepsilon) \tag{4.15}$$

where γ is called the propagation constant of the medium and is measured in per meter. Similarly, the magnetic field H can be derived with the same technique:

$$\nabla^2 H - \gamma^2 H = 0 \tag{4.16}$$

Equations (4.14) and (4.16) are known as homogeneous vector Helmholtz's equations or simple vector wave equations. The propagation constant of the penetrable medium γ is basically a complex quantity which is governed by:

$$\gamma = \alpha + j\beta = j\omega\sqrt{\mu\varepsilon}\sqrt{1 - j\frac{\sigma}{\omega\varepsilon}} \tag{4.17}$$

$$\alpha = \omega\sqrt{\frac{\mu\varepsilon}{2}\left[\sqrt{1+\left[\frac{\sigma}{\omega\varepsilon}\right]^2} - 1\right]} \tag{4.18}$$

$$\beta = \omega\sqrt{\frac{\mu\varepsilon}{2}\left[\sqrt{1+\left[\frac{\sigma}{\omega\varepsilon}\right]^2}+1\right]} \tag{4.19}$$

where α is known as the attenuation constant or attenuation factor of the medium and is measured in Np/m or dB/m. The parameter β is a measure of the phase shift per length and is called the phase constant or wave number. μ, ε and σ are the permeability, permittivity and conductivity of the media respectively. ω is the angular frequency and is measured in radian. Both the wave velocity u and wavelength λ can be written in terms of β as depicted in equation (4.6). It should be noted that the solution of the basic plane wave can be found by considering the wave that propagates in z direction and polarises in x direction. Hence, equation (4.14) can be expressed as:

$$\frac{d^2E_x}{dz^2} - \gamma^2 E_x = 0 \tag{4.20}$$

The solution of equation (4.20) is given by:

$$E_x(z) = E^+e^{-\gamma z} + E^-e^{\gamma z} \tag{4.21}$$

where E^+ and E^- are arbitrary amplitude constants. The positive travelling wave has a propagation factor in terms of the attenuation constant α and phase constant β:

$$e^{-\gamma z} = e^{-\alpha z} e^{-j\beta z} \tag{4.22}$$

Equation (4.22) can be expressed in the time domain as:

$$e^{-\gamma z} = e^{-\alpha z} \cos(\omega t - \beta z) \tag{4.23}$$

This equation shows a wave travelling in the $+z$ direction. The wave has a wavelength $\lambda = 2\pi/\beta$, phase velocity $v_p = \omega/\beta$ and an exponential damping factor. The attenuation constant α represents the decay rate with distance. The negative part of the travelling wave term in the equation (4.21) is similarly damped along the $-z$-axis. The solution for positive electric travelling wave $E(z,t)$ is thus achieved by:

$$E(z,t) = \mathrm{Re}(E_o e^{-\alpha z} e^{j(\omega t - \beta z)} a_x) = E_o e^{-\alpha z} \cos(\omega t - \beta z) a_x \tag{4.24}$$

The solution for the positive magnetic travelling wave $H(z,t)$ can be realised in the same way by solving equation (4.16).

$$H(z,t) = \mathrm{Re}(H_o e^{-\alpha z} e^{j(\omega t - \beta z)} a_y) = H_o e^{-\alpha z} \cos(\omega t - \beta z) a_y \tag{4.25}$$

The relationship between E_o and H_o can be achieved by applying Faraday's law to equation (4.8), Ampere's law to equation (4.9) and comparing the solution of both equations. From Faraday's law, equation (4.8) can be expressed as:

$$\nabla \times E = -\mu \frac{\partial H}{\partial t} \tag{4.26}$$

$$H = -\frac{1}{\mu}\int (\nabla \times E)dt \tag{4.27}$$

By definition, ∇ × *E* is given by the expression:

$$\nabla \times E = \begin{vmatrix} i & j & k \\ \partial/\partial x & \partial/\partial y & \partial/\partial z \\ E_x & 0 & 0 \end{vmatrix} = \frac{\partial}{\partial z} E_x = -E_o e^{-\alpha z}(\alpha + j\beta)e^{j(\omega t - \beta z)} a_y \tag{4.28}$$

Inserting equation (4.28) into equation (4.27) gives:

$$H = \frac{1}{j\mu\omega} E_o (\alpha + j\beta) e^{-\alpha z} e^{j(\omega t - \beta z)} a_y \tag{4.29}$$

From Ampere’s law, equation (4.9) can be expressed as:

$$\nabla \times H = \sigma E + \varepsilon \frac{\partial E}{\partial t} \tag{4.30}$$

By definition, ∇ × *H* is given by the expression:

$$\nabla \times H = \begin{vmatrix} i & j & k \\ \partial/\partial x & \partial/\partial y & \partial/\partial z \\ 0 & H_y & 0 \end{vmatrix} = -\frac{\partial}{\partial z} H_y = \frac{E_o(\alpha + j\beta)^2}{j\omega\mu} e^{-\alpha z} e^{j(\omega t - \beta z)} a_x \tag{4.31}$$

Next, equation (4.31) is simplified to give:

$$\nabla \times H = (\sigma + j\omega\varepsilon) E_o e^{-\alpha z} e^{j(\omega t - \beta z)} \tag{4.32}$$

Equations (4.31) and (4.32) are compared to obtain the expression:

$$(\alpha + j\beta) = \sqrt{(\sigma + j\omega\varepsilon)(j\omega\mu)} \tag{4.33}$$

Substituting equation (4.33) into equation (4.29) gives the relation between E_o and H_o:

$$H_o = \frac{E_o}{\eta} \tag{4.34}$$

where η is a complex quantity known as the intrinsic impedance of the medium. It is measured in ohms. It can also be written in the following form:

$$\eta = \sqrt{\frac{j\omega\mu}{\sigma + j\omega\varepsilon}} = |\eta| \angle \theta_\eta = |\eta| e^{j\theta_\eta} \tag{4.35}$$

$$|\eta| = \frac{\sqrt{\frac{\mu}{\varepsilon}}}{\left[1+\left(\frac{\sigma}{\omega\varepsilon}\right)^{2}\right]^{1/4}}, \qquad \tan 2\theta_{\eta} = \frac{\sigma}{\omega\varepsilon} \tag{4.36}$$

where $0^{\circ} \leq \theta_{\eta} \leq 45^{\circ}$. The relationship between $H(z,t)$ and $E(z,t)$ is determined replacing equations (4.34) and (4.35) into equation (4.25), which is stated as:

$$H(z,t) = \mathrm{Re}\left(\frac{E_o}{|\eta| e^{j\theta_{\eta}}} e^{-\alpha z} e^{j(\omega t-\beta z)} a_y\right) \tag{4.37}$$

By taking the real part of equation (4.37), the final expression is given by:

$$H(z,t) = \frac{E_o}{|\eta| e^{j\theta_{\eta}}} e^{-\alpha z} \cos(\omega t - \beta z - \theta_{\eta}) a_y \tag{4.38}$$

4.3.3 Plane Wave in Lossless Medium

In a lossless dielectric, $\sigma << \omega\varepsilon$. It is a special case from previous section except that:

$$\sigma \cong 0, \qquad \varepsilon = \varepsilon_o \varepsilon_r, \qquad \mu = \mu_o \mu_r \tag{4.39}$$

In this case, ε_o and μ_o are the permittivity and permeability of the media in vacuum, ε_r and μ_r are the relative permittivity and relative permeability of the media respectively.

Inserting these into equations (4.18) and (4.19) gives the equations:

$$\alpha = 0, \qquad \beta = \omega\sqrt{\mu\varepsilon} \tag{4.40}$$

$$u = \frac{\omega}{\beta} = \frac{1}{\sqrt{u\varepsilon}}, \qquad \lambda = \frac{2\pi}{\beta} \tag{4.41}$$

$$\eta = \sqrt{\frac{\mu}{\varepsilon}}\angle 0^{\circ} \tag{4.42}$$

It should be noted that from equation (4.42), the electric field E and magnetic field H are revealed to be in time phase with each other in a lossless medium.

4.4 Modified Berenger's PML

Finite-difference time-domain method is generally derived from the solution of differential time-domain Maxwell's equations. It is regarded as very efficient method since its invention by K. S. Yee in 1966 [2]. The method is considered as a very practical tool in designing anisotropy and inhomogeneous complex structures. However, problem arises when open-region geometry is modelled. The development of an artificial boundary condition at the boundaries of the computational space has been applied to circumvent this difficulty. The establishment of perfectly matched layer (PML) has greatly improved the performance of this technique. It should be noted that the implementation of absorbing boundary condition (ABC) is very important in FDTD computation to truncate the outgoing electromagnetic waves at the bounded region. There have been several effort to circumvent this problem by means of analytical ABC, such as Mur [3], Liao *et al*. [25] and Mei *et al*. [26]. The proposed techniques provide effective reflection at the boundary in the order of -35 to -60 dB for most FDTD computational simulations. However, the performance of the ABC has been improved significantly by Berenger in 1994 [27] in the order of below -80 dB reflection at the boundary. It is basically based on surrounding the FDTD computational space with highly lossy medium with matched non-physical absorber. Later, he developed the technique in 3-D [28-30] with some numerical experiments to illustrate its efficiency. The state of art of the original contribution by Berenger's PML thus became the choice of the boundary for the simulation problems of this chapter.

The general matching impedance condition between free space and a dispersionless medium is given by [27]:

$$\frac{\sigma}{\varepsilon_o} = \frac{\sigma^*}{\mu_o} \tag{4.43}$$

If equation (4.43) is satisfied, an incident plane wave from free space is perfectly transmitted to a dispersionless medium without any spurious reflection. In other words, it is stated to be matched across a plane boundary for all incoming incident electromagnetic waves. The matching criteria in free space for PML explained previously are extended to lossy and lossless media:

$$\frac{\sigma}{\varepsilon_r \varepsilon_o} = \frac{\sigma^*}{\mu_r \mu_o} \tag{4.44}$$

where σ is the electric conductivity, σ^* is the magnetic resistivity, ε_r is the relative permittivity and μ_r is the relative permeability of the medium. ε_o and μ_o are the permittivity and permeability in vacuum respectively. An optimum value of the geometric grading factor g has been selected to reduce the reflection on the interface layer between the FDTD problem space and the PML, using an empirical expression given by Berenger in 1996 [29]:

$$\sigma = -\frac{\varepsilon c}{2\Delta x} \frac{\ln g}{g^N - 1} \ln R(0) \tag{4.45}$$

where c is the velocity of the travelling electromagnetic waves in free space or lossy medium, Δx is the spatial increment of FDTD lattice, N is the number of the cells in the PML and $R(0)$ is the normal reflection factor.

4.5 Floquet Boundary Condition

The study of scattering characteristic of structures that are periodic in one or more dimensions due to propagating plane wave is very important in electromagnetics. In general, the structures are assumed to be infinite along the axis in order to perform scattering analysis with reasonable simulation time. The analysis can be simplified into a single unit FDTD cell problem by means of Floquet theorem [31, 32]. The primary advantage of applying this theorem is that it can be used to design large structure much simpler and more computationally efficient rather than designing the whole structure since the unit cell has linear dimension of less than one wavelength. Some examples of using the same boundary theorem in electromagnetic analysis are frequency selective surface (FSS) [33-35], antenna array [36], infinite periodic scatterers [37] and photonic bandgap (PBG) [38]. Recently, several absorbing boundary conditions have been compared for numerical analysis of periodic structures [39]. It was found from written literature that floquet theorem has been successfully implemented inside FDTD to analyse the case of normal incidence [37, 40] and oblique incidence [41, 42] for 2-D and 3-D cases. The case of normal incidence method for 2-D and 3-D problems is explained in the following section, to understand basic theory and implementation of floquet periodic boundary into FDTD.

4.5.1 Two-dimensional TM Case

Figure 4.1 shows the basic periodic structure illuminated by plane wave at broadside incidence parallel to y-axis. From the figure, it can be seen that the fraction of the scatterer is replicated alongside x direction. The magnetic barriers are formed along y-axis at $x = 0$ and $x = d$. In this case, the boundary from $x = 0$ and $x = d$ is called a unit cell boundary of the FDTD computational grid. The absorbing boundary condition is applied at the upper and lower edges alongside y direction to solve the electromagnetic wave propagation in unbounded y-axis regions in order to simulate the extension of the grid to infinity [3, 27]. The problem of solving periodic geometries can thus be facilitated on the basis of a single unit cell structure due to the scatterer periodicity characteristic along y-axis.

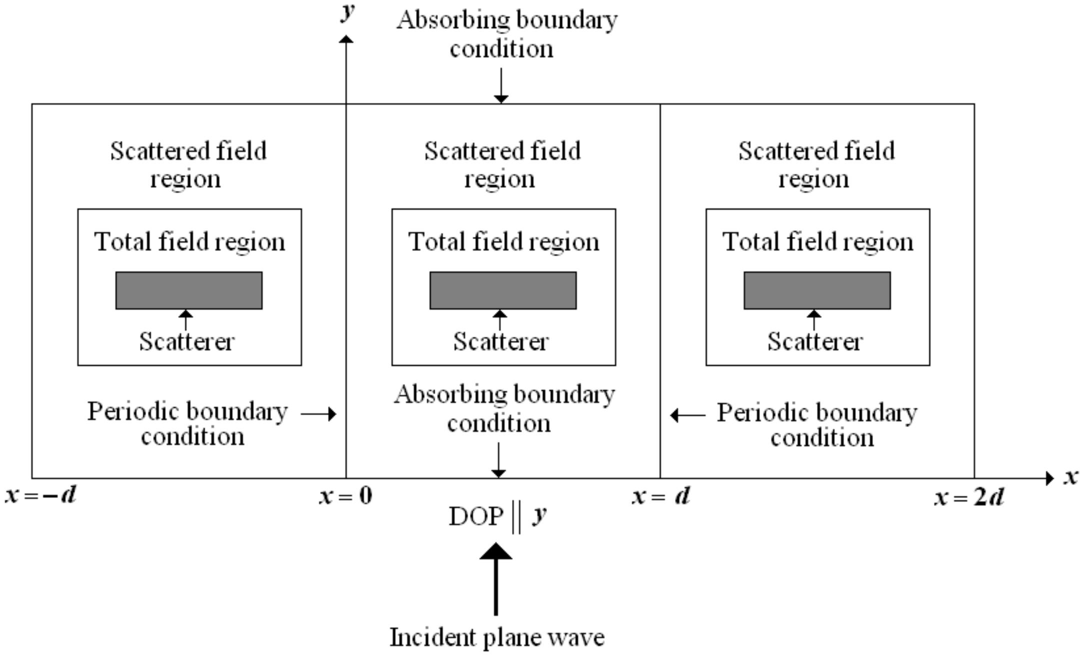

Figure 4.1: General periodic boundary structure in 2-D.

In 2-D TM case analysis, the electric field component involved is E_z whereas the magnetic field components are H_x and H_y. For simplicity, a lossless medium with $\sigma = 0$, $\varepsilon = \varepsilon_o\varepsilon_r$ and $\mu = \mu_o$ is considered, in which σ, ε and μ are the conductivity, permittivity and permeability of the lossless medium respectively, ε_o and μ_o are the free space permittivity and permeability respectively, and ε_r is the relative permittivity. Thus, the 3-D FDTD updating equations of (2.21), (2.22) and (2.26) for H_x, H_y and E_z respectively can be reduced to 2-D TM case periodic analysis. These equations can be written in the following simplified form:

$$E_z\Big|_{i,j}^{n+1} = E_z\Big|_{i,j}^{n} + \frac{\Delta t}{\varepsilon\Delta}\begin{pmatrix} H_y\Big|_{i+1/2,j}^{n+1/2} - H_y\Big|_{i-1/2,j}^{n+1/2} \\ + H_x\Big|_{i,j-1/2}^{n+1/2} - H_x\Big|_{i,j+1/2}^{n+1/2} \end{pmatrix} \tag{4.46}$$

$$H_x\Big|_{i,j}^{n+1/2} = H_x\Big|_{i,j}^{n-1/2} + \frac{\Delta t}{\mu\Delta}\left(E_z\Big|_{i,j-1/2}^{n} - E_z\Big|_{i,j+1/2}^{n}\right) \tag{4.47}$$

$$H_y\Big|_{i,j}^{n+1/2} = H_y\Big|_{i,j}^{n-1/2} + \frac{\Delta t}{\mu\Delta}\left(E_z\Big|_{i+1/2,j}^{n} - E_z\Big|_{i-1/2,j}^{n}\right) \tag{4.48}$$

Δt is the time step (s)

Δ is the size of the FDTD mesh (m)

The periodic boundary conditions have to be imposed at the border of $x = 0$ and $x = d$, in order to copy the periodic structure of the problem. This can be done by modifying equation (4.48) of the tangential component H_y along $x = 0$ and $x = d$, in the following forms [37]:

$$H_y\Big|_{i,j}^{n+1/2} = H_y\Big|_{i,j}^{n-1/2} + \frac{\Delta t}{\mu\Delta}\left(E_z\Big|_{i+1/2,j}^{n} - E_z\Big|_{i_N-1/2,j}^{n}\right) \tag{4.49}$$

$$H_y\Big|_{i_N,j}^{n+1/2} = H_y\Big|_{i,j}^{n+1/2} \tag{4.50}$$

where i_N is the largest FDTD grid number in the x direction. Equations (4.49) and (4.50) are well known as a periodic boundary condition. For TE case, the magnetic walls are replaced with the electric walls at $x = 0$ and $x = d$, and a dual forms of the previous equations can be obtained.

4.5.2 Three-dimensional TM Case

Figure 4.2 depicts the basic infinite periodic geometry illuminated by normal incident plane wave parallel to z-axis. In this case, the periodic boundaries are imposed on the x- and y-axis of the structures, while ABCs are applied along z-axis. The coordinate point (i_o, j_o, k_o) and (i_N, j_N, k_N) denote a space point in a uniform rectangular mesh, where i_o, j_o and k_o are the smallest FDTD grid number in x, y and z direction respectively and i_N, j_N and k_N are the largest FDTD gird number in x, y and z direction respectively.

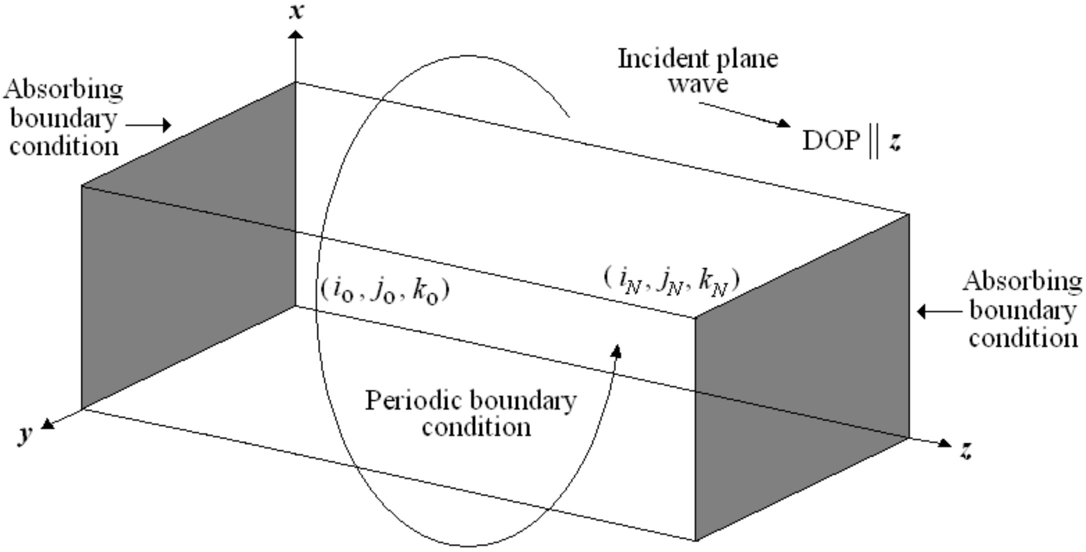

Figure 4.2: General infinite periodic structure in 3-D.

For simplicity, the dielectric volume inside problem space is filled with the lossless medium whose $\sigma = 0$, $\varepsilon = \varepsilon_o\varepsilon_r$ and $\mu = \mu_o$. The tangential electric fields distribution on planes $i = i_o$ and $i = i_N$, and planes $j = j_o$ and $j = j_N$ are shown in Figures 4.3 and 4.4 respectively.

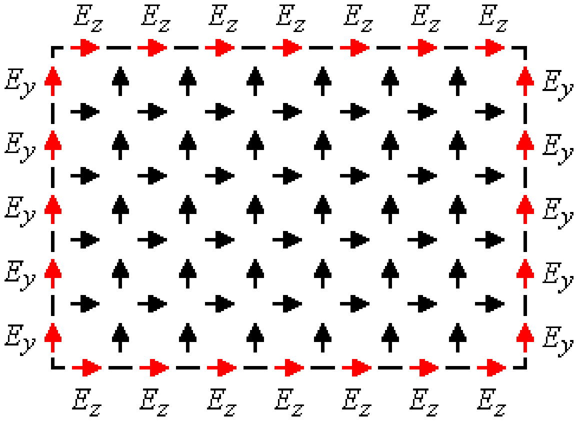

Figure 4.3: Location of E_y(↑) and E_z(→) components in planes $i = i_o$ and $i = i_N$.

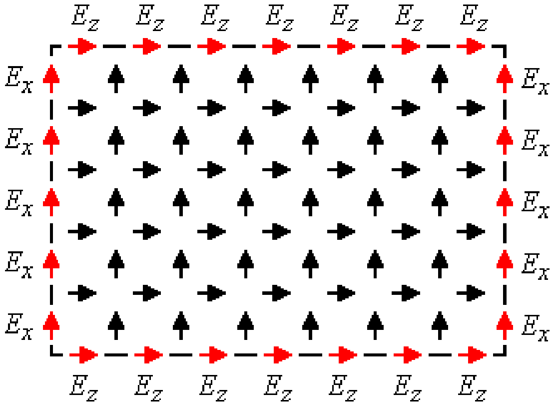

Figure 4.4: Location of E_x(↑) and E_z(→) components in planes $j = j_o$ and $j = j_N$.

The red arrows stand for the tangential electric field components which are located on edge of the surface plane. The black arrows represent the least of the tangential electric field components which are located on the surface plane.

Consider four surface planes at $i = i_o$ and $i = i_N$, and $j = j_o$ and $j = j_N$, in which the floquet periodic boundary condition is applied. From Figure 4.3, the tangential electric field updating equation components E_y and E_z which are not located on the edge of the surface plane at $i = i_o$ and $i = i_N$, can be derived from equations (2.25) and (2.26) to give the expressions:

$$E_y\Big|_{i,j,k}^{n+1} = E_y\Big|_{i,j,k}^{n} + \frac{\Delta t}{\varepsilon\Delta}\left(\begin{array}{l} H_x\Big|_{i,j,k+1/2}^{n+1/2} - H_x\Big|_{i,j,k_N-1/2}^{n+1/2} \\ + H_z\Big|_{i-1/2,j,k}^{n+1/2} - H_z\Big|_{i+1/2,j,k}^{n+1/2} \end{array} \right) \tag{4.51}$$

$$E_y\Big|_{i_N,j,k}^{n+1} = E_y\Big|_{i,j,k}^{n+1} \tag{4.52}$$

$$E_z\Big|_{i,j,k}^{n+1} = E_z\Big|_{i,j,k}^{n} + \frac{\Delta t}{\varepsilon\Delta}\left(\begin{array}{l} H_y\Big|_{i+1/2,j,k}^{n+1/2} - H_y\Big|_{i_N-1/2,j,k}^{n+1/2} \\ + H_x\Big|_{i,j-1/2,k}^{n+1/2} - H_x\Big|_{i,j+1/2,k}^{n+1/2} \end{array} \right) \tag{4.53}$$

$$E_z\Big|_{i_N,j,k}^{n+1} = E_z\Big|_{i,j,k}^{n+1} \tag{4.54}$$

where Δt is the time increment and Δ is the space mesh increment. From Figure 4.4, the tangential updating equation components E_x and E_z which are not located on the edge of the surface plane at $j = j_o$ and $j = j_N$, can be modified from equations (2.24) and (2.26) to give the following forms:

$$E_x\Big|_{i,j,k}^{n+1} = E_x\Big|_{i,j,k}^{n} + \frac{\Delta t}{\varepsilon\Delta}\begin{pmatrix} H_z\Big|_{i,j+1/2,k}^{n+1/2} - H_z\Big|_{i,j_N-1/2,k}^{n+1/2} \\ + H_y\Big|_{i,j,k-1/2}^{n+1/2} - H_y\Big|_{i,j,k+1/2}^{n+1/2} \end{pmatrix} \tag{4.55}$$

$$E_x\Big|_{i,j_N,k}^{n+1} = E_x\Big|_{i,j,k}^{n+1} \tag{4.56}$$

$$E_z\Big|_{i,j,k}^{n+1} = E_z\Big|_{i,j,k}^{n} + \frac{\Delta t}{\varepsilon\Delta}\begin{pmatrix} H_y\Big|_{i+1/2,j,k}^{n+1/2} - H_y\Big|_{i-1/2,j,k}^{n+1/2} \\ + H_x\Big|_{i,j_N-1/2,k}^{n+1/2} - H_x\Big|_{i,j+1/2,k}^{n+1/2} \end{pmatrix} \tag{4.57}$$

$$E_z\Big|_{i,j_N,k}^{n+1} = E_z\Big|_{i,j,k}^{n+1} \tag{4.58}$$

The tangential electric components of E_x, E_y and E_z located on the edge of the surface plane at $i = i_o$, $i = i_N$, $j = j_o$ and $j = j_N$, and due to the E_x and E_y components are on the edge of the ABC are assumed to be updated by the ABC updating equations. As a result, only the edged E_z tangential components are derived here for periodic boundary condition.

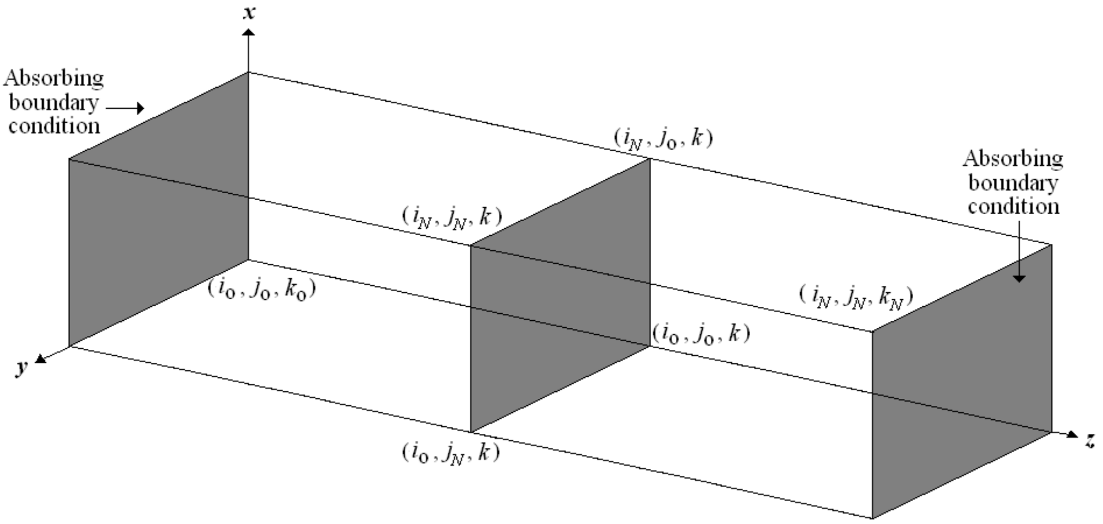

Figure 4.5: Location of the orthogonal E_z components at the edges due to the normal incident plane wave parallel to z-axis.

Four equations of E_z tangential components can be updated at once due to the normal incidence plane wave as illustrated in Figure 4.5. Thus, the following four formulations can be written by modifying equation (2.26):

$$E_z\Big|_{i,j,k}^{n+1} = E_z\Big|_{i,j,k}^{n} + \frac{\Delta t}{\varepsilon\Delta}\left(\begin{array}{l} H_y\Big|_{i+1/2,j,k}^{n+1/2} - H_y\Big|_{i_N-1/2,j,k}^{n+1/2} \\ + H_x\Big|_{i,j_N-1/2,k}^{n+1/2} - H_x\Big|_{i,j+1/2,k}^{n+1/2} \end{array} \right) \tag{4.59}$$

$$E_z\Big|_{i_N,j_N,k}^{n+1} = E_z\Big|_{i,j,k}^{n+1} \tag{4.60}$$

$$E_z\Big|_{i_N,j_0,k}^{n+1} = E_z\Big|_{i,j,k}^{n+1} \tag{4.61}$$

$$E_z\Big|_{i_0,j_N,k}^{n+1} = E_z\Big|_{i,j,k}^{n+1} \tag{4.62}$$

4.6 Biological Cell Tissue Modelling

The enormous rise of electronic, information and communication technologies has motivated the explosive usage of mobile handsets over the last decade. The possible mechanism of biological effect on human cells which might contribute to complex cellular process that leads to cancer, by using mobile phone, has prompted the public concern over recent years. As a result, this leads to a high demand on modelling biological structure used to clarify the uncertainty of the electromagnetic behaviour of cells exposed to these fields. In this work, finite-difference time-domain (FDTD) method has been dominating over other numerical methods due to its simplicity and the ability to treat highly nonhomogeneous structures [1].

Research on the interaction mechanism of electromagnetic field with the living tissue at mobile communication frequencies have been performed previously by See *et al.* [43] and Emili *et al.* [22] by adapting modified FDTD technique. However, the accuracy of the model is questionable due to the thickness of the cell membrane in the model (1 μm) and a minimum of one FDTD cell is used to represent the membrane. Cell membrane has been identified as the primary target for the study of possible actions of electromagnetic fields on biological structures. In order to facilitate deeper investigation of the field distribution inside the membrane, where the previous proposed models in [22, 43] cannot be clarified, a modified subgridding finite-difference time-domain (SGFDTD) scheme is used to model a high definition biological tissue.

The traditional FDTD is not capable to model extremely small object which is much smaller than a wavelength. This is due to the unaffordable computational resource required to perform the calculation. By adapting the frequency scaled FDTD method [18, 22, 43], this problem can be easily overcome. Many structures of electromagnetic interest are extremely large and periodic in one or more dimensions. In order to perform the EM analysis of these types of structures with reasonable computational time, the structures are assumed to be an infinite grid and subsequently reducing the problem into a unit-cell analysis by using Floquet boundary condition [44]. This will enable the numerical solution to simulate the effect of the periodic replication. In order to include the membrane effect on the biological tissue model, lumped-element membrane model [22, 43] is used as a working hypothesis to develop the modelling technique.

Standard FDTD suffers from staircase error due to cartesian grids everywhere in the computational grid [45] and this error makes it less favour to use for complex geometry and small object modelling. Many researchers such as in [46, 47] have extended FDTD to handle multi-resolution problems by using finer grids near structures with small geometrical features abutted to coarse grids in regions of empty space. It is well-known that the subgridding scheme in FDTD always encounters the late time instability problems due to the interpolation and extrapolation of neighbouring field values in the FDTD computation domain. However, this is a challenge to implement this technique to establish a novel sophisticated biological tissue model.

A computer program was written in Fortran to implement the analysis. A cubical FDTD cells was implemented in which the cell size was set with $\Delta x = \Delta y = \Delta z = 20$ μm. It was chosen such that the length of the grid remained at a fraction of a wavelength only. The time step was set at 1.5 ps to satisfy the Courant stability condition. An interpolation algorithm was required to predict the missing fields between the coarse and fine region of the FDTD lattice. There were many articles published in the literature with different updating field methods at the unknown cell of the boundary by means of both interpolation and extrapolation techniques. In general, some of them were based on separated time and space interpolation interfaces [48], spatial field interpolation algorithm [10], dielectric transverse capability [11], interpolation of current density [7], time interpolation subgridding algorithm [9], finite element formulation [12, 13] and quadratic interpolation [49]. In this research area, the magnetic field in the fine region was interpolated by the six neighbouring magnetic fields in the coarse region. The mesh ratio of the coarse-to-fine grids was 1:2. Generally, the basis of the fields in 2-D domain was determined due to solving the electric and magnetic fields in a plane. The magnetic field basis in 2-D domain can be written as:

$$H_x = H(x, y) = a + b(x) + c(y) + d(xy) + e(x^2) + f(y^2) \tag{4.63}$$

where a is the constant, b, c, d, e and f are the coefficient of the equation. It can be deduced in matrix form as:

$$\begin{bmatrix} H_{x_1} \\ H_{x_2} \\ H_{x_3} \\ H_{x_4} \\ H_{x_5} \\ H_{x_6} \end{bmatrix} = \begin{bmatrix} 1 & x_1 & y_1 & x_1y_1 & x_1^2 & y_1^2 \\ 1 & x_2 & y_2 & x_2y_2 & x_2^2 & y_2^2 \\ 1 & x_3 & y_3 & x_3y_3 & x_3^2 & y_3^2 \\ 1 & x_4 & y_4 & x_4y_4 & x_4^2 & y_4^2 \\ 1 & x_5 & y_5 & x_5y_5 & x_5^2 & y_5^2 \\ 1 & x_6 & y_6 & x_6y_6 & x_6^2 & y_6^2 \end{bmatrix} \begin{bmatrix} a \\ b \\ c \\ d \\ e \\ f \end{bmatrix} \tag{4.64}$$

The coefficients can then be obtained by the following matrix inversion:

$$\begin{bmatrix} a \\ b \\ c \\ d \\ e \\ f \end{bmatrix} = \begin{bmatrix} 1 & x_1 & y_1 & x_1y_1 & x_1^2 & y_1^2 \\ 1 & x_2 & y_2 & x_2y_2 & x_2^2 & y_2^2 \\ 1 & x_3 & y_3 & x_3y_3 & x_3^2 & y_3^2 \\ 1 & x_4 & y_4 & x_4y_4 & x_4^2 & y_4^2 \\ 1 & x_5 & y_5 & x_5y_5 & x_5^2 & y_5^2 \\ 1 & x_6 & y_6 & x_6y_6 & x_6^2 & y_6^2 \end{bmatrix}^{-1} \begin{bmatrix} H_{x_1} \\ H_{x_2} \\ H_{x_3} \\ H_{x_4} \\ H_{x_5} \\ H_{x_6} \end{bmatrix} \tag{4.65}$$

Hence, the magnetic field in the fine region of subgridding can be calculated by:

$$H_x = a + b(x_o) + c(y_o) + d(x_o y_o) + e(x_o^2) + f(y_o^2) \tag{4.66}$$

where x_o and y_o are the reference points at the interpolation region.

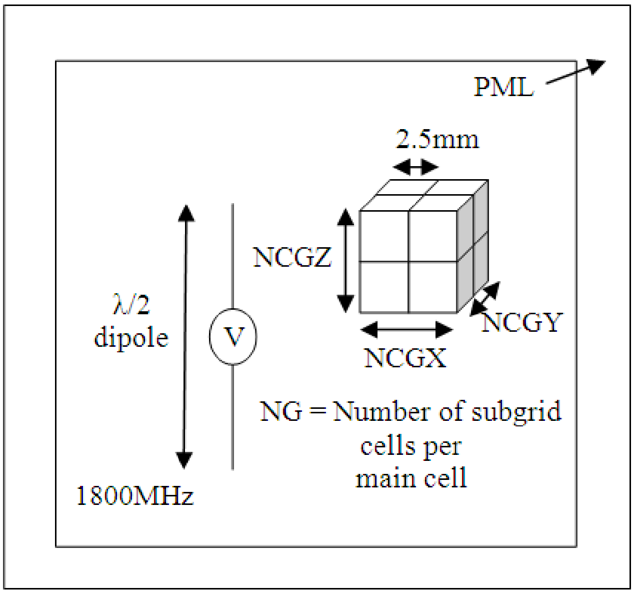

Figure 4.6: A half-wavelength dipole antenna was used as current source excitation to the subgrid cells. NCGX, NCGY and NCGZ are the number of cells to be subgridded in the direction of *x*-axis, *y*-axis and *z*-axis respectively.

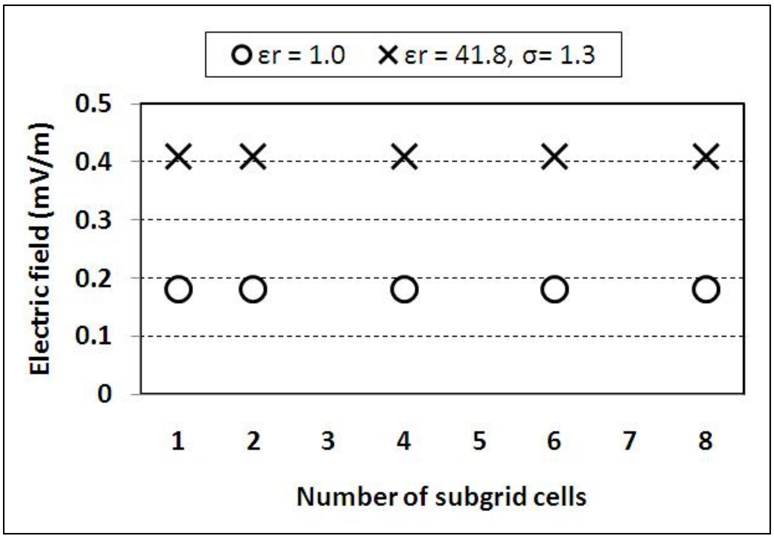

Figure 4.7: Stability analysis for different number of subgrid cells in one main FDTD cell.

Figure 4.6 depicts the configuration of the stability analysis simulation environment inside the FDTD computational domain. A half-wavelength dipole was used to excite a sinusoidal voltage source of 1 V/m at 1800 MHz. The subgrid cells can be represented by free space or by a dielectric with different electrical characteristics. They were located near the voltage source as a scatterer. The interpolation scheme discussed earlier can be extended to the other mesh ratios such as 1:4, 1:6 and 1:8. In this case, the subgridding scheme is considered to be the same as normal FDTD if 1:1 mesh ratio is used inside the computational domain. Two separate simulations were done for free space (ε_r = 1.0) and a dielectric medium with ε_r = 41.8 and σ = 1.3 S/m for different number of subgrid cells. The results in Figure 4.7 illustrate the stability of the simulation inside the problem space. The electric field remained at 0.18 mV/m when using different values of subgrid cells for free space. Furthermore, it remained at 0.41 mV/m when a dielectric was inserted inside the subgrid area.

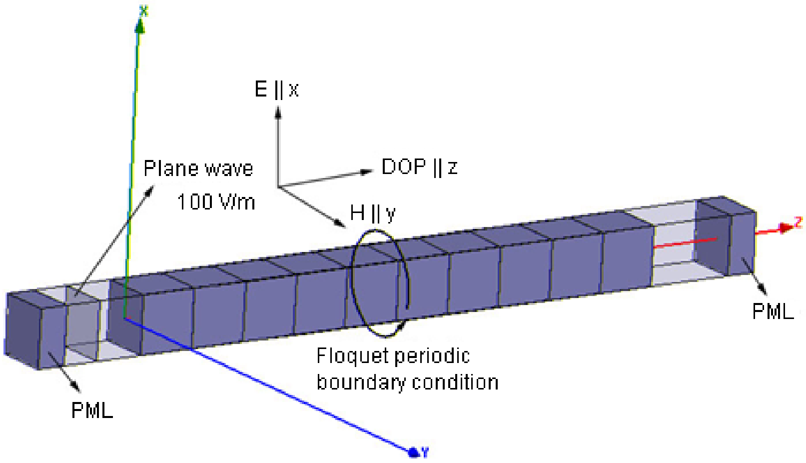

Figure 4.8: 3-D view of the basic simulated cubical structures in FDTD computational domain. The direction of propagation (DOP) is in the *z*-axis.

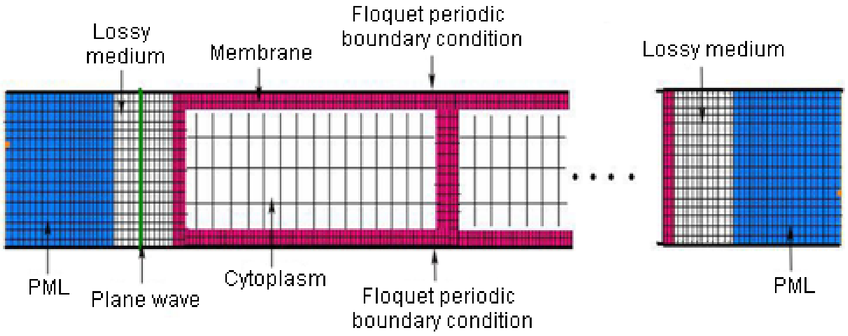

Figure 4.9: New proposed high definition biological tissue model by using modified subgridding FDTD model.

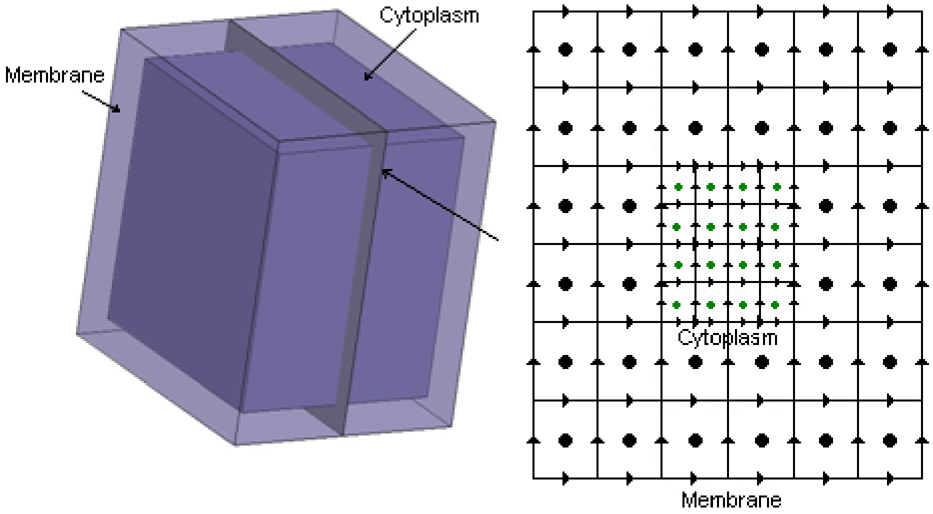

Figure 4.10: 2-D view of subgridding on a face of a single biological cell (not to scale).

Figure 4.8 shows a stack of ten cubical cells tissue model. The reason behind using cubical cell is, when compacted into connected tissues, living cells are not perfectly spheres. Thus, a cluster of cubical cells was assumed. The model consists of cytoplasm, membrane and extracellular medium. The side length of each cell was 20 μm in which the thickness of the membrane was 1 μm. The problem space was 20 × 20 × 220 cells of which the cell size was 1 µm. A plane wave of 100 V/m propagating in the *z*-direction and polarized in *x*-direction was used as excitation source. Six FDTD cells were used for PML model. The floquet boundary condition was imposed along the *x* and *y*-axes to effectively extend the grid structure to infinity. The detailed description and electrical properties of the structure can be found in [43]. Applying the subgridding approach into the similar model of Figure 4.8, a new high definition biological tissue model can be considered as shown in Figure 4.9. The subgridding was imposed on cytoplasm cells in which a cell size of 0.5 µm was used (2 cells). In other words, the ratio of coarse to fine grids was 1:2. The cell size used for cell cytoplasm was 1 µm. Since the cell cytoplasm dominant the entire volume of the model then the entire problem space was descretised with membrane cell size except the cytoplasm volume which was kept at 1 µm. The simulation parameters are tabulated in Table 4.1. The dielectric properties of the media were obtained from [50] as summarised in Table 4.2.

Table 4.1: Biological cell simulation parameters.

Parameter	Measurement
FDTD spatial resolution	20 × 20 × 220
Subgrid spatial resolution	10 × 10 × 10
Number of FDTD PML cells	6
Coarse grid cell size	1.0 µm
Fine grid cell size	0.5 µm
Number of subgrid cells	8
Time step	1.3 fs
Operating frequency	10 GHz

Table 4.2: Electrical properties of cubical cell composition at 2450 MHz.

Parameter	ε_r
Cytoplasm	0.9360
Membrane	0.9838
Extracellular medium	0.9301

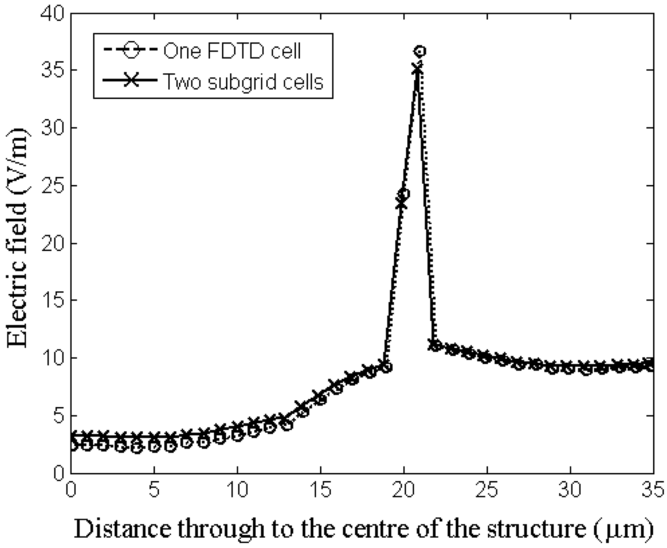

Figure 4.11: Electric field distribution along z-axis through the centre of the cubical cell.

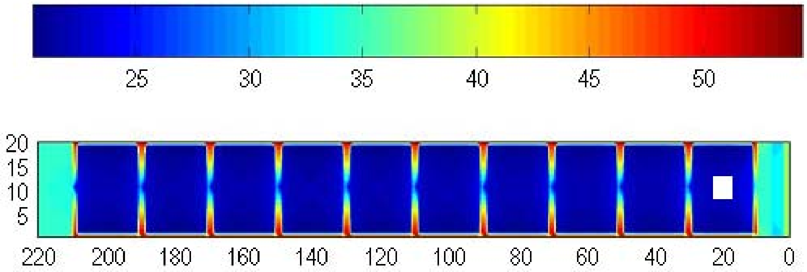

Figure 4.12: Modulus of the electric field on xz-plane at intermediate frequency 10 GHz.

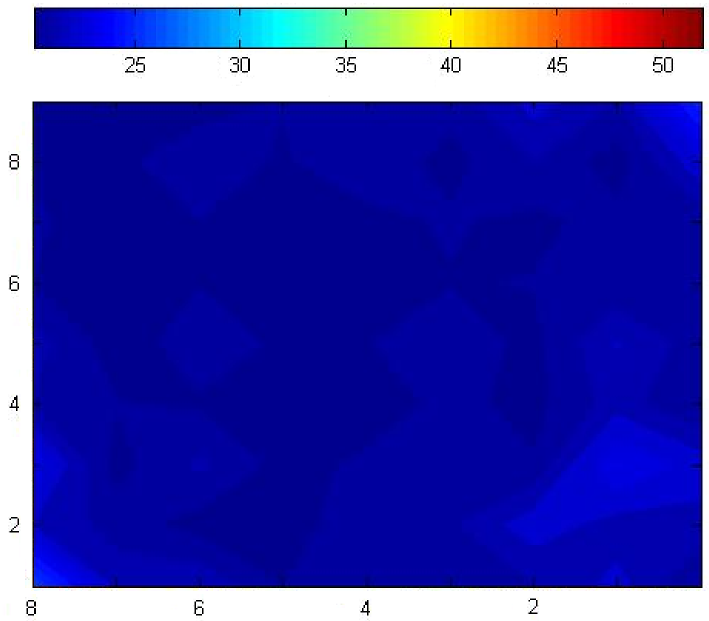

Figure 4.13: Modulus of the electric field inside subgrid region on *xz*-plane at intermediate frequency 10 GHz.

The proposed subgridding approach was shown in Figure 4.10. The distributions of the electric field through the centre of the simulated structure, along the incident wave propagation direction at 2450 MHz are given in Figure 4.11 to verify the proof of concept. The electric field distributions (in dB scale) along the problem space are illustrated in Figure 4.12. Figure 4.13 shows the field distribution (in dB scale) inside subgrid region.

4.7 Interaction Between OHTL and Buried Pipeline

The sharing of route by overhead high voltage power transmission lines (OHTL) and buried utility pipelines has become quite common nowadays. Most of the countries in the world typically follow the same procedure to distribute the energy to rural and urban territories. The primary reason of this tendency is the restriction imposed by government and private organisations concerning the environmental effect due to the development of the facilities needed on a given location of interest. The numerous constraints become more alarming as new construction reaches high density urban areas. This sharing of way prompts the question to the public concern as to the effect of OHTL has on underground pipelines. In some situations, the underground utility pipelines may be very close in proximity to OHTL. In this case, it is necessary to take into account the electromagnetic absorption energy in the pipelines. Electromagnetic interference can be generated in the pipelines due to the electromagnetic induction between the underground pipelines and OHTL when they are close to each other in the vicinity. In general, the interference can be composed into two; namely conductive interference and inductive interference. Conductive interference is the potential increase of the ground in the vicinity of the pipelines. It happens from a large current injected into the ground from the transmission line particularly due to the lightning strikes between the tower and the overhead transmission line. In contrast, inductive interference is the voltage generated in the pipelines due to the induction of the electromagnetic field of the OHTL.

This work presents the development of a new approach of modelling the source excitation and the penetration of structures by continuous propagating electromagnetic plane waves. The technique incorporates the solution of time-dependent Maxwell's equations and the initial value problem as the structures are illuminated by the plane waves. The propagation of waves from source excitation is simulated by solving a finite-difference Maxwell's equation in the time domain. Finite-difference based on integral formulation [1, 51, 52] has been used in the published literature to improve the accuracy of the finite-difference formulation near the surfaces that does not fit in the lattice or small objects such as thin wires which alter the electromagnetic field distribution significantly. In this case, analytical expressions have been established to express the field near a particular object for precise evaluation of the integrals. Many researchers in the past have been prompted to investigate the subgridding technique as an approach to circumventing the problem [53, 54]. In general, this technique is used to condense the lattice at the point of interest locally and does not require any analytical formula to be taken into account, and hence it is appropriate for objects of any shape.

The method mentioned above has two main advantages relative to the other modelling approaches. First, it is simple to implement for complicated dielectric or metal structures due to arbitrary electrical parameters can be assigned to each cell on the grid. Second, the entire computational spaces need not to be discretised with a fine grid as it put unreasonable burden on the computer processing time.

The ultimate objective of research in this area is to access the appropriateness of the method in determining the amount of electromagnetic penetrating fields between OHTL and underground utility pipeline. The three-phase OHTL are modelled as the AC sources and the pipeline as the dielectric material. In this case, the pipeline is defined as the fine grid and the residual spaces as the coarse grid in the computational spaces. The fields between these two grids are unknown in nature and have to be calculated. Interpolation algorithm is thus required between the grids. The aim of the present work is to develop the general code for solving the electric and magnetic fields within arbitrary metal or dielectric structures, while maintaining a boundary of uncertainty low reflection level in two-dimensional approach.

Two-dimensional finite-difference time-domain with subgridding method has been used in the literature with different applications. Chilton and Lee [55] developed a subgridding method based on multigrid finite element principles in 2-D. The work was then extended to 3-D. The method was applied to the parallel plate waveguide with different dielectric material and shape for validation purposes. Later, they developed a higher order FDTD with appropriate media boundary conditions. The method which was called conservative subgridding was derived for Lobatto Cell [56]. Lin and Kuo [57] used Crank-Nicolson algorithm in the subgridding scheme to handle problems involving fine structural features. Numerical results were presented for unilateral fin-line and dielectric cylinder scattering. Some attempts have been taken in the analysis of cavity with one and two perfect electric conductor (PEC) fins [58, 59], metamaterial slab [60], electrostatic plate condensator, circular coaxial waveguide and circular waveguide [61], PEC cylinder with a current filament in free space [62, 63], lossy dielectric block located near a short linear antenna [64] and passive equivalent circuit [65].

FDTD technique has been well known over the years of its strength with robust simulation technique for transient electromagnetic interactions. In this research work, two-dimensional FDTD technique is used with subgridding to model the utility pipeline and the overhead high voltage power transmission line. FDTD technique has been applied to the high voltage power transmission line analysis in the published literature. Dedkova and Kriz [66] proposed a new effective approach to evaluate the distribution of voltage and current along the nonlinear transmission line by using FDTD method. An improved technique was proposed by Tang *et al.* [67] to calculate the transient inductive interference in underground metallic pipelines due to a fault in nearby power lines. The frequency-dependent problem in the analysis of transient interference was solved in phase domain based on FDTD method. Lu and Cui [68] used FDTD method to calculate the wave processes of voltage and current distributed along the three-phase 500 kV busbars and the power lines without load in the substation of multi-conductor transmission lines (MTL). The iterative formulas were presented to determine the boundary conditions at the node of the branches. The work was extended to transmission line network and non-uniform line [69]. Vector fitting method was adopted in FDTD to treat with the frequency dependent parameters [70]. In this case, the corresponding voltage and current recursion formulations in FDTD technique were presented based on the recursive algorithm for time domain convolution. The comparison of transient analysis method using Bergeron's method, FDTD method and time-domain finite-element (TDFE) was discussed in [71]. Numerical results of MTL simulations based on Laplace transform and FDTD method was presented and compared in [72].

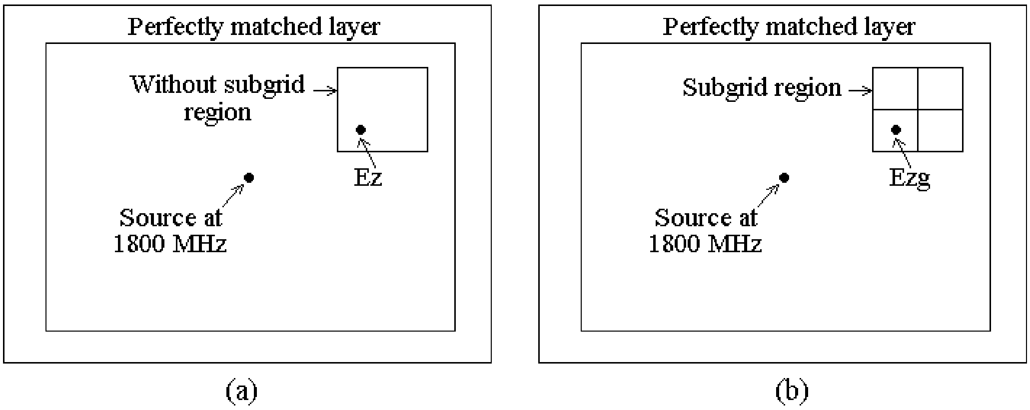

Figure 4.14: Case 1: The observed field was located inside subgrid area: (a) Without subgrid, (b) With subgrid.

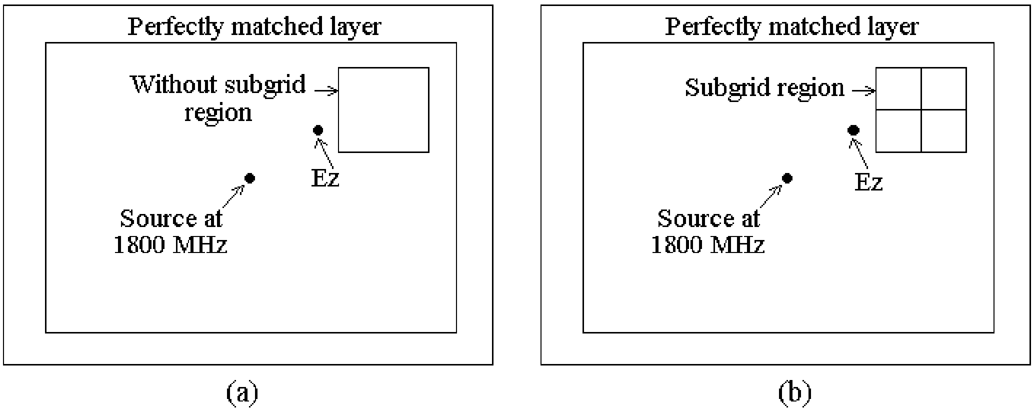

Figure 4.15: Case 2: The observed field was located outside subgrid area: (a) Without subgrid, (b) With subgrid.

Subgrid technique was validated by illustrating example in two cases. Case 1 was considered when the observed field was located inside subgrid area with two conditions: (a) Without subgrid, and (b) With subgrid, as shown in Figure 4.14. Case 2 was considered when the observed field was located outside subgrid area with two conditions: (a) Without subgrid, and (b) With subgrid, as depicted in Figure 4.15. The problem space was excited by sinusoidal wave and gaussian pulse at 1800 MHz. The electric fields at the same point for case 1 and case 2 were observed and compared as illustrated in Figures 4.16 and 4.17 respectively. The magnetic fields at the same point for case 1 and case 2 were also observed and compared as illustrated in Figures 4.18 and 4.19 respectively.

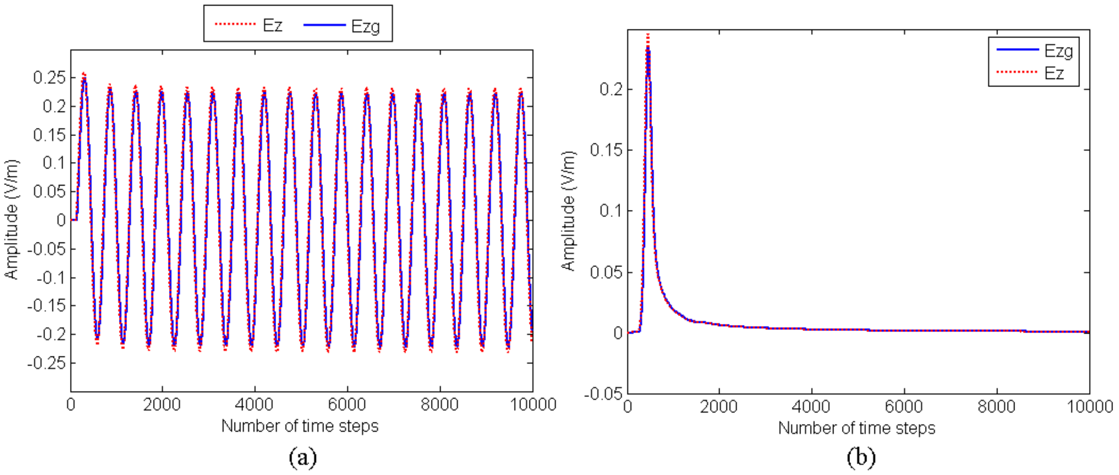

Figure 4.16: Case 1: The electric field in subgrid region (E_{zg}) and at normal grid (E_z): (a) When sinusoidal wave was excited, (b) When gaussian pulse was excited.

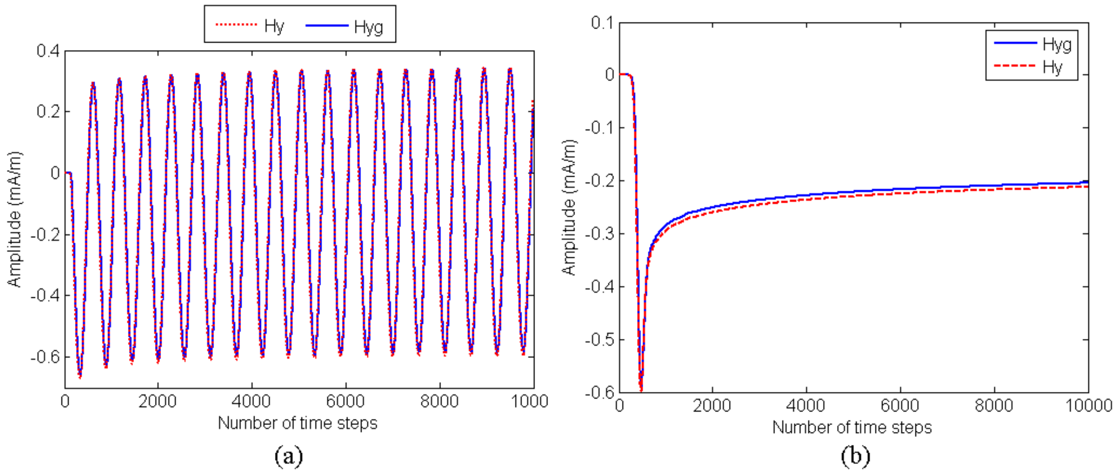

Figure 4.17: Case 1: The magnetic field in subgrid region (H_{yg}) and at normal grid (H_y): (a) When sinusoidal wave was excited, (b) When gaussian pulse was excited.

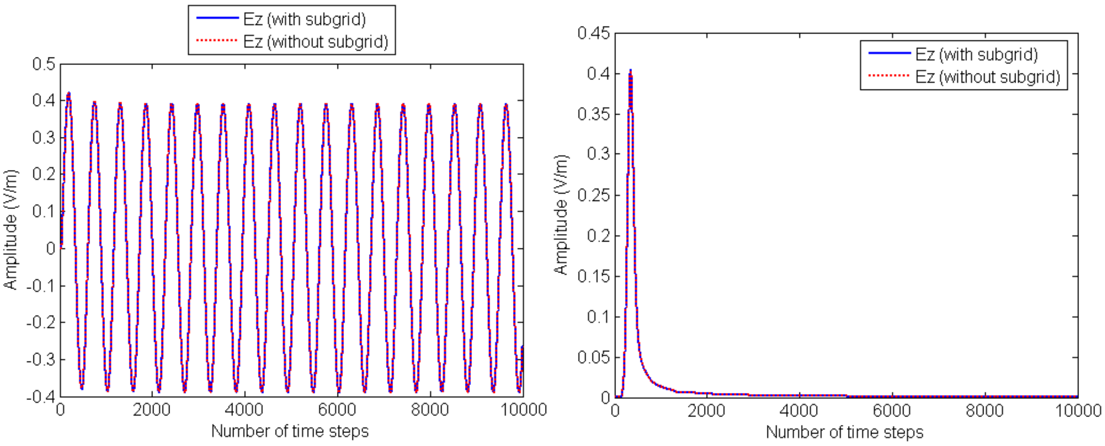

(a) (b)

Figure 4.18: Case 2: The electric field E_z with and without subgrid: (a) When sinusoidal wave was excited, (b) When gaussian pulse was excited.

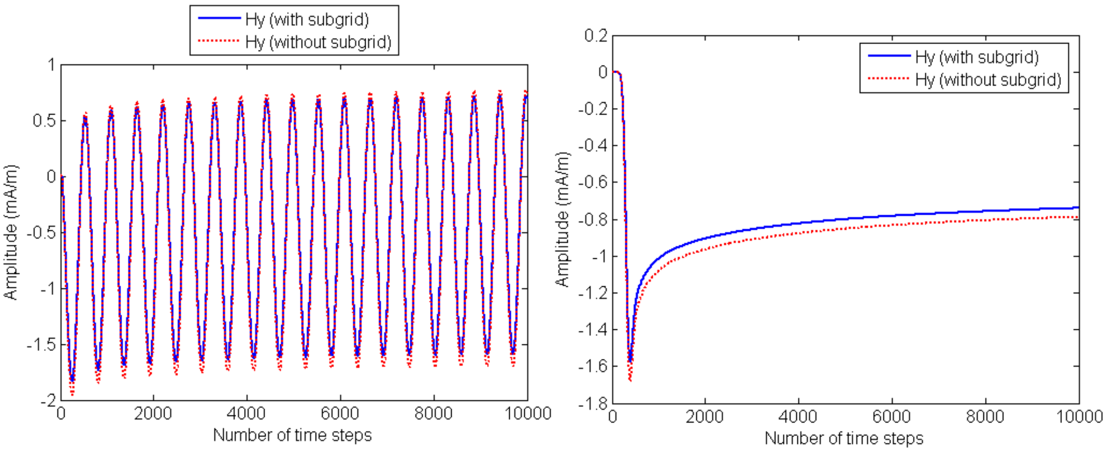

(a) (b)

Figure 4.19: Case 2: The magnetic field H_y with and without subgrid: (a) When sinusoidal wave was excited, (b) When gaussian pulse was excited.

The electric fields in subgrid region (E_{zg}) and at normal grid (E_z) for case 1 were found to be identical to each other to confirm the proof of concept. The electric fields E_z with and without subgrid for case 2 were also found to be identical to each other. A similar explanation also applies for the magnetic fields for both case 1 and 2.

Example 1: A source code was written to implement the design and analysis of the interaction between overhead high voltage power transmission lines and buried utility pipeline. Fortran 90 was used as a programming language platform. The work was devoted to 2-D TM case. Figure 4.20 depicts the cross section and the dimension of a common corridor in which a buried utility pipeline runs parallel to a 132 kV overhead power transmission line. The height from the ground to the bottom conductors is 15 m. The overhead ground wire was located at the top of the tower. In this case, the height to the earth surface is 27 m. The phase conductors for the bottom, middle and top were collocated horizontally with a separation of 4.0 m, 4.5 m and 4.0 m respectively between two adjacent conductors. Sinusoidal wave excitation of 460 kHz ($\lambda = 652.17$ m) was applied at each of the power transmission line cables. In this case, the three phase steel lattice transmission high voltage suspension tower was designed with 6 cables.

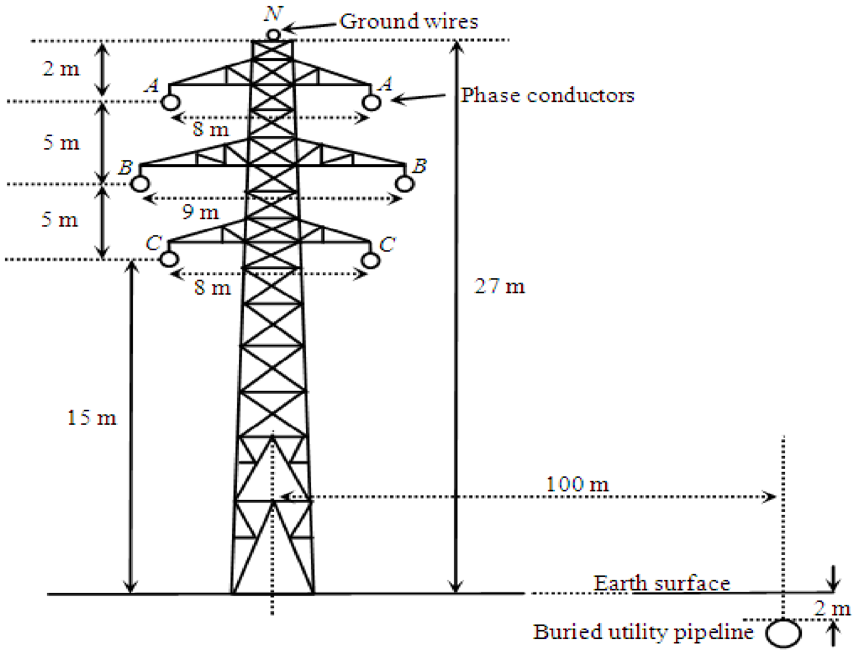

Figure 4.20: Outline of standard circuit 132 kV steel lattice transmission high voltage suspension towers with normal span of 300 m (not to scale) [73, 74].

These cables were used as the source signal which propagates inside the problem space. Each of the 2 cables carries the same phase of the AC current. The general equations of phase A, phase B and phase C cables were given respectively by the expressions:

$$Phase\ \ A = \sin(2\pi ft) \tag{4.67}$$

$$Phase\ \ B = \sin\left(2\pi ft + \frac{2}{3}\pi\right) \tag{4.68}$$

$$Phase\ \ C = \sin\left(2\pi ft + \frac{4}{3}\pi\right) \tag{4.69}$$

where f is the frequency (Hz) and t is the time (s). The pipeline was separated at a distance of 100 m from the steel lattice suspension towers and buried 2 m beneath the surface of the earth. It was made from metal with a very high conductivity of 4.75×10^6 S/m. The radius of the pipeline was 25 cm. The soil in the common corridor was designed to be inhomogeneous. It was modelled with different relative permittivity by means of random number generator. It was known that the relative permittivity of soil varies from 1 to 5 at 460 kHz [75]. Figure 4.21 and 4.22 depict the histogram and cumulative distribution function of soil relative permittivity respectively. The representation of Figures 4.21 and 4.22 clearly indicates that the soil was designed as arbitrarily inhomogeneous.

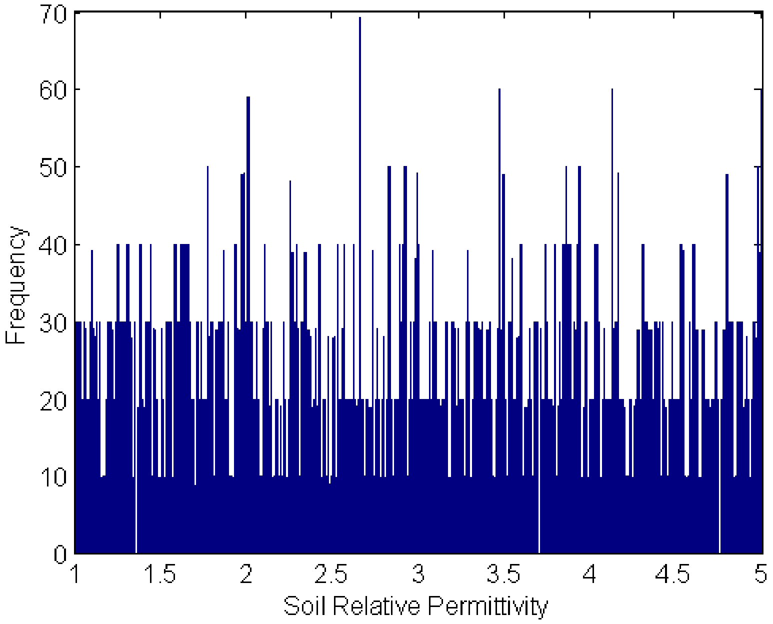

Figure 4.21: Histogram of soil relative permittivity.

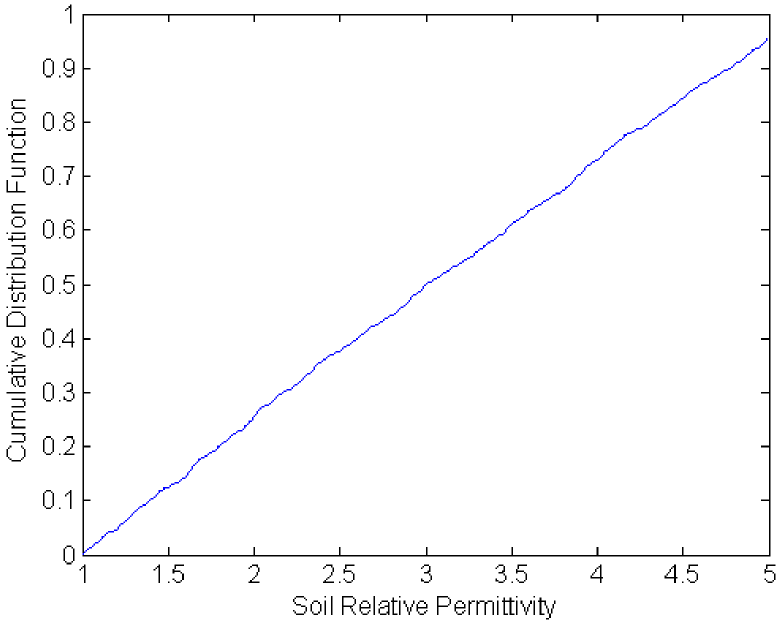

Figure 4.22: Cumulative distribution function of soil relative permittivity.

The cumulative distribution function (CDF) is given by:

$$CDF(x) = \int_{1}^{x_1} \frac{1}{4}\, dx \tag{4.70}$$

where x_1 is the variable of which is unknown in nature and must be determined by using random number generator. Basically, random number generator is given by the expression:

$$R_g(0 \to 1) = \frac{1}{4}(x_1 - 1) \tag{4.71}$$

where $R_g(0 \to 1)$ is the random number generator that generates random number from zero to one. Rearranging equation (4.71), the x_1 term can be deduced as:

$$x_1 = 4R_g(0 \to 1) + 1 \tag{4.72}$$

In addition, the conductivity of soil mainly depends on the water content in it and slightly on the granularity. In general, its value was very small typically in the order of 2.0×10^{-3} S/m or less [75]. The computational region at the coarse grids was discretised at a spatial resolution of 2,609 cells per wavelength ($\Delta y = \Delta z = 25$ cm). Subgridding involves local mesh refinement in the pipeline and some part of the ground in order to determine the propagation of the waves inside that area while observing the change in the electric and magnetic fields.

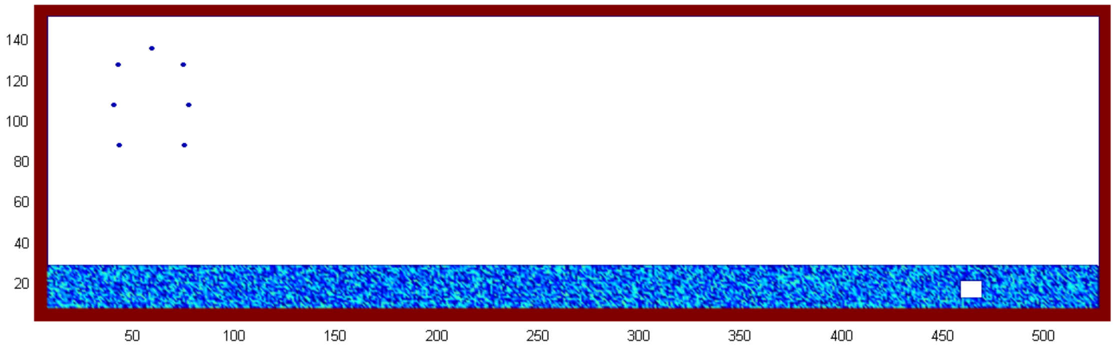

Figure 4.23: The main region in the computational domain for 132 kV steel lattice transmission high voltage suspension towers model.

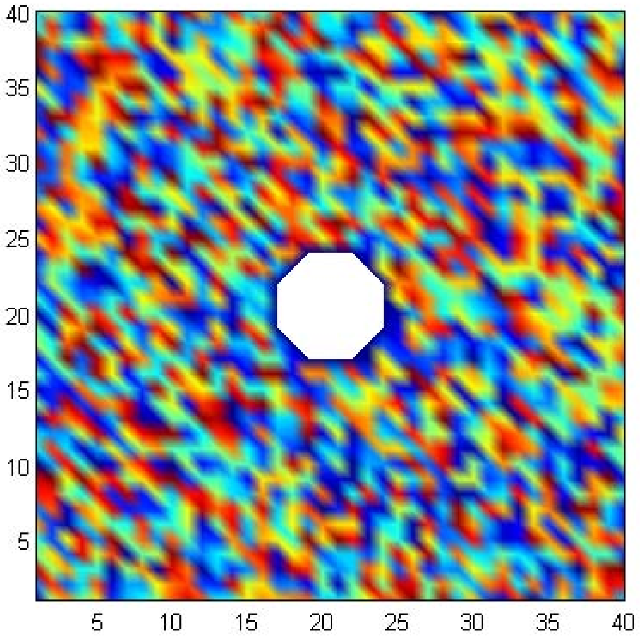

Figure 4.24: The subgrid region in the computational domain for 132 kV steel lattice transmission high voltage suspension towers model.

The computational space for the main region was 521 cells × 145 cells (130.25 m × 36.25 m) as illustrated in Figure 4.23. The value of 130.25/λ was checked and found to be 0.1997 to secure the quasi-static approximation can be implemented for the electric and magnetic field components. The computational space for subgrid area was 10 cells × 10 cells (250 cm × 250 cm) or 40 subgrid cells × 40 subgrid cells as depicted in Figure 4.24. The distribution of ground surrounding the pipeline was generated by using random number to simulate the inhomogeneity of the media. The fine grids was discretised at a spatial resolution of 10,435 cells per wavelength ($\Delta y = \Delta z = 6.25$ cm). In other words, the ratio of the coarse to the fine grids was 4:1. The length of the coarse grids remained at 3.83×10^{-4} of the wavelength. The length of the fine grids remained at 9.58×10^{-5} of the wavelength. The induced EM fields section above the pipeline were observed for 30 cells × 20 cells (7.5 m × 5 m). The Courant stability condition for 2-D case is given by:

$$\Delta t \leq \frac{h}{c\sqrt{2}} \tag{4.73}$$

where h is the spatial homogeneous FDTD grid ($h = \Delta y = \Delta z$) and c is the speed of light in free space. According to this equation, the time step was set at 0.4 ns to satisfy the Courant stability condition. The simulation was run for 21,160 time steps to allow for the wave to fully traverse the spatial domain for 4 cycles.

Example 2: Figure 4.25 illustrates the cross section and the dimension of a common corridor in which a buried utility pipeline runs parallel to a 275 kV overhead power transmission line. The height from the ground to the bottom conductors is 20 m. The distance from the overhead ground wire to the earth surface is 38 m. The phase conductors for the bottom, middle and top were collocated horizontally with a separation of 6.0 m, 6.5 m and 6.0 m respectively between two adjacent conductors. The computational space for main region was 521 cells × 189 cells (130.25 m × 47.25 m) as shown in Figure 4.26. The subgrid computational space was 40 subgrid cells × 40 subgrid cells as shown in Figure 4.27. Other parameters were set to be the same as in example 1. In general, these parameters were shown in Table 4.3, Table 4.4 and Table 4.5.

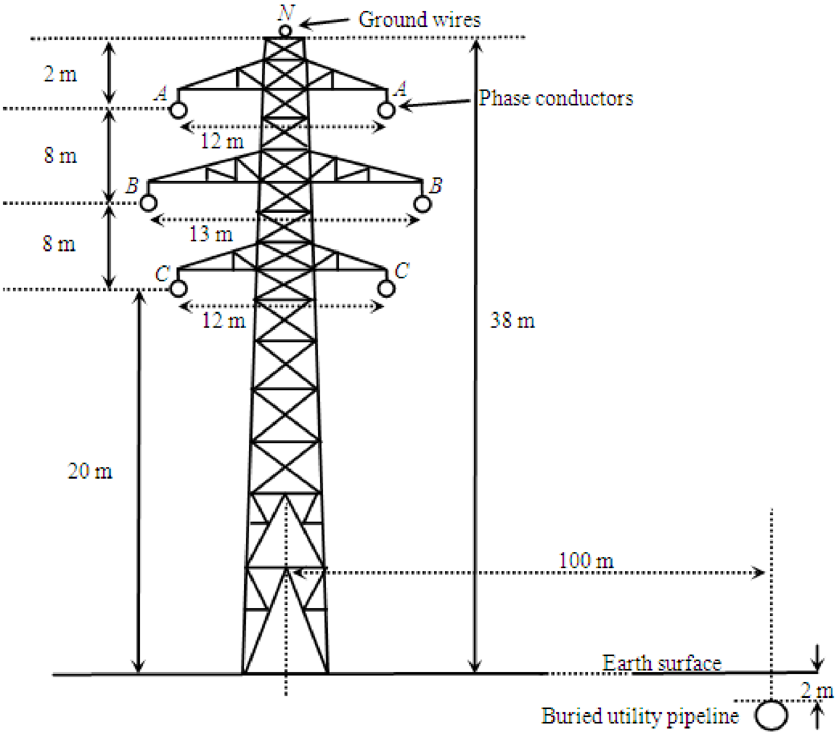

Figure 4.25: Outline of standard circuit 275 kV steel lattice transmission high voltage suspension towers with normal span of 365 m (not to scale) [73, 74].

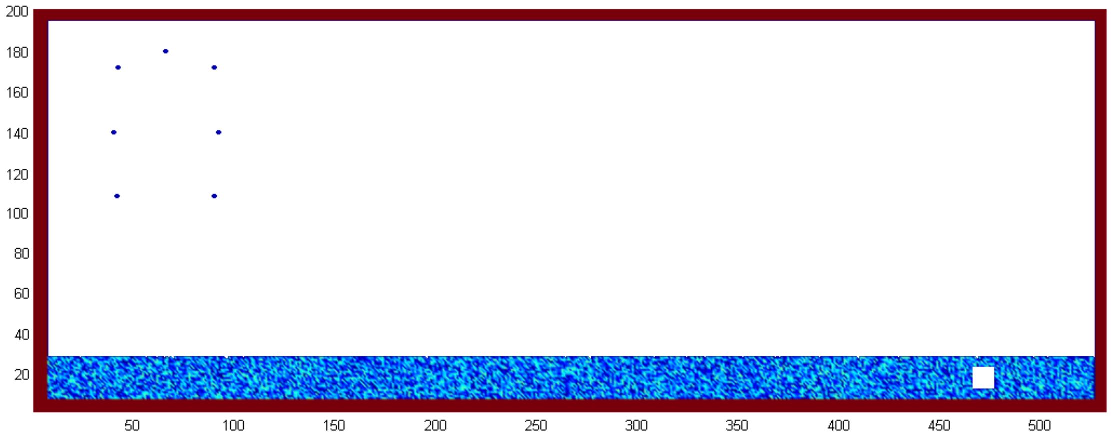

Figure 4.26: The main region in the computational domain for 275 kV steel lattice transmission high voltage suspension towers model.

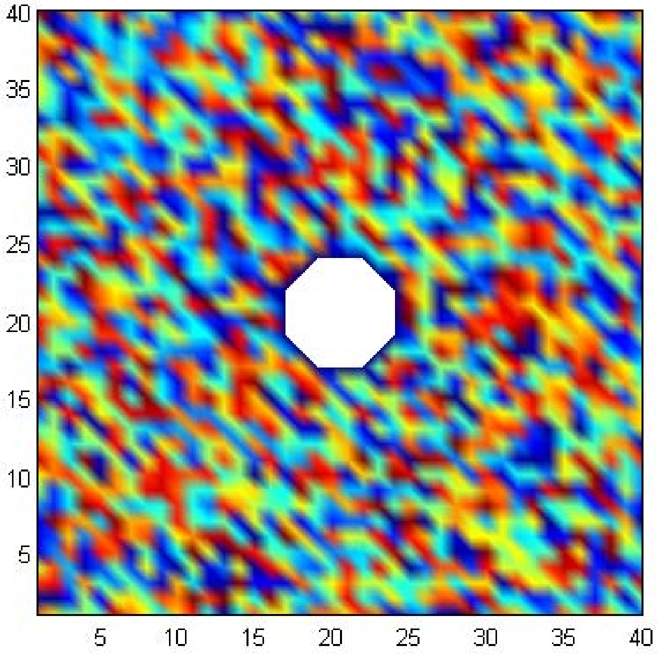

Figure 4.27: The subgrid region in the computational domain for 275 kV steel lattice transmission high voltage suspension towers model.

Table 4.3: FDTD simulation parameters.

Parameter	Measurement
Source frequency	460 kHz
Coarse grids	25 cm
Fine grids	6.25 cm
Refinement factor	4
Time step	0.4 ns
Number of time steps	21,160
Number of cycles	4
Subgrid spatial resolution	40 subgrid cells × 40 subgrid cells
Induced EM fields spatial resolution	30 cells × 20 cells

Table 4.4: Pipeline parameters.

Parameter	Measurement
Distance from steel lattice suspension towers	100 m
Radius	25 cm

Table 4.5: Material properties at 460 kHz.

Material	Type	σ (S/m)
Pipeline	Metal	4.75×10^{6}
Soil	Dry, $1 \leq \varepsilon_r \leq 5$	2.0×10^{-3}

Example 3: Figure 4.28 illustrates the cross section and the dimension of a common corridor in which a buried utility pipeline runs parallel to a 400 kV overhead power transmission line. It is designed with low height construction. The height from the ground to the bottom conductors is 17 m. The distance from the overhead ground wire to the earth surface is 32 m. Phase *A* conductors at the top were collocated horizontally with a separation of 3.0 m. The bottom conductors of phase *B*, phase *B* to *C* and phase *C* were collocated horizontally with a separation of 1.75 m, 3.5 m and 1.75 m between two adjacent conductors respectively. The computational space for main region was 521 cells × 185 cells (130.25 m × 46.25 m) as shown in Figure 4.29. The subgrid computational space was 40 subgrid cells × 40 subgrid cells as illustrated in Figure 4.30. The values for the other parameters were shown in Table 4.3, Table 4.4 and Table 4.5.

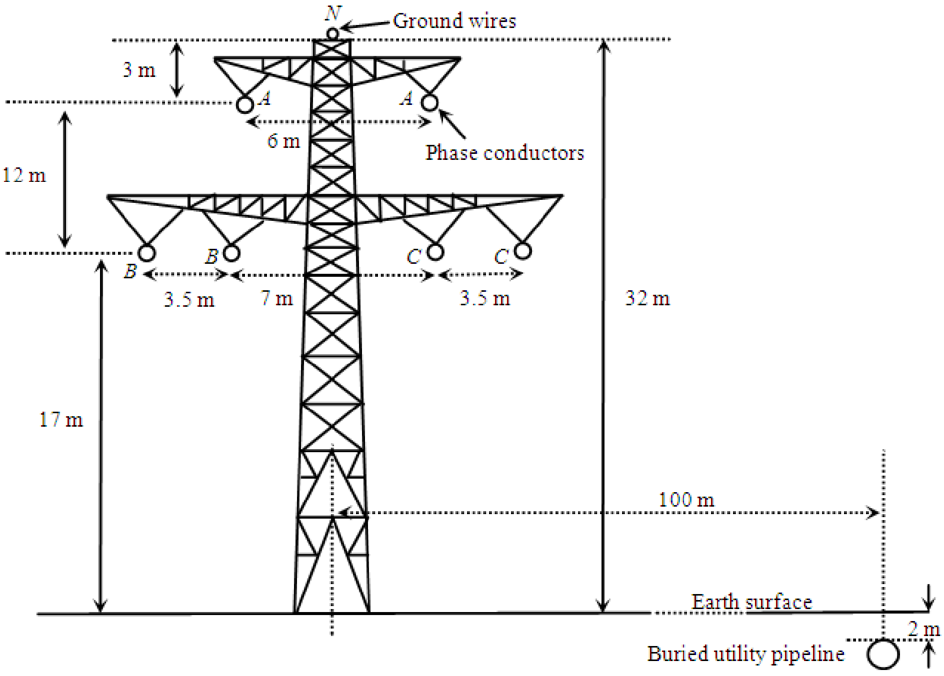

Figure 4.28: Outline of standard circuit 400 kV steel lattice transmission high voltage suspension towers with normal span of 300 m
(low height construction design, not to scale) [73, 74].

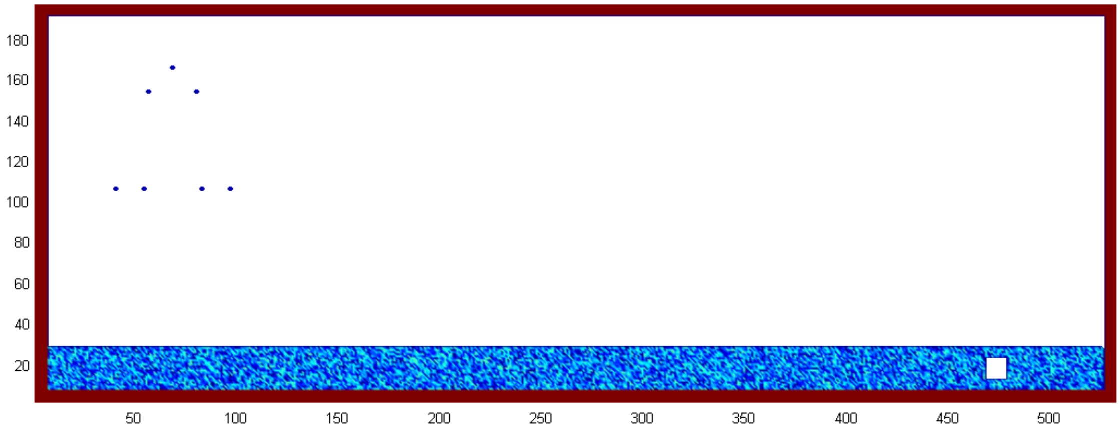

Figure 4.29: The main region in the computational domain for 400 kV steel lattice transmission high voltage suspension towers model.

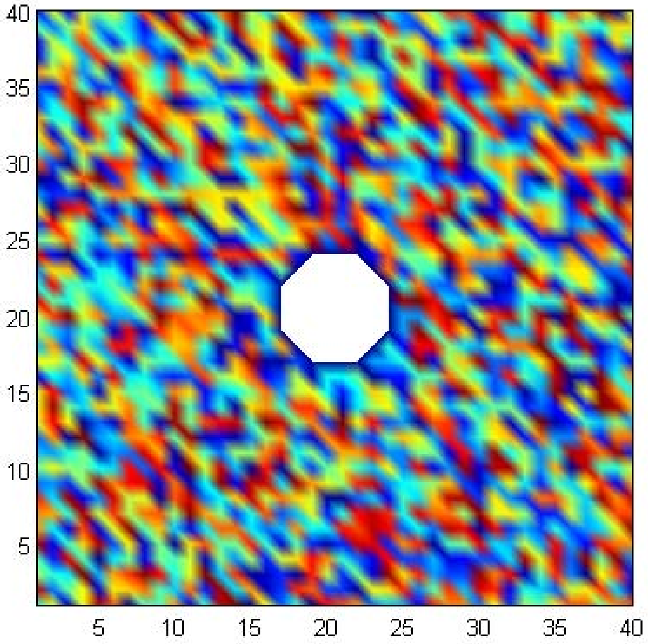

Figure 4.30: The subgrid region in the computational domain for 400 kV steel lattice transmission high voltage suspension towers model.

4.5.1 Near Field Simulation

In this section, the electric and magnetic field distributions are discussed for examples 1, 2 and 3. Except in time, all fields are plotted in dB scale.

Example 1: The interaction results between 132 kV steel lattice transmission high voltage suspension towers and underground metallic pipeline are presented in this section. In general, the simulation was carried out at the transformed intermediate frequency of 460 kHz and the overall model was then transformed back to the proposed lower frequency of 50 Hz. Figure 4.31 shows the three-phase 132 kV sinusoidal sources driven from the steel lattice transmission suspension towers.

In common, each of the sinusoidal AC source was separated by 120^{o} phase. Figure 4.32 depicts the amplitude of the electric field constituent E_{zg} inside subgrid area which was plotted against time. The amplitude of the magnetic field components H_{yg} and H_{xg} plotted against time were illustrated in Figure 4.33. E_{zg}, H_{yg} and H_{xg} were observed at point (31.25 cm, 31.25 cm) inside subgrid spatial section.

The EM wave propagates from the 6 cables of the suspension tower to the surrounding area of air, ground and the pipeline. It varies from 1.0 V/km (0 dBV/km) to 1.78×10^{9} V/km (185 dBV/km). The distribution of the electric field E_z, magnetic fields H_y and H_x through the simulated problem space, along the incident wave propagation direction were given in Figures 4.34, 4.35 and 4.36 respectively. In the subgrid region, the distribution of E_{zg}, H_{yg} and H_{xg} were demonstrated in Figures 4.37, 4.38 and 4.39 respectively.

From assessment of Figures 4.37, 4.38 and 4.39, the fields inside the metallic pipeline were found to be zero due to the excess electrons at the surface of the metal preventing any incoming propagating waves from penetrating the pipeline. The electric field distribution surrounding the pipeline alters from 3.16 V/km (10 dBV/km) to 1.0×10^3 V/km (60 dBV/km). The variation of the field was high which can be seen from the plots represented by red colour, from 50 dBV/km to 60 dBV/km. However, the distribution at close proximity to the pipeline was small, typically from 5 dBV/km to 10 dBV/km. Some of the waves were reflected back to the surface of the ground thus producing induced EM fields which were illustrated in Figures 4.40, 4.41 and 4.42 respectively.

The results were verified by comparing them with [76] which shows good agreements. In normal condition, the OTHL circuit carried currents in each phase. Phase imbalance in the line may be produced due to the difference in the relative distance of each phase from the nearby pipeline. Under fault condition, the currents on the faulty phases of transmission lines were high. This in turn will induce AC voltage on the pipeline and create shock hazard rather than corrosion.

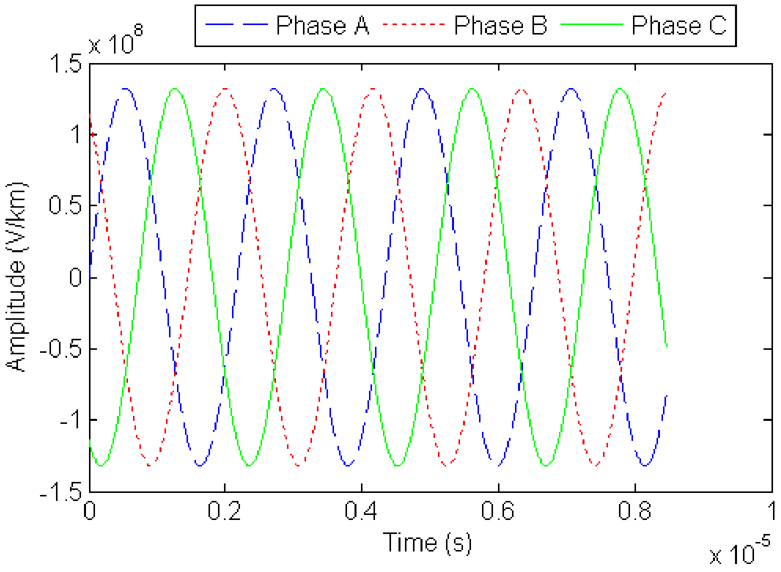

Figure 4.31: Three-phase sinusoidal sources driven from 132 kV steel lattice transmission high voltage suspension towers.

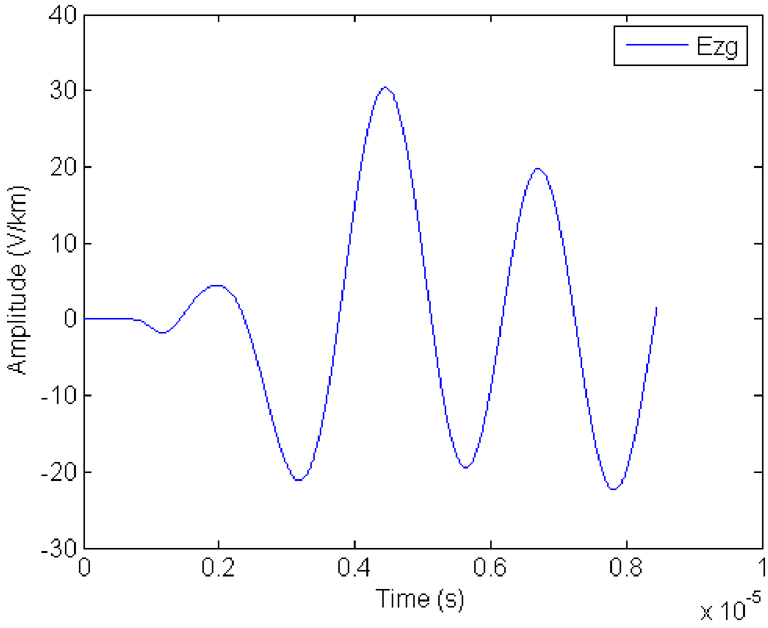

Figure 4.32: The amplitude of electric field E_{zg} plotted against time inside subgrid region.

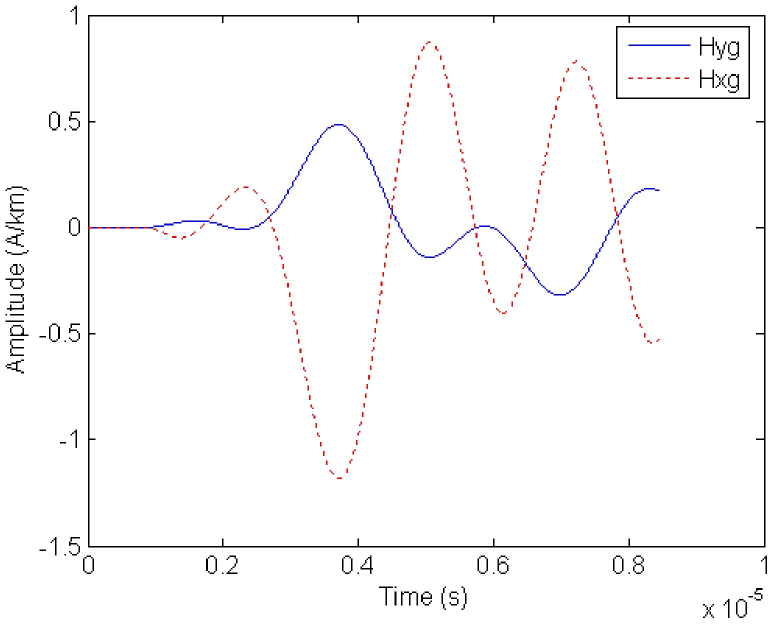

Figure 4.33: The amplitude of magnetic field H_{yg} and H_{xg} plotted against time inside subgrid region.

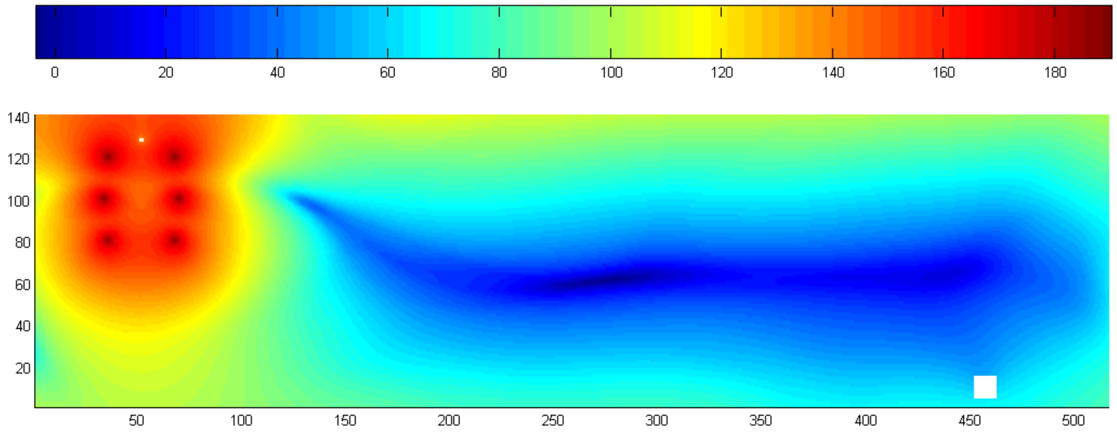

Figure 4.34: The electric field E_z distribution in the main FDTD grid.

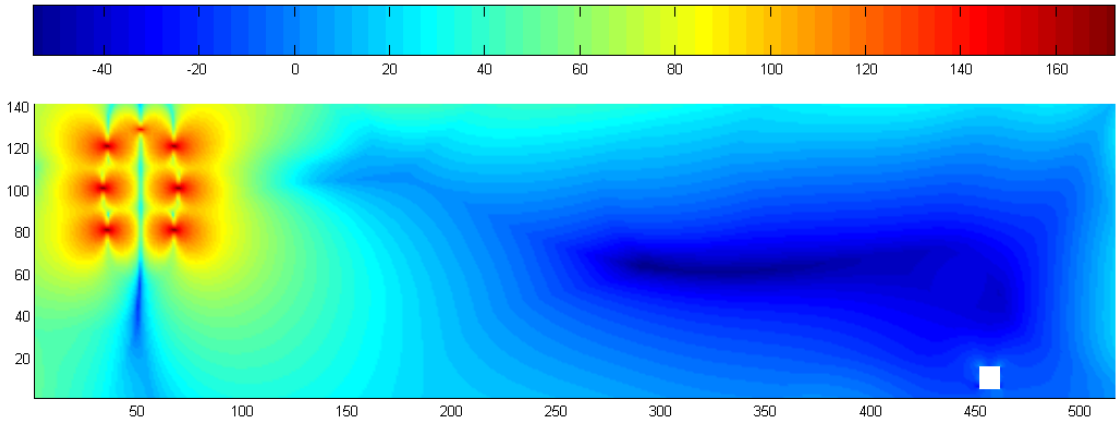

Figure 4.35: The magnetic field H_y distribution in the main FDTD grid.

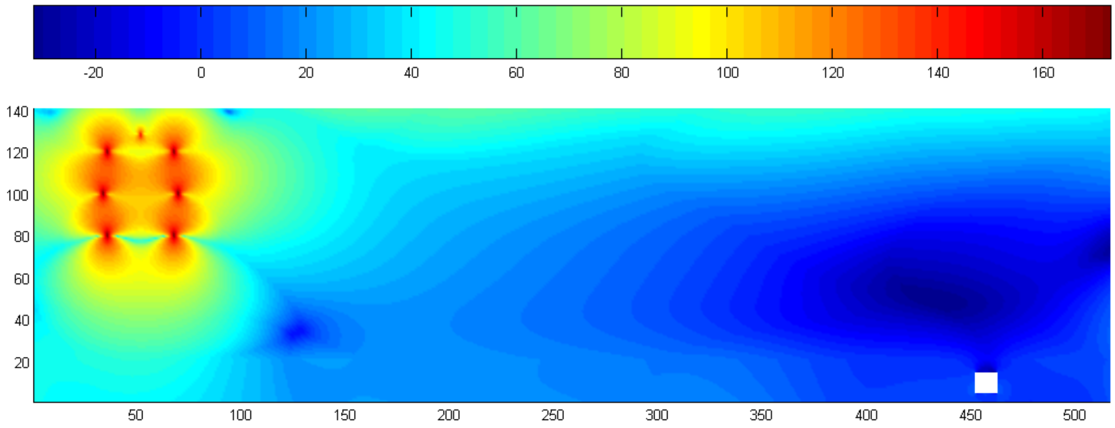

Figure 4.36: The magnetic field H_x distribution in the main FDTD grid.

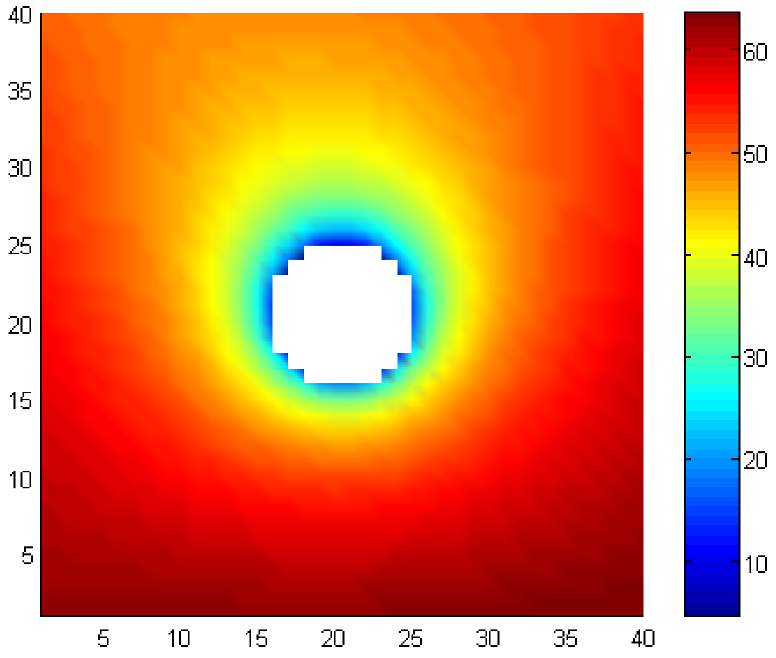

Figure 4.37: The electric field E_{zg} distribution in the subgrid section.

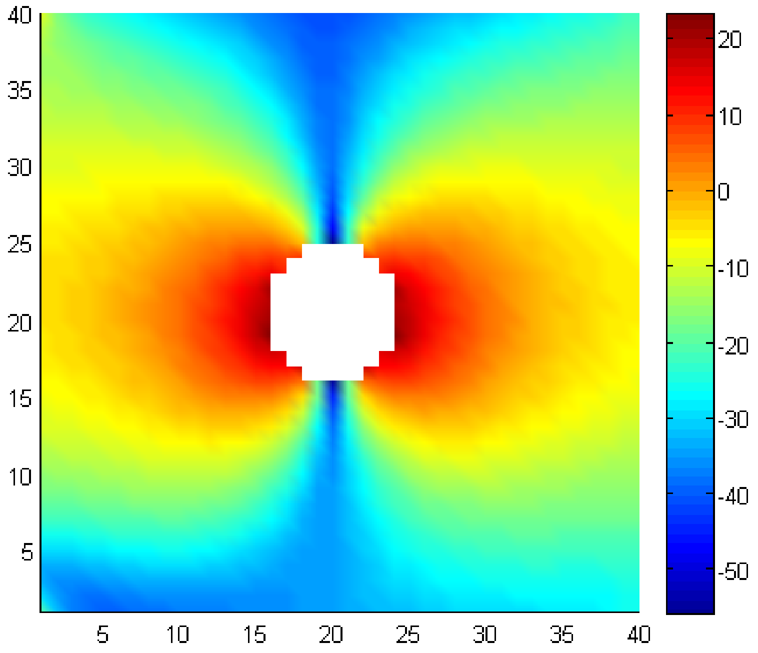

Figure 4.38: The magnetic field H_{yg} distribution in the subgrid section.

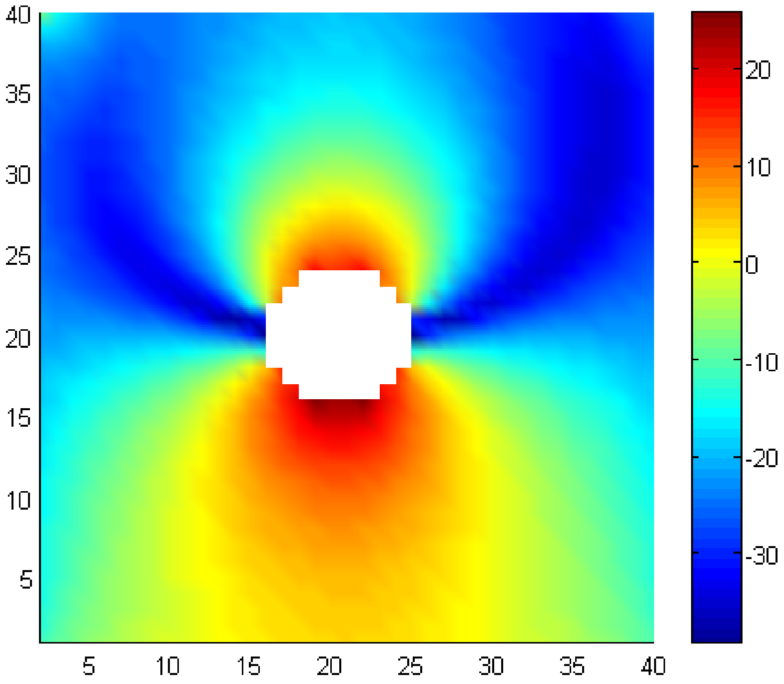

Figure 4.39: The magnetic field H_{xg} distribution in the subgrid section.

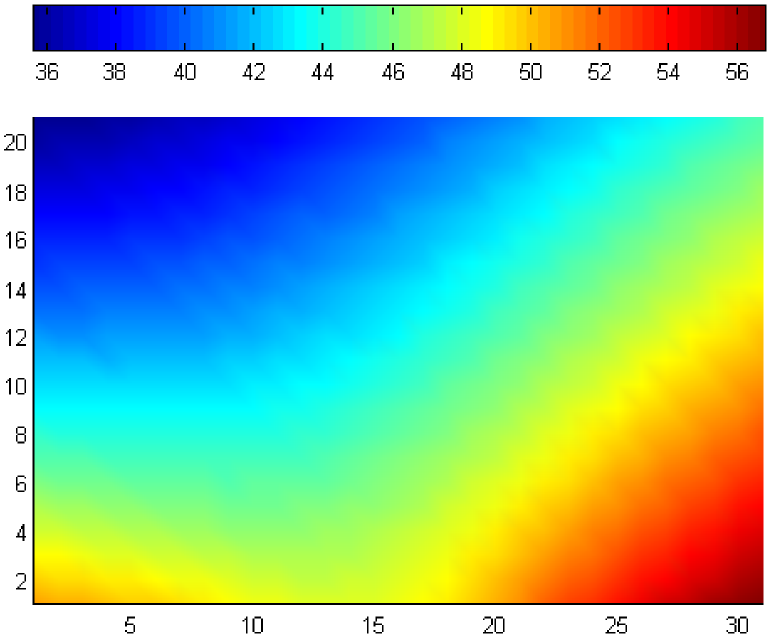

Figure 4.40: The induced electric field E_z at 1.75 m above metallic pipeline.

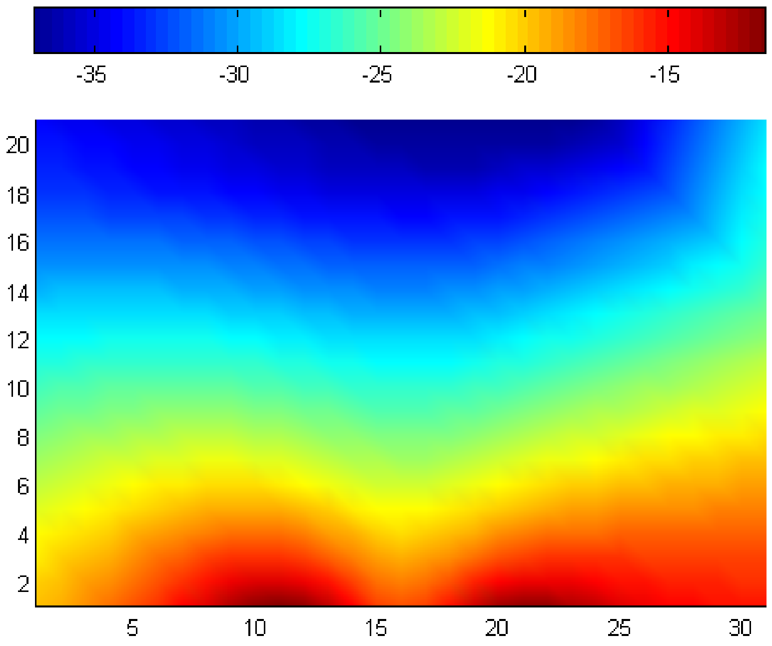

Figure 4.41: The induced magnetic field H_y at 1.75 m above metallic pipeline.

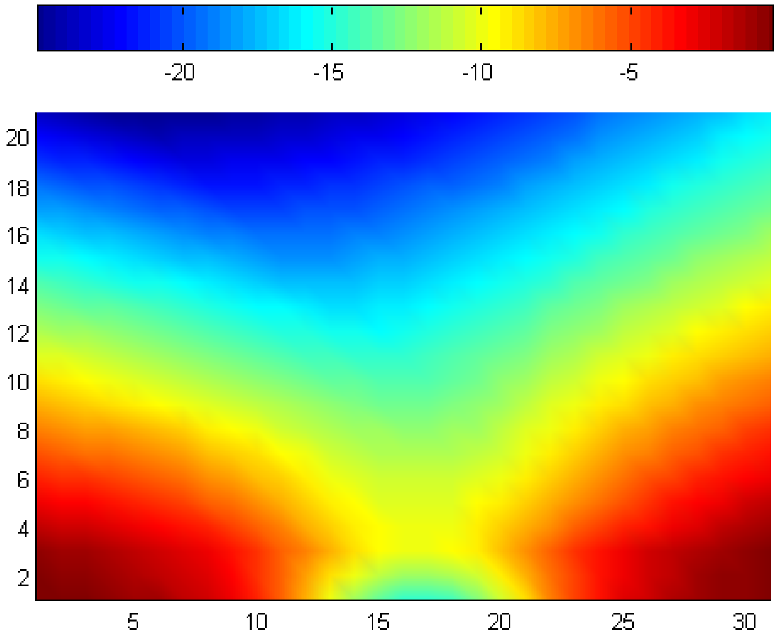

Figure 4.42: The induced magnetic field H_x at 1.75 m above metallic pipeline.

Example 2: This section presents the EM interaction results between 275 kV OHTL suspension towers and underground metallic pipeline. The frequency of 460 kHz was employed in the FDTD simulation before scaled back to the powerline frequency. Figure 4.43 shows the three-phase 275 kV sinusoidal sources separated by 120^{o} phase shift. The amplitude variation of electric field E_{zg} within subgrid region was represented by Figure 4.44. The amplitude variation of magnetic fields H_{yg} and H_{xg} within subgrid area were illustrated in Figure 4.45. The observation point at (31.25 cm, 31.25 cm) within subgrid spatial section was employed for measuring E_{zg}, H_{yg} and H_{xg}. The distribution of E_z varies from 1.0 V/km (0 dBV/km) to 1.0×10^{10} V/km (200 dBV/km). Figures 4.46, 4.47 and 4.48 represent the distribution of the electric field E_z, magnetic fields H_y and H_x in the coarse grid respectively. Figures 4.49, 4.50 and 4.51 demonstrate the distribution of E_{zg}, H_{yg} and H_{xg} in the fine mesh respectively. From inspection of Figures 4.49, 4.50 and 4.51, the fields inside the metallic pipeline were found to be zero. Finally, Figures 4.52, 4.53 and 4.54 show the induced EM fields at 1.75 m above the pipeline due to the arriving reflected waves. The electric field distribution surrounding the pipeline changes from 5.62 V/km (15 dBV/km) to 3.16×10^{3} V/km (70 dBV/km) which shows good agreements with [76]. The difference in relative distance of each phase from the nearby pipeline can create phase imbalance in the transmission line. Under fault condition, the currents on the faulty phases of transmission lines were high causing induced AC voltage on the pipeline.

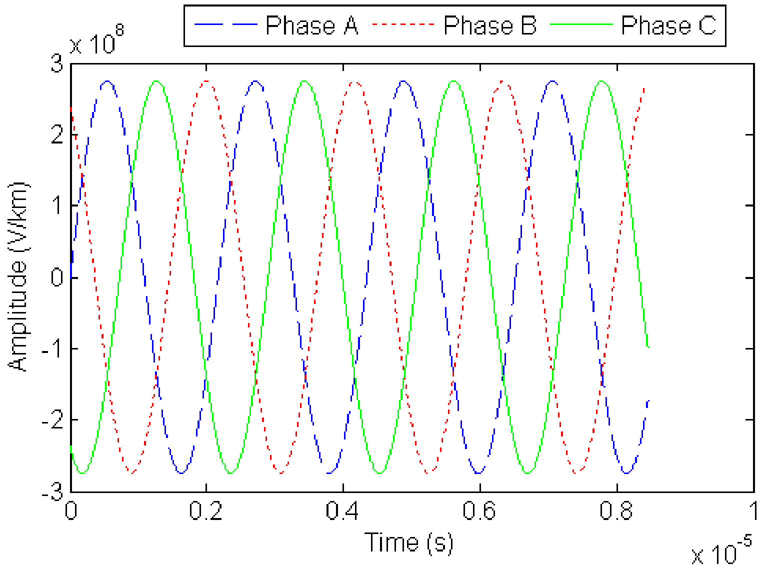

Figure 4.43: Three-phase sinusoidal sources driven from 275 kV steel lattice transmission high voltage suspension towers.

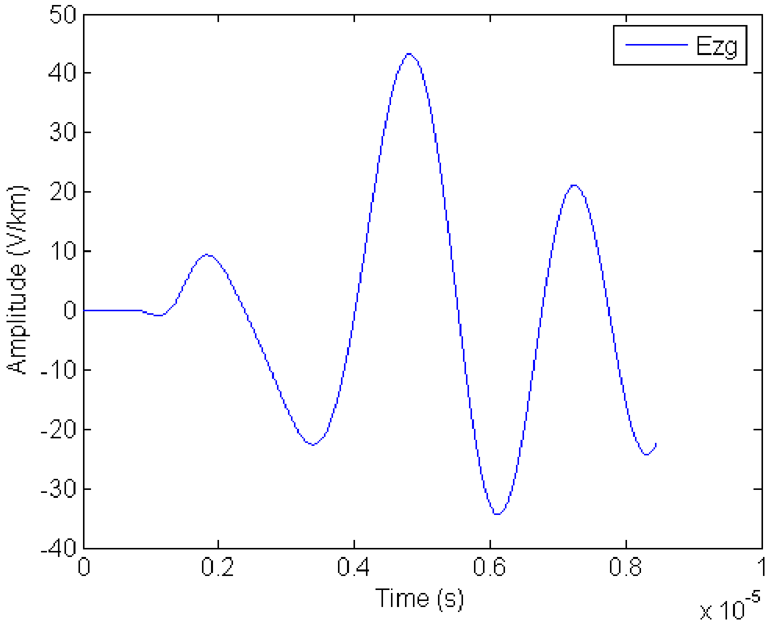

Figure 4.44: The amplitude of electric field E_{zg} plotted against time inside subgrid region.

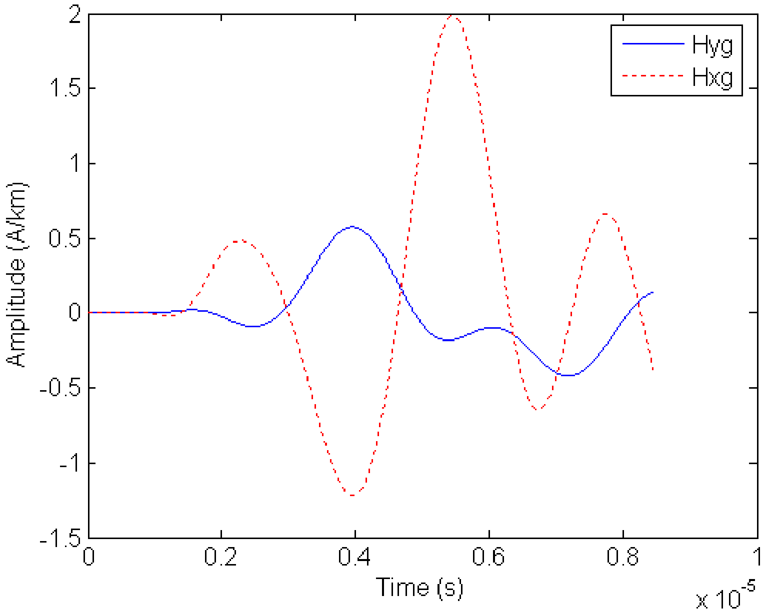

Figure 4.45: The amplitude of magnetic field H_{yg} and H_{xg} plotted against time inside subgrid region.

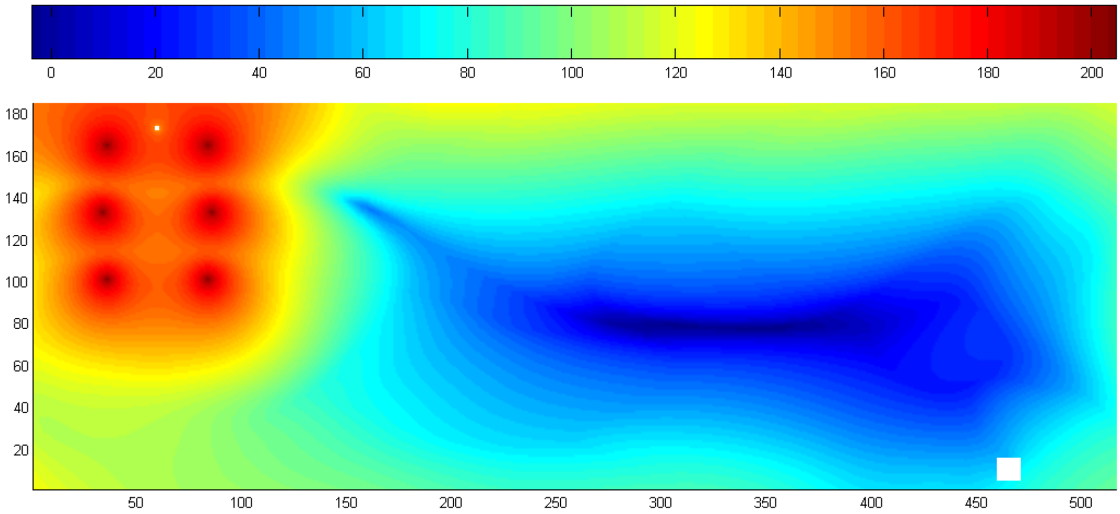

Figure 4.46: The electric field E_z distribution in the main FDTD grid.

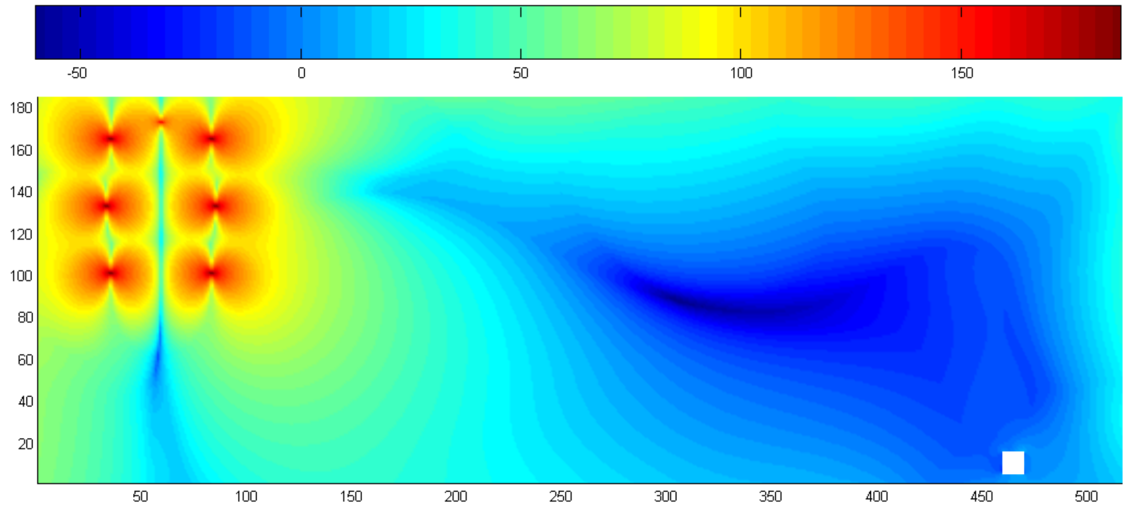

Figure 4.47: The magnetic field H_y distribution in the main FDTD grid.

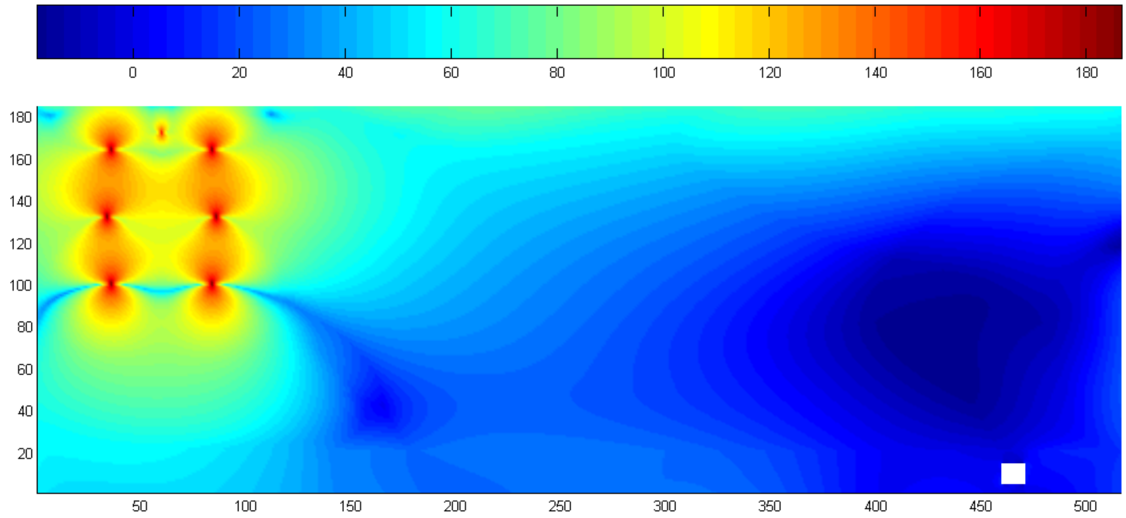

Figure 4.48: The magnetic field H_x distribution in the main FDTD grid.

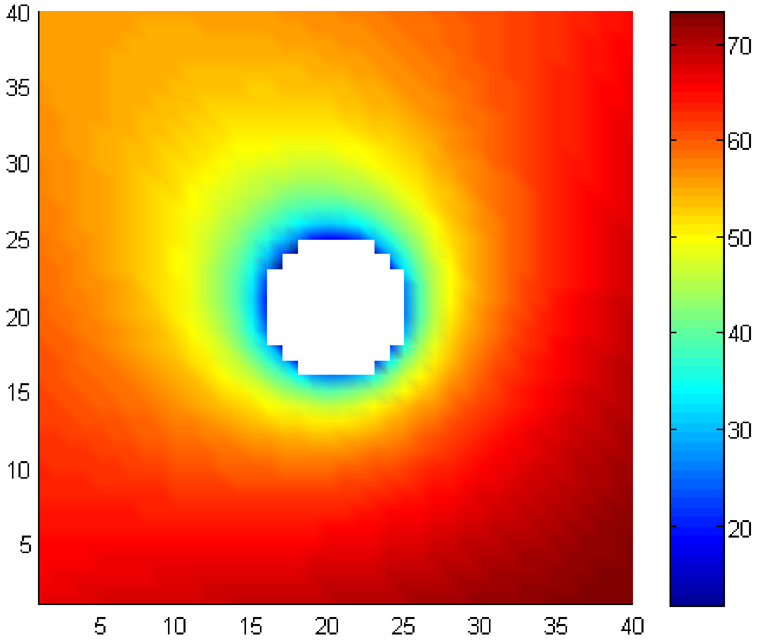

Figure 4.49: The electric field E_{zg} distribution in the subgrid section.

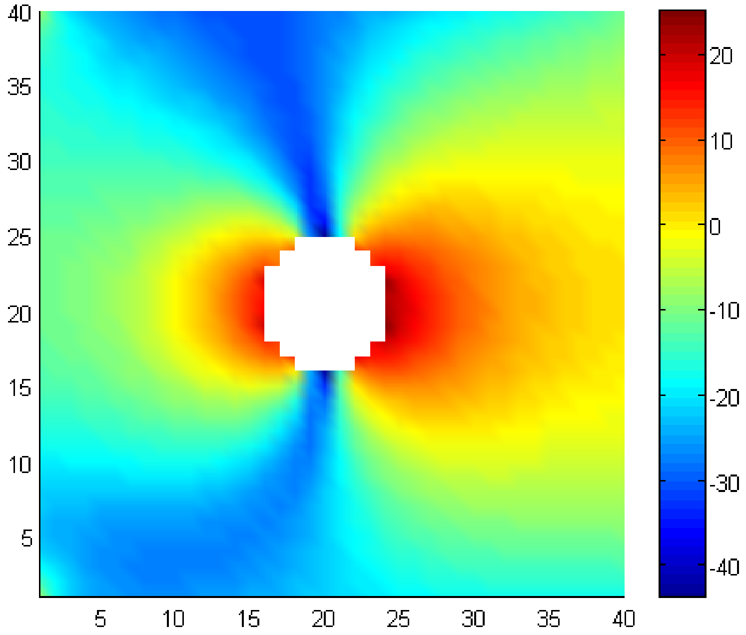

Figure 4.50: The magnetic field H_{yg} distribution in the subgrid section.

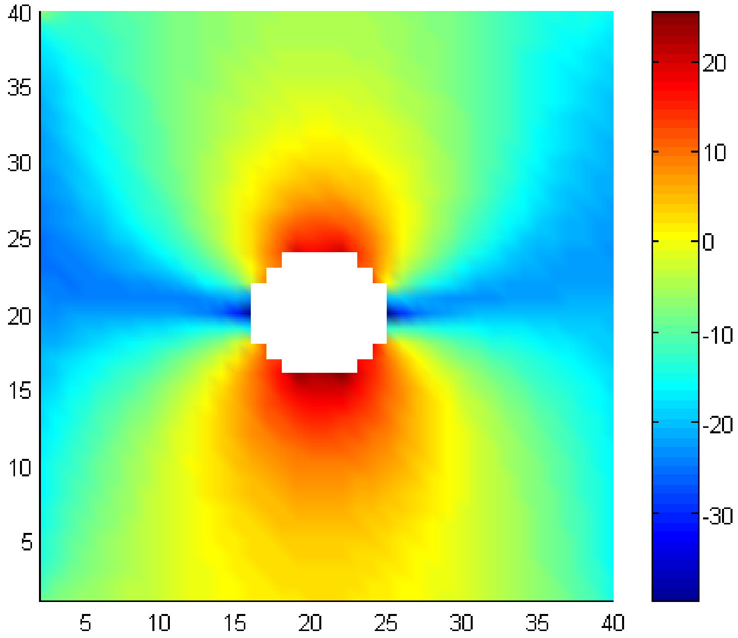

Figure 4.51: The magnetic field H_{xg} distribution in the subgrid section.

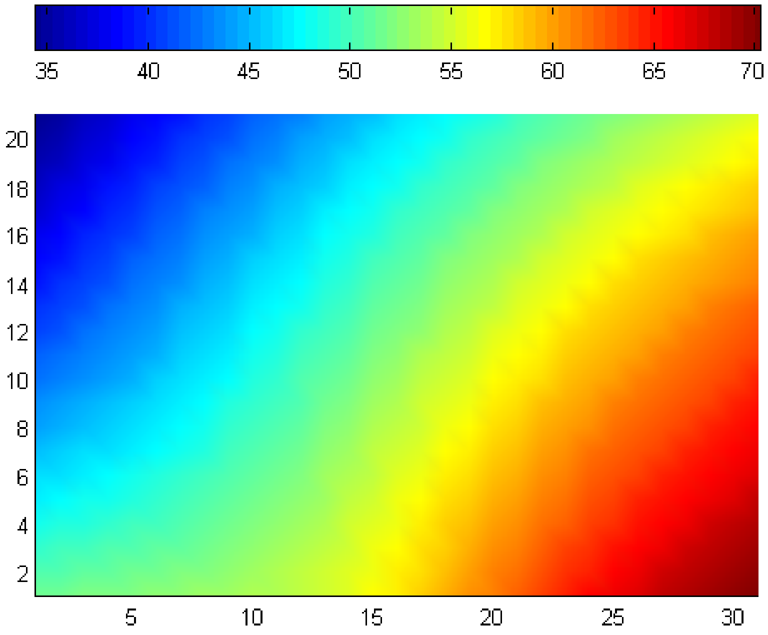

Figure 4.52: The induced electric field E_z at 1.75 m above metallic pipeline.

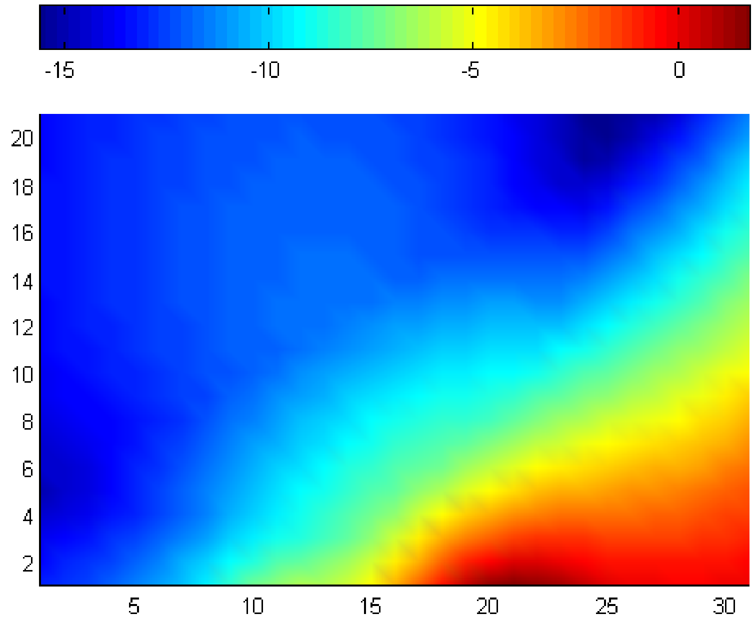

Figure 4.53: The induced magnetic field H_y at 1.75 m above metallic pipeline.

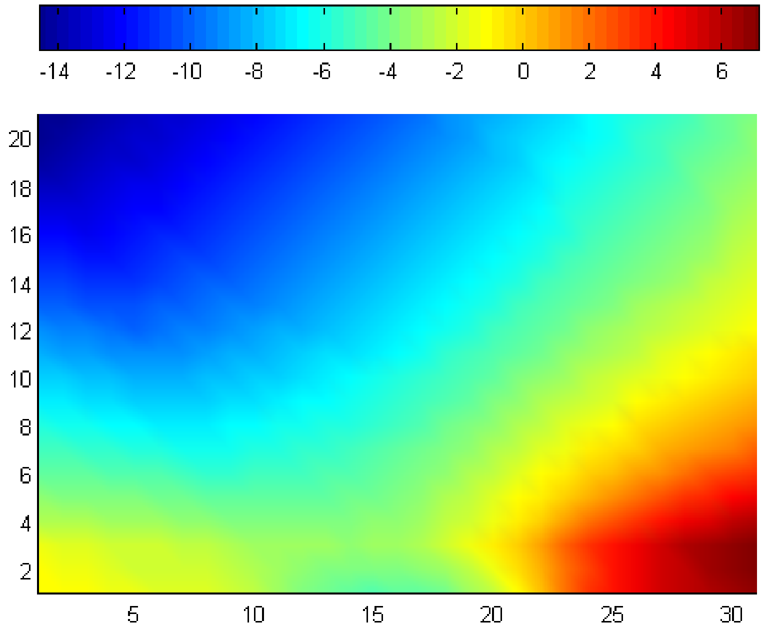

Figure 4.54: The induced magnetic field H_x at 1.75 m above metallic pipeline.

Example 3: The interaction results between 400 kV steel suspension towers and metallic cylinder are presented in this section. The frequency of 460 kHz was employed to get the fields before they were altered back to 50 Hz. Figure 4.55 shows the three-phase 400 kV sinusoidal sources separated by 120^{o} phase shift. The fields E_{zg}, H_{yg} and H_{xg} were observed at point (31.25 cm, 31.25 cm) within subgrid section. E_{zg} was plotted in Figure 4.56 whereas H_{yg} and H_{xg} were plotted in Figure 4.57. The EM wave which travels from the suspension tower to the pipeline varies from 1.0 V/km (0 dBV/km) to 3.16×10^{10} V/km (210 dBV/km). The distribution of the electric field E_z, magnetic fields H_y and H_x through the simulated FDTD computational space were given in Figures 4.58, 4.59 and 4.60 respectively. In subgrid region, the distribution of E_{zg}, H_{yg} and H_{xg} were demonstrated in Figures 4.61, 4.62 and 4.63 respectively. Here, the fields inside the metallic pipeline were also found to be zero. The reason for this phenomenon was due to the excess electrons at the surface of the metal preventing any incoming propagating waves from penetrating the pipeline. It was shown that the electric field distribution surrounding the pipeline alters from 10 V/km (20 dBV/km) to 3.16×10^{3} V/km (70 dBV/km) which shows good conformity with [76]. The difference in relative distance of each phase from the nearby pipeline can create phase imbalance in the transmission line. Under fault condition, the currents on the faulty phases of transmission lines were high causing induced AC voltage on the pipeline. The induced field will not contribute to shock hazard in normal condition. Figures 4.64, 4.65 and 4.66 illustrate the induced EM fields for E_z, H_y and H_x respectively.

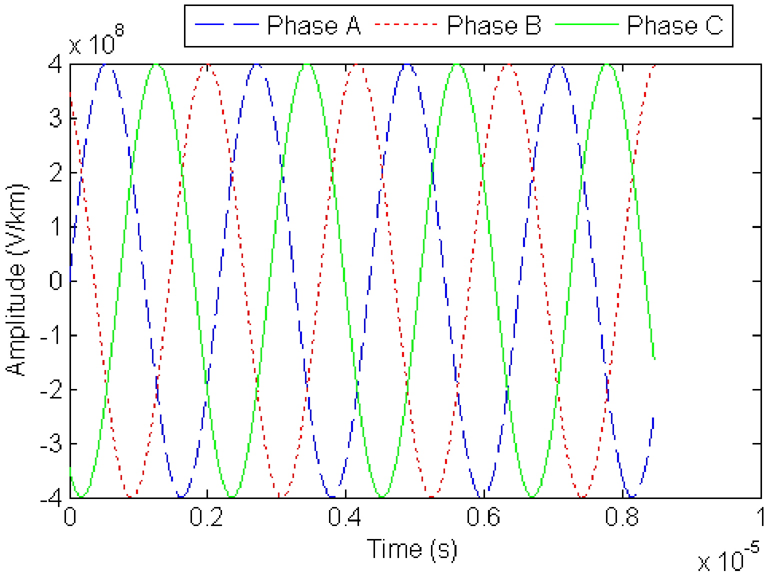

Figure 4.55: Three-phase sinusoidal sources driven from 400 kV steel lattice transmission high voltage suspension towers.

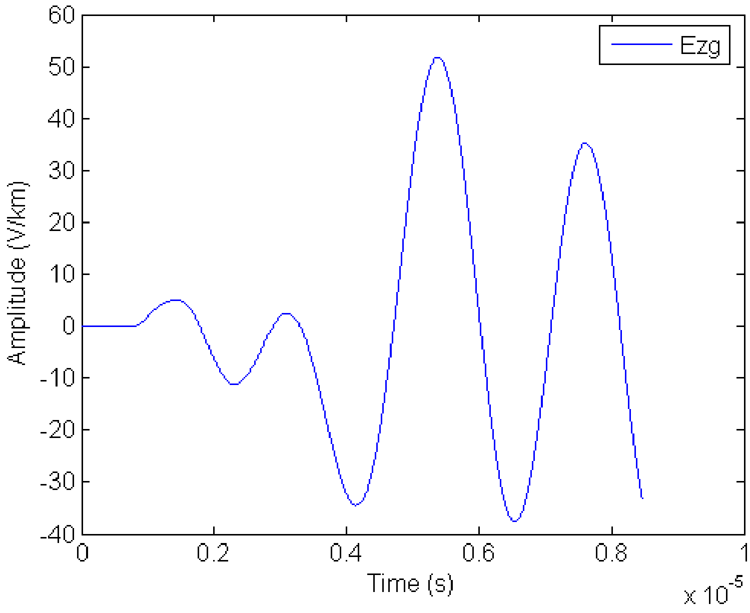

Figure 4.56: The amplitude of electric field E_{zg} plotted against time inside subgrid region.

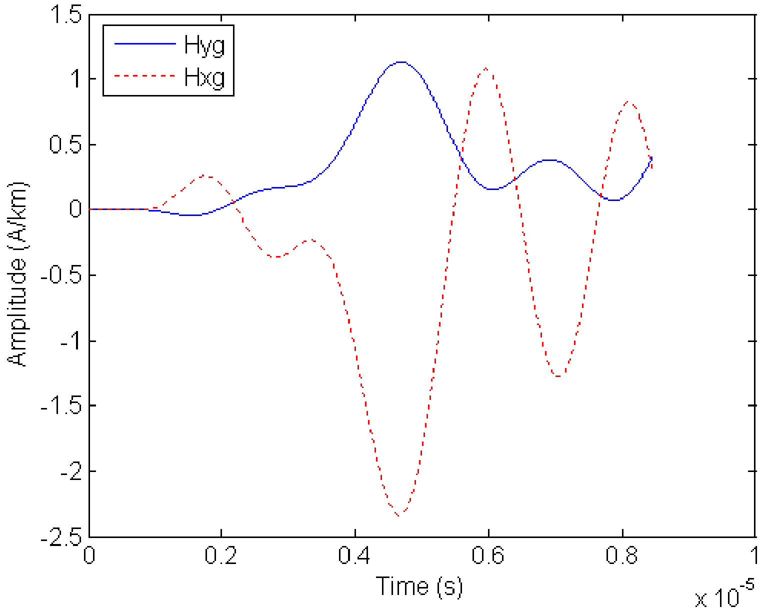

Figure 4.57: The amplitude of magnetic field H_{yg} and H_{xg} plotted against time inside subgrid region.

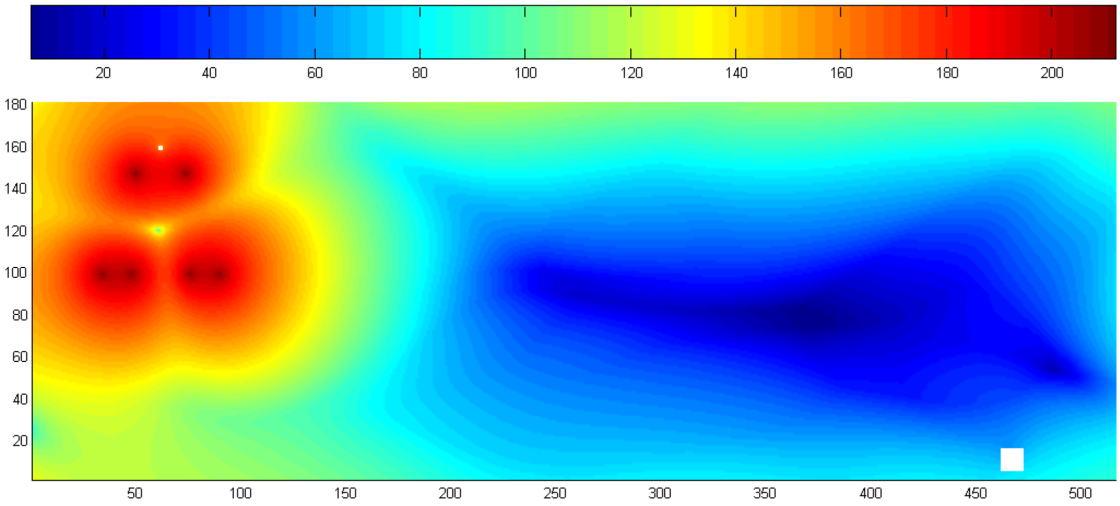

Figure 4.58: The electric field E_z distribution in the main FDTD grid.

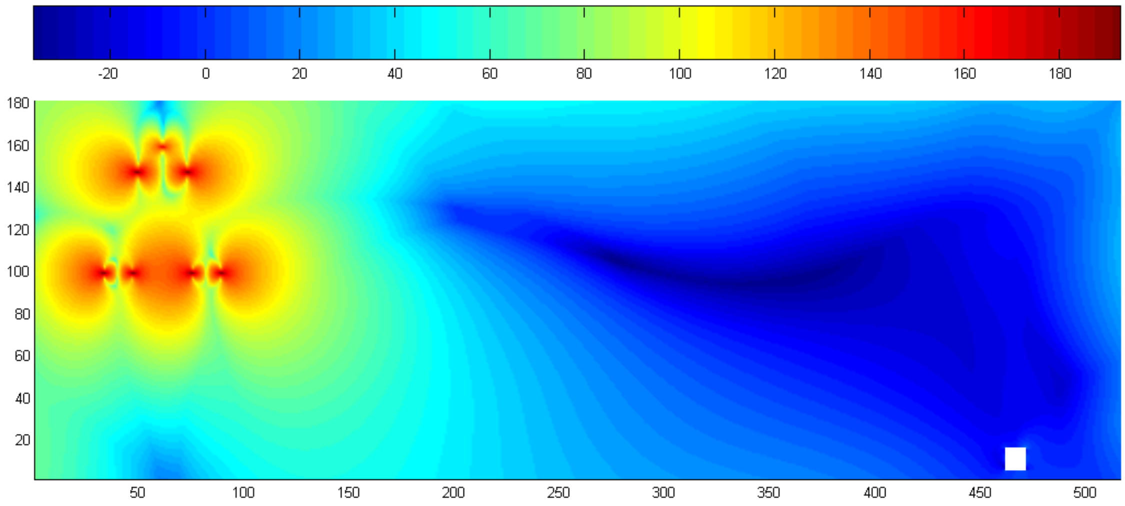

Figure 4.59: The magnetic field H_y distribution in the main FDTD grid.

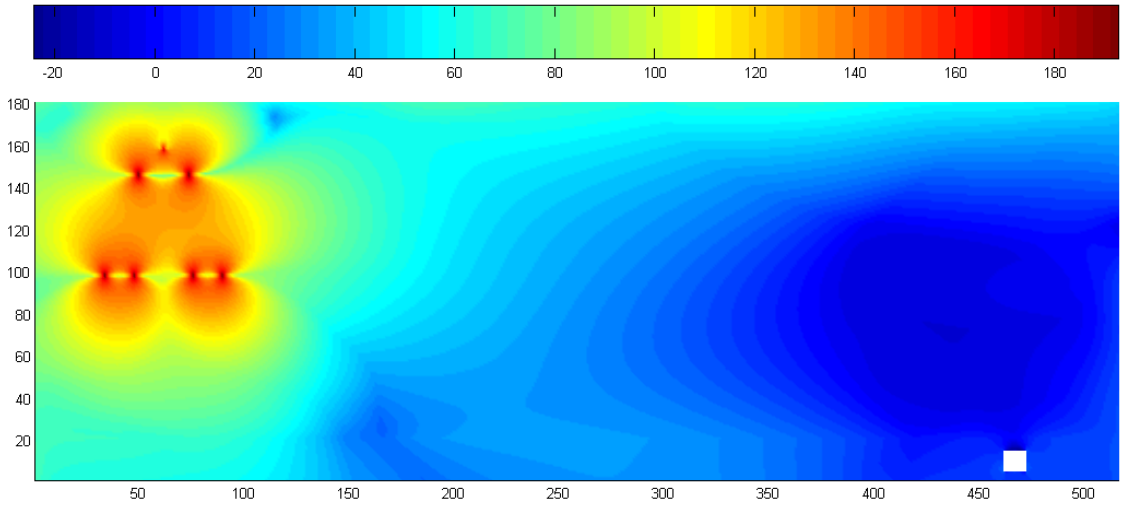

Figure 4.60: The magnetic field H_x distribution in the main FDTD grid.

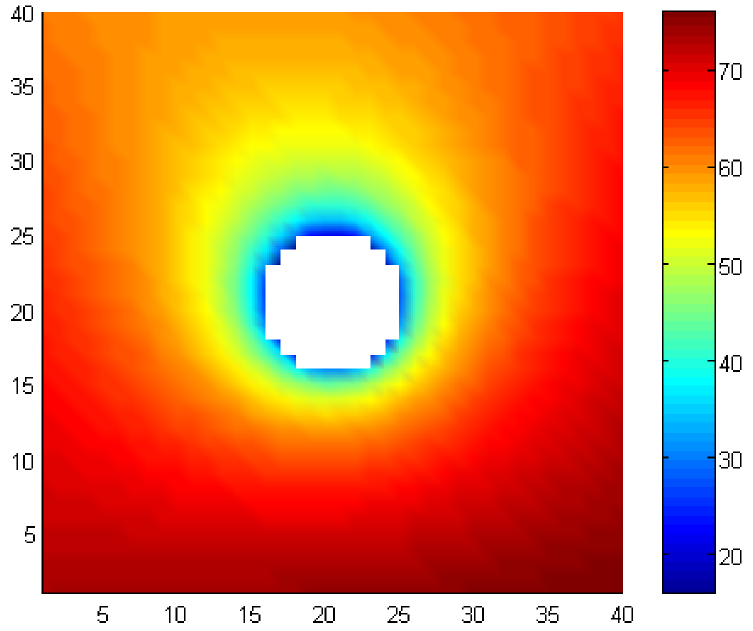

Figure 4.61: The electric field E_{zg} distribution in the subgrid section.

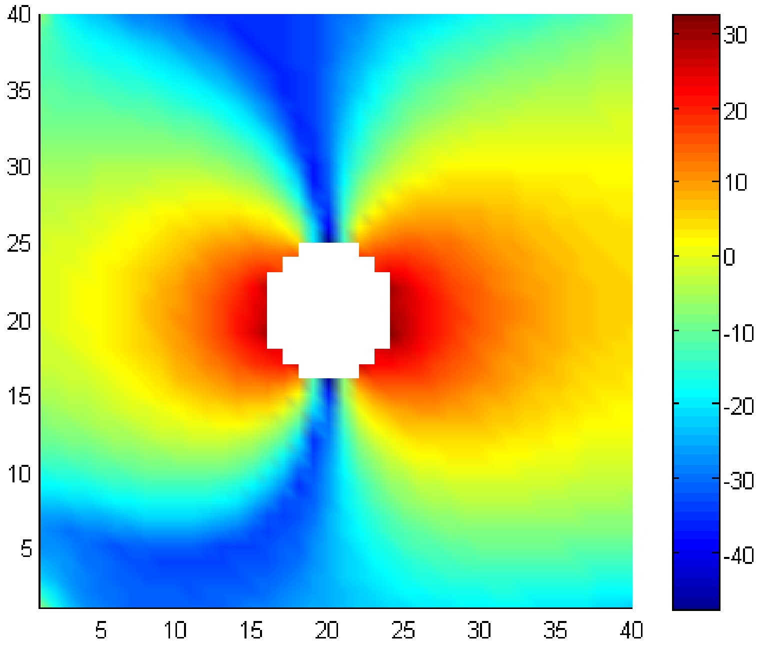

Figure 4.62: The magnetic field H_{yg} distribution in the subgrid section.

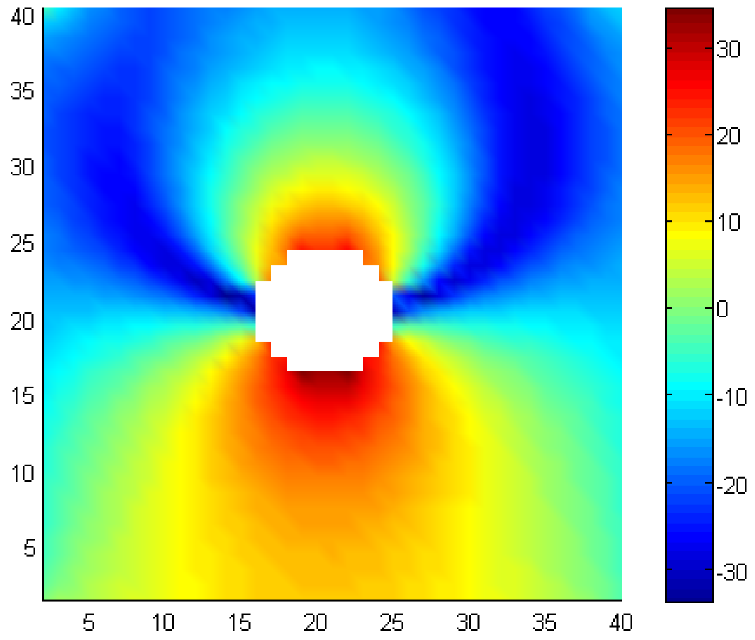

Figure 4.63: The magnetic field H_{xg} distribution in the subgrid section.

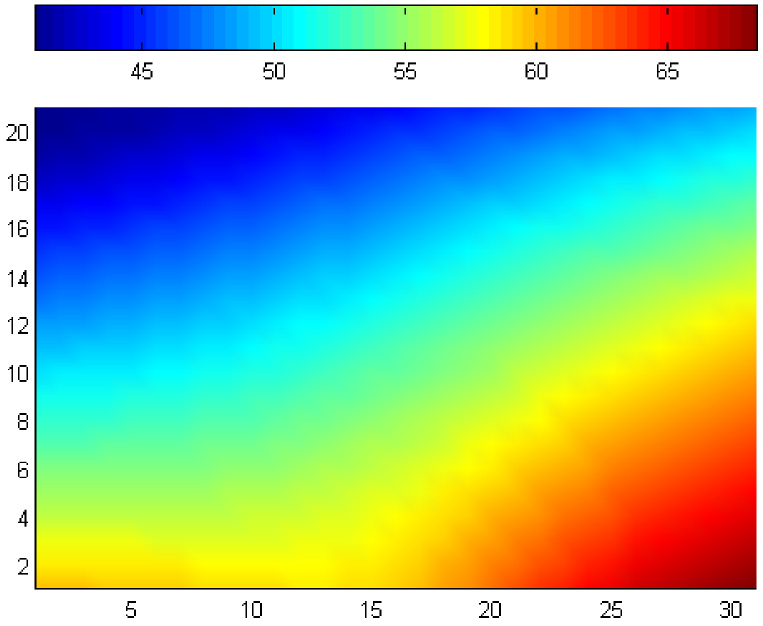

Figure 4.64: The induced electric field E_z at 1.75 m above metallic pipeline.

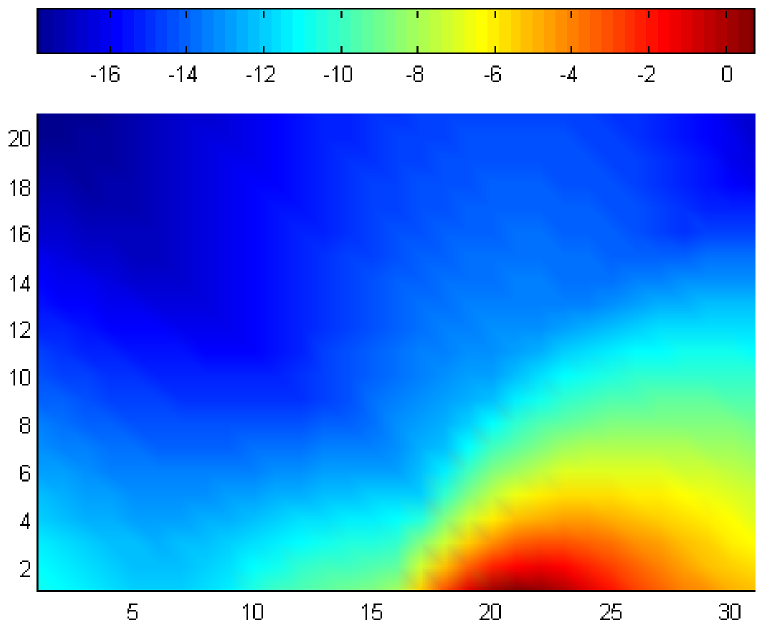

Figure 4.65: The induced magnetic field H_y at 1.75 m above metallic pipeline.

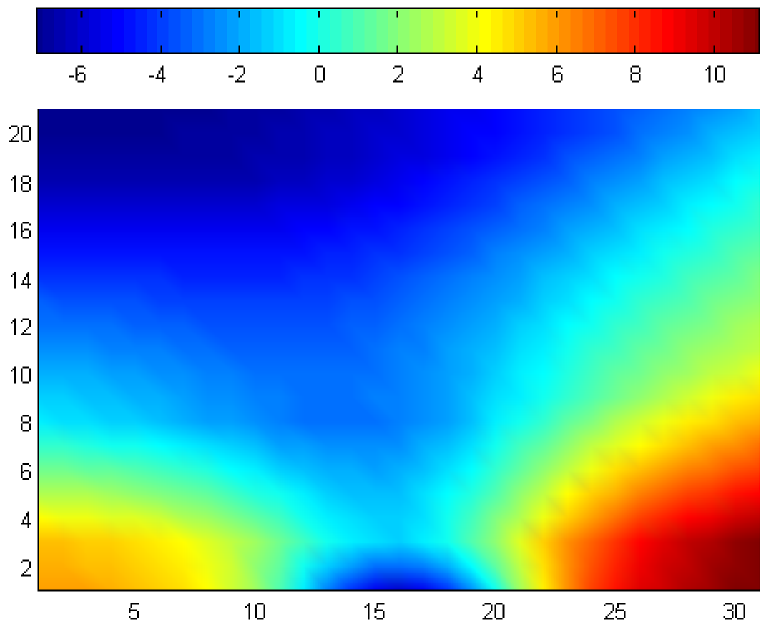

Figure 4.66: The induced magnetic field H_x at 1.75 m above metallic pipeline.

4.8 Conclusion

An approach to model the interaction between overhead transmission lines and underground utility pipeline at power-line frequency has been presented. This uses the FDTD technique for the whole structure of the problem combined with subgridding method at the object of interest particularly at the underground pipeline. By implementing a modified version of Berenger's PML, the reflection on the boundary layers inside the spatial FDTD computational region has been successfully decreased, although it is surrounded by lossy penetrable media. The computational burden due to huge number of time steps in the order of tens of millions has been eased to tens of thousands by employing the method called quasi-static approximation scheme. A new approach to microdosimetric modelling of bioelectromagnetic interactions at higher definition cellular level by using modified subgridded finite-difference time-domain (SGFDTD) has been presented. The utility of the method has been demonstrated, in which the SGFDTD technique was applied to model detailed biological cell structure. In addition, the use of inhomogeneous soil in the common corridor permits a non-trivial proximity region of authentic ground properties to be simulated. Profound investigation of the interaction between electromagnetic fields and natural or utility arrangement with different electrical characteristics at different level of spatial resolution can be assisted by such tools. The combination of frequency scaling SGFDTD approach with arbitrary inhomogeneous dielectric volume, floquet periodic boundary theorem and the modified Berenger's PML paves a way as a good candidate model of EM fields interaction modelling for complex geometries.

4.9 References

[1] A. Taflove and S. C. Hagness, *Computational electrodynamics: The finite-difference time-domain method*, 3rd ed. Boston, MA: Artech House, 2005.

[2] K. S. Yee, "Numerical solution of initial boundary value problems involving Maxwell's equations in isotropic media," *IEEE Transactions on Antennas and Propagation*, vol. AP-14, pp. 302-307, 1966.

[3] G. Mur, "Absorbing boundary conditions for the finite-difference approximation of the time-domain electromagnetic-field equations," *IEEE Transactions on Electromagnetic Compatibility*, vol. EMC-23, pp. 377-382, 1981.

[4] R. Wu, G. Benqing, and Y. Shiming, "An improved method in FDTD simulation to reduce reflection from non-uniform mesh," *3rd International Conference on Microwave and Millimeter Wave Technology Proceedings*, pp. 646-649, 2002.

[5] S. Kapoor, "Sub-cellular technique for finite-difference time-domain method," *IEEE Transactions on Microwave Theory and Techniques*, vol. 45, pp. 673-677, 1997.

[6] R. Holland, "Finite-difference solution of Maxwell's equations in generalized nonorthogonal coordinates," *IEEE Transactions on Nuclear Science*, vol. 30, pp. 4589-4591, 1983.

[7] K. Xiao, D. J. Pommerenke, and J. L. Drewniak, "A three-dimensional FDTD subgridding algorithm based on interpolation of current density," *IEEE International Symposium on Electromagnetic Compatibility*, vol. 1, pp. 118-123, 2004.

[8] K. M. Krishnaiah and C. J. Railton, "A stable subgridding algorithm and its

application to eigenvalue problems," *IEEE Transactions on Microwave Theory and Techniques*, vol. 47, pp. 620-628, 1999.

[9] T. Ohtani, K. Taguchi, and T. Kashiwa, "A subgridding technique for the complex nonstandard FDTD method," *Electronics and Communications in Japan Part 2 - Electronics*, vol. 87, pp. 1-9, 2004.

[10] K. Xiao, D. J. Pommerenke, and J. L. Drewniak, "A three-dimensional FDTD subgridding algorithm with separated temporal and spatial interfaces and related stability analysis," *IEEE Transactions on Antennas and Propagation*, vol. 55, pp. 1981-1990, 2007.

[11] M. J. White, Z. Q. Yun, and M. F. Iskander, "A new 3-D FDTD multigrid technique with dielectric traverse capabilities," *IEEE Transactions on Microwave Theory and Techniques*, vol. 49, pp. 422-430, 2001.

[12] M. Bonilla, M. F. Wong, and V. F. Hanna, "A finite-element formulation for FDTD subgridding," *Microwave and Optical Technology Letters*, vol. 32, pp. 104-108, 2002.

[13] N. V. Venkatarayalu, R. Lee, Y. B. Gan, and L. W. Li, "A stable FDTD subgridding method based on finite element formulation with hanging variables," *IEEE Transactions on Antennas and Propagation*, vol. 55, pp. 907-915, 2007.

[14] J. D. Moerloose, T. W. Dawson, and M. A. Stuchly, "Application of the finite difference time domain algorithm to quasi-static field analysis," *Radio Science*, vol. 32, pp. 329-341, 1997.

[15] W. T. Kaune and M. F. Gillis, "General properties of the interaction between animals and ELF electric fields," *Bioelectromagnetics*, vol. 2, pp. 1-11, 1981.

[16] A. W. Guy, S. Davidow, G. Y. Yang, and C. K. Chou, "Determination of electric current distributions in animals and humans exposed to a uniform 60-Hz high-intensity electric field," *Bioelectromagnetics*, vol. 3, pp. 47-71, 1982.

[17] L. Golestani-Rad, B. Elahi, and J. Rashed-Mohassel, "Investigating the effects of external fields polarization on the coupling of pure magnetic waves in the human body in very low frequencies," *BioMagnetic Research and Technology*, vol. 5, pp. 1-5, 2007.

[18] O. P. Gandhi and J. Chen, "Numerical dosimetry at power-line frequencies using anatomically based model," *Bioelectromagnetics*, vol. 13, pp. 43-60, 1992.

[19] M. A. Stuchly and T. W. Dawson, "Human organ and tissue induced currents by 60 Hz electric and magnetic fields," *Proceedings of the 19th Annual International Conference of the IEEE Engineering in Medicine and Biology Society*, vol. 6, pp. 2464-2467, 1997.

[20] T. W. Dawson, K. Caputa, and M. A. Stuchly, "High-resolution organ dosimetry for human exposure to low-frequency electric fields," *IEEE Transactions on Power Delivery*, vol. 13, pp. 366-373, 1998.

[21] M. E. Potter, M. Okaniewski, and M. A. Stuchly, "Low frequency finite difference time domain (FDTD) for modeling of induced fields in humans close to line sources," *Journal of Computational Physics*, vol. 162, pp. 82-103, 2000.

[22] G. Emili, A. Schiavoni, M. Francavilla, L. Roselli, and R. Sorrentino, "Computation of electromagnetic field inside a tissue at mobile communications frequencies," *IEEE Transactions on Microwave Theory and Techniques*, vol. 51, pp. 178-186, 2003.

[23] M. N. O. Sadiku, *Elements of electromagnetics*, 3rd ed. New York: Oxford

University Press Inc., pp. 417-435, 2001.

[24] D. M. Pozar, *Microwave engineering*, 3rd ed. Hoboken, New Jersey: John Wiley and Sons Inc., pp. 14-44, 2005.

[25] Z. P. Liao, H. L. Wong, B. P. Yang, and Y. F. Yuan, "A transmitting boundary for transient wave analysis," *Scientia Sinica (Series A)*, vol. XXVII, pp. 1063-1076, 1984.

[26] K. K. Mei and J. Y. Fang, "Superabsorption - A method to improve absorbing boundary conditions," *IEEE Transactions on Antennas and Propagation*, vol. 40, pp. 1001-1010, 1992.

[27] J. P. Berenger, "A perfectly matched layer for the absorption of electromagnetic waves," *Journal of Computational Physics*, vol. 114, pp. 185-200, 1994.

[28] J. P. Berenger, "Three-dimensional perfectly matched layer for the absorption of electromagnetic waves," *Journal of Computational Physics*, vol. 127, pp. 363-379, 1996.

[29] J. P. Berenger, "Perfectly matched layer for the FDTD solution of wave-structure interaction problems," *IEEE Transactions on Antennas and Propagation*, vol. 44, pp. 110-117, 1996.

[30] J. P. Berenger, "Improved PML for the FDTD solution of wave-structure interaction problems," *IEEE Transactions on Antennas and Propagation*, vol. 45, pp. 466-473, 1997.

[31] R. E. Collin, *Field theory of guided waves*, 2nd ed. New York: The Institute of Electrical and Electronics Engineers Inc., 1995.

[32] R. E. Collin, *Foundations for microwave engineering*, 2nd ed. London: McGraw Hill, 1992.

[33] J. J. Ma, W. Z. Lu, and Z. W. Xiao, "Analysis of dielectric frequency selective surfaces using the FDTD method," *3rd International Conference on Computational Electromagnetics and Its Applications (ICCEA)*, pp. 25-28, 2004.

[34] G. Marrocco and F. Capolino, "Transient radiation by periodic structures: Accuracy of the (time domain-floquet wave)-FDTD algorithm," *IEEE Antennas and Propagation Society International Symposium*, vol. 3, pp. 643-646, 2002.

[35] W. Ko and R. Mittra, "Implementation of Floquet boundary condition in FDTD for FSS analysis," *IEEE Antennas and Propagation Society International Symposium*, vol. 1, pp. 14-17, 1993.

[36] J. Ren, O. P. Gandhi, L. R. Walker, J. Fraschilla, and C. R. Boerman, "Floquet-based FDTD analysis of two-dimensional phased array antennas," *IEEE Microwave and Guided Wave Letters*, vol. 4, pp. 109-111, 1994.

[37] W. J. Tsay and D. M. Pozar, "Application of the FDTD technique to periodic problems in scattering and radiation," *IEEE Microwave and Guided Wave Letters*, vol. 3, pp. 250-252, 1993.

[38] J. A. Roden, S. D. Gedney, M. P. Kesler, J. G. Maloney, and P. H. Harms, "Time-domain analysis of periodic structures at oblique incidence: Orthogonal and nonorthogonal FDTD implementations," *IEEE Transactions on Microwave Theory and Techniques*, vol. 46, pp. 420-427, 1998.

[39] A. Y. Butrym and M. N. Legenkiy, "Comparison of absorbing boundary conditions for numerical analysis of periodic structures," *6th International Conference on Antenna Theory and Techniques*, pp. 239-242, 2007.

[40] E. A. Navarro, B. Gimeno, and J. L. Cruz, "Modelling of periodic structures using the finite difference time domain method combined with the Floquet theorem," *Electronics Letters*, vol. 29, pp. 446-447, 1993.

[41] D. T. Prescott and N. V. Shuley, "Extensions to the FDTD method for the analysis of infinitely periodic arrays," *IEEE Microwave and Guided Wave Letters*, vol. 4, pp. 352-354, 1994.

[42] M. E. Veysoglu, R. T. Shin, and J. A. Kong, "A finite-difference time-domain analysis of wave scattering from periodic surfaces: Oblique incidence case," *Journal of Electromagnetic Waves Application*, vol. 7, pp. 1595-1607, 1993.

[43] C. H. See, R. A. Abd-Alhameed, and P. S. Excell, "Computation of electromagnetic fields in assemblages of biological cells using a modified finite-difference time-domain scheme," *IEEE Transactions on Microwave Theory and Techniques*, vol. 55, pp. 1986-1994, 2007.

[44] A. Alexanian, N. J. Kolias, R. C. Compton, and R. A. York, "Three-dimensional FDTD analysis of quasi-optical arrays using Floquet boundary conditions and Berenger's PML," *IEEE Microwave and Guided Wave Letters*, vol. 6, pp. 138-140, 1996.

[45] A. Akyurtlu, D. H. Werner, V. Veremey, D. J. Steich, and K. Aydin, "Staircasing errors in FDTD at an air-dielectric interface," *IEEE Microwave and Guided Wave Letters*, vol. 9, pp. 444-446, 1999.

[46] A. Vaccari, R. Pontalti, C. Malacarne, and L. Cristoforetti, "A robust and efficient subgridding algorithm for finite-difference time-domain simulations of Maxwell's equations," *Journal of Computational Physics*, vol. 194, pp. 117-139, 2004.

[47] C. H. See, R. A. Abd-Alhameed, R. S. Zadeh, and P. S. Excell, "FDTD

subgridding scheme for bioelectromagnetics application," *Commission B, URSI Symposium, University of Portsmouth, UK*, pp. 11, 2007.

[48] P. Chow, T. Kubota, and T. Namiki, "A stable FDTD subgridding method for both spatial and temporal spaces," *IEEE Antennas and Propagation Society International Symposium*, pp. 1-4, 2008.

[49] S. S. Zivanovic, K. S. Yee, and K. K. Mei, "A subgridding method for the time-domain finite-difference method to solve Maxwell's equations," *IEEE Transactions on Microwave Theory and Techniques*, vol. 39, pp. 471-479, 1991.

[50] T. Kotnik and D. Miklavcic, "Theoretical evaluation of the distributed power dissipation in biological cells exposed to electric fields," *Bioelectromagnetics*, vol. 21, pp. 385-394, 2000.

[51] P. Przybyszewski and M. Mrozowski, "A conductive wedge in Yee's mesh," *IEEE Microwave and Guided Wave Letters*, vol. 8, pp. 66-68, 1998.

[52] A. M. Shreim and M. F. Hadi, "Integral PML absorbing boundary conditions for the high-order M24 FDTD algorithm," *Progress in Electromagnetics Research*, vol. 76, pp. 141-152, 2007.

[53] K. N. Ramli and R. A. Abd-Alhameed, "Modelling of complex electromagnetic problems using FDTD subgridding methods," *9th Informatics Workshop for Research Students, University of Bradford, UK*, pp. 200-201, 2008.

[54] S. M. Wang, F. L. Teixeira, R. Lee, and J. F. Lee, "Optimization of subgridding schemes for FDTD," *IEEE Microwave and Wireless Components Letters*, vol. 12, pp. 223-225, 2002.

[55] R. A. Chilton and R. Lee, "Conservative and provably stable FDTD subgridding,"

IEEE Transactions on Antennas and Propagation, vol. 55, pp. 2537-2549, 2007.

[56] R. A. Chilton and R. Lee, "Conservative subgridding for lobatto cell FDTD method," *IEEE Antennas and Propagation Society International Symposium*, pp. 1-4, 2008.

[57] T. C. Lin and C. W. Kuo, "A novel and efficient subgridding scheme in FDTD method using the Crank-Nicolson algorithm," *Microwave and Optical Technology Letters*, vol. 49, pp. 3103-3106, 2007.

[58] S. H. Sun and C. T. M. Choi, "A new multilevel subgridding scheme for two-dimensional FDTD method," *IEEE Transactions on Magnetics*, vol. 40, pp. 1025-1028, 2004.

[59] S. H. Sun and C. T. M. Choi, "A new subgridding scheme for two-dimensional FDTD and FDTD (2,4) methods," *IEEE Transactions on Magnetics*, vol. 40, pp. 1041-1044, 2004.

[60] B. Donderici and F. L. Teixeira, "Improved FDTD subgridding algorithms via digital filtering and domain overriding," *IEEE Transactions on Antennas and Propagation*, vol. 53, pp. 2938-2951, 2005.

[61] O. Podebrad, M. Clemens, and T. Weiland, "New flexible subgridding scheme for the finite integration technique," *IEEE Transactions on Magnetics*, vol. 39, pp. 1662-1665, 2003.

[62] C. C. Chang and S. K. Jeng, "A multilevel subgridding scheme for two-dimensional finite-difference time-domain method," *IEEE Antennas and Propagation Society International Symposium*, vol. 1, pp. 36-39, 2001.

[63] C. C. Chang and S. K. Jeng, "Modified subgridding algorithm with multilevel

scheme for two-dimensional finite-difference time-domain method," *Asia-Pacific Microwave Conference Proceedings*, vol. 1-3, pp. 831-834, 2001.

[64] W. H. Yu and R. Mittra, "A new subgridding method for the finite-difference time-domain (FDTD) algorithm," *Microwave and Optical Technology Letters*, vol. 21, pp. 330-333, 1999.

[65] K. M. Krishnaiah and C. J. Railton, "Passive equivalent circuit of FDTD: An application to subgridding," *Electronics Letters*, vol. 33, pp. 1277-1278, 1997.

[66] J. Dedkova and T. Kritz, "FDTD analysis of a nonlinear transmission line," *Progress in Electromagnetics Research Symposium, Beijing, China*, pp. 282-285, 2009.

[67] J. Tang, X. Cui, L. Qi, T. Lu, L. Li, P. Zhu, G. Yang, and W. Zhang, "Analysis of transient inductive interference in underground pipelines due to faults on nearby power lines," *COMPEL: The International Journal for Computation and Mathematics in Electrical and Electronic Engineering*, vol. 26, pp. 1346-1363, 2007.

[68] T. Lu and X. Cui, "Transient analysis of wave processes for multi-conductor transmission lines with branches using FDTD," *IEEE International Symposium on Electromagnetic Compatibility*, vol. 2, pp. 699-703, 2000.

[69] T. Lu, L. Qi, J. Li, and X. Cui, "Application of multi-conductor transmission lines on the transient analysis in power substation," *Asia-Pacific Conference on Environmental Electromagnetics*, pp. 198-201, 2003.

[70] T. Lu, L. Qi, L. Guo, X. Cui, and X. Gu, "Research on experiments and the FDTD Method of multi-conductor transmission lines for transient analysis," *International Symposium on Electromagnetic Compatibility*, vol. 2, pp. 708-712, 2004.

[71] C. Jiao and Y. Sun, "Progress in studies of transients analysis method of multiconductor transmission lines," *Progress in Electromagnetics Research Symposium, Beijing, China*, pp. 249-253, 2009.

[72] J. Dedkova and L. Brancik, "Laplace transform and FDTD approach applied to MTL simulation," *PIERS Online*, vol. 4, pp. 16-20, 2008.

[73] A. J. Pansini, *Power transmission and distribution*, 2nd ed. Georgia: The Fairmont Press Inc., 2005.

[74] G. A. Goulty, *Visual amenity aspects of high voltage transmission*. Somerset, England: Research Studies Press Ltd., 1990.

[75] W. M. Middleton and M. E. V. Valkenburg, *Reference data for engineers: Radio, electronics, computer, and communications*, 9th ed. Boston, 2002.

[76] G. M. Amer, "Novel technique to calculate the effect of electromagnetic field of H.V.T.L. on the metallic pipelines by using EMTP program," *18th International Conference and Exhibition on Electricity Distribution (CIRED), Turin, Italy*, pp. 1-5, 2005.

Chapter 5

Interaction of EM fields to the Human Body Using Hybrid Computational Method

5.1 Introduction

The precise determination of electromagnetic fields within an arbitrary, anisotropy, inhomogeneous dielectric bodies is an important study for researchers exploring the microwaves consequence upon living tissue. The problem related to the penetration of electromagnetic wave upon scatterer is difficult to treat with analytical or numerical technique due to the inability of these methods to deal with the effects curvature, corner and aperture. In addition, a relatively simple geometry is explored in an attempt to gain insight the key penetration mechanisms and to permit prediction of the penetration for more complex problems. The exact solutions for simple dielectric scatterer such as circular cylinder and sphere can be obtained analytically by means of variables separation. On the other hand, numerical technique must be used for complicated dielectric scatterer such as most of human body organs if an accurate model is to be investigated. Nowadays, the environment is irradiated with a vast number of electromagnetic signals which comes from the terrestrial and satellite broadcasting, and the enormous number of mobile phones. Despite the full usage of the transmitted signal, some radiation can cause energy leakage from devices that have no radiation properties due to inadequate shielding and unblocked apertures such as those found in metal masses. The possible hazard of non-ionising electromagnetic radiation has become a concern to the public whether this effect is produced thermally or non-thermally to the living tissue, and if so, whether such effects present a hazard to human health. This question has been asked of every technology that has utilised electromagnetic energy, ranging in frequency from power transmission systems operating at tens of hertz to radar and microwave systems at tens or hundreds of gigahertz. Electromagnetic field is induced inside any biological system such as human body when it is illuminated by an electromagnetic wave. The electromagnetic wave is scattered externally by the body. It is known that the human body is an irregularly shaped heterogeneous conducting medium whose permittivity and conductivity depend on the frequency of the incident wave. In other words, the distribution of the electromagnetic field and the scattered electromagnetic wave depend on the body's physiological parameters and geometry, as well as the polarization and frequency of operation.

In the past, much effort has been put in the study and analysis of the energy absorption of RF induced in the human body by a source of EM radiation such as mobile phone or RFID tag. Abalenkov *et al.* [1] reported the safety assessment of the influence of complex UWB MIMO communication systems which operate close proximity to the human beings and UWB on-body sensors. They proposed a method called Huygens Subgridding (HSG) in one-dimensional, to relate different mesh regions based on the

Huygens-Kirchhoff principle. Antenna performance at 2.4 GHz on the human body was analysed by [2] and its effect on the radio channel characteristics. An efficient numerical technique based on the FDTD technique and the equivalence principle was developed. The equivalence principle was used as an interface between the two computational domains. In addition, there was an effort by [3] to apply parallel FDTD method to provide a simulation environment for subject-specific radio channel modelling in wireless body sensor networks (WBSN). The simulation environment takes into account realistic antenna radiation patterns in channel modelling to analyse their effects on WBSN. An attempt to calculate the electromagnetic fields radiated from an intestine-ingested source in the human body model was originally performed by [4] using the FDTD. The propagation characteristics of the vertically polarized components of the electric fields at the receiving points vertically placed on the model surface were analysed from 100 MHz to 700 MHz frequency range. However, the human body model was simplified by means of homogeneous circular cylinder. Bahillo *et al*. [5] proposed case studies using FDTD to assess the electric field strength errors caused by the presence of the human body on Received Signal Strength (RSS) based localisation schemes in theoretical and experimental approach. The error could reach up to 15 dB in worst case scenario. There was an effort by [6] to use Alternating Direction Implicit FDTD (ADI-FDTD) method to compute induced current densities in the human body due to contact electrodes for human electromuscular devices at frequencies below 200 kHz. Using quasi-static assumptions, discrete Fourier transforms had been used to average the electric field values at the desired frequencies. This study suggests that the ADI-FDTD method can be used for the solution of low-frequency large-scale bioelectromagnetic problems. ADI-FDTD approach was also suggested by [7] to model antenna mounted either in-body or on-body which renders the simulation of Body Area Networks (BAN). The study on human body with wearable devices that includes a receiver on a wall was performed by [8]. Fundamental characteristics were numerically analyzed by using FDTD method. Some work to assess the exposure limit of electromagnetic field generated by wireless devices was done by [9] using FDTD technique. Examples of SAR computations inside the human body were presented and analysed. The computation of SAR was also done by the authors in [10-14]. An attempt has been taken to evaluate the SAR for a full scale homogeneous model of a human body by CST Microwave Studio simulation [15] and by measurement using a computer-controlled scanning system [16]. All documented work pertain to the realisation of FDTD computational space to discretise inhomogeneous anisotropy structure of the human body and the source of EM radiation in Cartesian coordinate system. Perfectly matched layer (PML) was used to circumvent open region difficulties in the FDTD computational domain.

The work reported by [1] applies the advantage of subgridding technique in their design and computational analysis. However, none of the published literature used hybrid MoM-FDTD-SGFDTD in three-dimensional method which paves the way to the state of art of the original contribution of the present research work discussed here. The ultimate advantage of using subgridding over critical regions in the computational space is the ability to visualise the near field deviation in high resolution. The integral equation technique such as Method of Moment is basically well suited for modelling complex type of antenna in free space. In other words, it has the strength in solving PEC structures effectively. MoM is basically a scheme that employs a technique known as the method of weighted residuals. All weighted residual techniques begin by establishing a set of trial solution functions with one or more variable parameters. The residuals are obtained by measuring the difference between the trial and true solution. The variable parameters are determined in a manner that guarantees a best fit of the trial function based on a minimization technique. In contrast, FDTD technique is best outfit for modelling electromagnetic fields inside and outside inhomogeneous media particularly human body. The presence of arbitrary inhomogeneous objects inside FDTD computational domain does not seriously impact on the number of unknowns which must to be determined. The prime advantage of using hybrid approach is the increase in efficiency of the problem solving methodology due to the best attributes offered by different techniques to solve problems that neither technique alone can be modelled precisely.

There are many techniques in the past which has been hybridised with different numerical procedures. An effort to crossbreed Multistructure MoM with Genetic Algorithm (MSMoM-GA) was completed by Arnaud-Cormos *et al*. [17] particularly employed to the bandwidth and the axial ratio optimization of an antenna fed by electromagnetic coupling with a microstrip line. Becker and Hansen [18] published their study on multitemporal resolution (MTR) time domain MoM and time domain geometrical theory of diffraction (GTD) hybridisation which works entirely in the time domain to calculate the transient fields radiated by antennas in the presence of large objects. However, the time-domain MoM is not at the state of maturity and flexibility when compared to the frequency-domain integral technique. The hybridisation of FEM-MoM was advocated by [19] in which its performance rigorously evaluated for far field radiation and scattering patterns of antennas and scatterers. A hybrid time-domain technique in conjunction with the FEM, FDTD and MoM was suggested by Monorchio *et al*. [20] to solve complex electromagnetic problems by means of the time-domain version of the solution to couple the methods. A hybrid MoM-FDTD computational electromagnetics formulation for simulation of antennas coupled to lossy and dielectric volumes was studied by Abd-Alhameed *et al*. [21] in which the coupling of multiple regions was investigated and applied to complex antenna structures. The work was extended to include a broadband antenna response using the hybrid method [22]. A similar technique was also proposed by [23] to predict human body exposure to the near field of a mobile communication device such as 900 MHz half wavelength dipole antenna, [24] to handle large multiscale structures such as an antenna placed on the top of large ship and the recently [25] to predict the current distribution and radiation pattern for HF antenna located above heterogeneous ground.

In this area of research, the interaction between RFID antenna and human body particularly the chest, tummy and back part is investigated and analysed. The antenna is assumed to be operating at 900 MHz. The near field and far field exposure of the antenna is investigated, with the antenna mounted on different locations of the human body. The distributions of radiated and absorbed power are computed for the antenna in the various locations, and with different polarizations. Moreover, the radiation efficiency and the ratio of the absorbed power over radiated power of the antenna operating in proximity to the human body are inferred; the cumulative distribution function (CDF) of the radiation efficiency and the ratio of the absorbed power over radiated power for these locations are also evaluated.

5.2 Modified Total/Scattered Field Formulation

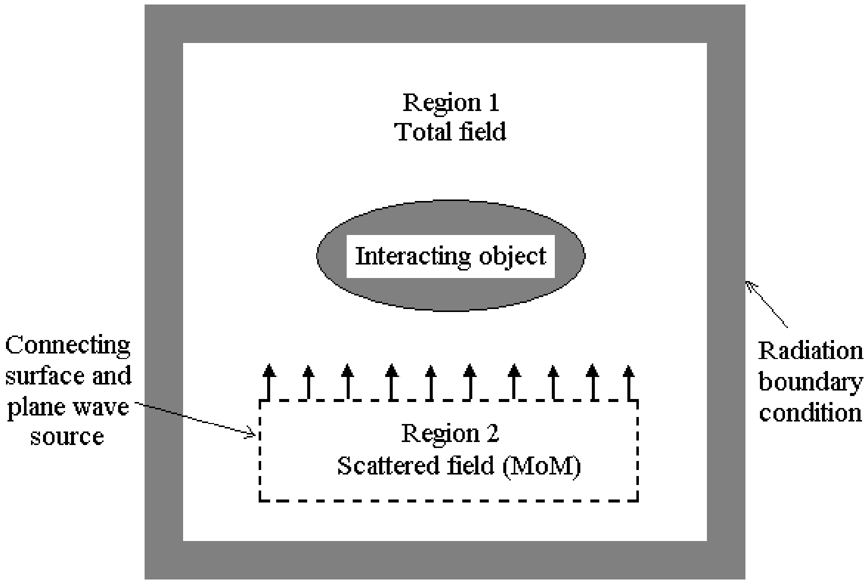

Figure 5.1: Overview of the modified total and scattered field region for hybrid method.

Plane wave characterisation by the total/scattered field formulation, as reviewed in Chapter 2 section 2.4.2.2 represented by the equations (2.41) to (2.64) is implemented to the hybrid method in order to simulate the MoM-modelled antenna near field excitation into the FDTD computational domain. Instead of the known calculated plane wave incident electric field E_{inc} and incident magnetic field H_{inc} obtained from the look-up table and linear interpolation in those equations, the MoM calculated near field values of E_{MoM} and H_{MoM} are substituted to the five faces of the rectangular equivalent surface. This is mainly due to one of the surface is the finite ground plane in which the E-field is zero. This was discussed and implemented using the differential method in Chapter 2 section 2.4.2. A modified total/scattered field formulation is used to exchange the scattered and total field regions as illustrated in Figure 5.1. In this case, the field inside and outside the Huygens surface are considered to be the scattered field and the total field region respectively. The hybrid formulation is only suitable if the size of the source is smaller than the size of the scatterer. Before proceeding, the updating equations (2.37) to (2.40) for 1-D discussed in Chapter 2 section 2.4.2.1 can be modified with two different boundary treatments discussed hereafter.

5.2.1 Outside *H* Surface Method

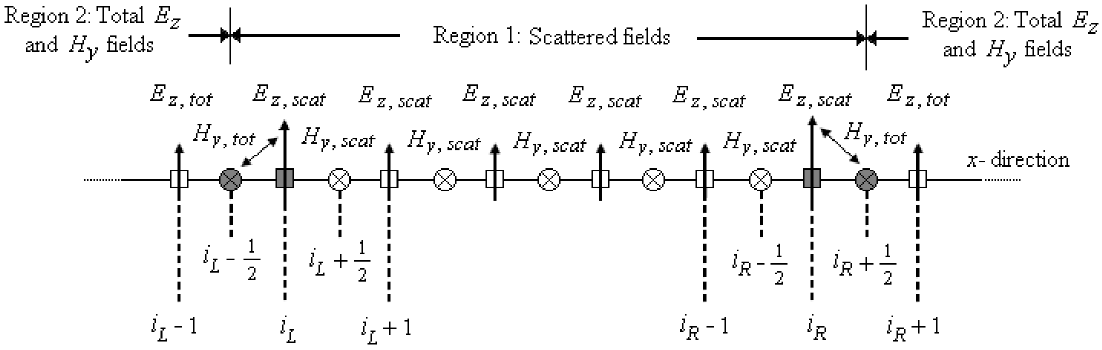

Figure 5.2: Modified total and scattered field components for one-dimensional FDTD hybrid method (outside *H* surface method).

$$E_z\Big|_{scat,i_L}^{n+1} = E_z\Big|_{scat,i_L}^{n} + \frac{\Delta t}{\varepsilon_o \Delta}\left(H_y\Big|_{scat,i_L+1/2}^{n+1/2} - H_y\Big|_{tot,i_L-1/2}^{n+1/2} \right) + \frac{\Delta t}{\varepsilon_o \Delta} H_y\Big|_{MoM,i_L-1/2}^{n+1/2} \qquad (5.1)$$

$$H_y\Big|_{tot,i_L-1/2}^{n+1/2} = H_y\Big|_{tot,i_L-1/2}^{n-1/2} + \frac{\Delta t}{\mu_o \Delta}\left(E_z\Big|_{scat,i_L}^{n} - E_z\Big|_{tot,i_L-1}^{n} \right) + \frac{\Delta t}{\mu_o \Delta} E_z\Big|_{MoM,i_L}^{n} \qquad (5.2)$$

$$E_z\Big|_{tot,i_R}^{n+1} = E_z\Big|_{tot,i_R}^{n} + \frac{\Delta t}{\varepsilon_o \Delta}\left(H_y\Big|_{scat,i_R+1/2}^{n+1/2} - H_y\Big|_{tot,i_R-1/2}^{n+1/2} \right) - \frac{\Delta t}{\varepsilon_o \Delta} H_y\Big|_{MoM,i_R+1/2}^{n+1/2} \qquad (5.3)$$

$$H_y\Big|^{n+1/2}_{scat,i_R+1/2} = H_y\Big|^{n-1/2}_{scat,i_R+1/2} + \frac{\Delta t}{\mu_o \Delta}\left(E_z\Big|^{n}_{tot,i_R+1} - E_z\Big|^{n}_{tot,i_R}\right) - \frac{\Delta t}{\mu_o \Delta} E_z\Big|^{n}_{MoM,i_R} \qquad (5.4)$$

It should be noted that for one-dimensional case, the surface of the special *H* field components (surface electric current *J*) is situated at the outside of the FDTD Huygens surface grids and the boundary of the total/scattered field regions is H_y components as shown by the grey-coloured fields in Figure 5.2.

5.2.2 Inside *H* Surface Method

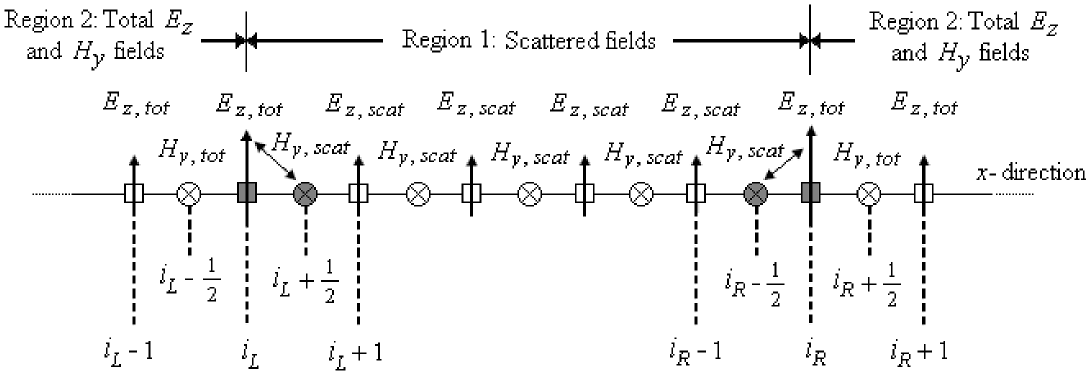

Figure 5.3: Modified total and scattered field components for one-dimensional FDTD hybrid method (inside *H* surface method).

$$E_z\Big|^{n+1}_{tot,i_L} = E_z\Big|^{n}_{tot,i_L} + \frac{\Delta t}{\varepsilon_o \Delta}\left(H_y\Big|^{n+1/2}_{scat,i_L+1/2} - H_y\Big|^{n+1/2}_{tot,i_L-1/2}\right) + \frac{\Delta t}{\varepsilon_o \Delta} H_y\Big|^{n+1/2}_{MoM,i_L+1/2} \qquad (5.5)$$

$$H_y\Big|^{n+1/2}_{scat,i_L+1/2} = H_y\Big|^{n-1/2}_{scat,i_L+1/2} + \frac{\Delta t}{\mu_o \Delta}\left(E_z\Big|^{n}_{scat,i_L+1} - E_z\Big|^{n}_{tot,i_L}\right) + \frac{\Delta t}{\mu_o \Delta} E_z\Big|^{n}_{MoM,i_L} \qquad (5.6)$$

$$E_z\Big|_{tot,i_R}^{n+1} = E_z\Big|_{tot,i_R}^{n} + \frac{\Delta t}{\varepsilon_o \Delta}\left(H_y\Big|_{tot,i_R+1/2}^{n+1/2} - H_y\Big|_{scat,i_R-1/2}^{n+1/2} \right) - \frac{\Delta t}{\varepsilon_o \Delta} H_y\Big|_{MoM,i_R-1/2}^{n+1/2} \tag{5.7}$$

$$H_y\Big|_{scat,i_R-1/2}^{n+1/2} = H_y\Big|_{scat,i_R-1/2}^{n-1/2} + \frac{\Delta t}{\mu_o \Delta}\left(E_z\Big|_{scat,i_R}^{n} - E_z\Big|_{tot,i_R-1}^{n} \right) - \frac{\Delta t}{\mu_o \Delta} E_z\Big|_{MoM,i_R}^{n} \tag{5.8}$$

It should be noted that for one-dimensional case, the surface of the special *H* field components (surface electric current *J*) is situated at the inside of the FDTD Huygens surface grids and the boundary of the total/scattered field regions is E_z components as shown by the grey-coloured fields in Figure 5.3.

5.2.3 Boundary Field Components Update Equation in 3-D

The modified total/scattered field formulation for three-dimensional case used in the hybrid computational code is as the same as equations (2.41) to (2.64) but with changes in the sign for incident field components, when referring to the one-dimensional reassessed in Chapter 2 section 2.4.2.2. For the case of outside *H* surface method, equations (2.41) to (2.42) for *E* field components and equations (2.53) to (2.54) for *H* field components can be rewritten as follows. For instance, consider only face i_o as shown in Figure 2.9 (Chapter 2), E_y ($i = i_o$; $j = j_o + ½, \ldots, j_1 - ½$; $k = k_o, \ldots, k_1$) is given by:

$$E_y\Big|_{i_0,j,k}^{n+1} = \{E_y\Big|_{i_0,j,k}^{n+1}\}_{(2.25)} - C_{b,E_y}\Big|_{i_0,j,k} H_{z,MoM}\Big|_{i_0-1/2,j,k}^{n+1/2} \tag{5.9}$$

E_z $(i = i_o;\ j = j_o, \ldots, j_1;\ k = k_o + ½, \ldots, k_1 - ½)$ is given by:

$$E_z\Big|^{n+1}_{i_0,j,k} = \{E_z\Big|^{n+1}_{i_0,j,k}\}_{(2.26)} + C_{b,E_z}\Big|_{i_0,j,k} H_{y,MoM}\Big|^{n+1/2}_{i_0-1/2,j,k} \tag{5.10}$$

H_y $(i = i_o - ½;\ j = j_o, \ldots, j_1;\ k = k_o + ½, \ldots, k_1 - ½)$ is given by:

$$H_y\Big|^{n+1/2}_{i_0-1/2,j,k} = \{H_y\Big|^{n+1/2}_{i_0-1/2,j,k}\}_{(2.22)} + D_{b,H_y}\Big|_{i_0-1/2,j,k} E_{z,MoM}\Big|^{n}_{i_0,j,k} \tag{5.11}$$

H_z $(i = i_o - ½;\ j = j_o + ½, \ldots, j_1 - ½;\ k = k_o, \ldots, k_1)$ is given by:

$$H_z\Big|^{n+1/2}_{i_0-1/2,j,k} = \{H_z\Big|^{n+1/2}_{i_0-1/2,j,k}\}_{(2.23)} - D_{b,H_z}\Big|_{i_0-1/2,j,k} E_{y,MoM}\Big|^{n}_{i_0,j,k} \tag{5.12}$$

The same changes are also applied to equations (2.43) to (2.52) and equations (2.55) to (2.64) for E and H field components respectively. For the case of inside H surface method, those equations can be rewritten in the following forms:

E_y $(i = i_o;\ j = j_o + ½, \ldots, j_1 - ½;\ k = k_o, \ldots, k_1)$ is given by:

$$E_y\Big|^{n+1}_{i_0,j,k} = \{E_y\Big|^{n+1}_{i_0,j,k}\}_{(2.25)} - C_{b,E_y}\Big|_{i_0,j,k} H_{z,MoM}\Big|^{n+1/2}_{i_0+1/2,j,k} \tag{5.13}$$

E_z $(i = i_o;\ j = j_o, \ldots, j_1;\ k = k_o + ½, \ldots, k_1 - ½)$ is given by:

$$E_z\Big|_{i_0,j,k}^{n+1} = \{E_z\Big|_{i_0,j,k}^{n+1}\}_{(2.26)} + C_{b,E_z}\Big|_{i_0,j,k} H_{y,MoM}\Big|_{i_0+1/2,j,k}^{n+1/2} \tag{5.14}$$

H_y ($i = i_o + ½$; $j = j_o, \ldots, j_1$; $k = k_o + ½, \ldots, k_1 - ½$) is given by:

$$H_y\Big|_{i_0+1/2,j,k}^{n+1/2} = \{H_y\Big|_{i_0+1/2,j,k}^{n+1/2}\}_{(2.22)} + D_{b,H_y}\Big|_{i_0+1/2,j,k} E_{z,MoM}\Big|_{i_0,j,k}^{n} \tag{5.15}$$

H_z ($i = i_o + ½$; $j = j_o + ½, \ldots, j_1 - ½$; $k = k_o, \ldots, k_1$) is given by:

$$H_z\Big|_{i_0+1/2,j,k}^{n+1/2} = \{H_z\Big|_{i_0+1/2,j,k}^{n+1/2}\}_{(2.23)} - D_{b,H_z}\Big|_{i_0+1/2,j,k} E_{y,MoM}\Big|_{i_0,j,k}^{n} \tag{5.16}$$

The similar treatment is also implemented at the other five faces of the cubic FDTD cell related equations. Consider the geometry illustrated in Figure 5.1 for hybrid arrangement, a change of sign must be applied on the right hand part of equations (5.9) to (5.12) together with the other five faces of the cubic cell.

5.3 Hybrid MoM-FDTD-SGFDTD Theoretical Formulation

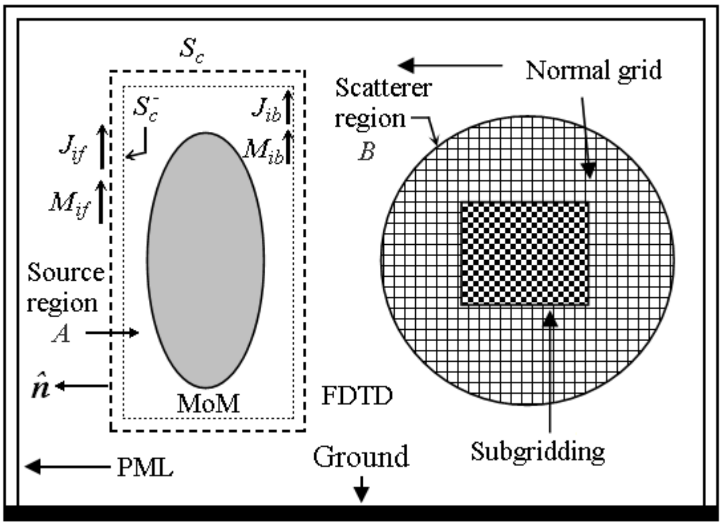

Figure 5.4: Hybrid MoM-FDTD-SGFDTD configuration for the single source and scatterer geometries.

Consider the electromagnetic hybrid geometry illustrated in Figure 5.4. The figure depicts two regions, one representing the source in region *A*, and the other the scatterer in region *B*. The source region is bounded by a closed Huygens surface S_c. The method starts by computing the fields due to the real currents of the source region on the surface S_c, excluding the scatterer region *B*. These fields are computed by applying Galerkin's method with a set of variable polynomial basis functions [26]. The equivalent surface currents on the surface S_c represent the outward travelling wave-fields from the source to the scatterer, due to the fields of the source. These may be expressed as:

$$J_{if} = \hat{n} \times H_{if} \tag{5.17}$$

$$M_{if} = E_{if} \times \hat{n} \tag{5.18}$$

$\hat{n}$ is the outwardly directed unit vector normal to the surface from the source region. H_{if} and E_{if} are the equivalent forward scattered magnetic and electric fields respectively from the source region on the equivalent surface S_c. J_{if} and M_{if} are the corresponding electric and magnetic source currents on the surface S_c respectively. These currents are hence treated as the source in the FDTD computational province, propagating fields to the scatterer by using the E and H curl equations given by the expression:

$$\nabla \times E = -\frac{\partial B}{\partial t} - M_{if} \tag{5.19}$$

$$\nabla \times H = -\frac{\partial D}{\partial t} + J_{if} \tag{5.20}$$

The FDTD updating equations for the field components are expanded with a three-dimensional modified total/scattered FDTD formulation for the special components on the Huygens surface as reviewed in section 5.2.3, while the rest of the spatial field components follow the normal updating equations. The back-scattered fields were computed by FDTD at S_c^- (the closed surface interior to the surface S_c and bounding the region A). This surface is closed in the scattered field region, so that the calculated surface currents are due to the scattered field only. The equivalent surface currents due to these fields, representing an additional source to the MoM domain (region A), are given by:

$$J_{ib} = H_{ib} \times \hat{n} \tag{5.21}$$

$$M_{ib} = \hat{n} \times E_{ib} \tag{5.22}$$

where H_{ib} and E_{ib} are the back-scattered fields computed at S_c^-. Note that $\hat{n}$ is as above, directed outwards from the source region. J_{ib} and M_{ib} are the electric and magnetic equivalent surface currents at S_c^-. Now, the voltage back scattered (the excitation for the MoM) on the source region can be evaluated using either of the following equations, defined by reciprocity theorem in the same way as in [26]:

$$V_b = \iint_{S_a} dS_a (J_{ms} \cdot E_{ib}) \tag{5.23}$$

$$V_b = \left\langle J_{ib} \cdot E_{ms} - M_{ib} \cdot H_{ms}, dS_c^- \right\rangle \tag{5.24}$$

$$V_b = \iint_{S_c^-} dS_c^- (J_{ib} \cdot E_{ms} - M_{ib} \cdot H_{ms}) \tag{5.25}$$

where

$$E_{ib} = -j\omega A(r) - \nabla V(r) - \frac{1}{\varepsilon} \nabla \times F(r) \tag{5.26}$$

$$A(r) = \mu \iint_{S_c^-} dS_c^- \left\{ J_{ib} G(r, r') \right\} \tag{5.27}$$

$$V(r) = -\frac{j}{\omega\varepsilon} \iint_{S_c^-} dS_c^- \left\{ \nabla_s' \cdot J_{ib} G(r, r') \right\} \tag{5.28}$$

$$F(r) = \varepsilon \iint_{S_c^-} dS_c^- \left\{ M_{ib} G(r, r') \right\} \tag{5.29}$$

$G(r,r')$ is the free space Green function. It is given by the expression:

$$G(r, r') = \frac{e^{-jk|r-r'|}}{|r - r'|} \tag{5.30}$$

The vectors r and r' apply to the source and observation points respectively and S_a is the conducting surface area of the structure within region A. J_{ms} is the electric test function used on the wire. E_{ms} and H_{ms} are the electric and magnetic fields respectively for the test function J_{ms}. Equation (5.23) explicitly requires a double integral to evaluate E_{ib} and integrate over the surface on the antenna; assuming that the FDTD discretisation is very small compared to the operating wavelength. In this case, equation (5.23) can be reduced by ignoring the surface integral and evaluating the voltage back-scattered corresponding to the centre of the cell surface, by a summation over grid cell surfaces, to get the following equation for the hybrid case:

$$V_b = \sum_{k=1}^{n_{S_c^-}} (J_{ib_k} \cdot E_{ms}(r_k, r') - M_{ib_k} \cdot H_{ms}(r_k, r'))a_k \tag{5.31}$$

where r_k is the position vector of the centre of the cell surface and a_k is the surface area of the cell surface. Therefore J_{ib_k} and M_{ib_k} are considered to be the equivalent surface currents at the centre of the surface cell n. Since the excitation voltages are known, the MoM can be executed to compute the new currents and the procedure can be repeated until the steady state solution is reached.

5.4 Development of the Antenna

The antenna adopted in this research has been previously described by the authors in [27]. The antenna structure is composed of two strips having multiple but equal meanders, where the horizontal lines control the radiation resistance and the vertical lines acts as storage of electric energy and loss resistance. It is basically a simple planar meander-line tag antenna for RFID application at 900 MHz UHF band designed and optimized using genetic algorithms (GA). The antenna dimensions are optimized and evaluated using GA in collaboration with NEC source code [28] with good efficiency, and maintain performance when held in proximity with the human body. Figure 5.5 and 5.6 depict the geometry of the antenna for linear horizontal and vertical polarisation respectively.

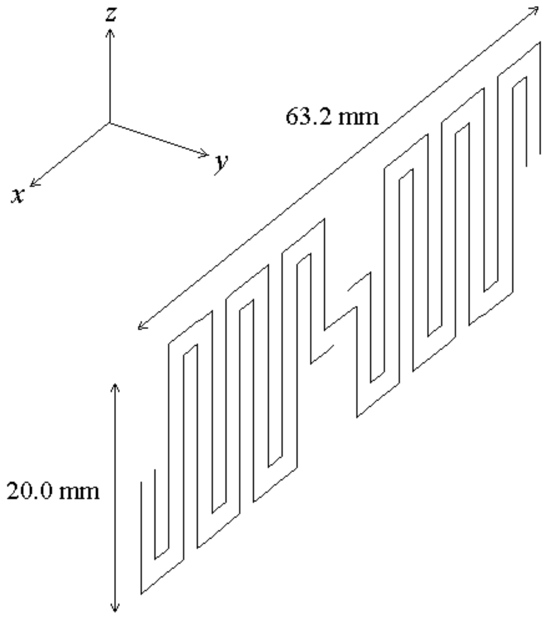

Figure 5.5: Antenna geometry for linear horizontal polarisation.

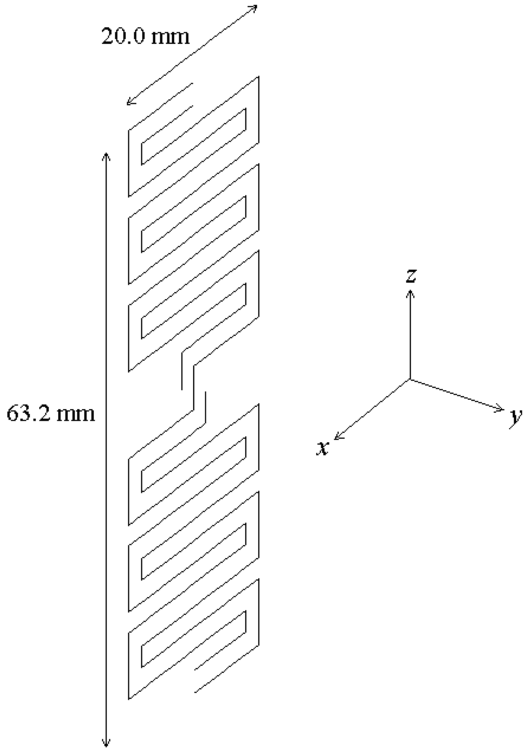

Figure 5.6: Antenna geometry for linear vertical polarisation.

5.5 Hybrid Model Technique

The operation begins by introducing a Huygens surface around the proposed antenna as illustrated in Figure 5.7 and 5.8 for linear horizontal and vertical polarisation respectively. The equivalent electric and magnetic source on the Huygens surface are produced at each time step from the electric and magnetic fields created by the antenna in free space using NEC [28]. This field data is used as an input source for the FDTD code. The overall FDTD spatial volume is 118 × 77 × 327. The Huygens box is set with volume of 16 × 4 × 10 and 10 × 4 × 16 FDTD cells for horizontal and vertical polarisation as illustrated in Figure 5.7 and 5.8 respectively. The FDTD method is applied over the entire computational domain. The equivalence principle is carried out in 3-D by applying the hybrid electromagnetic method described in section 5.2.3 with cell size $dx = dy = dz = 6.0$ mm and $dx = dy = dz = 3.0$ mm for the coarse and fine FDTD lattice respectively. The time step is set at 7.0 ps. A 6 cell PML is used to terminate the FDTD space, and the distance between the antenna Huygens surface box and human body is 12.0 mm (2 cells). The simulation parameters are summarised in Table 5.1. The human body model used in this study is known as the “visible man”, the tissue-classified numerical model for which was previously developed at Brooks Air Force Base, San Antonio, Texas, USA [29].

Table 5.1: Simulation parameters.

Formulation	Horizontal	Vertical
FDTD spatial resolution	118 × 77 × 327	118 × 77 × 327
Huygens surface box spatial resolution	16 × 4 × 10	10 × 4 × 16
Subgrid spatial resolution	10 × 10 × 10	10 × 10 × 10
Number of FDTD PML cells	6	6
Coarse grid cell size	6.0 mm	6.0 mm
Fine grid cell size	3.0 mm	3.0 mm
Time step	7.0 ps	7.0 ps
Operating frequency	900 MHz	900 MHz
Distance between the antenna Huygens surface box and human body	12.0 mm	12.0 mm
Distance between the antenna and subgrid FDTD boundary	30.0 mm	30.0 mm

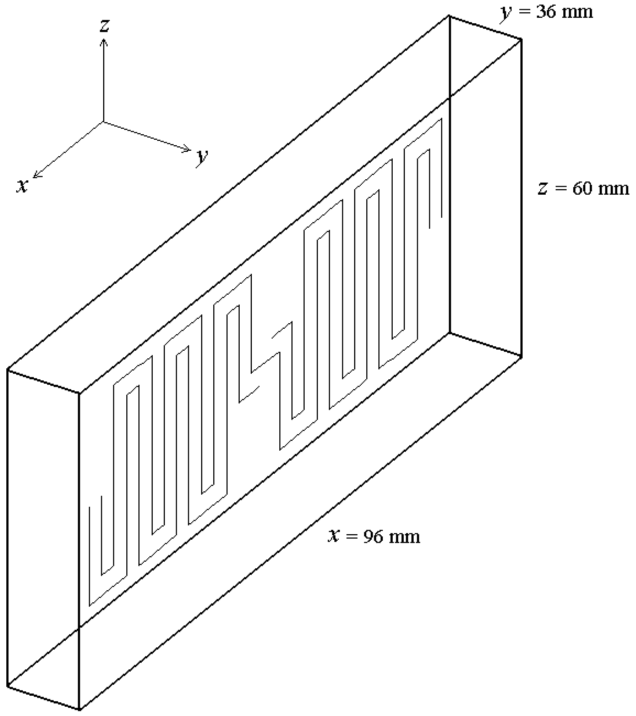

Figure 5.7: Equivalent Huygens surface enclosing the antenna for linear horizontal polarisation.

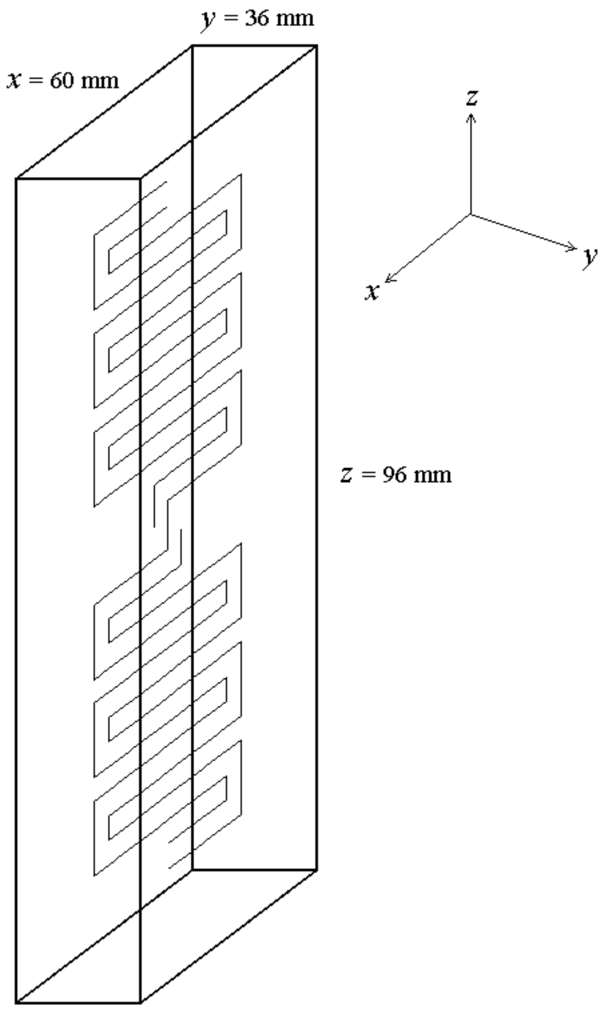

Figure 5.8: Equivalent Huygens surface enclosing the antenna for linear vertical polarisation.

5.5.1 Near Field and Far Field Simulation

The near and far field radiation of the antenna at 900 MHz for different locations has been analysed, in order to investigate the performance of the antenna in proximity to the human body. As shown in Figure 5.9, a total of 32 locations were investigated; 16 locations on the back, and 16 on the front, were taken.

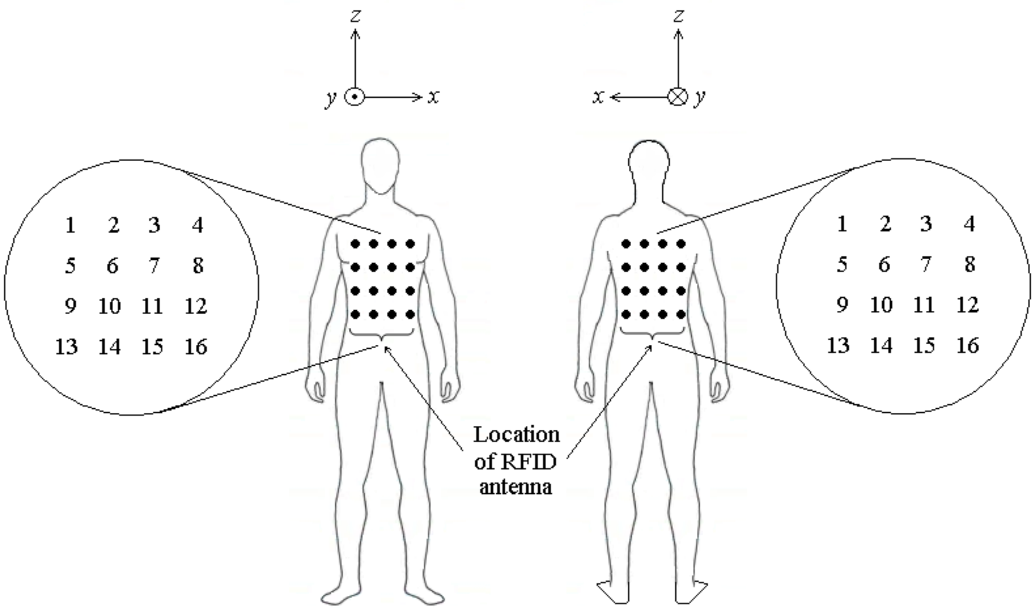

Figure 5.9: The location of the antenna in proximity to the human body represented by the black dots.

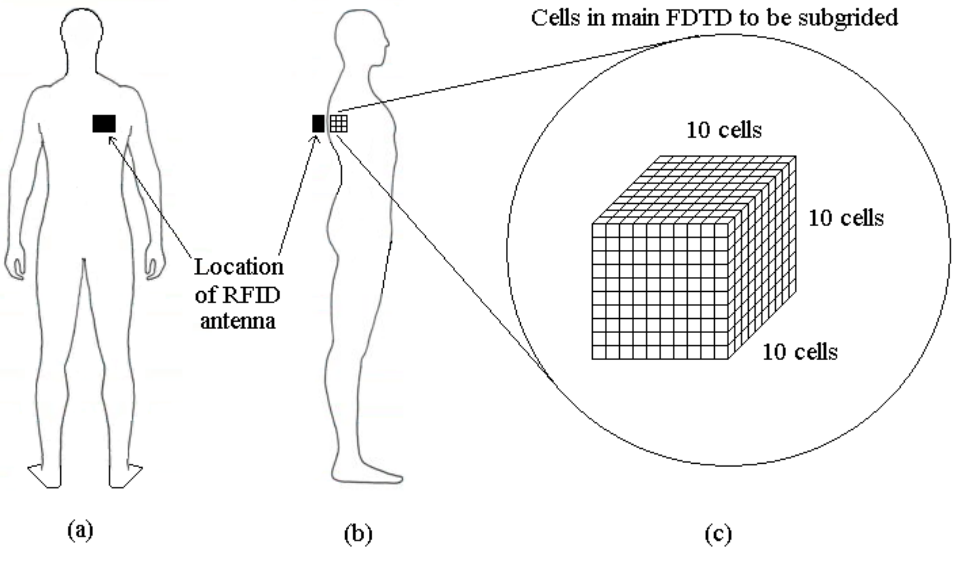

Figure 5.10: The antenna is located at the back of the human. Subgrid cells of 10 × 10 × 10 FDTD cells are taken inside the human body.

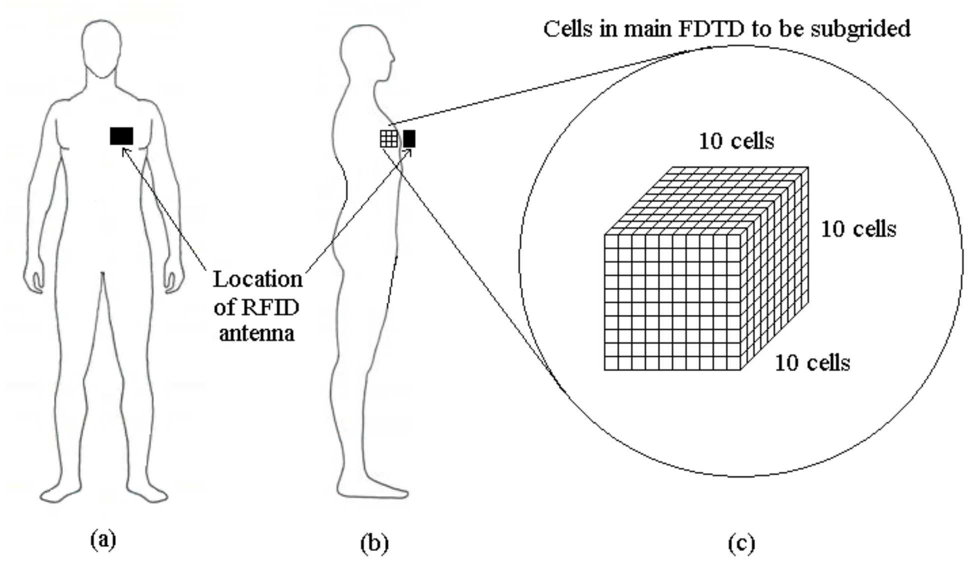

Figure 5.11: The antenna is located in front of the human. Subgrid cells of 10 × 10 × 10 FDTD cells are taken inside the human body.

Figure 5.10 and 5.11 show the location of the antenna at the back and in front of the human body respectively. In this case, subgrid cells of 10 × 10 × 10 FDTD cells were taken inside the human body for near field analysis. The fields between the coarse and fine grids were generally unknown in nature. The missing fields could be determined by means of interpolation. This has been discussed in Chapter 4 section 4.7.

The following example was chosen to validate the method accuracy [30]. A 900 MHz centre-fed half-wavelength dipole of 0.0025λ radius was considered as a transmitter source that represents as example the RFID reader, whereas the RFID tag was considered as a small half-wavelength meander antenna, as shown in Figure 5.12. The tag was designed in a zig-zag pattern with 17 turns in which subgridding cells of 6 × 6 × 6 volumetric were imposed. Two different distances between the source and the tag were studied and discussed.

Table 5.2: Input parameters for hybrid method validation.

Formulation	**Far field**	**Near field**
FDTD problem space	32×43×43	17×17×18
Huygens surface in the main grid	14×14×22	8×6×16
FDTD volume in length (cm)	38.4×51.6×51.6 cm	20×20×22 cm
FDTD cell size and time step	12 mm, 16.8 ps	12 mm, 16.8 ps
PML layers in cells	8×8×8	8×8×8
Subgridding cells	6×6×6	6×6×6
Subgridding FDTD cell size and time step	2 mm, 2.8 ps	2 mm, 2.8 ps
Operating frequency	900 MHz	900 MHz
D_t: distance between the centres of transmitter and the sensor.	16.8 cm (for Fig. 5.13), 33.6 cm (for Fig. 5.15)	16.8 cm (for Figs. 5.13 and 5.14)
D_f: distance between the centre of the sensor to the subgridding FDTD boundary	36 mm	36 mm

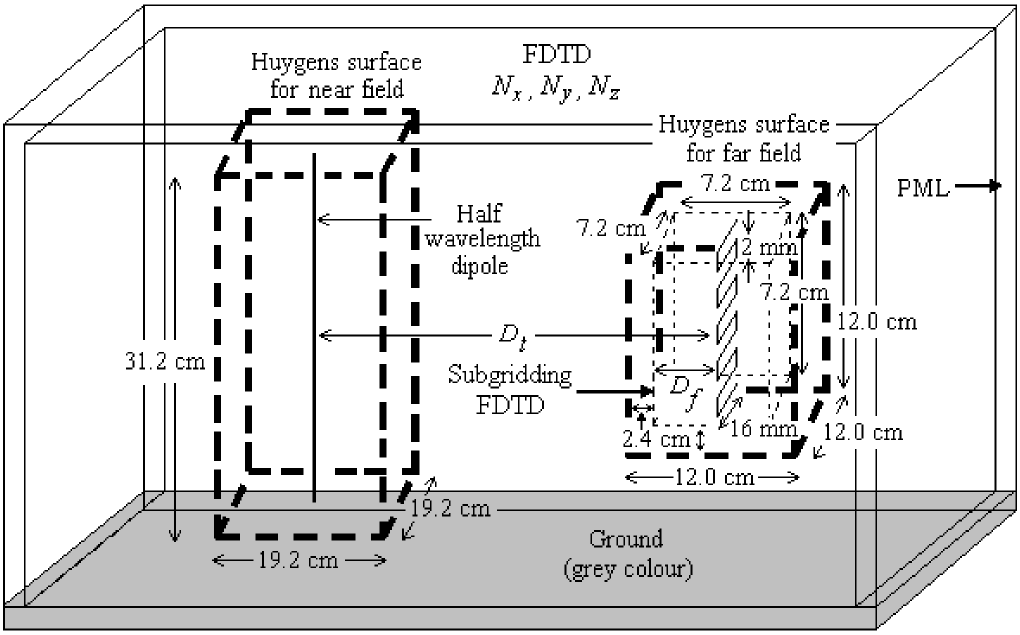

Figure 5.12: A basic geometry of FDTD-SGFDTD for near and far fields validation.

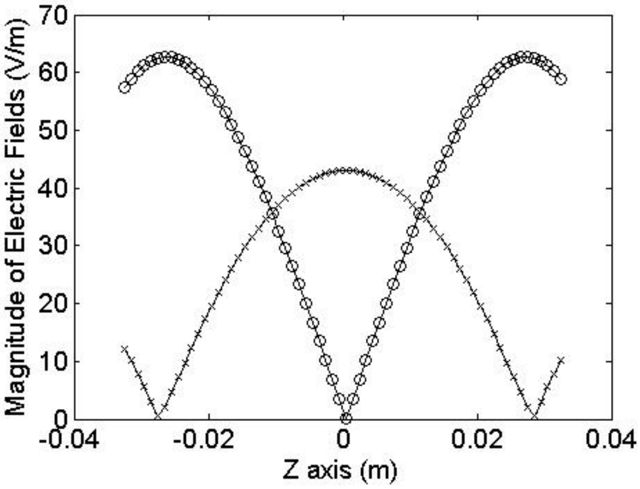

Figure 5.13: Magnitude of E_y and E_z electric field components along z axis at y=7.2 cm: Near field E_y (‘ooo’), E_z (‘xxx’), Far field E_y and E_z (‘——’).

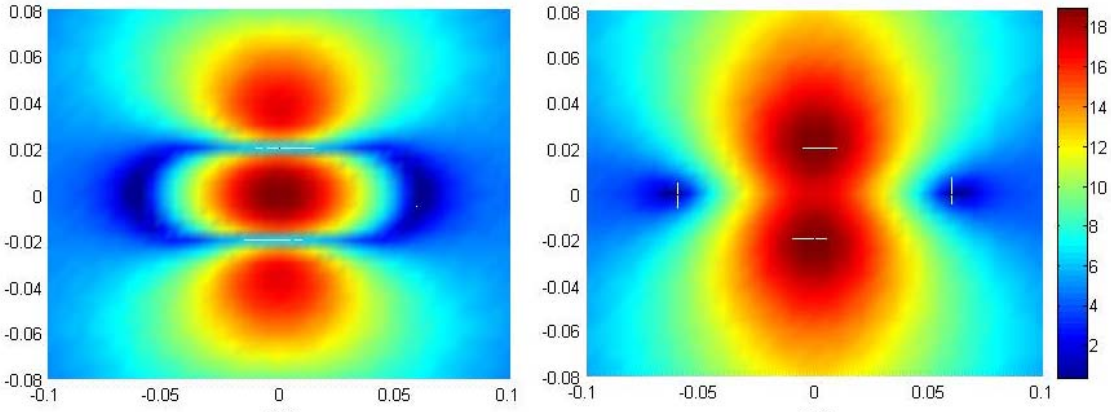

(a) (b)

Figure 5.14: Distribution of the E_z and E_{total} field components in dBs at 7.2 cm away from the sensor using near field method: (a) E_z, (b) E_{total}.

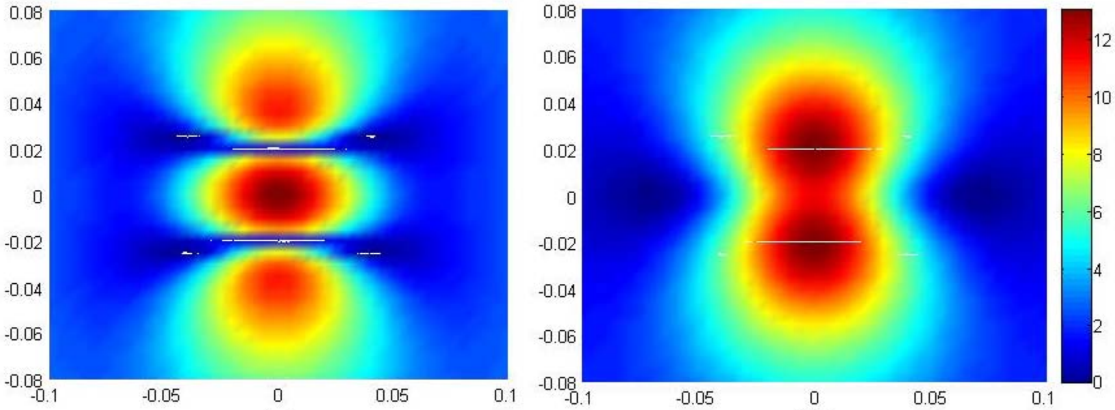

(a) (b)

Figure 5.15: Distribution of the E_z and E_{total} field components in dBs at 7.2 cm away from the sensor using far field method: (a) E_z, (b) E_{total}.

Two separate simulations were undertaken for each case, one with the far field application and other with near field application. The parameters used are summarized in Table 5.2. It should be noted that the centres of the source and the sensor were placed on the y axis and they are separated by the distance D_t (see Figure 5.12). For both simulations, a thin wire subroutine code inside the subgridded FDTD was used to include the effects of the wire radius of the meander antenna inside the new FDTD subgrid. In this example, for simplicity, the medium surrounding the source and the scatterer was considered as free space; however, the scatterer can be placed on dielectric objects in which part of its volume can be subgridded. A sinusoidal excitation voltage was applied at the centre of the antenna source. The antenna wires were assumed to be perfectly conducting. The magnitude of E_y electric field components along z axis at y = 7.2 cm were compared between near and far fields simulation. Both agreed well as shown in Figure 5.13. The E_z components were also assessed and found to be identical with each other (see Figure 5.13). The field distribution over an x-z plane 7.2 cm distant from the sensor for near field and far field techniques is shown in Figures 5.14 and 5.15

respectively. The plane size considered here was 20 cm × 16 cm for x and z axes respectively. The far field and near field techniques were checked for comparisons of one antenna geometry i.e. D_t was fixed to 16.8 cm for both techniques, the fields were found identical to the one shown in Figure 5.14. Both methods show a good stability and the results were convergent within four iterations. However, the total field components was found ±2% when compared to results computed using NEC software.

Subgrid technique was validated by illustrating example in two cases. Case 1 was considered when the observed field was located inside subgrid area with two conditions: (a) Without subgrid, and (b) With subgrid, as shown in Figure 5.16. Case 2 was considered when the observed field was located outside subgrid area with two conditions: (a) Without subgrid, and (b) With subgrid, as depicted in Figure 5.17. The problem space was excited by RFID antenna at 900 MHz. The electric fields at the same point for case 1 and case 2 were observed and compared as illustrated in Figures 5.18 and 5.19 respectively. The magnetic fields at the same point for case 1 and case 2 were also observed and compared as illustrated in Figures 5.20 and 5.21 respectively.

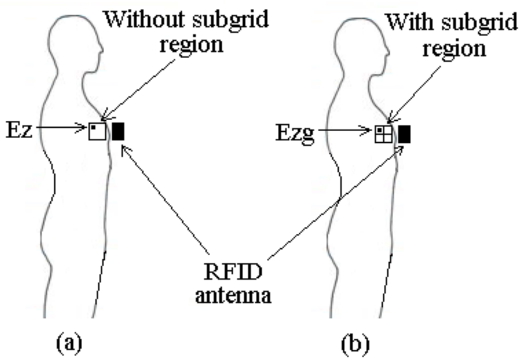

Figure 5.16: Case 1: The observed field was located inside subgrid area: (a) Without subgrid, (b) With subgrid.

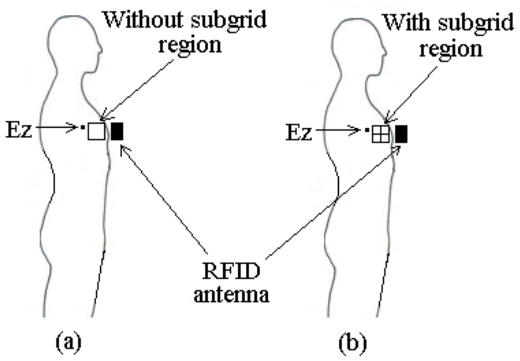

Figure 5.17: Case 2: The observed field was located outside subgrid area: (a) Without subgrid, (b) With subgrid.

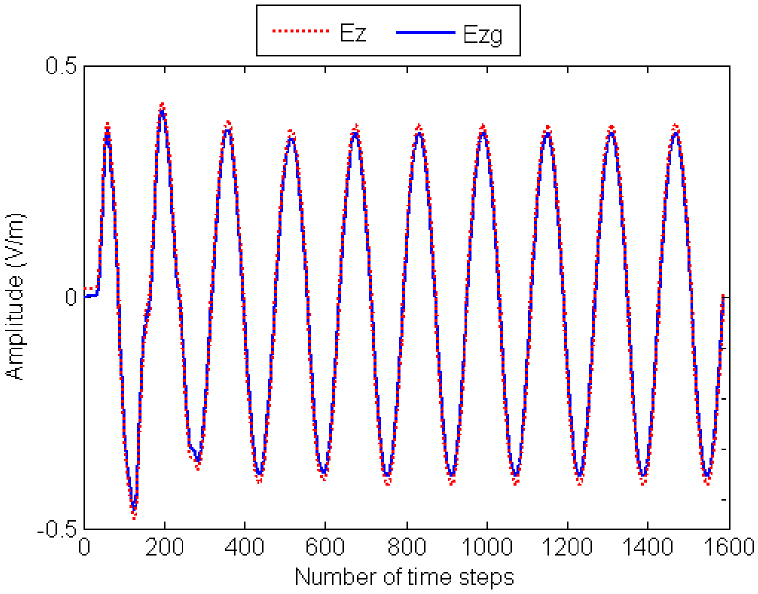

Figure 5.18: Case 1: The electric field in subgrid region (E_{zg}) and at normal grid (E_z).

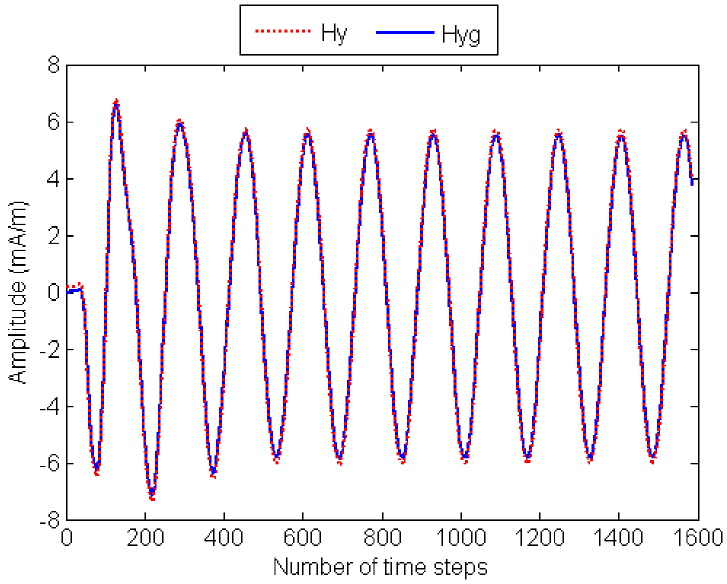

Figure 5.19: Case 1: The magnetic field in subgrid region (H_{yg}) and at normal grid (H_y).

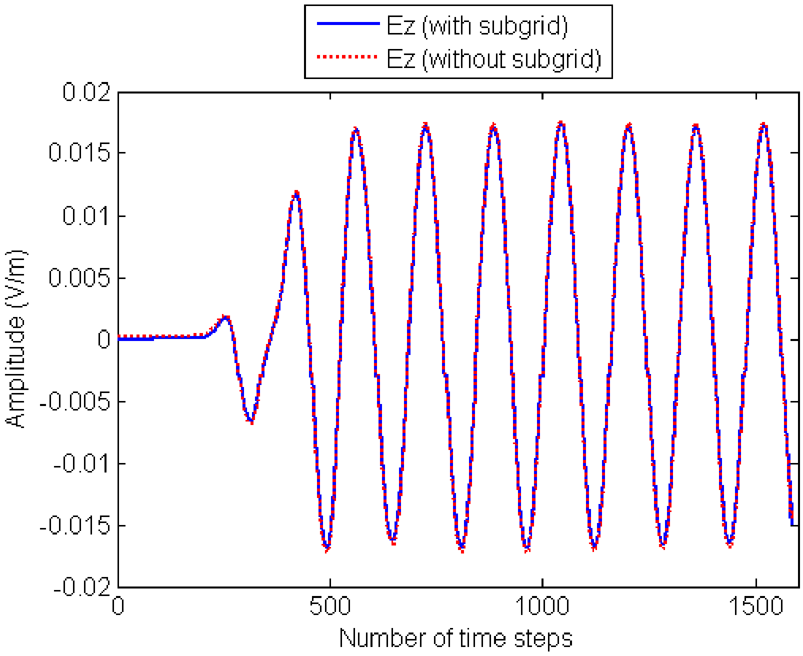

Figure 5.20: Case 2: The electric field E_z with and without subgrid.

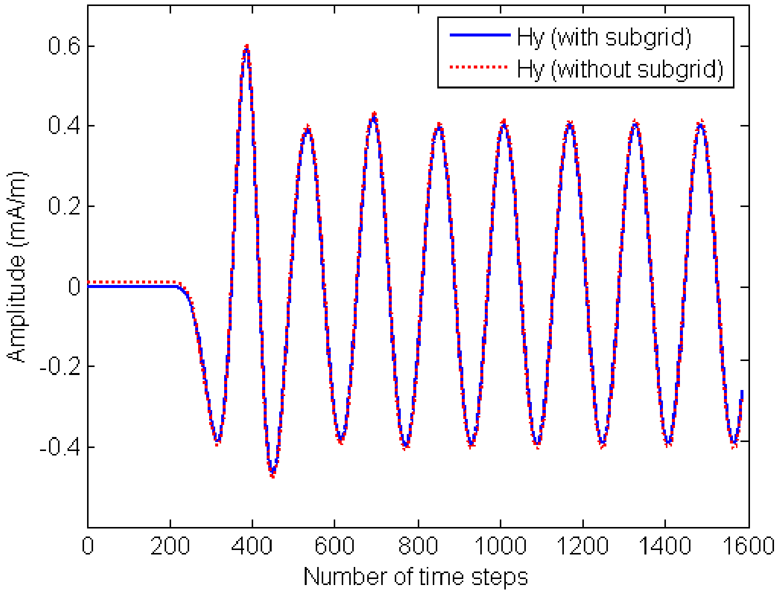

Figure 5.21: Case 2: The magnetic field H_y with and without subgrid.

The electric fields in subgrid region (E_{zg}) and at normal grid (E_z) for case 1 were found to be identical to each other to confirm the proof of concept. The electric fields E_z with and without subgrid for case 2 were also found to be identical to each other. A similar explanation also applies for the magnetic fields for both case 1 and 2.

Table 5.3 shows the electrical properties of different type of human tissues at 900 MHz. Figure 5.22 depicts the human body model at *xz* plane (front view) with different tissue at different cross-section of $y = 35$, $y = 47$ and $y = 55$. Figure 5.23 illustrates the human body model at *yz* plane (side view from left of the human to the right) with different tissue at different cross-section of $x = 43$, $x = 67$ and $x = 92$. Figure 5.24 shows the human body model at *xy* plane (top view) with different tissue at different cross-section of $z = 14$, $z = 67$ and $z = 150$. Similarly, Figure 5.25 shows the human body model at *xy* plane but at different cross-section of $z = 205$, $z = 247$ and $z = 300$. For the sake of simplicity, only 3 positions of the results will be shown in the following text. Figures 5.26 to 5.28 show the component inside the human body at subgrid region at position 1, 2 and 3 (front side). Figures 5.29 to 5.31 show the component inside the human body at subgrid region at position 1, 2 and 3 (back side). The electric field distributions in this section are plotted in dB scale. Figures 5.32, 5.34 and 5.36 illustrate the electric field distribution for horizontal polarised antenna placed at the front of the human from position 1 to position 3. Figures 5.33, 5.35 and 5.37 describe the electric field distribution in subgrid region for horizontal polarised antenna placed at the front of the human body from position 1 to position 3. Figures 5.38, 5.40 and 5.42 illustrate the electric field distribution for horizontal polarised antenna placed at the back of the human from position 1 to position 3. Figures 5.95, 5.41 and 5.43 describe the electric field distribution in subgrid region for horizontal polarised antenna placed at the back of the human body from position 1 to position 3. Figures 5.44, 5.46 and 5.48 illustrate the electric field distribution for vertical polarised antenna placed at the front of the human from position 1 to position 3. Figures 5.45, 5.47 and 5.49 describe the electric field distribution in subgrid region for vertical polarised antenna placed at the front of the human body from position 1 to position 3. Figures 5.50, 5.52 and 5.54 illustrate the electric field distribution for vertical polarised antenna placed at the back of the human from position 1 to position 3. Figures 5.51, 5.53 and 5.55 describe the electric field distribution in subgrid region for vertical polarised antenna placed at the back of the human body from position 1 to position 3.

Table 5.3: Human tissues properties at 900 MHz.

Tissue	ε_r	σ (S/m)	ρ (kg/m^3)
Air	1	0	1.3
Bile	70.19	1.838	1010
Body fluid	68.90	1.636	1010
Eye (cornea)	55.24	1.394	1076
Fat	5.462	0.05104	916
Lymph	59.68	1.039	1040
Muscous membrane	46.08	0.8448	1040
Nails	12.45	0.1433	1030
Nerve (spine)	32.53	0.5737	1038
Muscle	55.03	0.9430	1047
Heart	59.89	1.230	1030
White matter	38.89	0.5908	1038
Stomach	65.06	1.187	1050
Glands	59.68	1.039	1050
Blood vessel	44.78	0.6961	1040
Liver	46.83	0.855	1030
Gall bladder	59.14	1.257	1030
Spleen	57.18	1.273	1054
Cerebellum	49.44	1.263	1038
Bone (cortical)	12.45	0.1433	1990
Cartilage	42.65	0.7824	1097
Ligaments	45.83	0.7184	1220
Skin/dermis	41.41	0.8668	1125
Intestine (large)	57.94	1.080	1043
Tooth	12.45	0.1433	2160
Gray matter	52.73	0.9423	1038
Eye (lens)	46.57	0.7934	1053
Lung (outer)	51.42	0.858	1050
Intestine (small)	59.49	2.165	1043
Eye (sclera)	55.27	1.167	1026
Lung (inner)	22	0.4567	260
Pancreas	59.68	1.039	1045
Blood	61.36	1.538	1058
Cerebral spinal	68.64	2.413	1007
Eye (retina)	55.27	1.167	1026
Eye (aqueous)	68.9	1.636	1009
Kidneys	58.67	1.392	1050
Bone marrow	5.504	0.04022	1040
Bladder	18.94	0.3831	1030
Testicles	60.55	1.210	1044
Bone (cancellous)	20.79	0.34	1920

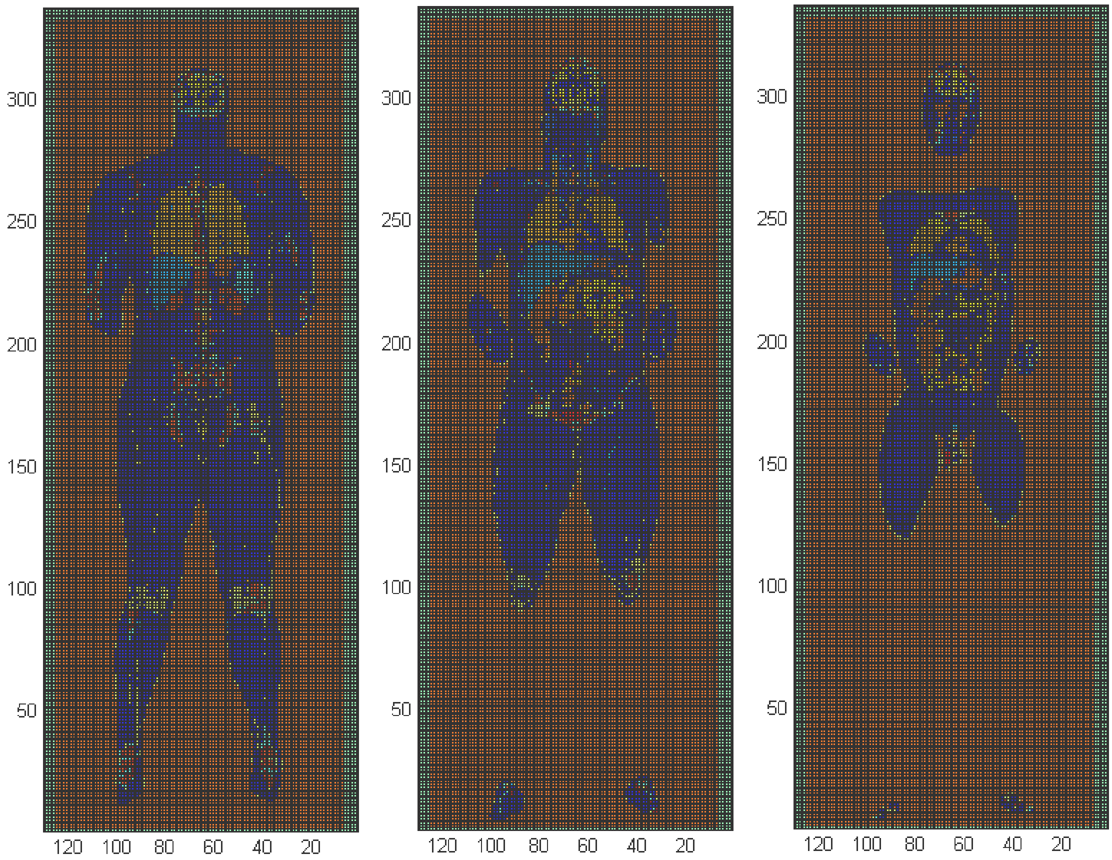

(a) (b) (c)

Figure 5.22: The human body model in *xz* plane of the computational domain. Cross-section at: (a) $y = 35$, (b) $y = 47$, (c) $y = 55$.

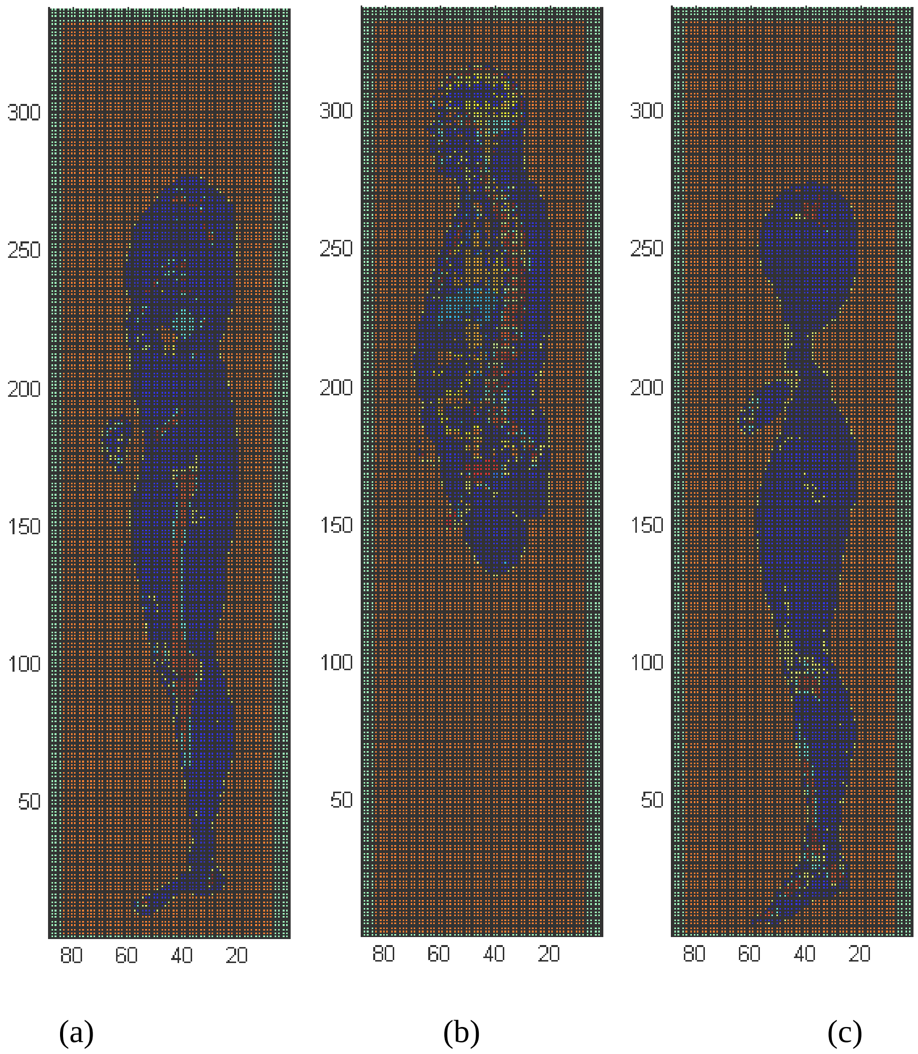

Figure 5.23: The human body model in *yz* plane of the computational domain. Cross-section at: (a) x = 43, (b) x = 67, (c) x = 92.

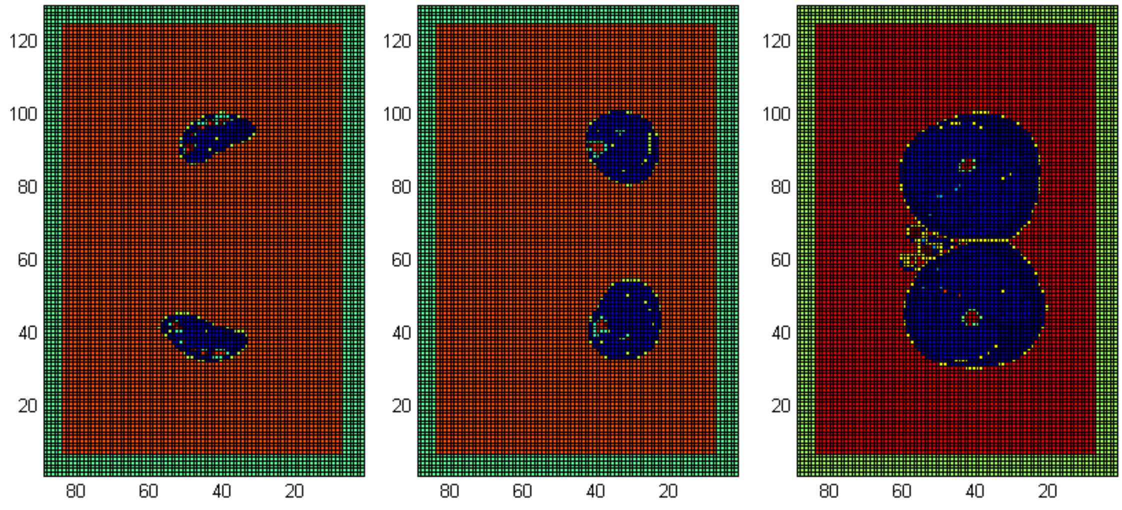

(a) (b) (c)

Figure 5.24: The human body model in *xy* plane of the computational domain. Cross-section at: (a) $z = 14$, (b) $z = 67$, (c) $z = 150$.

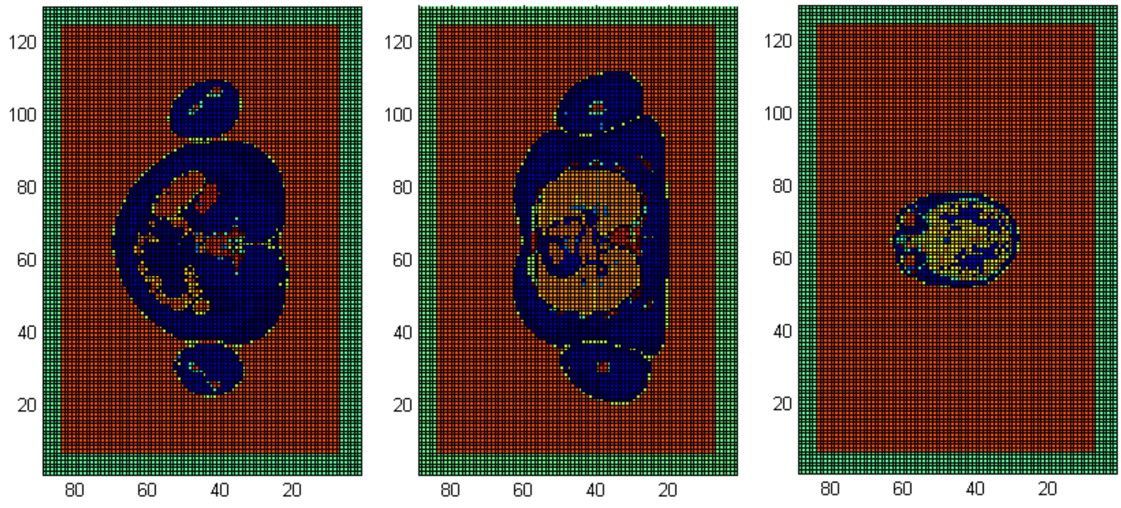

(a) (b) (c)

Figure 5.25: The human body model in *xy* plane of the computational domain. Cross-section at: (a) $z = 205$, (b) $z = 247$, (c) $z = 300$.

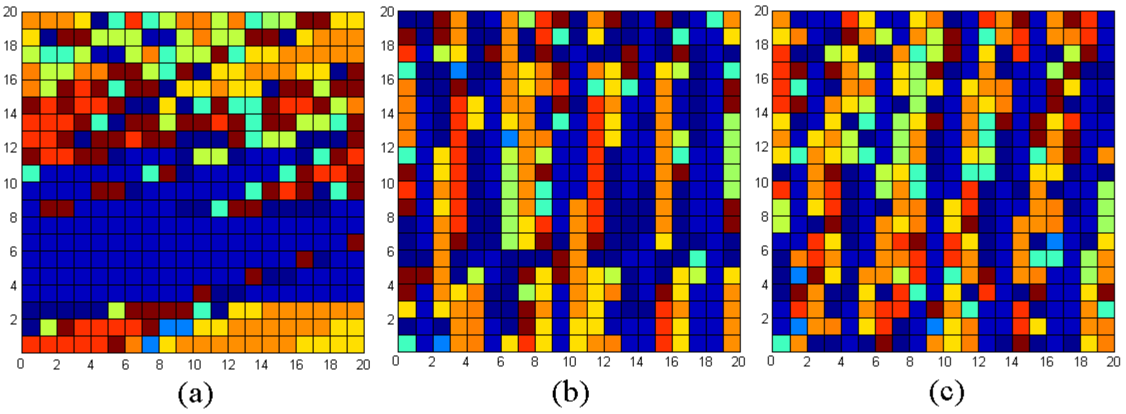

Figure 5.26: Subgrid cells composition inside the front of human body at position 1: (a) *xy* plane, (b) *xz* plane, (c) *yz* plane.

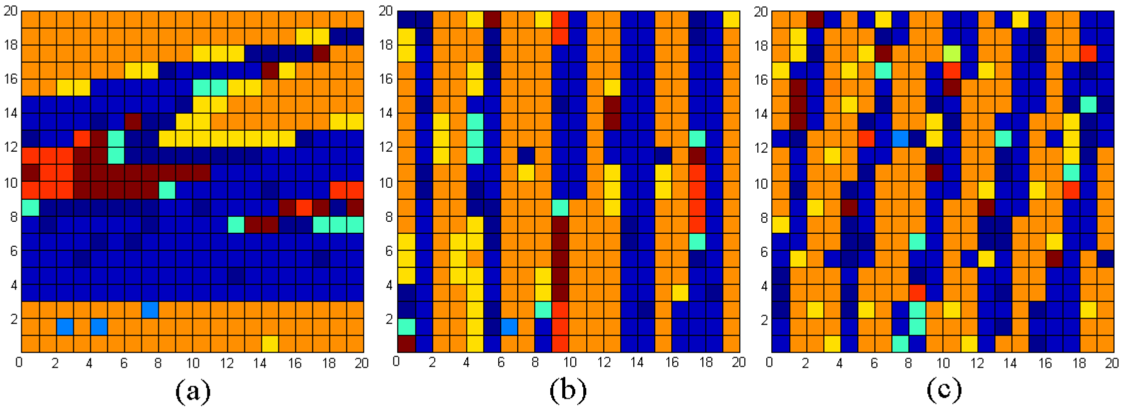

Figure 5.27: Subgrid cells composition inside the front of human body at position 2: (a) *xy* plane, (b) *xz* plane, (c) *yz* plane.

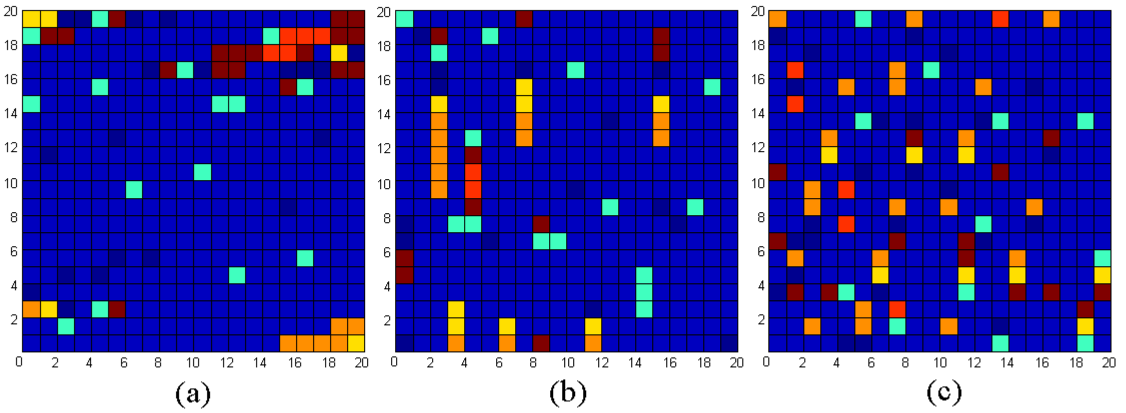

Figure 5.28: Subgrid cells composition inside the front of human body at position 3: (a) *xy* plane, (b) *xz* plane, (c) *yz* plane.

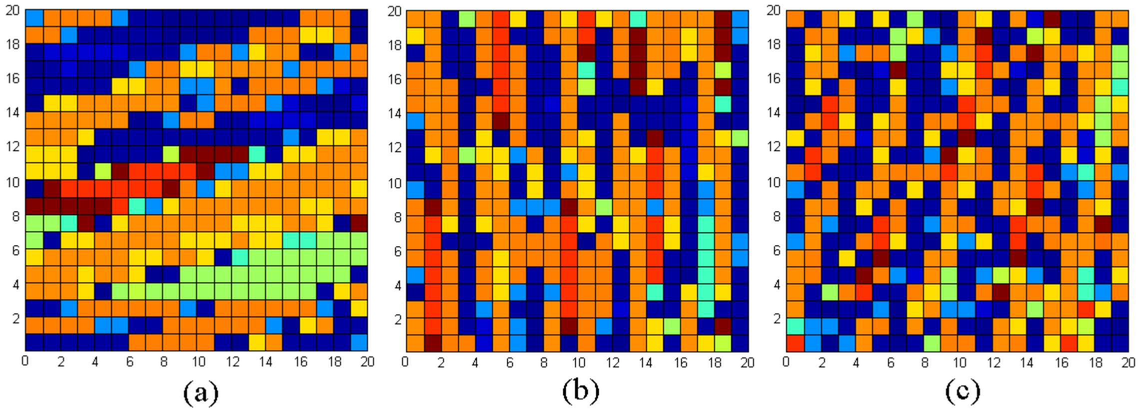

Figure 5.29: Subgrid cells composition inside the back of human body at position 1: (a) *xy* plane, (b) *xz* plane, (c) *yz* plane.

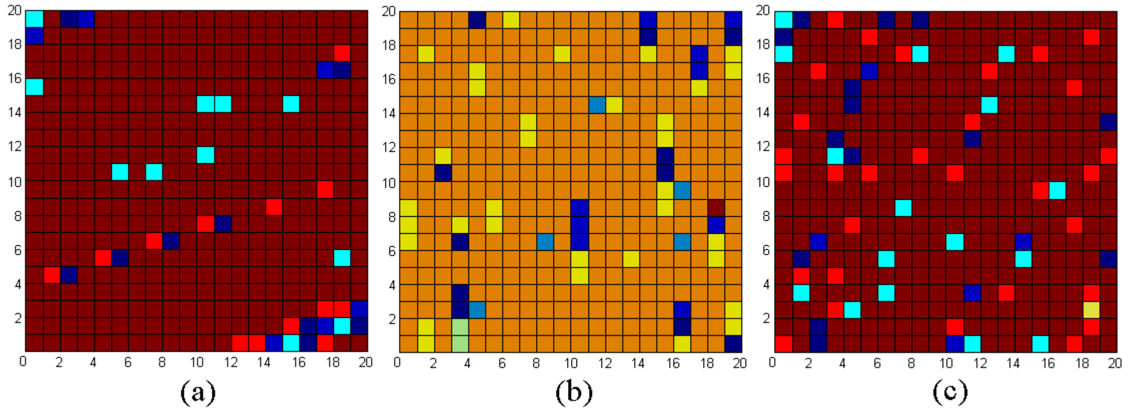

Figure 5.30: Subgrid cells composition inside the back of human body at position 2: (a) *xy* plane, (b) *xz* plane, (c) *yz* plane.

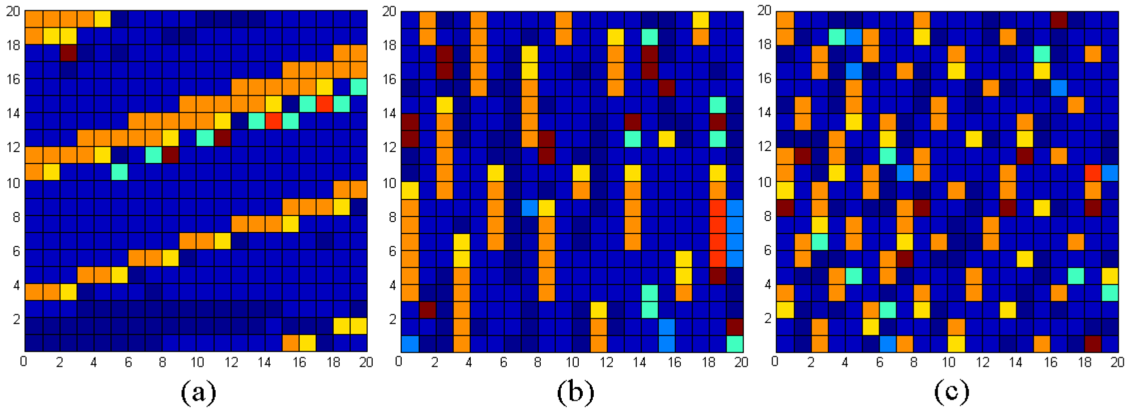

Figure 5.31: Subgrid cells composition inside the back of human body at position 3: (a) *xy* plane, (b) *xz* plane, (c) *yz* plane.

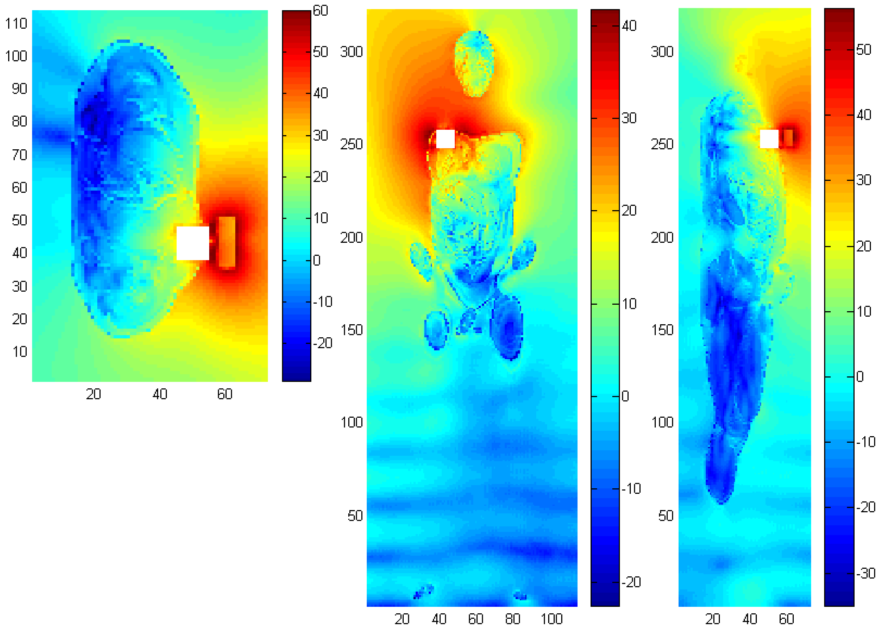

(a) (b) (c)

Figure 5.32: Electric field distribution for horizontal polarised antenna placed at the front of the human (position 1): (a) *xy* plane, (b) *xz* plane, (c) *yz* plane.

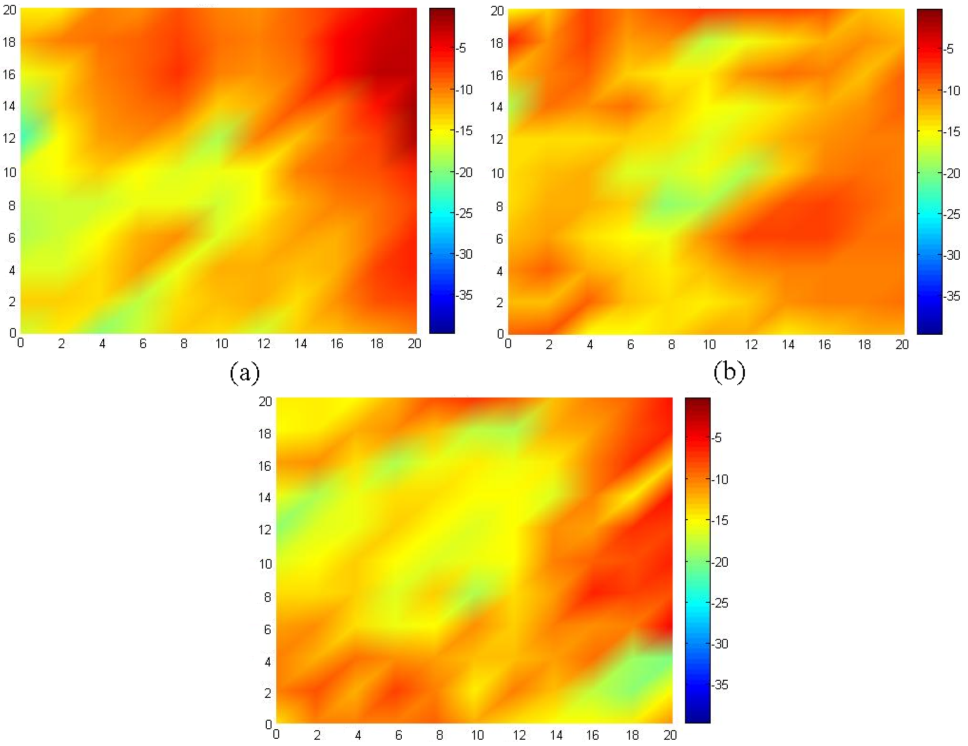

(a) (b)

(c)

Figure 5.33: Electric field distribution in subgrid area for horizontal polarised antenna placed at the front of the human (position 1): (a) *xy* plane, (b) *xz* plane, (c) *yz* plane.

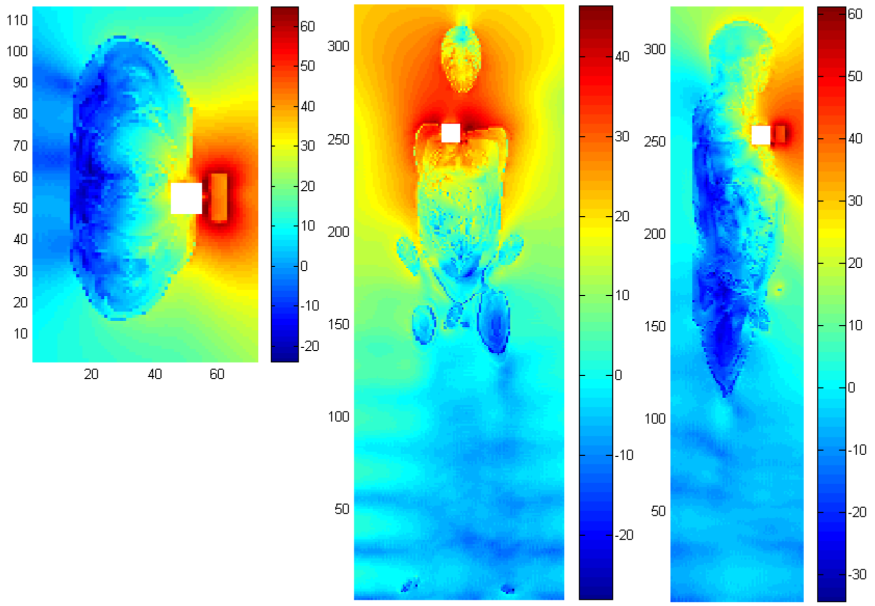

(a) (b) (c)

Figure 5.34: Electric field distribution for horizontal polarised antenna placed at the front of the human (position 2): (a) *xy* plane, (b) *xz* plane, (c) *yz* plane.

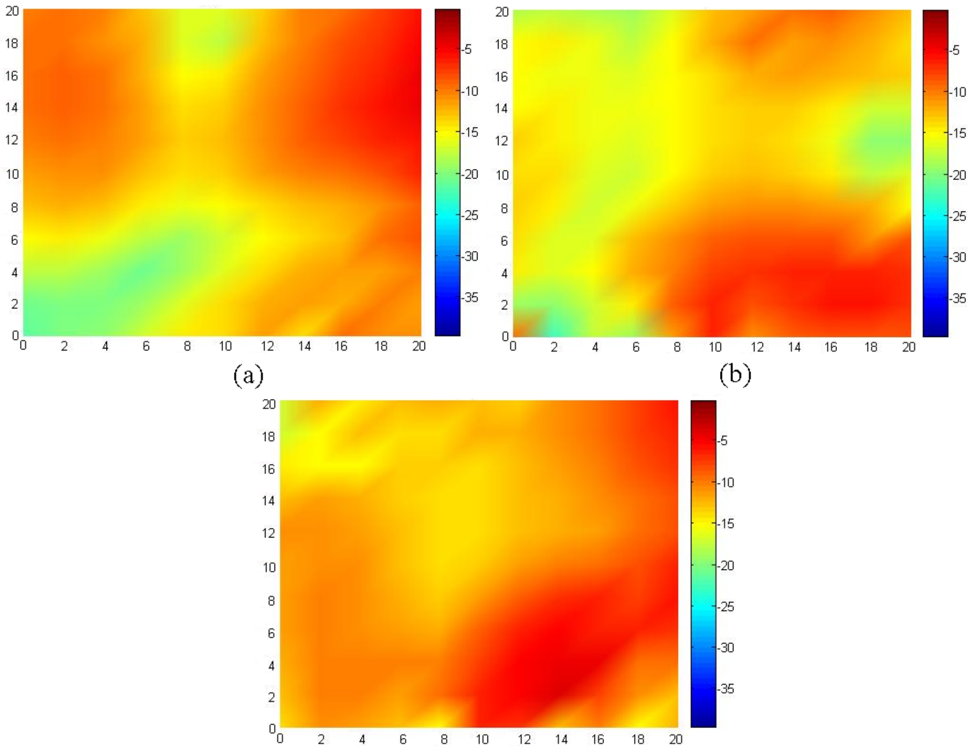

(c)

Figure 5.35: Electric field distribution in subgrid area for horizontal polarised antenna placed at the front of the human (position 2): (a) *xy* plane, (b) *xz* plane, (c) *yz* plane.

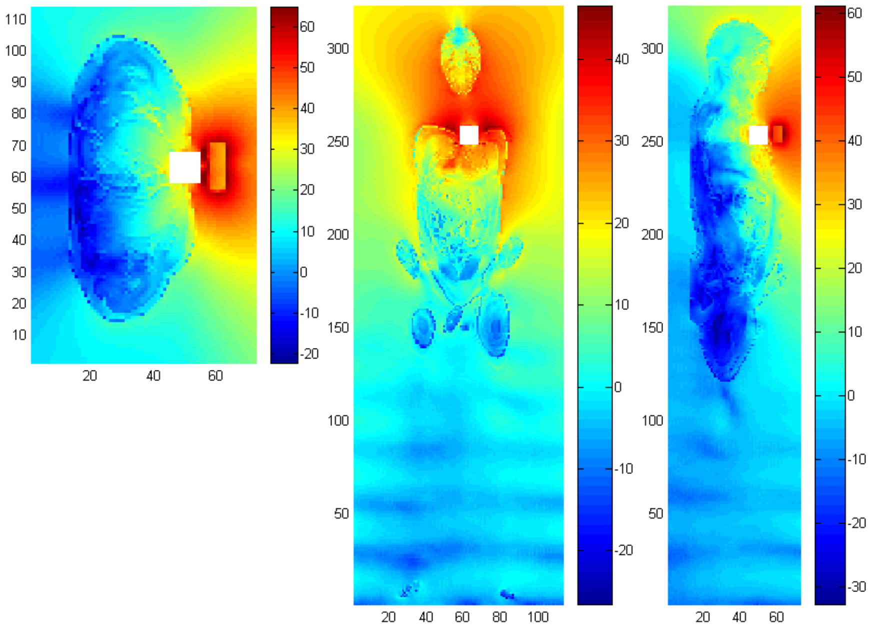

(a) (b) (c)

Figure 5.36: Electric field distribution for horizontal polarised antenna placed at the front of the human (position 3): (a) *xy* plane, (b) *xz* plane, (c) *yz* plane.

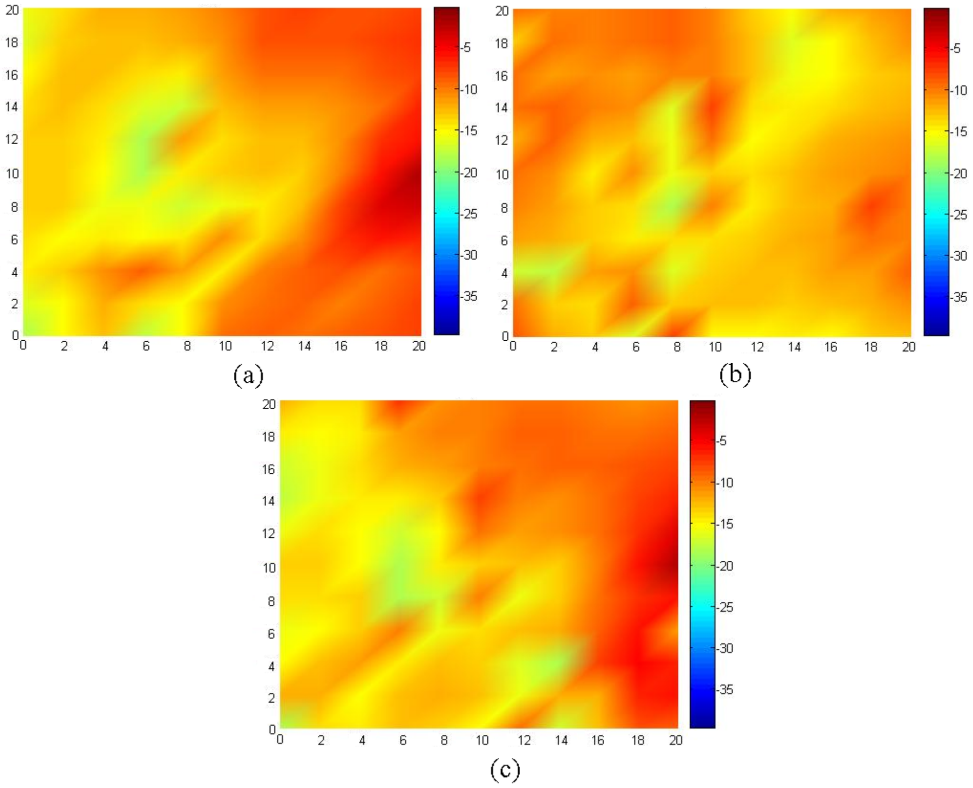

(c)

Figure 5.37: Electric field distribution in subgrid area for horizontal polarised antenna placed at the front of the human (position 3): (a) *xy* plane, (b) *xz* plane, (c) *yz* plane.

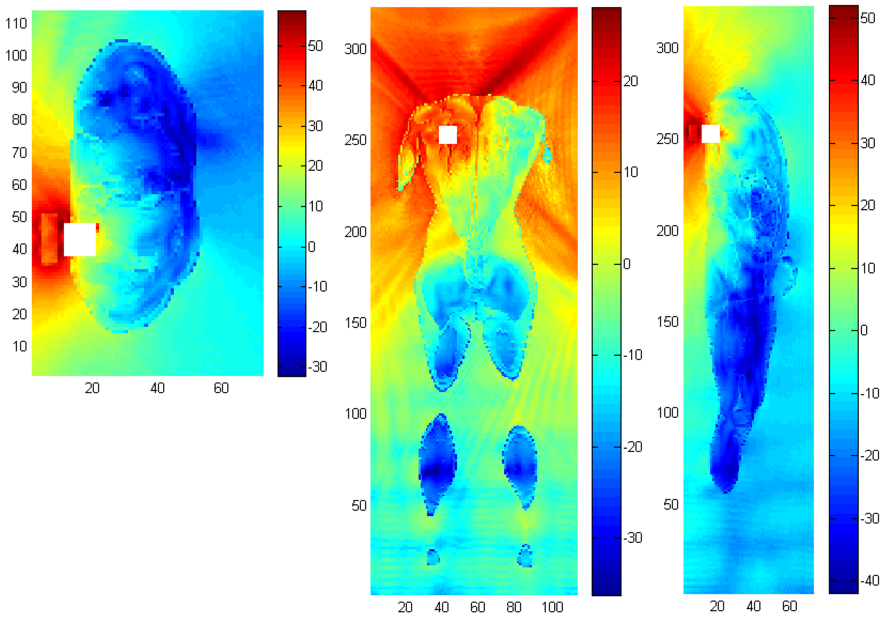

(a) (b) (c)

Figure 5.38: Electric field distribution for horizontal polarised antenna placed at the back of the human (position 1): (a) *xy* plane, (b) *xz* plane, (c) *yz* plane.

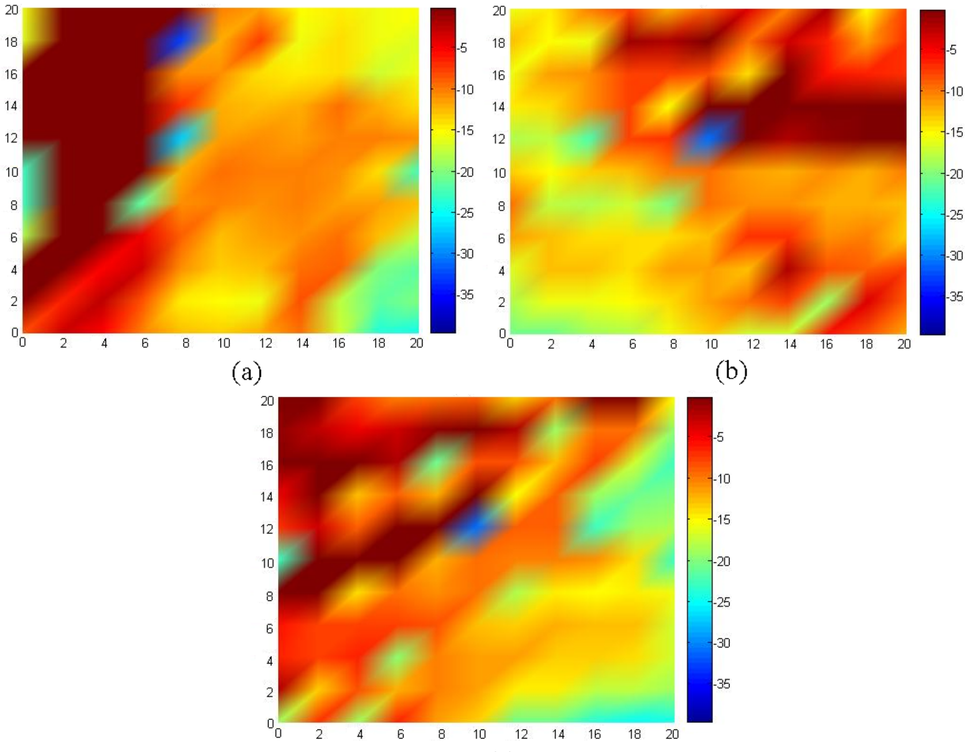

(a) (b)

(c)

Figure 5.39: Electric field distribution in subgrid area for horizontal polarised antenna placed at the back of the human (position 1): (a) *xy* plane, (b) *xz* plane, (c) *yz* plane.

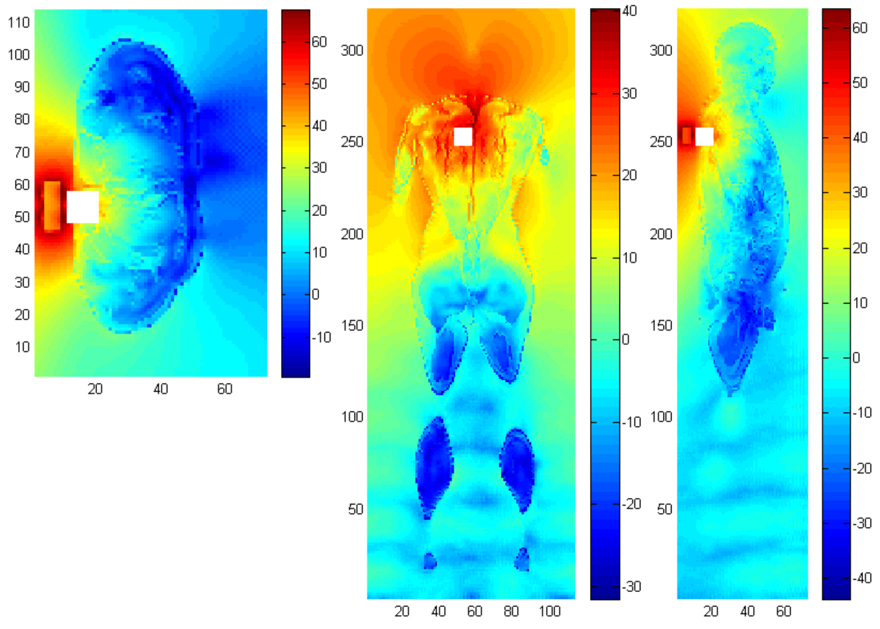

(a) (b) (c)

Figure 5.40: Electric field distribution for horizontal polarised antenna placed at the back of the human (position 2): (a) *xy* plane, (b) *xz* plane, (c) *yz* plane.

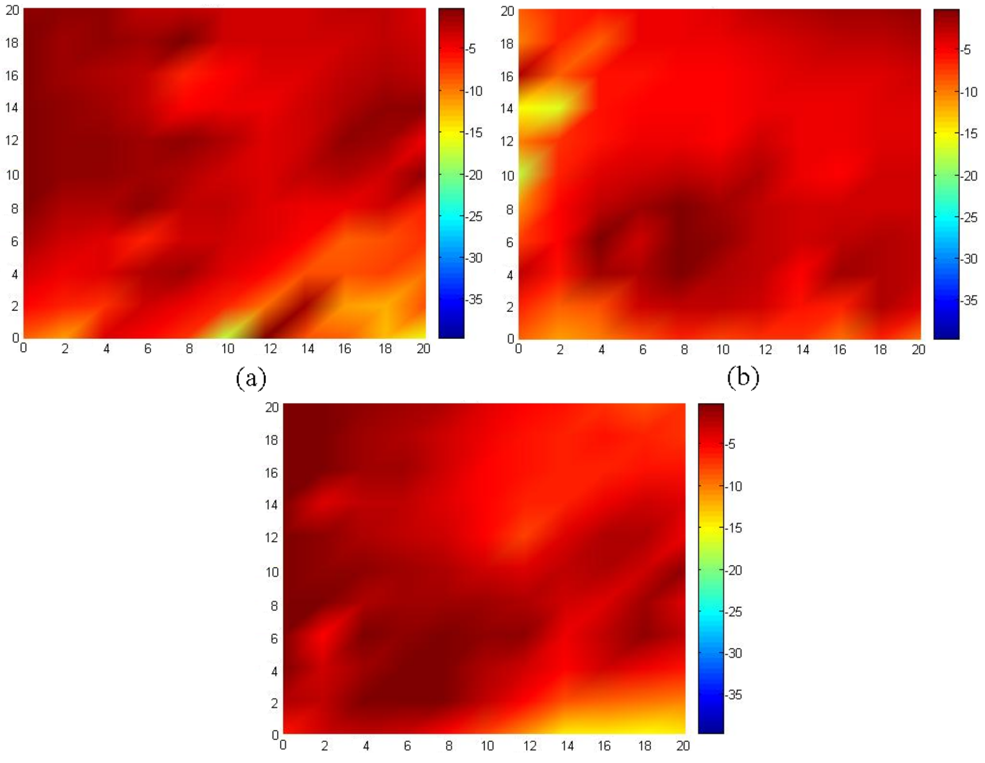

(a) (b)

(c)

Figure 5.41: Electric field distribution in subgrid area for horizontal polarised antenna placed at the back of the human (position 2): (a) *xy* plane, (b) *xz* plane, (c) *yz* plane.

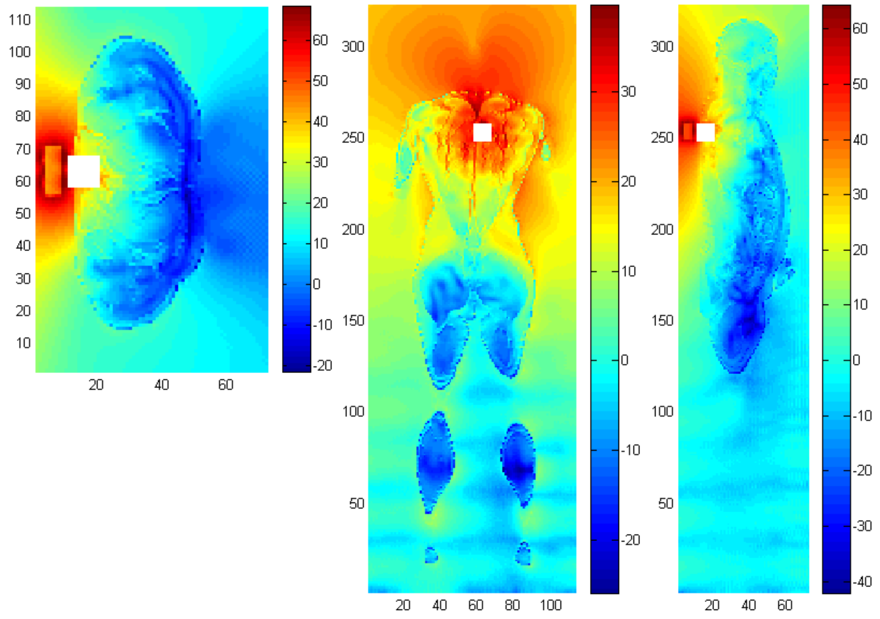

(a) (b) (c)

Figure 5.42: Electric field distribution for horizontal polarised antenna placed at the back of the human (position 3): (a) *xy* plane, (b) *xz* plane, (c) *yz* plane.

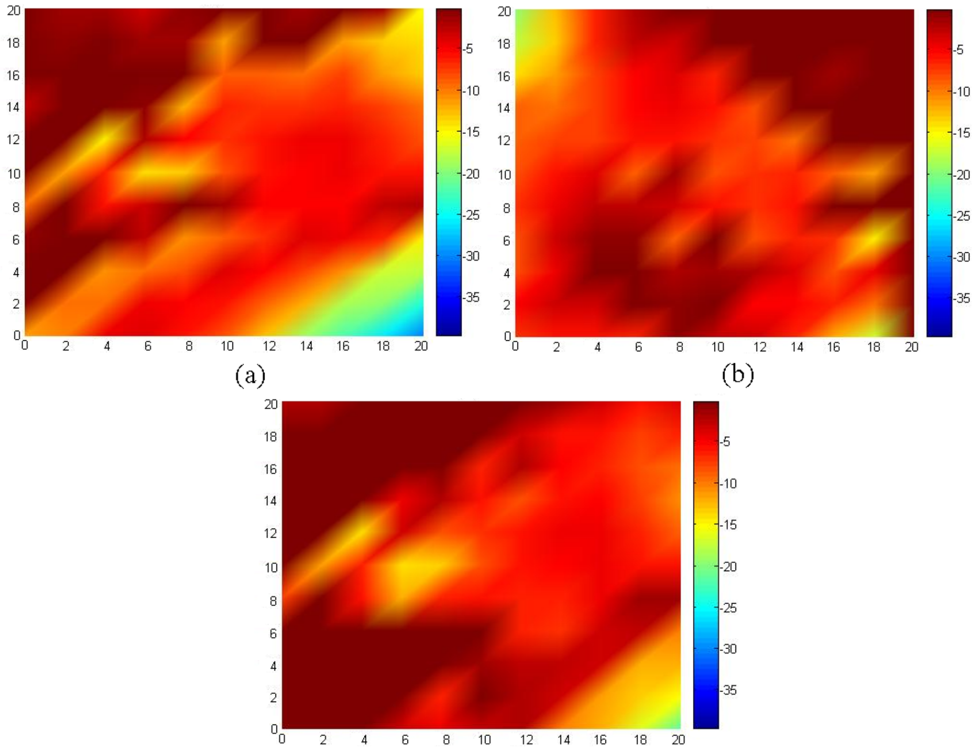

(a) (b)

(c)

Figure 5.43: Electric field distribution in subgrid area for horizontal polarised antenna placed at the back of the human (position 3): (a) *xy* plane, (b) *xz* plane, (c) *yz* plane.

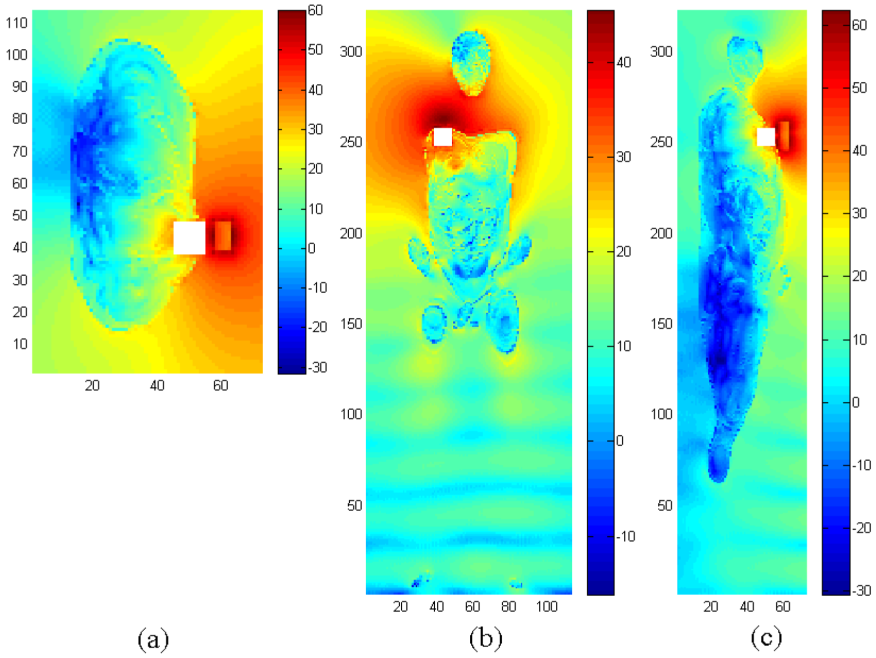

(a) (b) (c)

Figure 5.44: Electric field distribution for vertical polarised antenna placed at the front of the human (position 1): (a) *xy* plane, (b) *xz* plane, (c) *yz* plane.

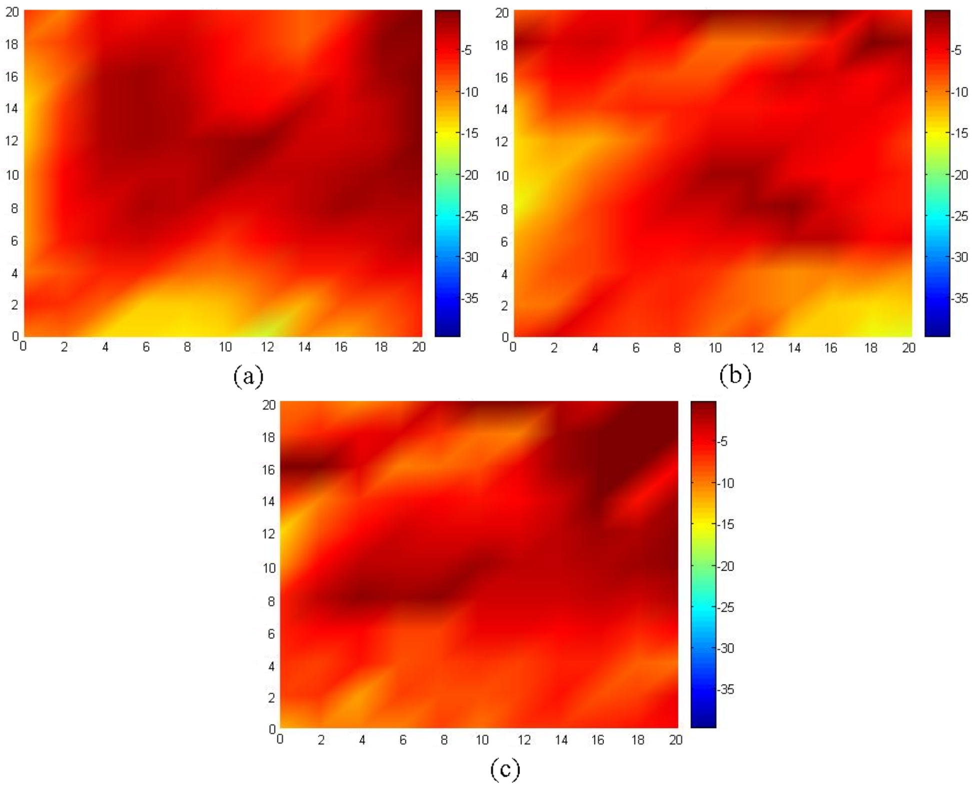

(a) (b) (c)

Figure 5.45: Electric field distribution in subgrid area for vertical polarised antenna placed at the front of the human (position 1): (a) *xy* plane, (b) *xz* plane, (c) *yz* plane.

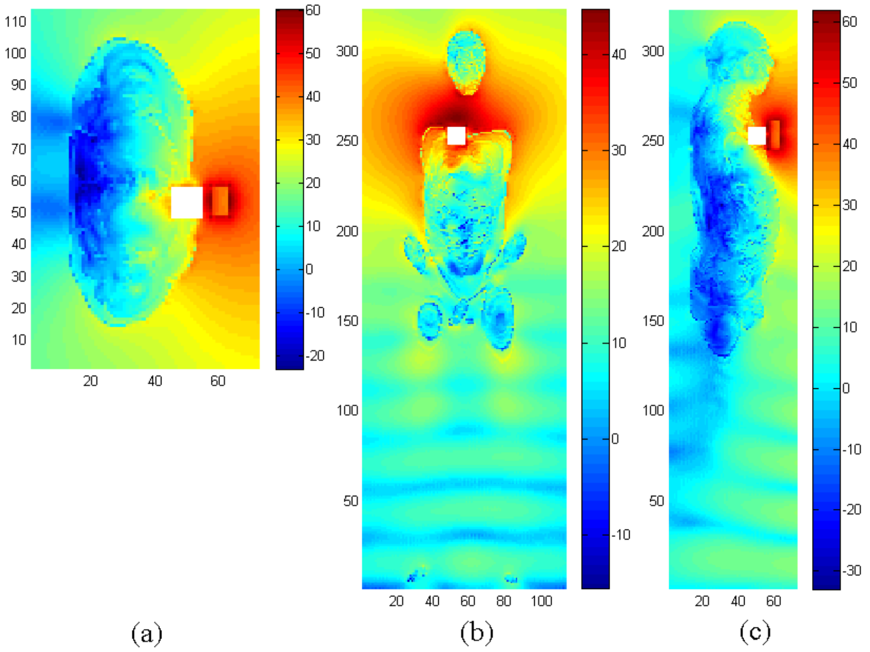

Figure 5.46: Electric field distribution for vertical polarised antenna placed at the front of the human (position 2): (a) *xy* plane, (b) *xz* plane, (c) *yz* plane.

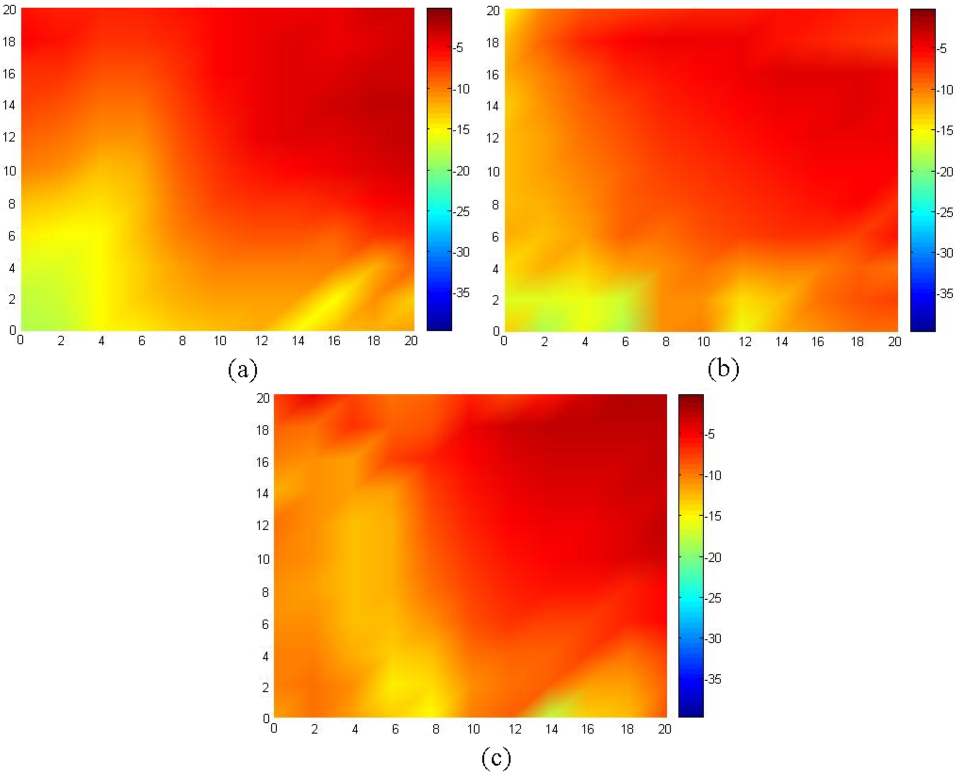

Figure 5.47: Electric field distribution in subgrid area for vertical polarised antenna placed at the front of the human (position 2): (a) *xy* plane, (b) *xz* plane, (c) *yz* plane.

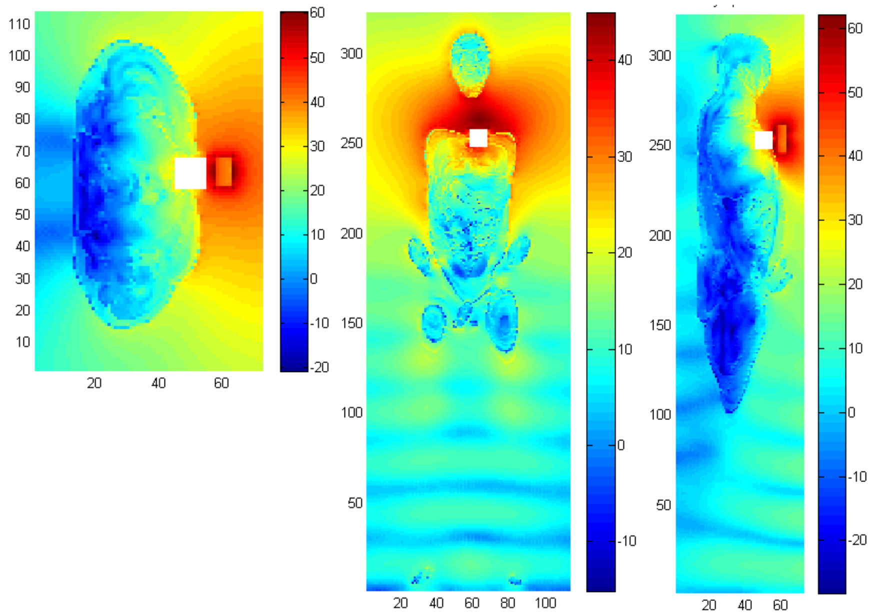

(a) (b) (c)

Figure 5.48: Electric field distribution for vertical polarised antenna placed at the front of the human (position 3): (a) *xy* plane, (b) *xz* plane, (c) *yz* plane.

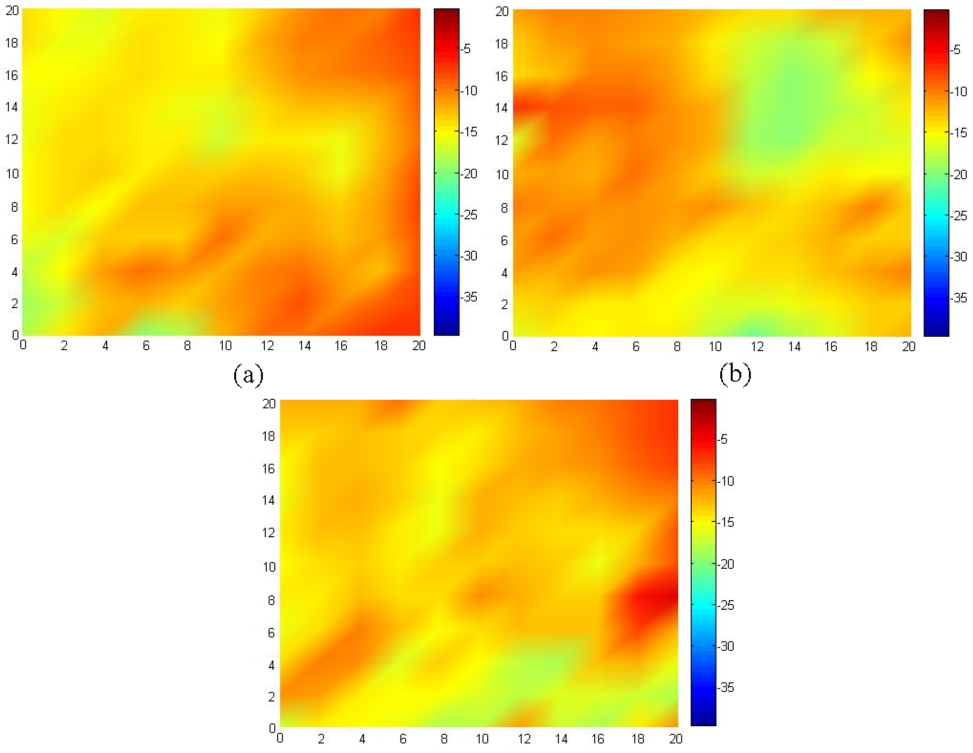

(a) (b)

(c)

Figure 5.49: Electric field distribution in subgrid area for vertical polarised antenna placed at the front of the human (position 3): (a) *xy* plane, (b) *xz* plane, (c) *yz* plane.

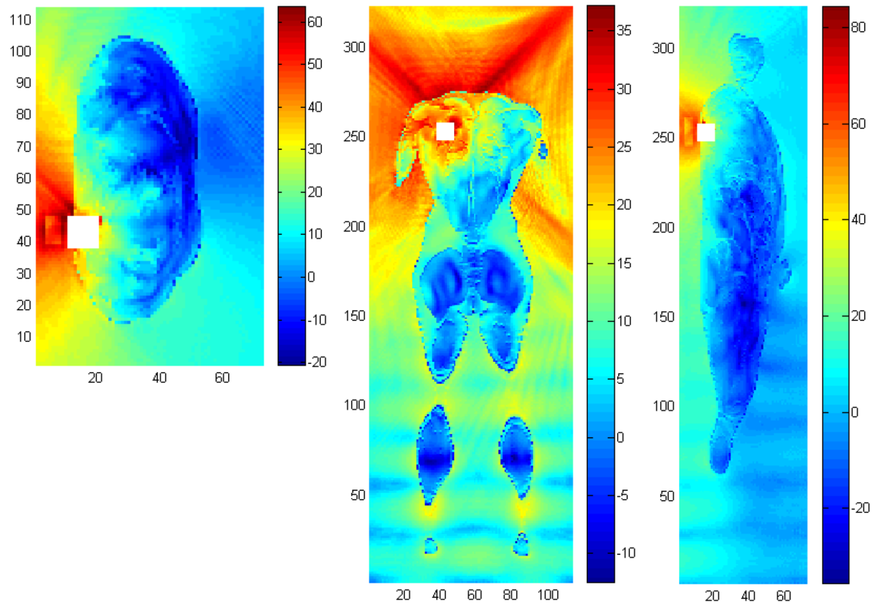

(a) (b) (c)

Figure 5.50: Electric field distribution for vertical polarised antenna placed at the back of the human (position 1): (a) *xy* plane, (b) *xz* plane, (c) *yz* plane.

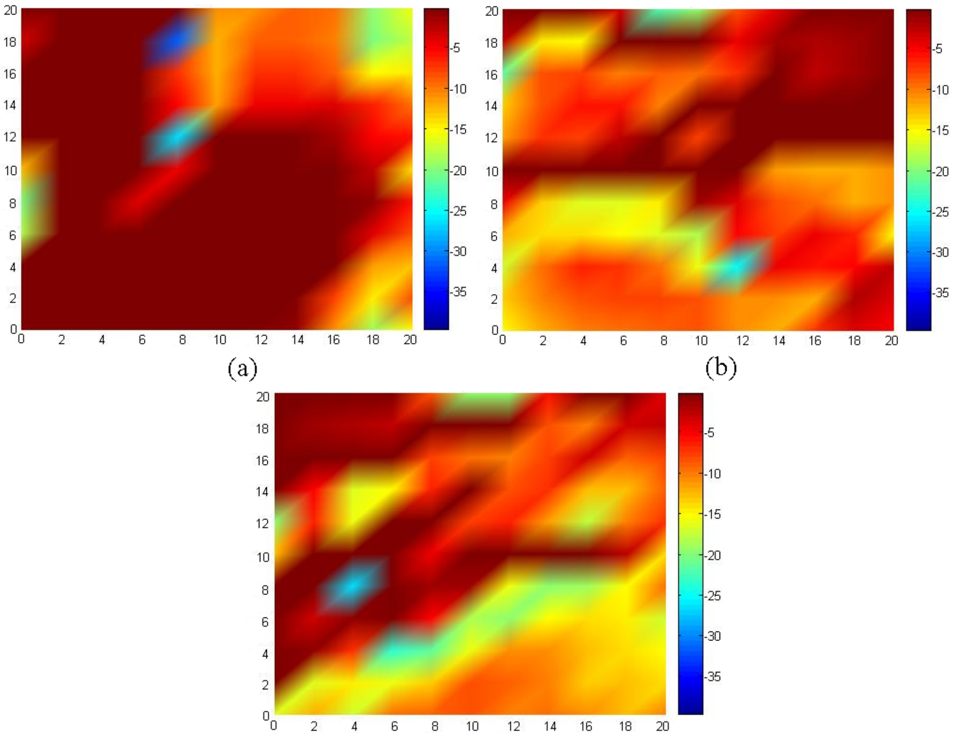

(c)

Figure 5.51: Electric field distribution in subgrid area for vertical polarised antenna placed at the back of the human (position 1): (a) *xy* plane, (b) *xz* plane, (c) *yz* plane.

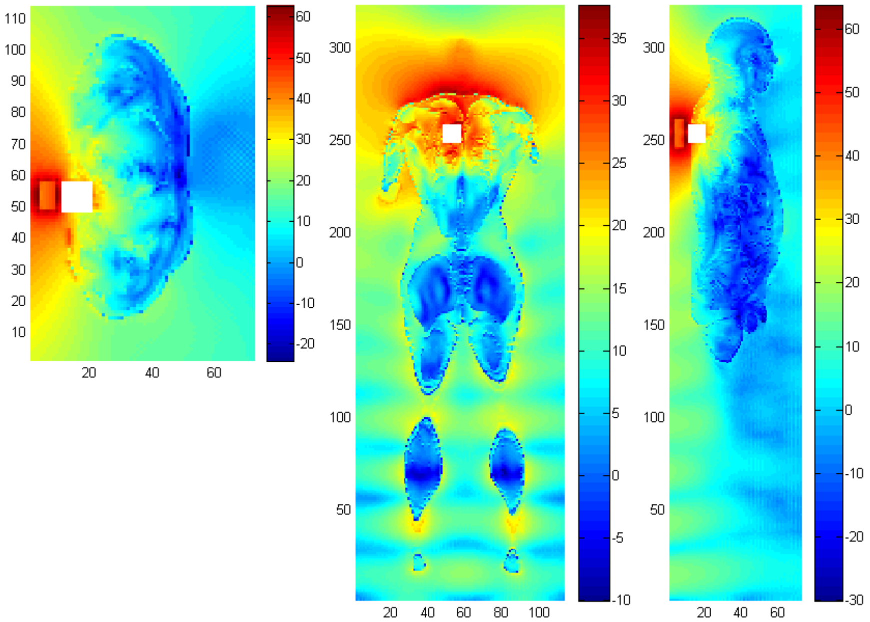

(a) (b) (c)

Figure 5.52: Electric field distribution for vertical polarised antenna placed at the back of the human (position 2): (a) *xy* plane, (b) *xz* plane, (c) *yz* plane.

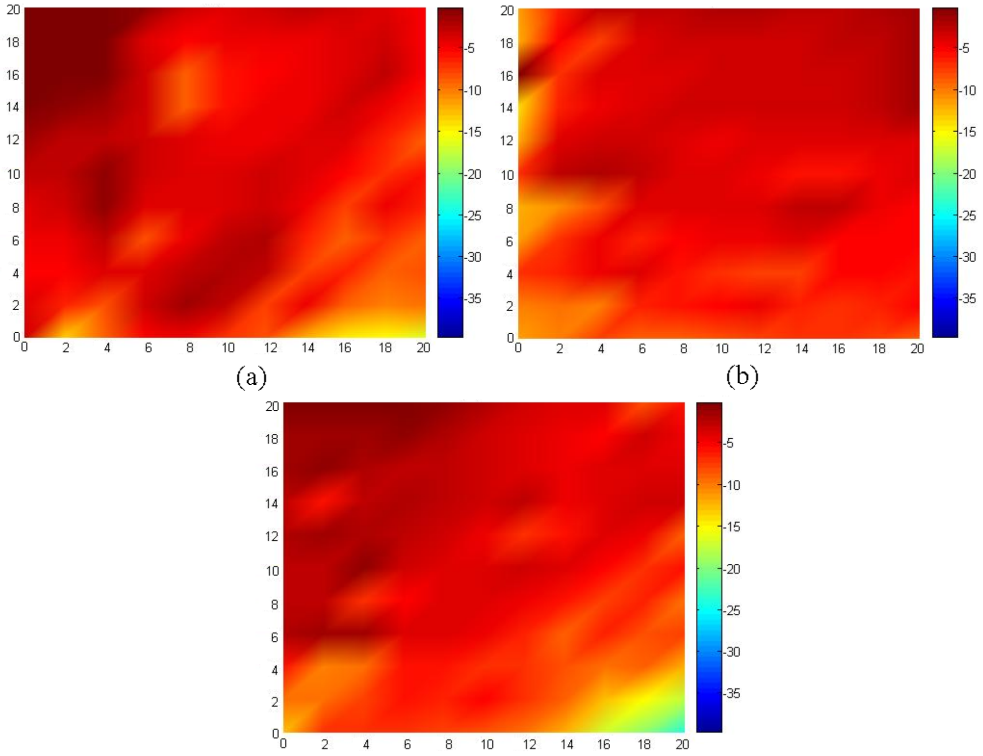

(a) (b) (c)

Figure 5.53: Electric field distribution in subgrid area for vertical polarised antenna placed at the back of the human (position 2): (a) *xy* plane, (b) *xz* plane, (c) *yz* plane.

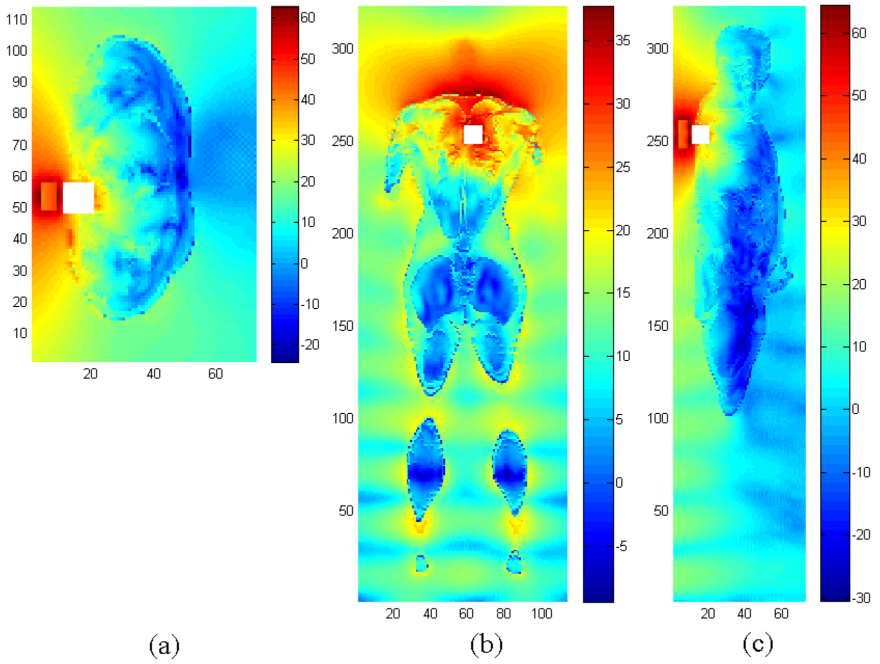

(a) (b) (c)

Figure 5.54: Electric field distribution for vertical polarised antenna placed at the back of the human (position 3): (a) *xy* plane, (b) *xz* plane, (c) *yz* plane.

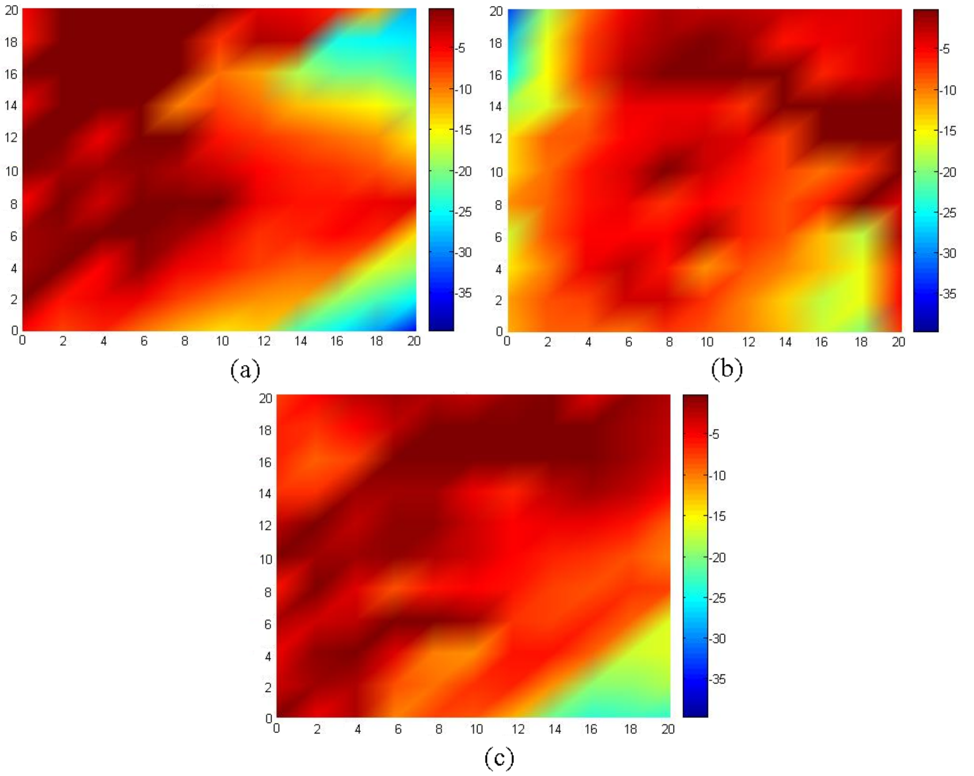

(a) (b)

(c)

Figure 5.55: Electric field distribution in subgrid area for vertical polarised antenna placed at the back of the human (position 3): (a) *xy* plane, (b) *xz* plane, (c) *yz* plane.

From the results, it can be concluded that the electric field distribution near the whole human body was almost the same when the mobile positions were changed regardless of any changes in the antenna polarisation. Similarly, the electric field distribution at subgrid section was almost the same when the mobile positions were changed regardless of any changes in the antenna polarisation. It can also be observed that the surrounding electric fields were very strong when the antenna was located in very close proximity to the human tissue, as indicated by the red colour distribution in the figures.

For far field radiation pattern, only 3 positions will be presented. Figures 5.56 to 5.58 show the far field radiation pattern for horizontal polarised antenna placed at the front of the human from position 1 to position 3 respectively. Figures 5.59 to 5.61 show the far field radiation pattern for horizontal polarised antenna placed at the back of the human from position 1 to position 3 respectively. Figures 5.62 to 5.64 show the far field radiation pattern for vertical polarised antenna placed at the front of the human from position 1 to position 3 respectively. Figures 5.65 to 5.67 show the far field radiation pattern for vertical polarised antenna placed at the back of the human from position 1 to position 3 respectively. All the far field figures are basically normalised to one watt input power.

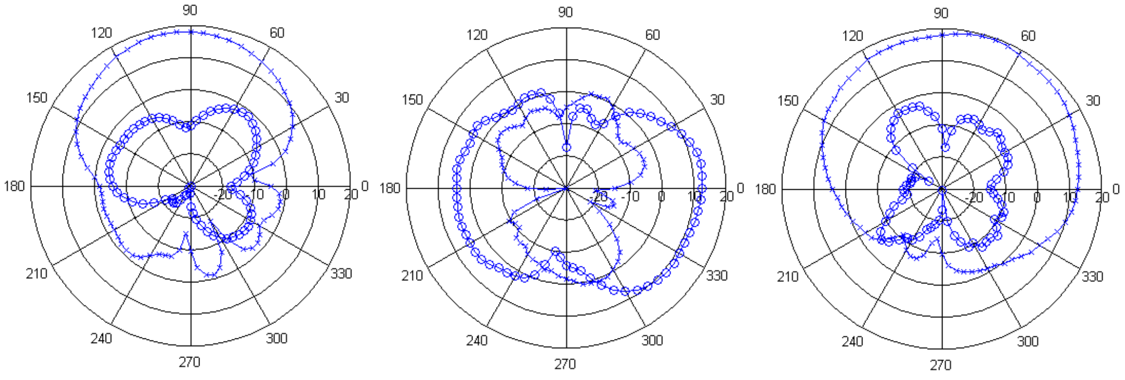

(a) (b) (c)

Figure 5.56: Far field pattern for horizontal polarised antenna placed at the front of the human (position 1): (a) *xy* plane, (b) *xz* plane, (c) *yz* plane; ‘o-o-o’: E_θ, ‘x-x-x’: E_ϕ.

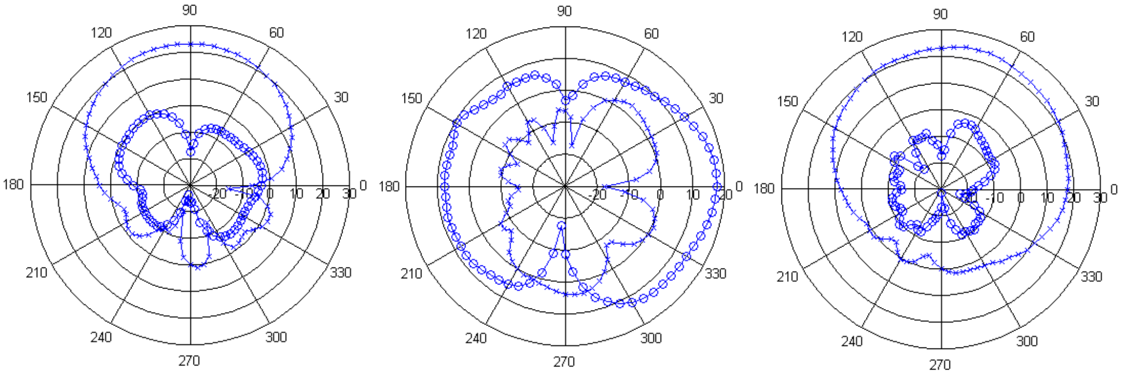

(a) (b) (c)

Figure 5.57: Far field pattern for horizontal polarised antenna placed at the front of the human (position 2): (a) *xy* plane, (b) *xz* plane, (c) *yz* plane; ‘o-o-o’: E_θ, ‘x-x-x’: E_ϕ.

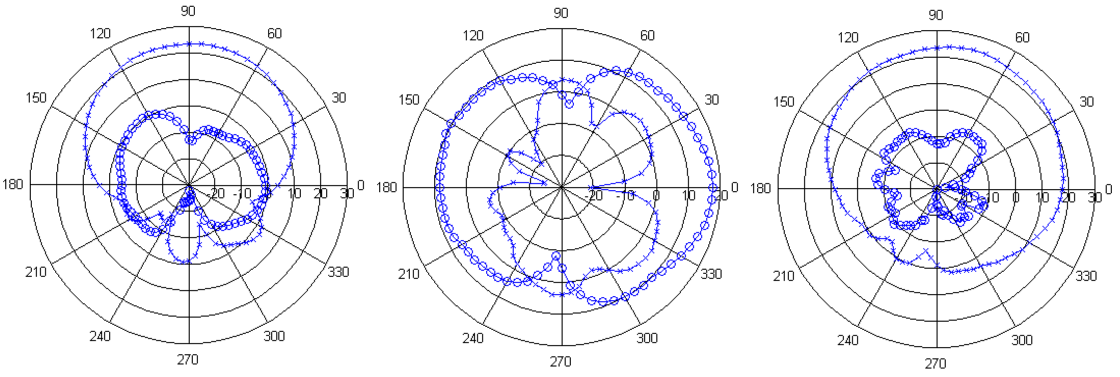

(a) (b) (c)

Figure 5.58: Far field pattern for horizontal polarised antenna placed at the front of the human (position 3): (a) *xy* plane, (b) *xz* plane, (c) *yz* plane; ‘o-o-o’: E_θ, ‘x-x-x’: E_ϕ.

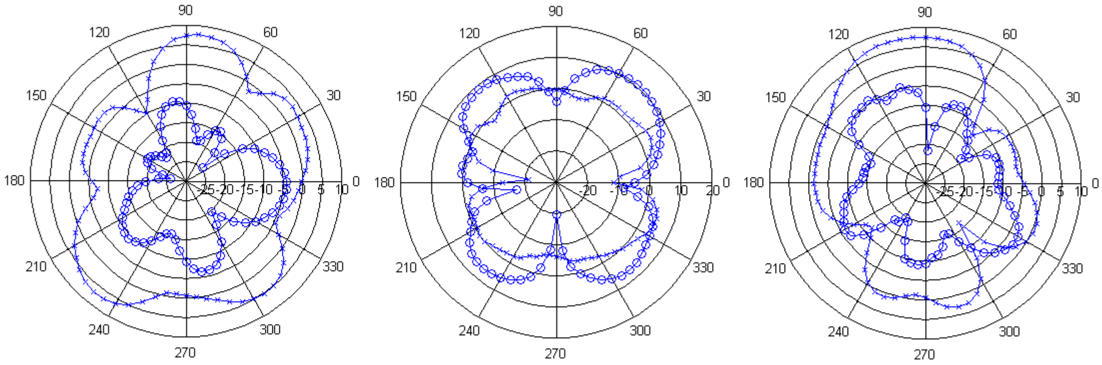

(a) (b) (c)

Figure 5.59: Far field pattern for horizontal polarised antenna placed at the back of the human (position 1): (a) *xy* plane, (b) *xz* plane, (c) *yz* plane; ‘o-o-o’: E_θ, ‘x-x-x’: E_ϕ.

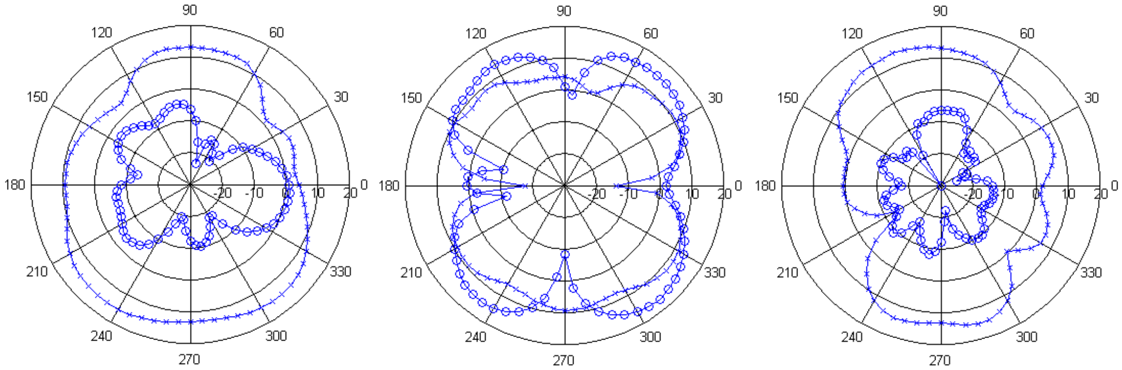

(a) (b) (c)

Figure 5.60: Far field pattern for horizontal polarised antenna placed at the back of the human (position 2): (a) *xy* plane, (b) *xz* plane, (c) *yz* plane; ‘o-o-o’: E_θ, ‘x-x-x’: E_ϕ.

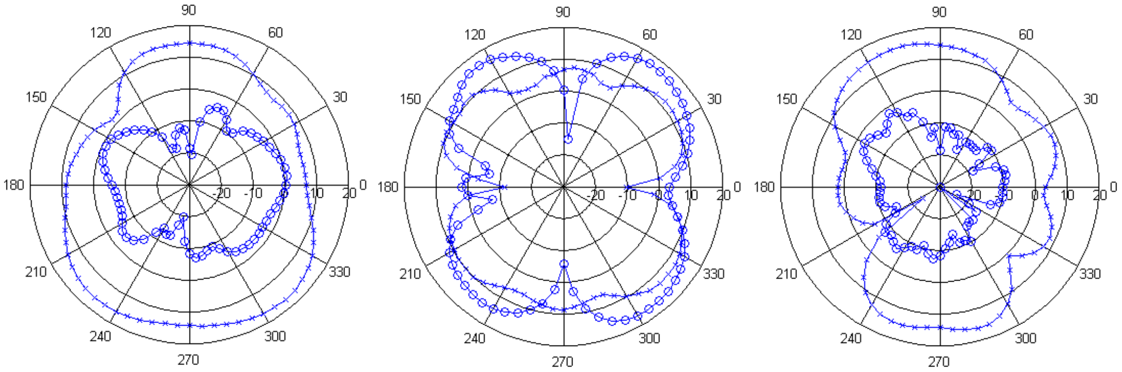

(a) (b) (c)

Figure 5.61: Far field pattern for horizontal polarised antenna placed at the back of the human (position 3): (a) *xy* plane, (b) *xz* plane, (c) *yz* plane; ‘o-o-o’: E_θ, ‘x-x-x’: E_ϕ.

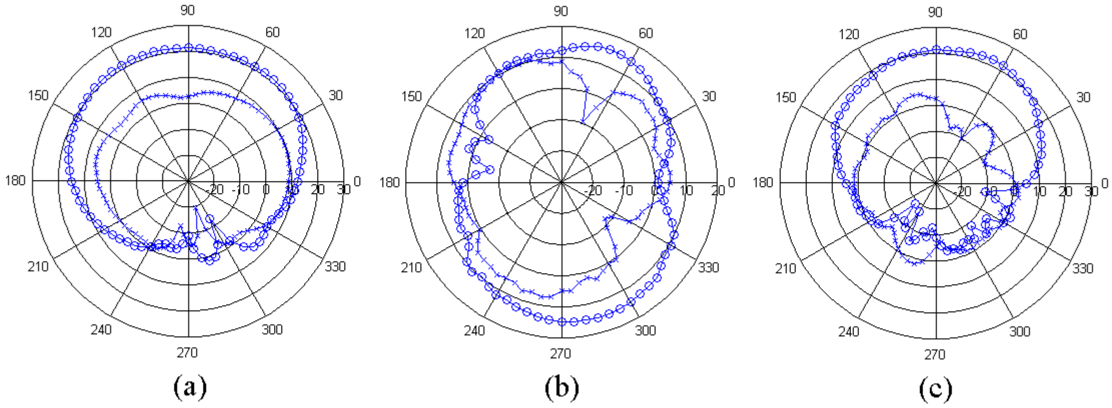

(a) (b) (c)

Figure 5.62: Far field pattern for vertical polarised antenna placed at the front of the human (position 1): (a) *xy* plane, (b) *xz* plane, (c) *yz* plane; 'o-o-o': E_θ, 'x-x-x': E_ϕ.

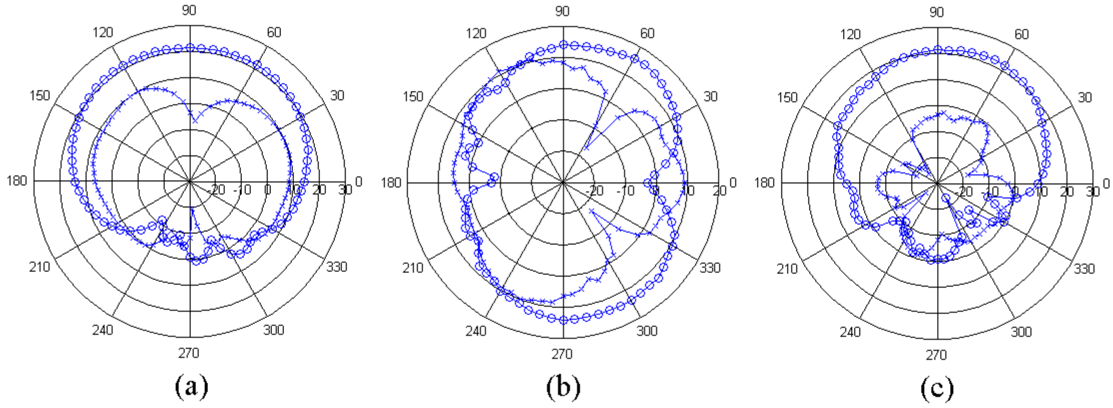

(a) (b) (c)

Figure 5.63: Far field pattern for vertical polarised antenna placed at the front of the human (position 2): (a) *xy* plane, (b) *xz* plane, (c) *yz* plane; 'o-o-o': E_θ, 'x-x-x': E_ϕ.

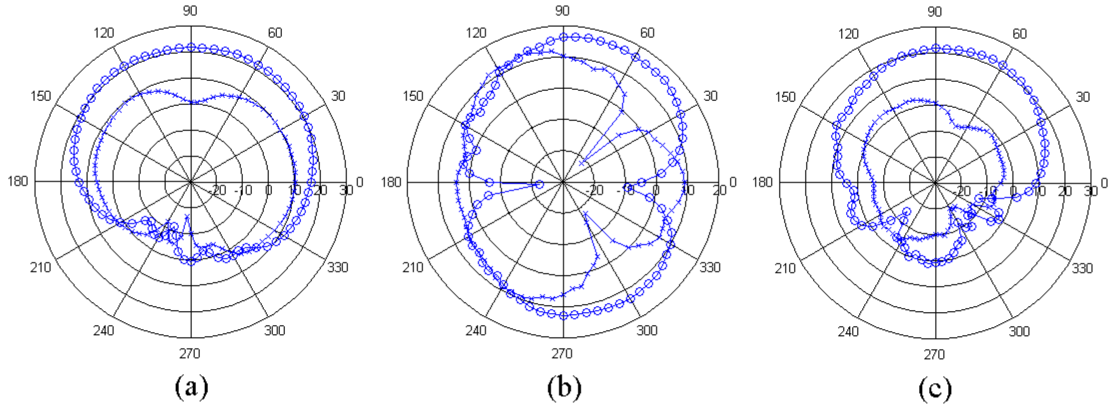

(a) (b) (c)

Figure 5.64: Far field pattern for vertical polarised antenna placed at the front of the human (position 3): (a) *xy* plane, (b) *xz* plane, (c) *yz* plane; 'o-o-o': E_θ, 'x-x-x': E_ϕ.

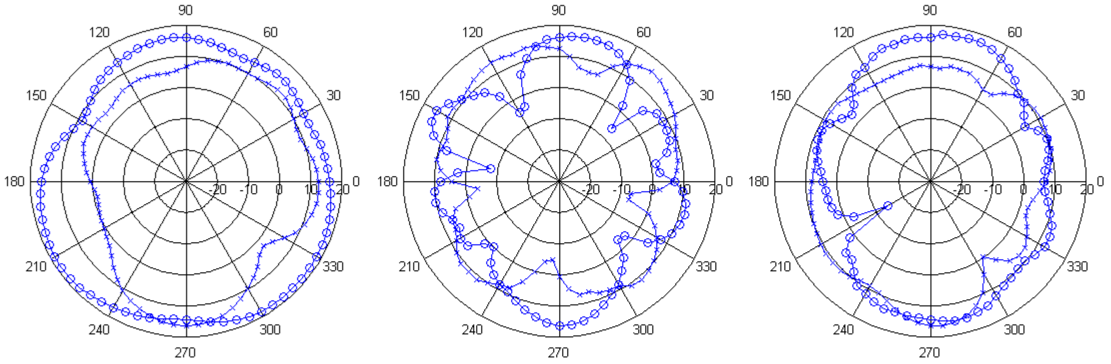

(a) (b) (c)

Figure 5.65: Far field pattern for vertical polarised antenna placed at the back of the human (position 1): (a) *xy* plane, (b) *xz* plane, (c) *yz* plane; ‘o-o-o’: E_θ, ‘x-x-x’: E_ϕ.

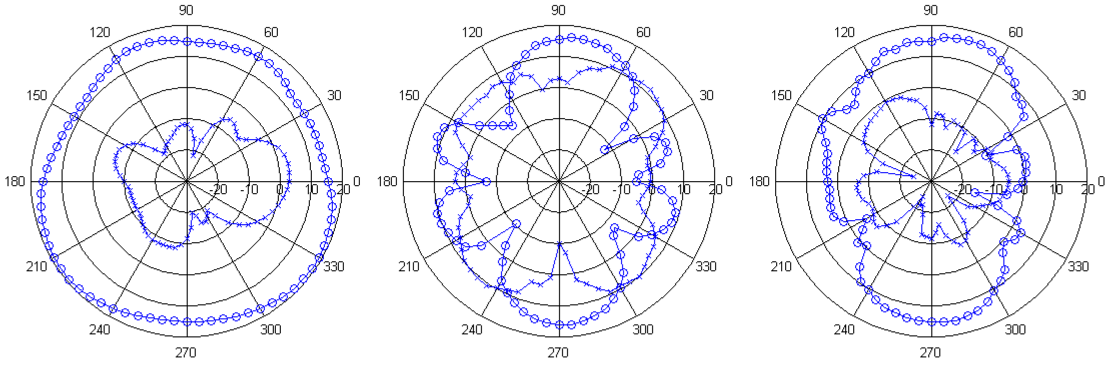

(a) (b) (c)

Figure 5.66: Far field pattern for vertical polarised antenna placed at the back of the human (position 2): (a) *xy* plane, (b) *xz* plane, (c) *yz* plane; ‘o-o-o’: E_θ, ‘x-x-x’: E_ϕ.

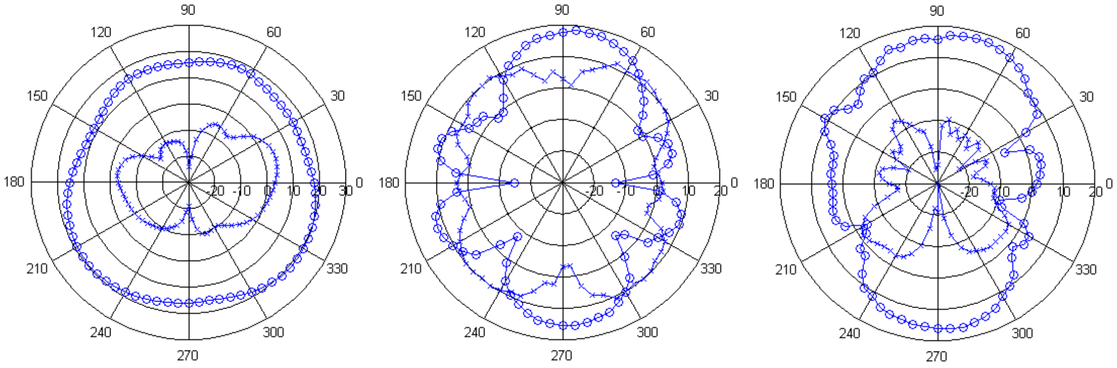

(a) (b) (c)

Figure 5.67: Far field pattern for vertical polarised antenna placed at the back of the human (position 3): (a) *xy* plane, (b) *xz* plane, (c) *yz* plane; ‘o-o-o’: E_θ, ‘x-x-x’: E_ϕ.

The variation of the far field patterns indicate that the fields were significantly stronger in the direction facing the normal axis of the RFID antenna and accordingly away from the human body. It should be noted that the magnitude of the field reduced between 10 dB to 20 dB due to the tailing effect of the human body.

5.5.2 Cumulative Distribution Function

The absorbed power inside the human body and inside subgrid region were taken during simulations. The radiated power from the antenna was also recorded from the simulation results. The radiation efficiency of the antenna can be calculated using:

$$efficiency = \frac{P_{radiated}}{P_{input} + P_{absorbed}} \tag{5.32}$$

The cumulative distribution function (CDF) is evaluated for each location in order to estimate the probability of the power absorbed and radiation efficiency on the human body. The CDF of radiation efficiency and absorbed power over radiated power ($P_{absorbed}$ / $P_{radiated}$) is difficult to predict from the result obtained due to the limited sample size generated through the simulation. A total of 32 different locations in parallel with the rest of the simulation have been considered, recognising the constraints surrounding simulation time and memory. The data from these locations was then combined to obtain the probability of the radiation efficiency and absorbed power over radiated power ($P_{absorbed}$ / $P_{radiated}$).

Figure 5.68 and 5.69 depict the histogram of radiation efficiency and $P_{absorbed}$ / $P_{radiated}$

for horizontal polarised antenna located at the front and back of the human respectively. Figure 5.70 shows the associate CDF calculated when the antenna was placed on these placed. The front and back histogram of radiation efficiency and $P_{absorbed}$ / $P_{radiated}$ for horizontal polarised antenna is illustrated in Figure 5.71. In this case, the related CDF evaluated on these locations is shown in Figure 5.72.

Figure 5.73 and 5.74 depict the histogram of radiation efficiency and $P_{absorbed}$ / $P_{radiated}$ for vertical polarised antenna located at the front and back of the human respectively. Figure 5.75 shows the associate CDF calculated when the antenna was placed on these placed. The front and back histogram of radiation efficiency and $P_{absorbed}$ / $P_{radiated}$ for vertical polarised antenna is illustrated in Figure 5.76. In this case, the related CDF evaluated on these locations is shown in Figure 5.77.

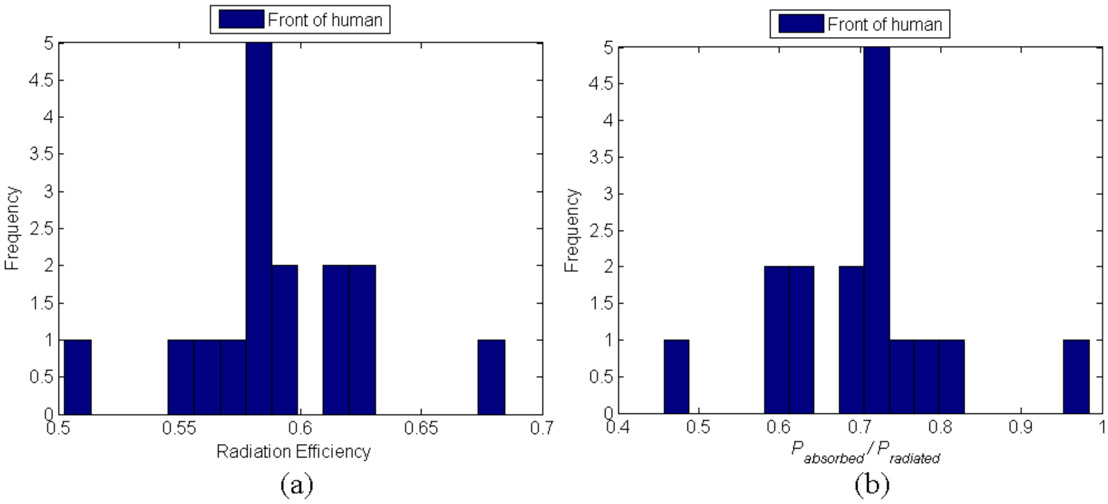

Figure 5.68: Histogram of horizontal polarised antenna located at the front of the human for: (a) radiation efficiency, (b) $P_{absorbed}$ / $P_{radiated}$.

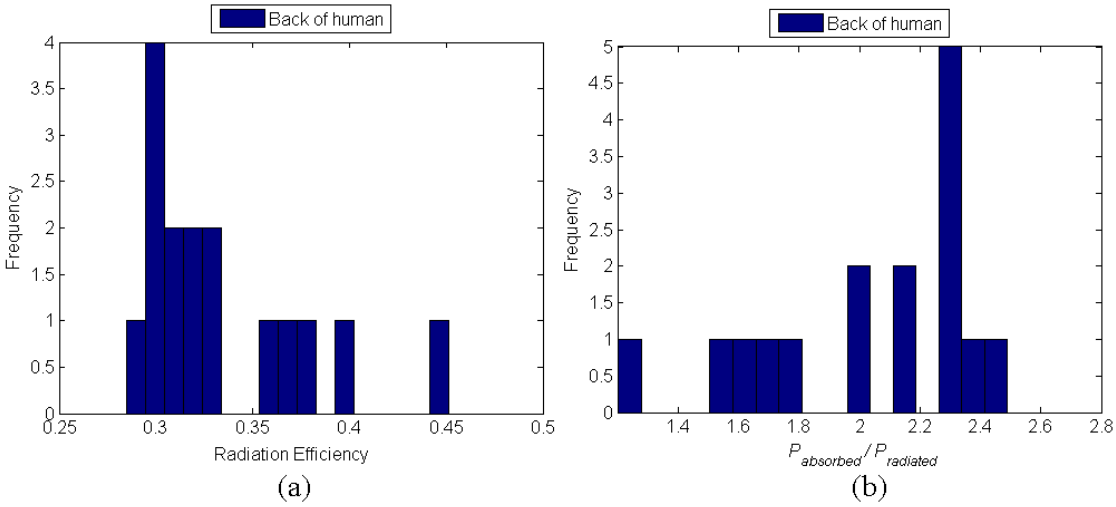

Figure 5.69: Histogram of horizontal polarised antenna located at the back of the human for: (a) radiation efficiency, (b) $P_{absorbed}$ / $P_{radiated}$.

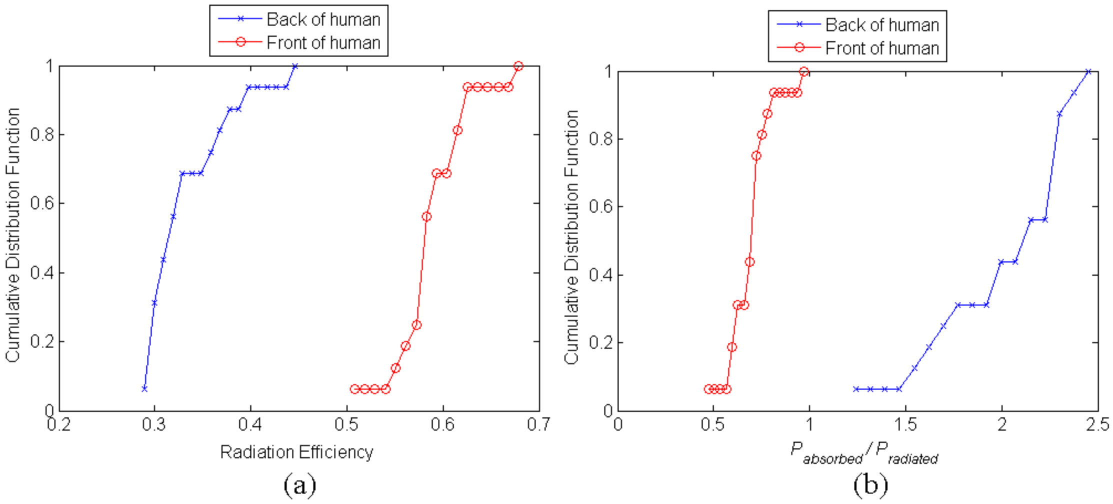

Figure 5.70: Cumulative distribution function of horizontal polarised antenna located at the front and back of the human for: (a) radiation efficiency, (b) $P_{absorbed}$ / $P_{radiated}$.

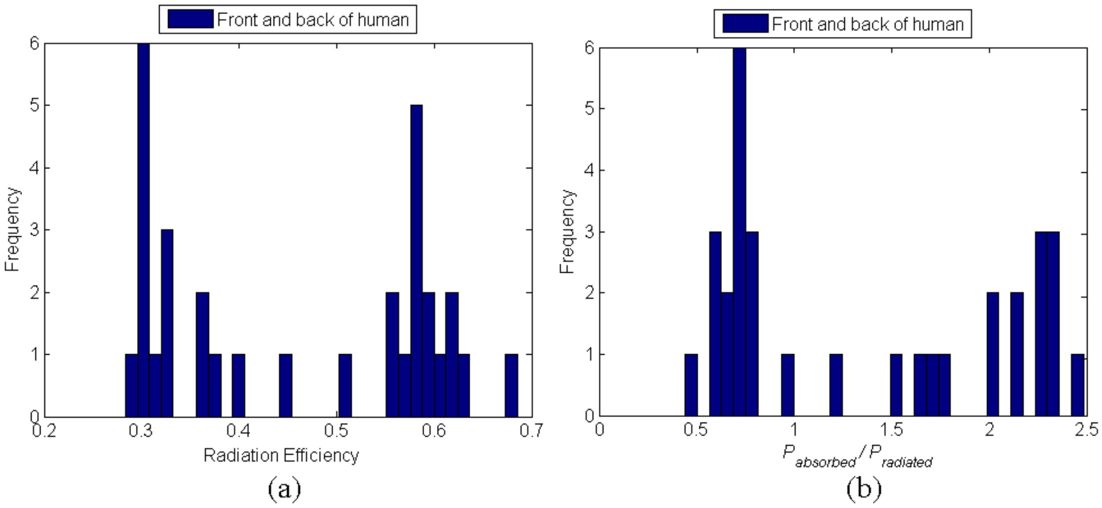

Figure 5.71: Histogram (front and back combination) of horizontal polarised antenna for: (a) radiation efficiency, (b) $P_{absorbed}$ / $P_{radiated}$.

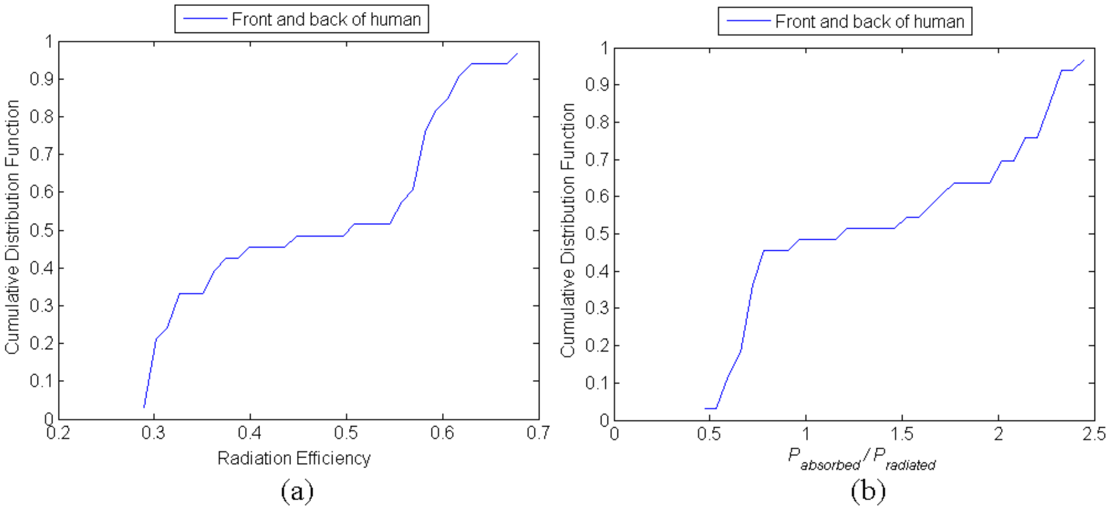

Figure 5.72: Cumulative distribution function (front and back combination) of horizontal polarised antenna for: (a) radiation efficiency, (b) $P_{absorbed}$ / $P_{radiated}$.

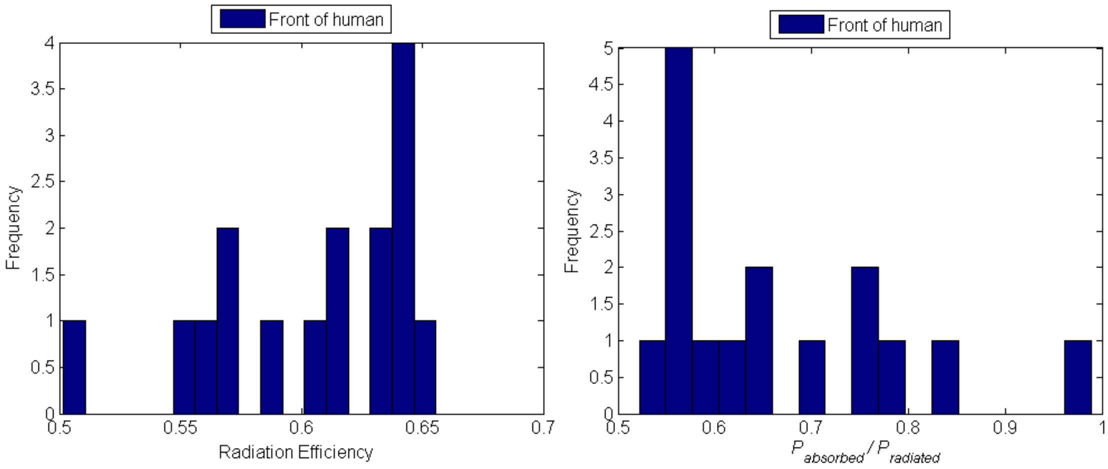

(a) (b)

Figure 5.73: Histogram of vertical polarised antenna located at the front of the human for: (a) radiation efficiency, (b) $P_{absorbed}$ / $P_{radiated}$.

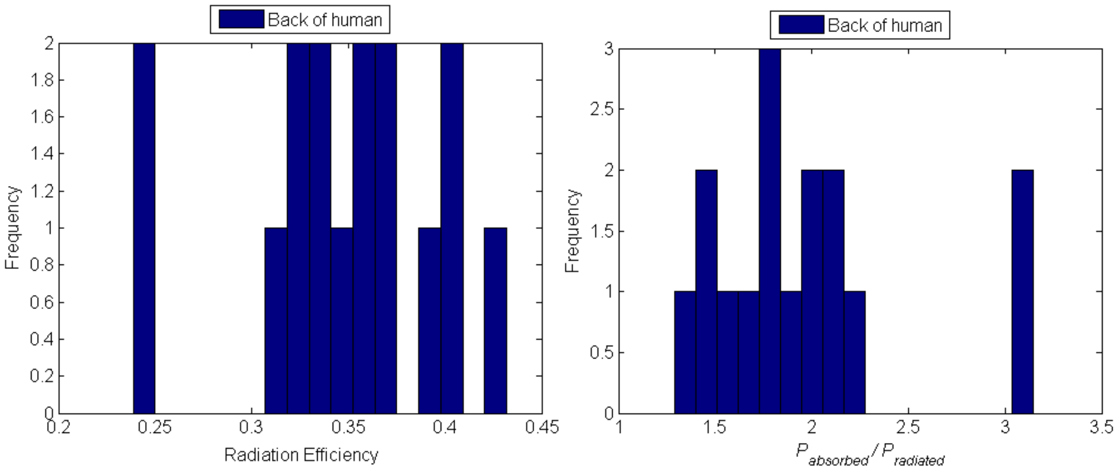

(a) (b)

Figure 5.74: Histogram of vertical polarised antenna located at the back of the human for: (a) radiation efficiency, (b) $P_{absorbed}$ / $P_{radiated}$.

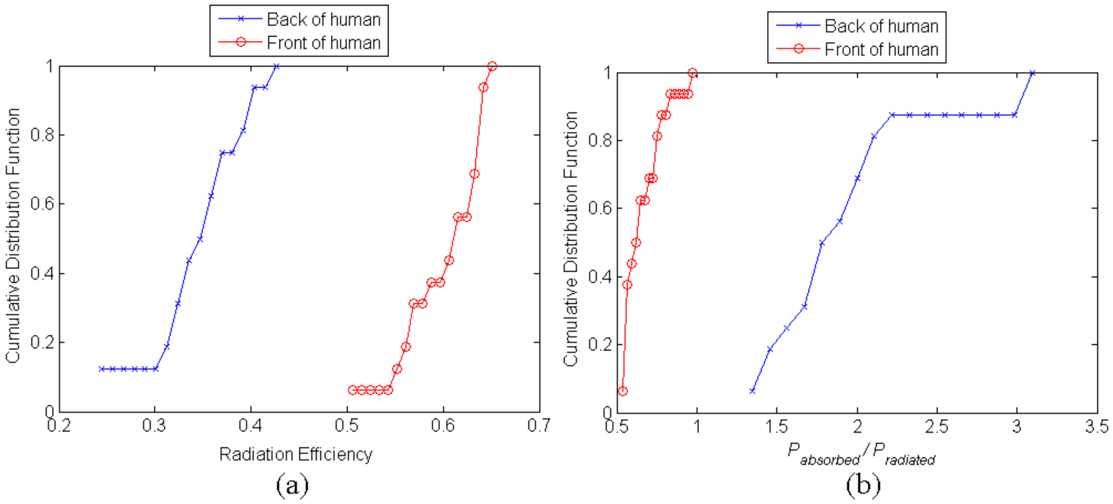

Figure 5.75: Cumulative distribution function of vertical polarised antenna located at the front and back of the human for: (a) radiation efficiency, (b) $P_{absorbed}$ / $P_{radiated}$.

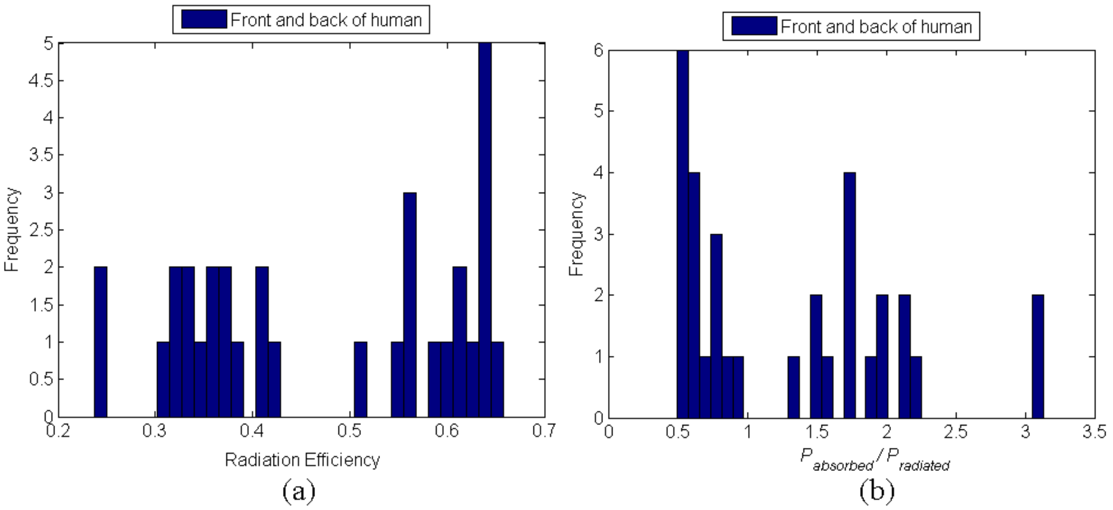

Figure 5.76: Histogram (front and back combination) of vertical polarised antenna for: (a) radiation efficiency, (b) $P_{absorbed}$ / $P_{radiated}$.

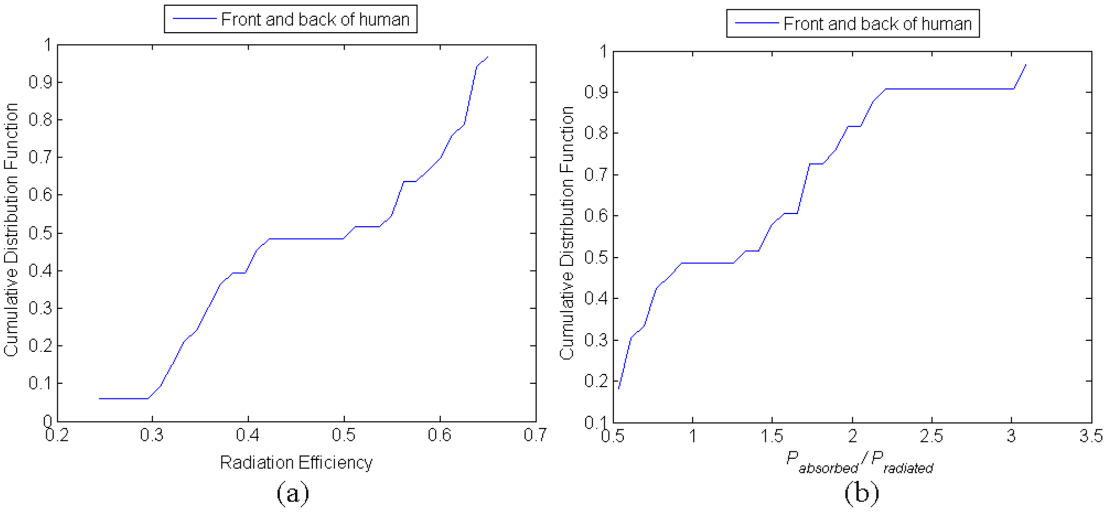

Figure 5.77: Cumulative distribution function (front and back combination) of vertical polarised antenna for: (a) radiation efficiency, (b) $P_{absorbed} / P_{radiated}$.

It can be observed from the histogram that the radiation efficiency values increase as the antenna moves from the back to the front of the human body. The antenna achieves better radiation efficiency of 43% mean percentage value for both horizontal and vertical polarisation when the antenna been located on the front of the human model compared to the case of the back position. The understanding for this appears to be due to a loss of characteristics in the tissue at the front, and a greater degree of absorbed power, as can be seen from the figures. The absorbed power is generally much higher at the back of the human body compared to the front side. This is clearly shown in some of the figures for subgrid area such as Figures 5.35 and 5.39 for horizontal polarisation, Figures 5.47 and 5.51 for vertical polarisation. Here, high electric field concentration inside the human tissue can be seen clearly. It can be concluded from the figures that the CDF has similar curves for horizontal and vertical polarisation for these locations. In addition, it is apparent that the standard deviation of the radiation efficiency when the mobile is located in the front is less compared to back location. Taking the previous simulation results into account, we may safely conclude that altering the position of the antenna on the front will not results in a large dispersion in the radiation efficiency of the antenna. In addition, the CDF has similar curves for horizontal and vertical cases for both locations.

5.6 Conclusion

A hybrid MoM-FDTD-SGFDTD approach has been adopted for modelling the human body interaction with short range RFID antenna. A total of 32 locations on the human body were investigated, 16 on the back and 16 on the front. In order to ensure the optimal quality of results were achieved through this limited sample, each point was investigated using two polarisations; essentially horizontal and vertical polarisations. MoM technique was used to produce the electric and magnetic fields created by the antenna in free space. From here, the equivalent electric and magnetic sources on the Huygens surface were produced at each time step. FDTD technique was then applied for the whole structure of the problem combined with subgridding method at the object of interest particularly inside the human body nearby the source excitation. The model of the human body was designed to be inhomogeneous at proximity to the RFID antenna operating at 900 MHz. The near and far field distributions were incorporated into the study to heighten the understanding of the impact on human tissue both facing the antenna, and not directly facing the antenna. The cumulative distribution function of the radiation efficiency and the ratio of absorbed power over radiated power of the antenna at these locations was also computed. The results support the conclusion that there was a clear improvement in the front of the human body model compared to the back position. The combination of hybrid MoM-FDTD-SGFDTD method approach with arbitrary inhomogeneous human body model sustains development of new EM fields interaction modelling approach. This study will robustly support the requirements of the total power dissipated of the human body samples to estimate the SAR values inside human tissue.

5.7 References

[1] M. Abalenkovs, F. Costen, J. P. Berenger, and A. Brown, "Application of huygens subgridding technique to human body modelling," *Antennas and Propagation Society International Symposium*, pp. 1-4, 2008.

[2] A. Sani, Y. Zhao, Y. Hao, A. Alomainy, and C. Parini, "An efficient FDTD algorithm based on the equivalence principle for analyzing onbody antenna performance," *IEEE Transactions on Antennas and Propagation*, vol. 57, pp. 1006-1014, 2009.

[3] Y. Z. Sani, A. Y. Hao, S.-L. Lee, and G.-Z. Yang, "A simulation environment for subject-specific radio channel modeling in wireless body sensor networks," *Sixth International Workshop on Wearable and Implantable Body Sensor Networks (BSN 2009), Berkeley, CA*, pp. 23-28, 2009.

[4] J.-H. Jung, S.-W. Kim, Y.-S. Kim, and S.-Y. Kim, "Electromagnetic propagation from the intestine-ingested source in the human body model," *IEEE Transactions on Antennas and Propagation*, vol. 58, pp. 1683-1688, 2010.

[5] A. Bahillo, J. Prieto, S. Mazuelas, R. M. Lorenzo, P. Fernandez, and E. J. Abril, "E-Field assessment errors caused by the human body on localization systems," *IEEE 71st Vehicular Technology Conference (VTC 2010-Spring), Taipei*, pp. 1-5, 2010.

[6] V. Singh, A. Ajeet, N. Kwatra, C. J. Cela, J. Ziriax, J. D'Andrea, and G. Lazzi, "Computation of induced current densities in the human body at low frequencies due to contact electrodes using the ADI-FDTD method," *IEEE Transactions on Electromagnetic Compatibility*, vol. 52, pp. 537-544, 2010.

[7] J. N. Bringuier and R. Mittra, "A new technique for modeling in-body and on-body antennas," *Proceedings of the Fourth European Conference on Antennas and Propagation (EuCAP)*, pp. 1-3, 2010.

[8] K. Ito, R. Suga, N. Haga, M. Takahashi, and K. Saito, "Link characteristics between wearable antenna and receivers equipped on external objects at MHz band," *Proceedings of the Fourth European Conference on Antennas and Propagation (EuCAP), Barcelona, Spain*, pp. 1-4, 2010.

[9] A. Schiavoni, "The role of FDTD technique in exposure assessment of wireless communication devices," *Workshop on Computational Electromagnetics in Time-Domain*, pp. 1-4, 2007.

[10] L. S. Xu, M. Q.-H. Meng, and Y. W. Chan, "Effects of dielectric parameters of human body on radiation characteristics of ingestible wireless device at operating frequency of 430 MHz," *IEEE Transactions on Biomedical Engineering*, vol. 56, pp. 2083-2094, 2009.

[11] L. S. Xu, M. Q.-H. Meng, and B. P. Li, "Effects of dielectric values of human body on specific absorption rate (SAR) following 800 MHz radio frequency exposure to ingestible wireless device," *Annual International Conference of the IEEE in Engineering in Medicine and Biology Society (EMBC), Minneapolis, MN*, pp. 5060-5063, 2009.

[12] L. S. Xu, M. Q.-H. Meng, and C. Hu, "Effects of dielectric values of human body on specific absorption rate following 430, 800, and 1200 MHz RF exposure to

ingestible wireless device," *IEEE Transactions on Information Technology in Biomedicine*, vol. 14, pp. 52-59, 2010.

[13] L. S. Xu, Y. P. Yao, Y. Wang, C. Feng, Y. Kang, and M. Q.-H. Meng, "Effects of dielectric values of human body on radiation characteristics of ingestible wireless device following 1200 MHz," *4th International Conference on Bioinformatics and Biomedical Engineering (iCBBE), Chengdu, China*, pp. 1-4, 2010.

[14] T. Hikage, Y. Kawamura, and T. Nojima, "Whole-body averaged SAR measurement based on electric field distributions on external cylindrical boundary," *Proceedings of the Fourth European Conference on Antennas and Propagation (EuCAP), Barcelona, Spain*, pp. 1-4, 2010.

[15] E. Cocherova, J. Surda, O. Ondracek, and V. Stofanik, "RF field orientation influence on the specific absorption rate in a biological object," *Conference on Microwave Techniques*, pp. 1-3, 2008.

[16] S. S. Stuchly, M. A. Stuchly, A. Kraszewski, and G. Hartsgrove, "Energy deposition in a model of man: Frequency effects," *IEEE Transactions on Biomedical Engineering*, vol. BME-33, pp. 702-711, 1986.

[17] D. Arnaud-Cormos, R. Loison, and R. Gillard, "Fast multistructure method of moments combined with a genetic algorithm (MSMoM/GA) for efficient optimization of printed antennas," *IEEE Antennas and Wireless Propagation Letters*, vol. 6, pp. 172-174, 2007.

[18] A. Becker and V. Hansen, "A hybrid method combining the multitemporal resolution time-domain method of moments with the time-domain geometrical theory of diffraction for thin-wire antenna problems," *IEEE Transactions on Antennas and Propagation*, vol. 54, pp. 953- 960, 2006.

[19] M. M. Ilic and B. M. Notaros, "Computation of FEM-domain fields in the higher order hybrid FEM-MoM solution," *IEEE Antennas and Propagation Society International Symposium (APSURSI)*, pp. 1-4, 2010.

[20] A. Monorchio, A. R. Bretones, R. Mittra, G. Manara, and R. G. Martin, "A hybrid time-domain technique that combines the finite element, finite difference and method of moment techniques to solve complex electromagnetic problems," *IEEE Transactions on Antennas and Propagation*, vol. 52, pp. 2666-2674, 2004.

[21] R. A. Abd-Alhameed, P. S. Excell, and M. A. Mangoud, "A hybrid computational electromagnetics formulation for simulation of antennas coupled to lossy and dielectric volumes," *IEEE Transactions on Broadcasting*, vol. 50, pp. 253- 259, 2004.

[22] R. A. Abd-Alhameed, P. S. Excell, and M. A. Mangoud, "Broadband antenna response using hybrid technique of frequency domain of MoM and FDTD," *ACES Applied Computational Electromagnetics Society Journal*, vol. 20, pp. 70-77, 2005.

[23] S. Mochizuki, S. Watanabe, M. Taki, Y. Yamanaka, and H. Shirai, "Novel iteration procedures of a hybrid method combining MoM and scattered-field FDTD method for electromagnetic dosimetry," *IEEE Topical Conference on Wireless Communication Technology*, pp. 200-201, 2003.

[24] R. Mittra, "Simulation of large multiscale structures using the finite difference time domain method (FDTD) hybridized with the Method of Moments (MoM)," *3rd European Conference on Antennas and Propagation (EuCAP)*, pp. 2749-2752, 2009.

[25] Z. Bo, H. Xiaojun, J. Bin, G. Hao, and S. Xujian, "An MoM/FDTD hybrid technique for modeling HF antennas located on ground," *International Conference*

on Microwave and Millimeter Wave Technology (ICMMT), pp. 1344-1347, 2010.

[26] M. A. Mangoud, *Hybrid computational electromagnetics methods for personal communications applications*. Ph. D. Thesis, Department of Electronic and Electrical Engineering: University of Bradford, UK, 2001.

[27] D. Zhou, R. A. Abd-Alhameed, C. H. See, M. S. Alkhambashi, Z. Zainal Abidin, K. N. Ramli, and M. M. Abusitta, "Meander-line antenna design for UHF RFID tag using a genetic algorithm," *Progress in Electromagnetics Research Symposium, Beijing, China*, pp. 1253-1256, 2009.

[28] G. J. Burke and A. J. Poggio, "Numerical electromagnetics code (NEC): method of moments," *US Naval Ocean Systems Centre, Rep. No. TD116*, 1981.

[29] P. A. Mason, W. D. Hurt, T. J. Walters, J. A. D'Andrea, P. Gajsek, K. L. Ryan, D. A. Nelson, K. I. Smith, and J. M. Ziriax, "Effects of frequency, permittivity, and voxel size on predicted specific absorption rate values in biological tissue during electromagnetic-field exposure," *IEEE Transactions on Microwave Theory and Techniques*, vol. 48, pp. 2050-2058, 2000.

[30] R. A. Abd-Alhameed, P. S. Excell, C. H. See, D. Zhou, and K. N. Ramli, "Accurate field distribution models for RFID applications using hybrid computational electromagnetics techniques," *Progress in Electromagnetics Research Symposium, Cambridge, USA*, pp. 436-442, 2008.

Chapter 6

Conclusion and Recommendation for Further Work

6.1 Summary of Thesis

The primary objective of this thesis is the development of hybrid MoM-FDTD-SGFDTD numerical method by using the principle of equivalence surface boundary to connect the three techniques. The hybridisation of MoM-FDTD-SGFDTD method is applicable to electromagnetic radiation and scattering problems due to its capability to overcome the drawbacks of homogeneous MoM and FDTD simulations including its appropriateness in modelling realistic electromagnetic analysis. The state of art of the original achievement of the present work can be summarised as follows:

- In chapter 2, the overview and formulation of FDTD concept has been discussed, including the implementation of FDTD code procedure with the adaptation of Berenger's PML absorbing boundary condition. The method has the advantage of discretising a continuous domain into finite number of sections which necessitate a set of difference equations to solve Maxwell's curl equations in the time domain. The parameters that control the accuracy and stability of the FDTD simulation and the modelling of the plane wave source technique by means of the equivalent surface were also described.

- Chapter 3 unfolds the theoretical concept behind MoM principles including the mathematical formulation of the surface kernel solution. The problem of singularity was alleviated by means of singular cancellation technique. The desired impedance matrix elements have been evaluated and its inversion was computed using standard inversion NAG subroutine code. The elements of impedance matrix were employed to calculate the current and then the radiation pattern of the radiating antenna element. The surface current distributions on structures with closely spaced parallel wires was computed with a general surface patch formulation. Two-dimensional electric surface patch integral equation formulation was solved by independent piecewise-linear basis function methods in the circumferential and axial directions of the wire.

- Chapter 4 presents the modelling and analysis of quasi-static FDTD subgridding technique in two-dimensional approach. The method has been applied to model biological cell with floquet theorem. Subgridding technique was imposed on cytoplasm cells to observe electric field distribution in high resolution. The interaction between high voltage overhead transmission lines and underground pipeline at power-line frequency is also modelled for validation purposes. FDTD technique was used for the whole structure in the computational domain combined with subgrid method employed at the object of interest particularly the underground pipeline and some surrounding medium. The soil in the common corridor has been designed as arbitrarily inhomogeneous to simulate real dry soil. The field distribution for the whole spatial problem and the area surrounding the pipeline has been reported. The induced EM fields above the ground where the pipeline was located has been investigated.

- Chapter 5 explains the new hybridisation technique of MoM-FDTD-SGFDTD computational electromagnetic and establishing the importance of past published literature survey on hybrid methods. The modelling on multiple-region hybrid techniques with frequency-domain MoM and time-domain FDTD including embedded subgridding were suggested and investigated. The method was validated for near field and far field applications, particularly on the interaction between electromagnetic fields and human body in which short range RFID antenna is located and moved at several positions in front and back of inhomogeneous human body model. Statistical analysis such as the cumulative distribution function of the radiation efficiency and $P_{absorbed}$ / $P_{radiated}$ ratio of the antenna at these locations was incorporated into the research work to enhance the understanding of the electromagnetic fields distribution impact on human tissue.

6.2 Conclusion

The project concerns the new modified development of numerical methods that involves the hybridisation of MoM and FDTD including the subgridding process within the problem space. The principle of the equivalent surface boundary was employed with a possibility of replacing one or two equivalent surface boundaries by conducting surfaces. For the proposed subgridding technique, a linear field interpolation technique of a maximum order of six divisions is used to predict the unknown fields between the coarse and fine area of the lattice. The implementation of subgridding which is embedded inside FDTD problem space involves local mesh refinement particularly inside the region or volume of interest which need more accurate discretisation to predict field distribution in high resolution. The method is particularly useful for analysing complex problems involving coupling between source excitation such as antenna and arbitrarily inhomogeneous dielectric volume such as human body. In general, hybrid approach takes advantage of the best attributes offered by different techniques to solve problems that neither technique alone can be modelled precisely. As a result, the electromagnetic computational problem solving methodology was increased efficiently. In other words, the antenna structure can be designed using the frequency-domain MoM whereas the inhomogeneous dielectric volume might be modelled by means of computationally-efficient FDTD. Several examples have been discussed and the results show good convergence stability. The combination of singular cancellation technique in surface kernel MoM solution, arbitrarily inhomogeneous dielectric volume model and the modified Berenger's absorbing boundary condition represent a significant advance in modelling the complex electromagnetic scattering problems.

6.3 Recommendation for Further Work

Finally, the following are examples of interesting themes that deserve further development in the future:

- Further study on accurate modelling of small sensors such as RFID tag antennas with dual polarisation mounted on complex dielectric structures can be carried out [1, 2]. The method can also be applied to other type of complex surface patch antennas working at different frequency band such as 3G UMTS frequency band (1920 MHz to 2170 MHz) [3], and dual bands planar inverted F-L antenna for 2.5 GHz cellular and 5.2 GHz WLAN applications [4].

- Different spatial resolution for subgrid region such as 30 × 30 × 30 or 40 × 40 × 40 can also be employed to observe the fields in more resolution pattern.
- The work can be further investigated by using different type of subgridding technique for comparison purposes such as non-uniform mesh [5] and lobatto cell [6, 7]. Figure 6.1(a), 6.1(b) and 6.1(c) describe the general geometry of normal subgridding, non-uniform mesh and lobatto cell procedure respectively.

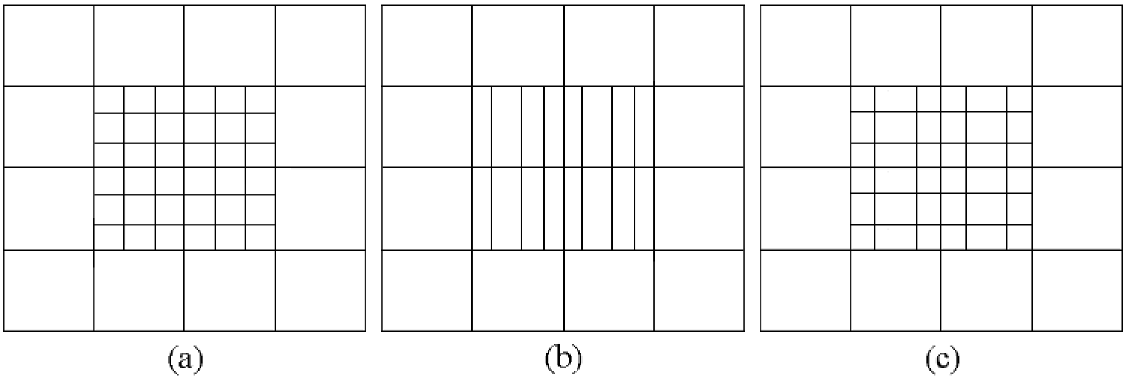

Figure 6.1: Comparison between subgridding method: (a) Normal subgridding, (b) Non-uniform mesh, (c) Lobatto cell method.

- 1 mm human tissue size can be proposed to model the inhomogeneous human body [8].
- The work presented here can be extended to study human body tissue heat absorption measured by SAR variation values [9, 10].

- The present work can be very attractive to include sub-surface radar application to predict the existance of breast cancer cells for modelling purposes in which the accurate field distribution inside the breast tissue can be obtained.

6.4 References

[1] W.-S. Chen and Y.-C. Huang, "A novel RFID reader antenna with circular polarization operation," *International Conference on Applications of Electromagnetism and Student Innovation Competition Awards (AEM2C)*, pp. 117-120, 2010.

[2] N. Nasimuddin, Z. Chen, and X. Qing, "Asymmetric-circular shaped slotted microstrip antennas for circular polarization and RFID applications," *IEEE Transactions on Antennas and Propagation*, pp. 1-8, 2010.

[3] C. H. See, R. A. Abd-Alhameed, D. Zhou, K. N. Ramli, N. J. McEwan, and P. S. Excell, "Folded and slotted internal antenna design for 3G IMT-2000 mobile handsets," *Microwave and Optical Technology Letters*, vol. 52, pp. 1549-1553, 2010.

[4] C. H. See, R. A. Abd-Alhameed, D. Zhou, E. A. Elkhazmi, M. M. Abusitta, K. N. Ramli, and P. S. Excell, "Miniature dual-frequency half planar inverted F-L-antenna for WLAN/cellular applications," *Asia-Pacific Microwave Conference*, pp. 2802-2804, 2009.

[5] R. Wu, G. Benqing, and Y. Shiming, "An improved method in FDTD simulation to reduce reflection from non-uniform mesh," *3rd International Conference on Microwave and Millimeter Wave Technology Proceedings*, pp. 646-649, 2002.

[6] R. A. Chilton and R. Lee, "Conservative subgridding for lobatto cell FDTD method," *IEEE Antennas and Propagation Society International Symposium*, pp. 1-4, 2008.

[7] R. A. Chilton and R. Lee, "The lobatto cell: Robust, explicit, higher order FDTD that handles inhomogeneous media," *IEEE Transactions on Antennas and Propagation*, vol. 56, pp. 2167-2177, 2008.

[8] V. Singh, A. Ajeet, N. Kwatra, C. J. Cela, J. Ziriax, J. D'Andrea, and G. Lazzi, "Computation of induced current densities in the human body at low frequencies due to contact electrodes using the ADI-FDTD method," *IEEE Transactions on Electromagnetic Compatibility*, vol. 52, pp. 537-544, 2010.

[9] L. S. Xu, M. Q.-H. Meng, and C. Hu, "Effects of dielectric values of human body on specific absorption rate following 430, 800, and 1200 MHz RF exposure to ingestible wireless device," *IEEE Transactions on Information Technology in Biomedicine*, vol. 14, pp. 52-59, 2010.

[10] T. Hikage, Y. Kawamura, and T. Nojima, "Whole-body averaged SAR measurement based on electric field distributions on external cylindrical boundary," *Proceedings of the Fourth European Conference on Antennas and Propagation (EuCAP), Barcelona, Spain*, pp. 1-4, 2010.

Appendix A

To find the tangent surface equation at a point on the curved surface can be stated in the following. For simplicity, assume each point on the curved surface *S* for all 3-D axes can be represented by two variables as *u* and *v* given by:

$$x = f(u,v), \qquad x_o = f(u_o, v_o) \tag{A.1}$$

$$y = g(u,v), \qquad y_o = g(u_o, v_o) \tag{A.2}$$

$$z = h(u,v), \qquad z_o = h(u_o, v_o) \tag{A.3}$$

It should be noted that the above equations must be differentiable at any given point such as (x_o, y_o, z_o). Hereafter, these should be differentiable at (u_o, v_o). Thus, the partial differentiation with respect to *u* and *v* evaluated at (u_o, v_o) is given by:

$$\underline{a} = \begin{bmatrix} f_u & g_u & h_u \end{bmatrix} \tag{A.4}$$

$$\underline{b} = \begin{bmatrix} f_v & g_v & h_v \end{bmatrix} \tag{A.5}$$

where $R_p = \partial R/\partial p$, *R* could be *f* or *g* or *h* and *p* might be *u* or *v*. The normal vector to the surface (i.e. orthogonal to the surface), can be expressed as:

$$\begin{bmatrix} L \\ M \\ N \end{bmatrix} = \underline{a} \times \underline{b} \tag{A.6}$$

The above notation can be extended using the cross product as in the following matrix:

$$\begin{bmatrix} L \\ M \\ N \end{bmatrix} = \begin{bmatrix} (g_u \times h_v) - (g_v \times h_u) \\ (f_v \times h_u) - (f_u \times h_v) \\ (f_u \times g_v) - (f_v \times h_u) \end{bmatrix} \tag{A.7}$$

The total length of the normal vector can be given by:

$$D = \sqrt{L^2 + M^2 + N^2} \tag{A.8}$$

The tangent plane should satisfy the following formula:

$$\frac{L}{D} x + \frac{M}{D} y + \frac{N}{D} z = Lx_o + My_o + Nz_o \tag{A.9}$$

Thus, the tangent surface for a point at (x_o, y_o, z_o) can simply be expressed by the following:

$$L(x - x_o) + M(y - y_o) + N(z - z_o) = 0 \tag{A.10}$$

Of course the result is equivalent to the following necessary condition:

$$F(x, y, z) = 0 \tag{A.11}$$

The above equations are also applicable to direct surface equation such as that given by the unit sphere at the origin:

$$x^2 + y^2 + z^2 - 1 = 0 \tag{A.12}$$

The equation of the tangent plane at (x_o, y_o, z_o):

$$\left.\frac{\partial F}{\partial x}\right|_{x_o, y_o, z_o} (x - x_o) + \left.\frac{\partial F}{\partial y}\right|_{x_o, y_o, z_o} (y - y_o) + \left.\frac{\partial F}{\partial z}\right|_{x_o, y_o, z_o} (z - z_o) = 0 \tag{A.13}$$

Keep in mind the required transformation can also be implemented for other coordinates such as between the spherical and the Cartesian coordinates, given by:

$$\begin{array}{ccc} r_o & & x_o \\ \theta_o & \rightarrow & y_o \\ \phi_o & & z_o \end{array} \tag{A.14}$$

Again the above derivation can be applied to simple surfaces such as the one given by the following example. Surface equation is $z = 4x^3y^2 + 2y$ and the tangent at point (1, -2, 12) can be derived as:

$$f\left(x,y\right)=4x^{3}y^{2}+2y \tag{A.15a}$$

$$\frac{\partial f}{\partial x}=12x^{2}y^{2} \tag{A.15b}$$

$$\frac{\partial f}{\partial y}=8x^{3}y+2 \tag{A.15c}$$

Substituting the value of x_o = 1 and y_o = -2 to equation (A.15b) and (A.15c) gives:

$$\left.\frac{\partial f}{\partial x}\right|_{x_o,y_o}=48 \tag{A.15d}$$

$$\left.\frac{\partial f}{\partial y}\right|_{x_o,y_o}=-14 \tag{A.15e}$$

Hence, the tangent plane is given by the expression:

$$48\left(x-1\right)-14\left(y+2\right)-\left(z-12\right)=0 \tag{A.15f}$$

$$48x-14y-z=64 \tag{A.15g}$$

Finally, the tangent surface of helix wire can be derived as follows:

Given the coordinates of the helix by the following:

$$x = \left(b + a\cos\theta\right)\cos\phi \tag{A.16}$$

$$y = \left(b + a\cos\theta\right)\sin\phi \tag{A.17}$$

$$z = \frac{P}{2\pi}\phi + a\sin\theta \tag{A.18}$$

$$\begin{bmatrix} L \\ M \\ N \end{bmatrix} = \begin{bmatrix} \left.\dfrac{\partial x}{\partial \theta}\right|_{\theta_o,\phi_o} \\ \left.\dfrac{\partial y}{\partial \theta}\right|_{\theta_o,\phi_o} \\ \left.\dfrac{\partial z}{\partial \theta}\right|_{\theta_o,\phi_o} \end{bmatrix} \times \begin{bmatrix} \left.\dfrac{\partial x}{\partial \phi}\right|_{\theta_o,\phi_o} \\ \left.\dfrac{\partial x}{\partial \phi}\right|_{\theta_o,\phi_o} \\ \left.\dfrac{\partial x}{\partial \phi}\right|_{\theta_o,\phi_o} \end{bmatrix} \tag{A.19}$$

Appendix B

The expression for C in equation (3.46) in Chapter 3 is given by:

$$
\begin{aligned}
C = {} & \log(t_1 + t + (v^2 + p^2 + 2pp_1 + p_1^2 + t^2 + 2tt_1 + t_1^2)^{\frac{1}{2}})p - p + \frac{1}{2}p_1 \\
& \times \log(v^2 + p^2 + 2pp_1 + p_1^2) + v \times \operatorname{atan}(\frac{1}{2}(2p + 2p_1)/v) + \frac{1}{2}t/((t+t_1)^2)^{\frac{1}{2}} \\
& \times \log((2t^2 + 4tt_1 + 2t_1^2 + 2(-v^2)^{\frac{1}{2}}(p + p_1 - (-v^2)^{\frac{1}{2}}) + 2((t+t_1)^2)^{\frac{1}{2}}((p + p_1 - (-v^2)^{\frac{1}{2}})^2 \\
& + 2(-v^2)^{\frac{1}{2}}(p + p_1 - (-v^2)^{\frac{1}{2}}) + t^2 + 2tt_1 + t_1^2)^{\frac{1}{2}})/(p + p_1 - (-v^2)^{\frac{1}{2}}))p_1 - \frac{1}{2}t(-v^2)^{\frac{1}{2}}/((t+t_1)^2)^{\frac{1}{2}} \\
& \times \log((2t^2 + 4tt_1 + 2t_1^2 + 2(-v^2)^{\frac{1}{2}}(p + p_1 - (-v^2)^{\frac{1}{2}}) + 2((t+t_1)^2)^{\frac{1}{2}}((p + p_1 - (-v^2)^{\frac{1}{2}})^2 \\
& + 2(-v^2)^{\frac{1}{2}}(p + p_1 - (-v^2)^{\frac{1}{2}}) + t^2 + 2tt_1 + t_1^2)^{\frac{1}{2}})/(p + p_1 - (-v^2)^{\frac{1}{2}})) + \frac{1}{2}t(-v^2)^{\frac{1}{2}}/((t+t_1)^2)^{\frac{1}{2}} \\
& \times \log((2t^2 + 4tt_1 + 2t_1^2 - 2(-v^2)^{\frac{1}{2}}(p + p_1 + (-v^2)^{\frac{1}{2}}) + 2((t+t_1)^2)^{\frac{1}{2}}((p + p_1 + (-v^2)^{\frac{1}{2}})^2 \\
& - 2(-v^2)^{\frac{1}{2}}(p + p_1 + (-v^2)^{\frac{1}{2}}) + t^2 + 2tt_1 + t_1^2)^{\frac{1}{2}})/(p + p_1 + (-v^2)^{\frac{1}{2}})) + \frac{1}{2}t/((t+t_1)^2)^{\frac{1}{2}} \\
& \times \log((2t^2 + 4tt_1 + 2t_1^2 - 2(-v^2)^{\frac{1}{2}}(p + p_1 + (-v^2)^{\frac{1}{2}}) + 2((t+t_1)^2)^{\frac{1}{2}}((p + p_1 + (-v^2)^{\frac{1}{2}})^2 \\
& - 2(-v^2)^{\frac{1}{2}}(p + p_1 + (-v^2)^{\frac{1}{2}}) + t^2 + 2tt_1 + t_1^2)^{\frac{1}{2}})/(p + p_1 + (-v^2)^{\frac{1}{2}}))p_1 + \frac{1}{2}t_1/((t+t_1)^2)^{\frac{1}{2}} \\
& \times \log((2t^2 + 4tt_1 + 2t_1^2 + 2(-v^2)^{\frac{1}{2}}(p + p_1 - (-v^2)^{\frac{1}{2}}) + 2((t+t_1)^2)^{\frac{1}{2}}((p + p_1 - (-v^2)^{\frac{1}{2}})^2 \\
& + 2(-v^2)^{\frac{1}{2}}(p + p_1 - (-v^2)^{\frac{1}{2}}) + t^2 + 2tt_1 + t_1^2)^{\frac{1}{2}})/(p + p_1 - (-v^2)^{\frac{1}{2}}))p_1 - \frac{1}{2}t_1(-v^2)^{\frac{1}{2}}/((t+t_1)^2)^{\frac{1}{2}} \\
& \times \log((2t^2 + 4tt_1 + 2t_1^2 + 2(-v^2)^{\frac{1}{2}}(p + p_1 - (-v^2)^{\frac{1}{2}}) + 2((t+t_1)^2)^{\frac{1}{2}}((p + p_1 - (-v^2)^{\frac{1}{2}})^2 \\
& + 2(-v^2)^{\frac{1}{2}}(p + p_1 - (-v^2)^{\frac{1}{2}}) + t^2 + 2tt_1 + t_1^2)^{\frac{1}{2}})/(p + p_1 - (-v^2)^{\frac{1}{2}}))t \\
& \times \log(p + p_1 + (v^2 + p^2 + 2pp_1 + p_1^2 + t^2 + 2tt_1 + t_1^2)^{\frac{1}{2}}) + t_1 \\
& \times \log(p + p_1 + (v^2 + p^2 + 2pp_1 + p_1^2 + t^2 + 2tt_1 + t_1^2)^{\frac{1}{2}}) + \frac{1}{2}t_1(-v^2)^{\frac{1}{2}}/((t+t_1)^2)^{\frac{1}{2}} \ldots
\end{aligned}
$$

$$\ldots\times\log((2t^2+4tt_1+2t_1^2-2(-v^2)^{\frac{1}{2}}(p+p_1+(-v^2)^{\frac{1}{2}})+2((t+t_1)^2)^{\frac{1}{2}}((p+p_1+(-v^2)^{\frac{1}{2}})^2$$

$$-2(-v^2)^{\frac{1}{2}}(p+p_1+(-v^2)^{\frac{1}{2}})+t^2+2tt_1+t_1^2)^{\frac{1}{2}})/(p+p_1+(-v^2)^{\frac{1}{2}}))+\frac{1}{2}t_1/((t+t_1)^2)^{\frac{1}{2}}$$

$$\times\log((2t^2+4tt_1+2t_1^2-2(-v^2)^{\frac{1}{2}}(p+p_1+(-v^2)^{\frac{1}{2}})+2((t+t_1)^2)^{\frac{1}{2}}((p+p_1+(-v^2)^{\frac{1}{2}})^2$$

$$-2(-v^2)^{\frac{1}{2}}(p+p_1+(-v^2)^{\frac{1}{2}})+t^2+2tt_1+t_1^2)^{\frac{1}{2}})/(p+p_1+(-v^2)^{\frac{1}{2}}))p_1$$

The expression for D in equation (3.46) in Chapter 3 is given by:

$$D=\frac{1}{4}(2p+2p_1)(v^2+p^2+2pp_1+p_1^2+t^2+2tt_1+t_1^2)^{\frac{1}{2}}+\frac{1}{2}$$

$$\times\log(p+p_1+(v^2+p^2+2pp_1+p_1^2+t^2+2tt_1+t_1^2)^{\frac{1}{2}})v^2-\frac{1}{2}$$

$$\times\log(p+p_1+(v^2+p^2+2pp_1+p_1^2+t^2+2tt_1+t_1^2)^{\frac{1}{2}})t_1^2+\frac{1}{2}$$

$$\times\log(p+p_1+(v^2+p^2+2pp_1+p_1^2+t^2+2tt_1+t_1^2)^{\frac{1}{2}})t^2-t_1p$$

$$\times\log(t_1+t+(v^2+p^2+2pp_1+p_1^2+t^2+2tt_1+t_1^2)^{\frac{1}{2}})+t_1p-\frac{1}{2}t_1tp_1/((t+t_1)^2)^{\frac{1}{2}}$$

$$\times\log((2t^2+4tt_1+2t_1^2+2(-v^2)^{\frac{1}{2}}(p+p_1-(-v^2)^{\frac{1}{2}})+2((t+t_1)^2)^{\frac{1}{2}}((p+p_1-(-v^2)^{\frac{1}{2}})^2+2(-v^2)^{\frac{1}{2}}$$

$$\times(p+p_1-(-v^2)^{\frac{1}{2}})+t^2+2tt_1+t_1^2)^{\frac{1}{2}})/(p+p_1-(-v^2)^{\frac{1}{2}})+t^2+2tt_1+t_1^2)^{\frac{1}{2}}))-\frac{1}{2}t_1tp_1/((t+t_1)^2)^{\frac{1}{2}}$$

$$\times\log((2t^2+4tt_1+2t_1^2-2(-v^2)^{\frac{1}{2}}(p+p_1+(-v^2)^{\frac{1}{2}})+2((t+t_1)^2)^{\frac{1}{2}}((p+p_1+(-v^2)^{\frac{1}{2}})^2-2(-v^2)^{\frac{1}{2}}$$

$$\times(p+p_1+(-v^2)^{\frac{1}{2}})+t^2+2tt_1+t_1^2)^{\frac{1}{2}})/(p+p_1+(-v^2)^{\frac{1}{2}}))-\frac{1}{2}t_1^2p_1/((t+t_1)^2)^{\frac{1}{2}}$$

$$\times\log((2t^2+4tt_1+2t_1^2+2(-v^2)^{\frac{1}{2}}(p+p_1-(-v^2)^{\frac{1}{2}})+2((t+t_1)^2)^{\frac{1}{2}}((p+p_1-(-v^2)^{\frac{1}{2}})^2+2(-v^2)^{\frac{1}{2}}$$

$$\times(p+p_1-(-v^2)^{\frac{1}{2}})+t^2+2tt_1+t_1^2)^{\frac{1}{2}})/(p+p_1-(-v^2)^{\frac{1}{2}}))-\frac{1}{2}t_1^2p_1/((t+t_1)^2)^{\frac{1}{2}}$$

$$\times\log((2t^2+4tt_1+2t_1^2-2(-v^2)^{\frac{1}{2}}(p+p_1+(-v^2)^{\frac{1}{2}})+2((t+t_1)^2)^{\frac{1}{2}}((p+p_1+(-v^2)^{\frac{1}{2}})^2+2(-v^2)^{\frac{1}{2}})^2$$

$$-2(-v^2)^{\frac{1}{2}}(p+p_1+(-v^2)^{\frac{1}{2}})+t^2+2tt_1+t_1^2)^{\frac{1}{2}})/(p+p_1+(-v^2)^{\frac{1}{2}}))-\frac{1}{2}t_1p_1$$

$$\times\log((v^2+p^2+2pp_1+p_1^2+\frac{1}{2}t_1t(-v^2)^{\frac{1}{2}}/((t+t_1)^2)^{\frac{1}{2}}\ldots$$

$$\ldots\times\log((2t^2+4tt_1+2t_1^2+2(-v^2)^{\frac{1}{2}}(p+p_1-(-v^2)^{\frac{1}{2}})+2((t+t_1)^2)^{\frac{1}{2}}((p+p_1-(-v^2)^{\frac{1}{2}})^2+2(-v^2)^{\frac{1}{2}}$$

$$\times(p+p_1-(-v^2)^{\frac{1}{2}})+t^2+2tt_1+t_1^2)^{\frac{1}{2}})/(p+p_1-(-v^2)^{\frac{1}{2}}))-\frac{1}{2}t_1t(-v^2)^{\frac{1}{2}}/((t+t_1)^2)^{\frac{1}{2}}$$

$$\times\log((2t^2+4tt_1+2t_1^2-2(-v^2)^{\frac{1}{2}}(p+p_1+(-v^2)^{\frac{1}{2}})+2((t+t_1)^2)^{\frac{1}{2}}((p+p_1+(-v^2)^{\frac{1}{2}})^2-2(-v^2)^{\frac{1}{2}}$$

$$\times(p+p_1+(-v^2)^{\frac{1}{2}})+t^2+2tt_1+t_1^2)^{\frac{1}{2}})/(p+p_1+(-v^2)^{\frac{1}{2}}))+\frac{1}{2}t_1^2(-v^2)^{\frac{1}{2}}/((t+t_1)^2)^{\frac{1}{2}}$$

$$\times\log((2t^2+4tt_1+2t_1^2+2(-v^2)^{\frac{1}{2}}(p+p_1-(-v^2)^{\frac{1}{2}})+2((t+t_1)^2)^{\frac{1}{2}}((p+p_1-(-v^2)^{\frac{1}{2}})^2+2(-v^2)^{\frac{1}{2}}$$

$$\times(p+p_1-(-v^2)^{\frac{1}{2}})+t^2+2tt_1+t_1^2)^{\frac{1}{2}})/(p+p_1-(-v^2)^{\frac{1}{2}}))-\frac{1}{2}t_1^2(-v^2)^{\frac{1}{2}}/((t+t_1)^2)^{\frac{1}{2}}$$

$$\times\log((2t^2+4tt_1+2t_1^2-2(-v^2)^{\frac{1}{2}}(p+p_1+(-v^2)^{\frac{1}{2}})+2((t+t_1)^2)^{\frac{1}{2}}((p+p_1+(-v^2)^{\frac{1}{2}})^2-2(-v^2)^{\frac{1}{2}}$$

$$\times(p+p_1+(-v^2)^{\frac{1}{2}})+t^2+2tt_1+t_1^2)^{\frac{1}{2}})/(p+p_1+(-v^2)^{\frac{1}{2}}))-t_1v\times\mathrm{atan}(\frac{1}{2}(2p+2p_1)/v)$$

Author’s Contribution

ARTICLES IN JOURNAL

1. **K. N. Ramli**, R. A. Abd-Alhameed and P. S. Excell, "The complete surface current distribution in a normal-mode helical antenna," *IEEE Antenna and Propagation Magazine*, submitted in June 2010, pp. 1-21 (Accepted subject to revision, revised version has been submitted by Jan 2011).

2. C. H. See, R. A. Abd-Alhameed, D. Zhou, **K. N. Ramli**, N. J. McEwan and P. S. Excell, "Folded and slotted internal antenna design for 3G IMT-2000 mobile handsets," *Microwave and Optical Technology Letters*, vol. 52, pp. 1549-1553, 2010.

CONFERENCES AND WORKSHOPS

1. **K. N. Ramli**, R. A. Abd-Alhameed, H. I. Hraga, D. T. W. Liang and P. S. Excell, "Electromagnetic field interaction between overhead high voltage power transmission line and buried utility pipeline," *Progress in Electromagnetics Research Symposium, Marrakesh, Morocco*, pp. 1-5, 2011. (Accepted and to be published in March 2011)

2. Z. Z. Abidin, Y. Ma, R. A. Abd-Alhameed, **K. N. Ramli**, D. Zhou, M. S. Bin-Melha, J. M. Noras and R. Halliwell, "Design of 2 x 2 U-shape MIMO slot antennas with EBG material for mobile handset applications," *Progress in Electromagnetics Research Symposium, Marrakesh, Morocco*, pp. 1-4, 2011. (Accepted and to be published in March 2011)

3. A. G. Alhaddad, **K. N. Ramli**, R. A. Abd-Alhameed and D. Zhou, "Interaction between electromagnetic field and human body for dual band balanced antenna

using hybrid computational method," *Loughborough Antennas & Propagation Conference, UK*, pp. 1-4, 2010.

4. **K. N. Ramli**, R. A. Abd-Alhameed, C. H. See, D. Zhou, E. A. Elkhazmi and P. S. Excell, "Precise computation of the induced fields inside biological cell tissue using floquet boundary and subgridding quasi-static FDTD method," *Asia-Pacific Microwave Conference, Singapore*, pp. 1533-1536, 2009.

5. C. H. See, R. A. Abd-Alhameed, D. Zhou, E. A. Elkhazmi, M. M. Abusitta, **K. N. Ramli** and P. S. Excell, "Miniature dual-frequency half planar inverted F-L-antenna for WLAN/cellular applications," *Asia-Pacific Microwave Conference, Singapore*, pp. 2802-2804, 2009.

6. Z. Zainal Abidin, R. A. Abd-Alhameed, N. J. McEwan, S. M. R. Jones, **K. N. Ramli** and A. G. Alhaddad, "Design and analysis of UC-EBG on mutual coupling reduction," *Loughborough Antennas & Propagation Conference, UK*, pp. 693-696, 2009.

7. J. Moustafa, R. A. Abd-Alhameed, D. Zhou, C. H. See, N. J. McEwan, P. S. Excell, **K. N. Ramli** and Z. Zainal Abidin, "SAR measurements for several two elements phased antenna array handsets," *3rd European Conference on Antennas and Propagation, Berlin, Germany*, pp. 1-4, 2009.

8. D. Zhou, R. A. Abd-Alhameed, C. H. See, M. S. Alkhambashi, Z. Zainal Abidin, **K. N. Ramli** and M. M. Abusitta, "Meander-line antenna design for UHF RFID tag using a genetic algorithm," *Progress in Electromagnetics Research Symposium, Beijing, China*, pp. 1253-1256, 2009.

9. R. A. Abd-Alhameed, P. S. Excell, C. H. See, D. Zhou and **K. N. Ramli**, "Accurate field distribution models for RFID applications using hybrid computational

electromagnetics techniques," *Progress in Electromagnetics Research Symposium, Cambridge, USA*, pp. 436-442, 2008.

10. **K. N. Ramli**, R. A. Abd-Alhameed, D. Zhou, P. S. Excell, C. H. See, Z. Zainal Abidin, M. S. Alkhambashi, M. M. Abusitta and H. Xu, "Accurate hybrid computational electromagnetics techniques," *9th Informatics Workshop for Research Students, University of Bradford, UK*, pp. 198-199, 2008.

11. **K. N. Ramli** and R. A. Abd-Alhameed, "Modelling of complex electromagnetic problems using FDTD subgridding methods," *9th Informatics Workshop for Research Students, University of Bradford, UK*, pp. 200-201, 2008.

Samples of Author's Publications

Accepted subject to revision by IEEE on Antennas and Propag.

THE COMPLETE SURFACE CURRENT DISTRIBUTION IN A NORMAL-MODE HELICAL ANTENNA

K. N. Ramli, R. A. Abd-Alhameed and P. S. Excell

Abstract: *An investigation of the surface current distribution in a Normal-Mode Helical Antenna (NMHA) is reported. This enables precise prediction of the performance of NMHAs, since traditional wire-antenna simulations ignore important details. A moment-method formulation was developed using two geometrically-orthogonal basis functions to represent the total non-uniform surface current distribution over the wire of the helix. Extended basis functions were used to reliably treat the discontinuity of the current at the free ends. A surface kernel was used all over the antenna structure. The surface current distribution was computed for different antenna geometries such as dipoles, loops and helices. For helices the currents were investigated for different pitch distances and number of turns. It was found that the axially-directed component of the current distribution around the surface of the wire was highly non-uniform and that there was also a significant circumferential current flow due to inter-turn capacitance, both effects that are overlooked by standard filamentary current representations using an extended kernel. The impedance characteristic showed good agreement with the predictions of a standard filamentary-current code, in the case of applied uniform excitation along the local axis of the wire. However, the power loss computations of the present technique produce significantly different results compared to those well established methods when wires are closely spaced.*

Index Terms — Method of Moments, Normal Mode Helical Antenna, Wire Antennas.

1. INTRODUCTION

When parallel wires are close together the surface current distribution becomes non-uniform. This effect has been investigated previously, subject to certain approximations. Smith [1,2] and Olaofe [3] assumed that the average current flowing in a set of parallel wires was equal, which means that the cross-sectional distribution of surface current remains constant along the wires. Tulyathan [4] used a more general treatment but still neglected the possibility of a circumferential component in the surface current: it is intuitively obvious that such a component must be present when there is significant displacement current flow in the inter-wire capacitance.

A more general detailed solution by Abd-Alhameed and Excell [5] included the modelling of two surface current components at any point on the wire surface, subject to certain geometry constraints. And more recently [6-8], in which two parallel dipoles and loop antennas were investigated for the existence of the non-uniform surface currents, in which the antenna power losses were fully covered in [8].

In addition, most of the methods used for analysis of wire antennas of arbitrary shape (including the possibility of closely parallel wires) assume a uniform surface current distribution across the cross section, (e.g. Djordjevic et al [9], Burke and Poggio [10], Richmond [11]). Hence, surface resistive losses and reactive effects that may be augmented by the non-uniform surface current will not be correctly predicted.

This problem is particularly significant for resonant coiled electrically-small antennas, such as the normal-mode helical antenna (NMHA: see Fig. 1), in which the surface current distribution has a critical effect on the efficiency and Q-factor. A moment-method (MoM) formulation uses two orthogonal basis functions on the surface of the wire including its ends was thus developed to investigate this problem in details. The work detailed a more generalised theory and results of the work done by the present authors [6]. It should be noted that there are more advanced commercial codes now available which, in particular, implement patch modelling more effectively (e.g. FEKO [12], CST [13], HFSS [14] and IE3 [15]).

Basically, the original motivation for this work was to assess the degree of benefit that would be obtained if an antenna of this type were to be realised in high-temperature superconductor. Electrically-small antennas have a low radiation resistance that is easily swamped by ohmic loss resistance, resulting in a low efficiency. Superconductors have the potential to remove much of the loss and hence raise the efficiency significantly. There is then the possible disadvantage that the inherent Q-factor of the antenna may become very high: whether this is a real disadvantage depends on the nature of the system into which the antenna is proposed for deployment.

To quantify the reduction in loss, and hence improvement in efficiency, which might accrue from the use of superconductor, it is necessary to quantify the surface loss P_s (W/m^2):

$$P_s = \frac{J_s^2}{\sigma_s} \text{ in W / m}^2 \tag{1}$$

where J_s is the surface current density (A/m) and σ_s is the surface conductivity (Ω). The self-resonant helix had already been identified as a convenient design of electrically-small antenna in which quite interesting results were reported for example, broad band V-helical antenna [16], circular NMHA [17], double pitch NMHA [18] and multiple pitches NMHA [19], however, for realisation in high-temperature superconductor, the superconducting element may be left electrically isolated. The detailed quantification of J_s in this particularly complex case was thus the main original objective of the work. The very detailed modelling procedure that has been developed has much wider uses, particularly in the accurate modelling of normally-conducting NMHAs, which see extensive use in mobile telecommunications.

Complete validation of the predictions of the procedure poses considerable difficulties, since it would require measurement of the surface current distribution on wire. This matter is an important topic for future work, but an adequate degree of validation can be claimed for the results that have been presented in this work from this type of modelling process.

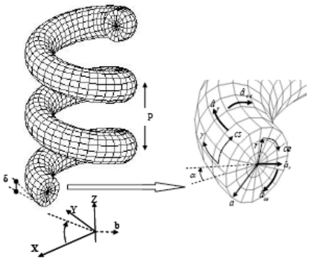

Figure 1: Basic geometry of the helical antenna driven by a voltage source at its centre. The directions of the orthogonal basis or test functions are shown on the right and represent the source or observations points on the wire surface and its ends.

2. MOMENT-METHOD FORMULATION

Initially, the normal MoM approach is followed, but no attempt was made to approximate the surface current or the scattered field observation points to a single point on the wire cross-section. Instead, both were allowed to be completely general points on the wire surface and the surface current was allowed to have components both parallel to, and transverse to, the wire axis. This leads to an equation of the form:

$$\sum_j \mathbf{I}_j . L(\mathbf{J}_j) = (\mathbf{E}_i) \tag{2}$$

where $\mathbf{I}_j$ is a basis function for the surface current $\mathbf{J}_j$, $\mathbf{E}_i$ is the incident electric field strength and L is the integro-differential operator given by:

$$L(\mathbf{J}) = (j\omega\mathbf{A} + \nabla\phi)_{\tan} \tag{3}$$

If a set of testing functions $\mathbf{W}_m$ is defined, Eqn. (1) may be rewritten as:

$$\sum_j I_j \left\langle \mathbf{W}_m, L(\mathbf{J}_j) \right\rangle = \left\langle \mathbf{W}_m, \mathbf{E}_i \right\rangle \quad \text{for } j=1,2,\ldots N \tag{4}$$

where:

$$\left\langle \mathbf{W}_m, L(\mathbf{J}_j) \right\rangle = \iint_s \iint_{s'} (\mathbf{W}_m . L(\mathbf{J}_j)) ds' ds = Z_{mj} \tag{5}$$

$$\left\langle \mathbf{W}_m, \mathbf{E}_i \right\rangle = \iint_{s'} (\mathbf{W}_m . \mathbf{E}_i) ds = V_m \tag{6}$$

where ds' and ds are the differential areas on the wire surface for the source and the observation points respectively, m=1,2,...N is the index of the testing functions and Z and V are the conventional abbreviations for the interaction matrix and excitation vector terms in the Method of Moments.

2.1 EVALUTION OF IMPEDANCE MATRIX ELEMENTS

The impedance matrix elements (Eqn. (5)) can be rewritten using the closed surface integral identity [16] as follows:

$$Z_{mj} = j\omega\mu \iint_s \iint_{s'} \left(\mathbf{J}_j . \mathbf{W}_m - \frac{1}{k^2} (\nabla . \mathbf{J}_j)(\nabla . \mathbf{W}_m) \right) G(R) ds' ds \tag{7}$$

where $G(R)$ is the free-space Green Function and R is the distance between the observation and source points on the wire surface. The xyz co-ordinates for a point on the surface of the helix wire can be given by:

$$\begin{aligned} x(\phi,\alpha) &= x'\cos(\phi) - y'\sin(\phi) \\ y(\phi,\alpha) &= x'\sin(\phi) + y'\cos(\phi) \\ z(\phi,\alpha) &= \tfrac{P}{2\pi}\phi + a\sin(\alpha)\cos(\delta) \end{aligned} \tag{8}$$

where

$$x' = b + a\cos(\alpha)$$

$$y' = -a\sin(\alpha)\sin(\delta)$$

$$\tan(\delta) = \frac{P}{2\pi b}$$

Where a is the radius of the helix wire, b is the radius of the helix, P is the pitch distance between the turns, α is the azimuth angle of the circumferential cross-section wire and δ is the pitch angle. Eqn. 8 is the exact co-ordinates of the helix geometry. Now defining the two orthogonal directions on the surface of the helix wire as shown in Fig. 1, the unit vectors of the curvilinear surface patches in both directions are as follows:

$$\hat{a}_\gamma = -\sin(\phi)\cos(\delta)\hat{a}_x + \cos(\phi)\cos(\delta)\hat{a}_y + \sin(\delta)\hat{a}_z \tag{9}$$

$$\begin{aligned} \hat{a}_{cs} = {} & (-\sin(\alpha)\cos(\phi) + \cos(\alpha)\sin(\phi)\sin(\delta))\hat{a}_x - \\ & (\sin(\alpha)\sin(\phi) + \cos(\alpha)\cos(\phi)\sin(\delta))\hat{a}_y + \\ & \cos(\alpha)\cos(\delta)\hat{a}_z \end{aligned} \tag{10}$$

where $\hat{a}_\gamma$ and $\hat{a}_{cs}$ are the unit vectors in the axial and the circumferential surfaces of the wire as shown in Fig. 1. The differential length in both directions:

$$d\gamma = b'' d\phi \tag{11}$$

$$dcs = a\,d\alpha \tag{12}$$

where $b'' = \sqrt{(\frac{P}{2\pi})^2 + b'^2}$, $b'^2 = (b + a\cos(\alpha))^2$. $d\phi$ and $d\alpha$ are the differential lengths in ϕ and α respectively.

Now, the x, y and z co-ordinates of the start end surface of the helix at $\phi = 0$ is given by:

$$\begin{aligned} x(r,\alpha) &= b + r\cos(\alpha) \\ y(r,\alpha) &= -r\sin(\alpha)\sin(\delta) \\ z(r,\alpha) &= r\sin(\alpha)\cos(\delta) \end{aligned} \tag{13}$$

where $0 \le r \le a$

Hence, the unit direction vectors of the basis function on the end surface can be given by:

$$\hat{a}_r = \cos(\alpha)\hat{a}_x - \sin(\alpha)\sin(\delta)\hat{a}_y + \sin(\alpha)\cos(\delta)\hat{a}_z \tag{14}$$

$$\hat{a}_{ce} = -\sin(\alpha)\hat{a}_x - \cos(\alpha)\sin(\delta)\hat{a}_y + \cos(\alpha)\cos(\delta)\hat{a}_z \tag{15}$$

where $\hat{a}_r$ and $\hat{a}_{ce}$ are the unit vectors in the radial and the circumferential directions on the end surface of the wire as shown in the Fig. 1. The differential area on the end surface can be given by:

$$dA_{end} = r\,dr\,d\alpha \tag{16}$$

Similarly, the unit directions vectors, co-coordinators and differential area on the other end of the helix can be defined.

Now, assume the surface current density over the wire surface can be expressed by two orthogonal currents components in $\hat{a}_\gamma$ and $\hat{a}_{cs}$ (similarly at the surface end directions $\hat{a}_r$ and $\hat{a}_{ce}$). Then if the surface current is expanded over the wire surface using triangular basis functions in which the divergence of the current continuity is finite [17], then as example, these functions into the axial direction can be given by:

$$f(\gamma) = \begin{cases} f^+ = \frac{\gamma}{\gamma_o} \\ f^- = 1 - \frac{\gamma}{\gamma_o} \end{cases} \quad \text{for} \quad 0 \le \gamma \le \gamma_o \quad \text{and} \quad \alpha_1 \le \alpha \le \alpha_2 \tag{17}$$

$$f'(\gamma) = f'^{\pm}(\gamma) = \pm\frac{\gamma}{\gamma_o} \quad \text{for} \quad 0 \le \gamma \le \gamma_o \quad \text{and} \quad \alpha_1 \le \alpha \le \alpha_2 \tag{18}$$

where $f'(\gamma)$ is the differentiation of $f(\gamma)$ and γ_o is the axial length of the curvilinear patch presented in Fig. 1 in the direction of γ for all angle values of α from α_1 to α_2. A similar basis functions in the directions of $\hat{a}_{cs}$, $\hat{a}_r$ and $\hat{a}_{ce}$ can be given. The testing functions were chosen to be identical to the expansion basis functions (Galerkin's method) yielding a symmetric impedance matrix. Hence, by substituting Eqns. 8-17 into Eqn. 7 the impedance matrix elements can be found; as example the impedance element for basis and test functions in the axial direction can be stated as follows:

$$Z_{\gamma\gamma'} = j\omega\mu \iint_s \iint_{s'} \left\{ \hat{\mathbf{a}}_\gamma . \hat{\mathbf{a}}_{\gamma'} f(\gamma) f(\gamma') - \frac{1}{k^2} f'(\gamma) f'(\gamma') \right\} G(R) ds' ds \tag{19}$$

where $ds = ab'' d\phi d\alpha$. The other self and mutual impedance elements for all other basis directions can be obtained in a similar way.

3. SIMULATION AND RESULTS

Initially, simple antenna geometries such as dipole and loop antennas were investigated and discussed as special cases of more complex geometries such as the helix. The antenna geometries of the parallel dipoles and loops are shown in Fig. 2. A similar procedure of placing orthogonal basis distribution over the wire surface and wire ends as for the dipoles are used. A computer program was written to implement the analysis given in the previous section. The surface patch subdivision was automatically generated by the program, subject to the number of the basis functions in both orthogonal directions. The impressed field $\mathbf{E}_i$ is modelled by a delta-function voltage source at the centre of the dipole and the helix whereas in loop it was placed at ϕ = 0°. A simple axial excitation (in the γ-direction) was considered. Thus the impressed field can be given by:

$$\mathbf{E}_i = \frac{1}{2\pi a}\delta(\gamma_c)\hat{a}_\gamma \quad \text{for } 0 \le \alpha \le 2\pi \tag{20}$$

where γ_c is the half axial length of the dipole or the helix. The antenna wire for all geometries was assumed to be perfectly conducting and surrounded by free space.

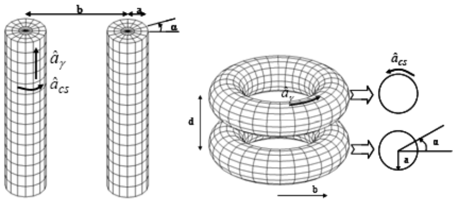

(a) (b)

Figure 2: The geometry models of two parallel dipoles and loop antennas including the directions of the basis or test functions used; (a) dipoles, (b) loops.

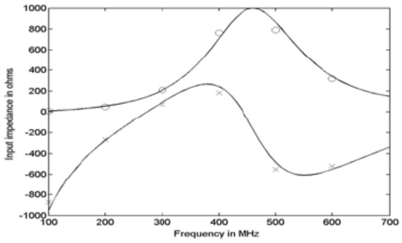

Figure 3: The input impedance versus frequency for two parallel dipoles separated by 15 mm; solid line: NEC [6], ('ooo' Resistance, 'xxx' Reactance present work).

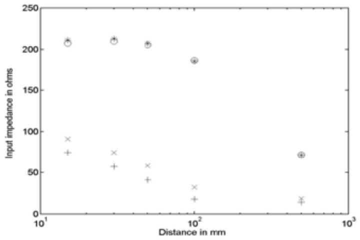

Figure 4: Input impedance at 300 MHz operating frequency of two parallel dipoles of 50 cm length and 5 mm wire radius versus the separated distance between them; ('***', '+++': Present work), ('ooo' and 'xxx': NEC).

Several examples were used to investigate the surface current distribution of dipoles, loops and NMHA as predicted by the formulation, as follows:

1) The response of the input impedance of two parallel dipoles of 50 cm length and 5 mm wire radius separated by 15 mm is presented in Fig. 3. In this example, both dipoles were centrally fed as presented in Eqn. (20). The axial and circumferential lengths were subdivided by 16 curvilinear patches of equal lengths in both directions. The attachment basis modes between the wire ends and the wire surface were placed subject to the corresponding number of axial and circumferential patches used. It is found that the results agree well with those calculated using NEC [10] (extended kernel solution), although it is to be expected that the latter will be less reliable, as less detail in the behaviour of the wire is taken into account. It is worth noting that Tulyathan and Newman [4], observed this behaviour on half wavelength dipoles when they ignored the circumferential surface current component.

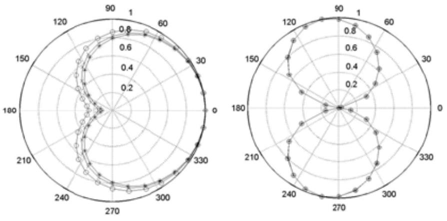

(a) (b)

Figure 5: The normalised magnitudes of the axial and circumferential surface current components of the antenna geometry given in Fig. 2 separated by 15 mm versus α at γ=6.25 cm for axial and γ=4.6845 cm for circumferential from the bottom of the dipoles for different operating frequencies: 'xxx' 100 MHz, '***' 300 MHz, 'ooo' 500 MHz; (a) axial component, (b) circumferential component.

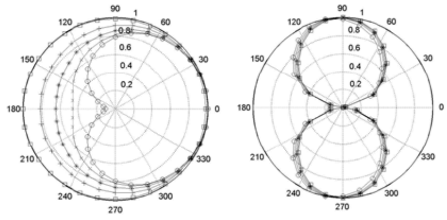

(a) (b)

Figure 6: The normalised magnitudes of the axial and circumferential surface current components versus α at similar location as Fig. 5, for different separated distances between the dipoles at 300 MHz (equivalent half wavelength dipoles with 0.005λ wire radius); (a) axial component, (b) circumferential component. ('ooo': 15 mm, 'xxx': 30 mm, '***': 50 mm, '+++': 100 mm, '□□□':500 mm).

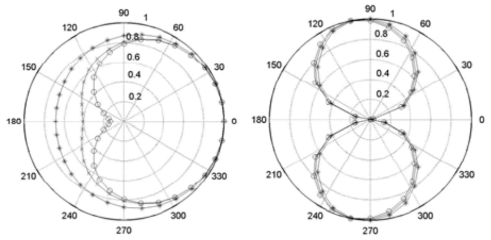

(a) (b)

Figure 7: The normalised magnitudes of the axial and circumferential surface current components versus α at similar locations as Fig. 5, for different separated distances between the dipoles at 300 MHz (equivalent to half wavelength dipoles with 0.01λ wire radius); (a) axial component, (b) circumferential component. ('ooo': 30 mm, 'xxx': 50 mm, '***': 100 mm).

For the same antenna geometry, the input impedance at 300 MHz (equivalent to half wavelength dipoles and 0.005 wavelength wire radius) versus the separated distance between the dipoles is shown in Fig. 4. It is clearly seen that there is good agreement between the results of the present work and those obtained from NEC except for the reactance values for closely spaced distances. However, the methods were completely different in their numerical solutions.

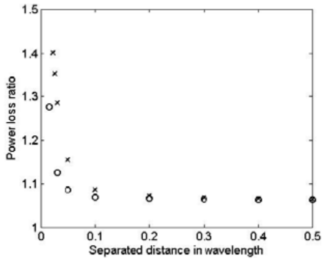

Figure 8: Power loss ratio of two parallel half wavelength dipoles for various separation distances; 'ooo': wire radius = 0.005 λ, 'xxx': wire radius = 0.01 λ.

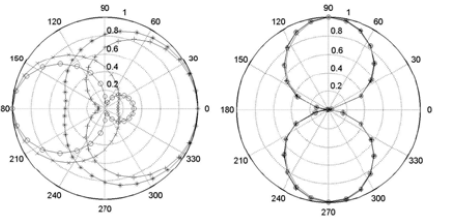

(a) (b)

Figure 9: The normalised magnitudes of the axial and circumferential surface current components versus α at $\phi = 0°$: axial component and $\phi = 33.75°$: circumferential component, for a single loop antenna for different operating frequencies. The loop radius and wire radius are 3 cm and 5 mm respectively; (a) axial component, (b) circumferential component. ('xxx': 400 MHz, 'ooo': 600 MHz, '+++': 800 MHz, '***': 900 MHz).

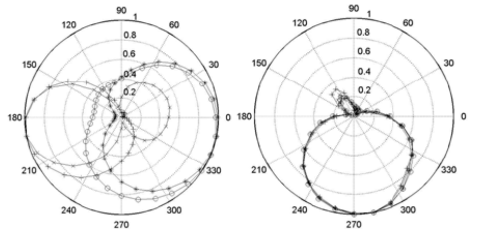

(a) (b)

Figure 10: The normalised magnitudes of the axial and circumferential surface current components versus α at $\phi = 0°$: axial component and $\phi = 33.75°$: circumferential component, for two parallel loops separated by 15 mm and each has a radius of 3 cm and 5 mm wire radius versus different operating frequencies. (a) axial component, (b) circumferential component. ('+++': 400 MHz, 'xxx': 600 MHz, '***': 800 MHz, 'ooo': 900 MHz).

The normalised magnitudes of the axial and circumferential surface current components of two parallel dipoles separated by 15 mm for the same wire radius as above are shown in Fig. 5, versus α (the azimuth of the circumferential cross-section wire) at 6.25 cm and 4.6845 cm respectively, considered from bottom of the dipoles of their local axes (equivalent to γ length measured from the bottom of the dipole), for different operating frequencies. It is very interesting to note that the non-uniform variations of these currents over different frequencies have small marginal differences. The maximum ratio of the axial component to the circumferential component was around 34:1. Similarly, these currents at 300 MHz (equivalent to half wavelength dipoles) for different separation distances are presented in Fig. 6a. It should be noted that the actual magnitudes of the circumferential component is inversely proportional to the distance between the dipoles in spite of their fixed variations shown in Fig. 6b. Also the axial component is still non-uniform even when the separation distance between the dipoles is 100 mm (0.1 wavelengths).

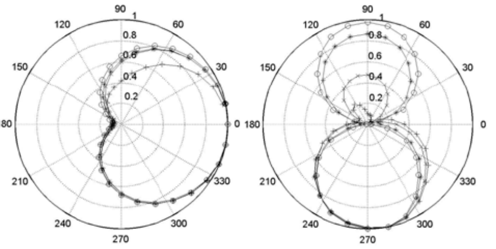

(a) (b)

Figure 11: The normalised magnitudes of the axial and circumferential surface current components versus α at $\phi = 0°$: axial component and $\phi = 33.75°$: circumferential component, for two half wavelength parallel loops each of radius 0.0796 wavelength and 0.013 wavelength wire radius, versus the separation distance 'd'. (a) axial component, (b) circumferential component.
('+++': $d = 3a$, 'xxx': $d = 6a$, '***': $d = 20a$, 'ooo': $d = 100a$).

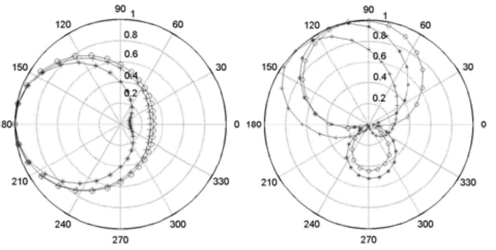

(a) (b)

Figure 12: The normalised magnitudes of the axial and circumferential surface current components of a half wavelength single turn helix antenna versus α at different positions from the first end of the helix. The helix radius, wire radius and pitch distance are 0.0796λ, 0.013λ and 3a respectively. (a) axial component: '***':0.031λ, 'ooo':0.125λ, '+++':0.25λ. (b) circumferential component: '***':0.0156λ, 'ooo':0.109λ, '+++':0.234λ.

The normalised surface currents for a thicker wire of radius of 10 mm (0.01 wavelengths) for the same antenna geometry above versus the separation distances between the dipoles are shown in Fig. 7. Comparing Figs. 6a and 7a the non-uniform effects on the axial components can be strongly seen on the thick wires, for example at the separation distance of 100 mm.

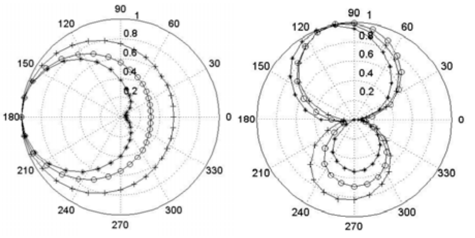

(a) (b)

Figure 13: The normalised magnitudes of the axial and circumferential surface current components of the same antenna geometry given in Fig. 11, except that the operating frequency is half than that used in Fig. 11 (i.e. operating wavelength 2λ).
(a) axial component: '***':0.031λ, 'ooo':0.125λ, '+++':0.25λ.
(b) circumferential component: '***':0.0156λ, 'ooo':0.109λ, '+++':0.234λ.

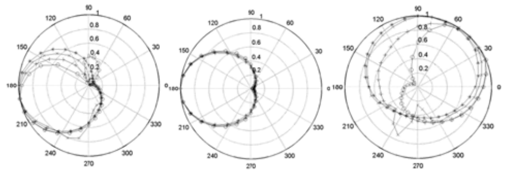

(a) (b) (c)

Figure 14: The normalised magnitudes of the axial and circumferential surface current components of a half wavelength two turns helix antenna versus α for different pitch distances. The helix radius and wire radius are 0.04λ and 0.006λ respectively. ('ooo': $P = 3a$, '+++': $P = 5a$, 'xxx': $P = 7a$, '***': $P = 9a$) (a) axial component: taken at 0.031λ from the bottom end of the helix. (b) axial component: taken at the centre of the helix. (c) circumferential component: taken at 0.023λ from the bottom end of the helix.

It is clear from Figs. 3 and 4 that the average current along the local axis of the dipoles will be similar to that computed using NEC, thus the expected field pattern will be similar, and is not reproduced here. The ratio of the power losses predicted from the non-uniform surface current distribution to those predicted from the average (or uniform) current distribution was considered as an equivalent measure of the improvement in modelling verisimilitude when using the new method. However, since the losses are small in most cases it is possible to assume that the antenna wire is perfectly conducting and surrounded by free space; then losses can be predicted by taking them as proportional to the surface current density squared. The variation of the power loss ratio against the separated distance between two parallel half wavelength dipoles, for two wire thicknesses, is shown in Fig. 8. It can be noticed that for high separation distances, the power loss converged to unity value as is expected. However, the variations show a significant power loss for closely spaced dipole antennas. For the following two antenna geometries we restrict our discussion on the presence of non-uniformity of the surface currents that clearly match the variations of the power loss ratios.

2) The normalised magnitudes of the axial and circumferential surface current components for single and two parallel loops versus α for different operating frequencies are shown in Figs. 9 and 10 respectively. For both figures the loop radius and wire radius are 3 cm and 5 mm respectively.

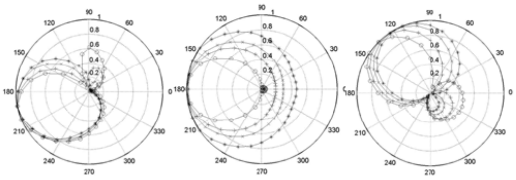

(a) (b) (c)

Figure 15: The normalised magnitudes of the axial and circumferential surface current components of a half wavelength three turns helix antenna versus α for different pitch distances. The helix radius and wire radius are 0.0265λ and 0.004λ respectively. ('ooo': $P = 3a$, '+++': $P = 5a$, 'xxx': $P = 7a$, '***': $P = 9a$) (a) axial component: taken at 0.0294λ from the bottom end of the helix. (b) axial component: taken at the centre of the helix. (c) circumferential component: taken at 0.022λ from the bottom end of the helix.

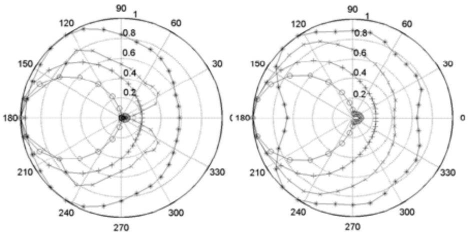

(a) (b)

Figure 16: The normalised magnitudes of the axial surface current components of a half wavelength four turns helix antenna versus α for different pitch distances. (a) four turns: the helix radius and wire radius are 0.02λ and 0.003λ respectively; (b) five turns: The helix radius and wire radius are 0.015λ and 0.002λ respectively. ('ooo': $P = 3a$, '+++': $P = 5a$, 'xxx': $P = 7a$, '***': $P = 9a$)

In the case of parallel loops the separation distance was selected to be 15 mm. The loops are fed by a simple delta excitation source at $\phi = 0°$. The axial component is taken at the source location whereas the circumferential is considered at $\phi = 33.75°$ (angles are simply used here to define the locations of the circumferential cross-section wire, and for this particular angle the γ length is 0.0177cm). It should be noted that the variations of the currents for two parallel loops are taken for the bottom loop as shown in Fig. 2b. It is clearly shown that the maximum variations of the axial currents for frequencies less that the expected parallel resonance frequency of the antenna structure are always pointed inside the loops geometries (i.e. α = 180°). The circumferential component for the single loop antenna is similar to that computed on the two parallel dipoles, and its ratio compared to the axial component was found to be 41:1. However, the same component for two parallel loops was reduced to minimum around α = 90°, whereas its ratio to axial component was 28:1.

Moreover, the normalised magnitudes of the axial and circumferential surface current components for two half wavelength parallel loops each of radius 0.0796 wavelength and 0.013 wavelength wire radius versus α for various separation distances 'd' are shown in Fig. 11. The locations of these currents are similar to those taken in Figs. 9 and 10. The axial component was reserved its variations for most of the distances considered in this example as in the case of the single loop antenna except when at very close distance. The variations of the circumferential component was also eliminated around α = 90° even the separation distance was $20a$.

3) The normalised magnitudes of the axial and circumferential surface current components of a half wavelength single turn helix antenna versus α at different positions from the first end of the helix are shown in Fig. 12. The helix radius, wire radius and pitch distance are 0.0796λ, 0.013λ and $3a$ respectively. It is shown that the strong effects of the axial component were pointed inside the helix for all locations presented. These results might help to approximate the equivalent of these variations into one curve that might be taken along all the local length of the helix to assess the total loss power in the axial direction. Similar variations were observed on the circumferential component except that the strong effect has shifted from α = 90° to α = 135° for the locations presented. However, considering the strong effect locations of these currents regardless of the locations of their maxima and taking into account the similarities in these variations it may be concluded that this indicates the approximate contribution of this current to the total loss power.

However, for the same antenna geometry given in Fig. 12, the currents were computed at half the operating frequency (i.e. operating wavelength 2λ) as shown in Fig. 13. It is clearly shown that the strong effects of these current variations are mostly similar to that presented in Fig. 12. Moreover, a strong correlation can be found in the variations of the circumferential currents for different locations for this example. However, a one turn helix is not sufficient to permit comment on the currents variations of a multi-turn helix antenna, thus the following examples are considered.

The normalised magnitudes of the axial and circumferential surface current components of a half wavelength of two, three, four and five turns helix antenna versus α for different pitch distances are shown in Figs. 14, 15 and 16. It is very clear that the axial and circumferential components were non-uniform even if the pitch distance between the helix turns was nine times the radius of the wire. Another interesting point is that the peak values of the axial component were pointed inside the helix (i.e. around α = 180°) for all helices presented. This is clearly shown in the variations of these currents at the feed points on Figs. 14b, 15b, 16a and 16b and the helix turns in Figs. 14a (first turn) and 15a (first turn). The similarities of these variations permit the approximate calculation of the effective power loss in that particular direction. It was also observed that the maximum variations of the circumferential component on the first turn confined between α = 0° and 180° as shown in Figs. 12b, 13b, 14c and 15c. However, the maximum ratio of the axial component to the circumferential component for all pitch distances was found between 15:1 and 40:1 for all helices more than one turn. General comments on the trend of these results are to predict the accurate or approximated equivalent power losses that are associated with non-uniform variations along the wire surfaces. Hence this will follow to affect the radiation efficiency of this kind of antennas.

4. CONCLUSIONS

The surface current distributions on structures with closely spaced parallel wires, such as dipoles, loops and helical antennas, can be computed by using the method of moments with a general surface patch formulation. The current distribution varies substantially from the common assumption that it is uniform around the wire cross-section. Transverse (circumferential) currents are shown to be present: they are relatively weak on thin wires (around 0.01λ wire radius) excited by axial component parallel to the local axis of the wire. The effect is still significant when the wire separation distance is relatively large. In spite the strong variations of the axial and circumferential currents, it was found that the input impedance and the average value of the axial surface current in reasonable good agreement with the results of thin wire codes such as NEC using an extended kernel solution. The power loss ratio resulting from use of non-uniform surface current, compared with the conventional uniform assumption of two parallel dipoles, shows a significant increase of power loss when they are closely separated. However, these current variations will dominate the radiation efficiency when predicting the accurate total power loss on these types of antennas and this can be important in some applications, e.g. highly resonant antennas and antennas realised in superconducting materials. As a matter of interest it was computed that the maximum ratio of the variations of the axial component to the circumferential component on a half wavelength helix of a few turns for different pitch distances was between 15:1 to 40:1. This behaviour is expected as the NMHA has a hybrid of dipole and loop behaviour. The modelling method employed a two-dimensional electric surface patch integral equation formulation solved by independent piecewise-linear basis function methods in the circumferential and axial directions of the wire. A similar orthogonal basis function was used on the end surface and appropriate attachments with the wire surface were employed to satisfy the requirements of current continuity. The results were stable and showed good agreement with less comprehensive earlier work by others.

REFERENCES:

1. G. Smith, "The Proximity Effect in Systems of Parallel Conductors and Electrically Small Multiturn Loop Antennas," *Technical Report 624, Division of Engineering and Applied Physics, Harvard University, USA*, 1971.
2. G. Smith, "The Proximity Effect in Systems of Parallel Conductors," *Journal of Applied Physics*, **43**, 5, 1972, pp. 2196-2203.

3. G. O. Olaofe, "Scattering by Two Cylinders," *Radio Science*, 5, 1970, pp. 1351-1360.
4. P. Tulyathan and E. H. Newman, "The Circumferential Variation of the Axial Component of Current in Closely Spaced Thin-Wire Antennas," *IEEE Transaction Antennas and Propagation*, **AP-27**, 1, January 1979, pp. 46-50.
5. R. A. Abd-Alhameed and P. S. Excell, "The Complete Surface Current for NMHA Using Sinusoidal Basis Functions and Galerkins Solution," *IEE Proceedings Science, Measurement and Technology on Computational Electromagnetics*, **149**, 5, 2002, pp. 272-276.
6. R. A. Abd-Alhameed and P. S. Excell, "Surface Current Distribution on Closely Parallel Wires Within Antennas," 2nd European Conference on Antennas and Propagation (EuCAP), Edinburgh, UK, November 11-16, 2007, pp. 1-4.
7. R. A. Abd-Alhameed and P. S. Excell, "Accurate Power Loss Computation of Closely Spaced Radiating Wire Elements for Mobile Phone MIMO Application," IEEE International Conference on Signal Processing and Communication (ICSPC), Dubai, United Arab Emirates, November 24-27, 2007, pp. 412 - 415.
8. R. A. Abd-Alhameed and P. S. Excell, "Non-Uniform Surface Current Distribution on Parallel Wire Loop Antennas Using Curved Patches in the Method of Moments," *Science, Measurement and Technology, IET*, **2**, 6, November 2008, pp. 493-498.
9. A. R. Djordjevic, M. B. Bazdar, V. V. Petrovic, D. I. Olcan, T. K. Sarkar and R. F. Harrington, *Analysis of Wire Antennas and Scatterers*, Boston, USA, Artech House, 1990.
10. G. J. Burke and A. J. Poggio, "Numerical Electromagnetics Code (NEC): Method of Moments," *US Naval Ocean Systems Centre*, Rep. No. TD116, 1981.
11. J. H. Richmond, "Radiation and Scattering by Thin-Wire Structures in the Complex Frequency Domain," *NASA*, Rep. No. CR-2396, 1974.
12. FEKO EM Software and Systems S. A., (Pty) Ltd, Stellenbosch, South Africa.
13. Computer Simulation Technology Corporation, CST Microwave Studio, Version 5.0, German.
14. HFSS v. 10, Ansoft [online], www.ansoft.com.
15. IE3D, Release 12, Zeland Software, Inc., Fremont CA, USA, 2007.
16. D. A. E. Mohamed, "Comprehensive Analysis of Broad Band Wired Antennas," National Radio Science Conference (NRSC), 2009, pp. 1-10.
17. W. G. Hong, Y. Yamada and N. Michishita, "Low Profile Small Normal Mode Helical Antenna," Asia-Pacific Microwave Conference (APMC), 2007, pp. 1-4.
18. H. Mimaki and H. Nakano, "Double pitch helical antenna," IEEE Antennas and Propagation Society International Symposium, **4**, June 21-26, 1998, pp. 2320-2323.
19. S. Ooi, "Normal Mode Helical Antenna Broad-banding Using Multiple Pitches," IEEE Antennas and Propagation Society International Symposium, **1**, June 22-27, 2003, pp. 860-863.
20. W. L. Stutzman and G. A. Thiele, *Antenna Theory and Design*, 2nd ed., New York, USA, John Wiley & Sons, 1981.
21. M. I. Aksun and R. Mittra, "Choices of Expansion and Testing Functions for the Method of Moments Applied to a Class of Electromagnetic Problems," *IEEE Transaction on Microwave Theory and Techniques*, **41**, 3, March 1993, pp. 503-509.

Electromagnetic Field Interaction between Overhead High Voltage Power Transmission Line and Buried Utility Pipeline

K. N. Ramli[1, 2], **Raed A. Abd-Alhameed**[1], **H. I. Hraga**[1], **D. T. W. Liang**[1], **and P. S. Excell**[3]

[1]Mobile and Satellite Communications Research Centre, University of Bradford, Bradford BD7 1DP, UK
[2]Faculty of Electrical and Electronic Engineering, Universiti Tun Hussein Onn Malaysia (UTHM)
Parit Raja 86400, Batu Pahat, Johor, Malaysia
[3]Centre for Applied Internet Research, Glyndwr University, Wrexham LL11 2AW, Wales, UK

Abstract— This work presents the development of a new approach of modelling the source excitation and the penetration of structures by continuous propagating electromagnetic (EM) plane waves. The technique incorporates the solution of time-dependent Maxwell's equations and the initial value problem as the structures are illuminated by the plane waves. The propagation of waves from source excitation is simulated by solving a finite-difference Maxwell's equation in the time domain. Subgridding method is used to condense the lattice at the point of interest locally for observing field distribution in high resolution. The computational burden due to huge number of time steps has been eased by employing quasi-static approach. An example of induced EM fields near an underground pipeline runs parallel to a 132 kV overhead power transmission line (OHTL) has been presented which paves the way in the development of new approach of EM fields interaction modelling.

1. INTRODUCTION

Finite-difference based on integral formulation [1, 2] has been used in the published literature to improve the accuracy of the finite-difference formulation near the surfaces that does not fit in the lattice or small objects such as thin wires which alter the electromagnetic field distribution significantly. In this case, analytical expressions have been established to express the field near a particular object for precise evaluation of the integrals. Many researchers in the past have been prompted to investigate the subgridding technique as an approach to circumventing the problem [3, 4]. The first advantage of using this method is simple to implement for complicated dielectric or metal structures due to arbitrary electrical parameters can be assigned to each cell on the grid. Second, the entire computational spaces need not to be discretised with a fine grid as it puts unreasonable burden on the computer processing time. The ultimate objective of research in this area is to access the appropriateness of the method in determining the amount of EM penetrating fields between OHTL and underground utility pipeline. The aim of the present work is to develop the general code for solving the electric and magnetic fields within arbitrary metal or dielectric structures, while maintaining a boundary of uncertainty low reflection level in two-dimensional approach.

FDTD technique has been well known over the years of its strength with robust simulation technique for transient electromagnetic interactions. In this research work, two-dimensional FDTD technique is used with subgridding to model the utility pipeline and the overhead high voltage power transmission line. FDTD technique has been applied to the high voltage power transmission line analysis in the published literature. Dedkova and Kriz [5] proposed a new effective approach to evaluate the distribution of voltage and current along the nonlinear transmission line by using FDTD method. An improved technique was proposed by Tang et al. [6] to calculate the transient inductive interference in underground metallic pipelines due to a fault in nearby power lines. The frequency-dependent problem in the analysis of transient interference was solved in phase domain based on FDTD method. Lu and Cui [7] used FDTD method to calculate the wave processes of voltage and current distributed along the three-phase 500 kV busbars and the power lines without load in the substation of multi-conductor transmission lines (MTL). The iterative formulas were presented to determine the boundary conditions at the node of the branches. The work was extended to transmission line network and non-uniform line [8].

2. METHOD

Figure 1 depicts the cross section and the dimension of a common corridor in which a buried utility pipeline runs parallel to a 132 kV overhead power transmission line. The height from the ground to

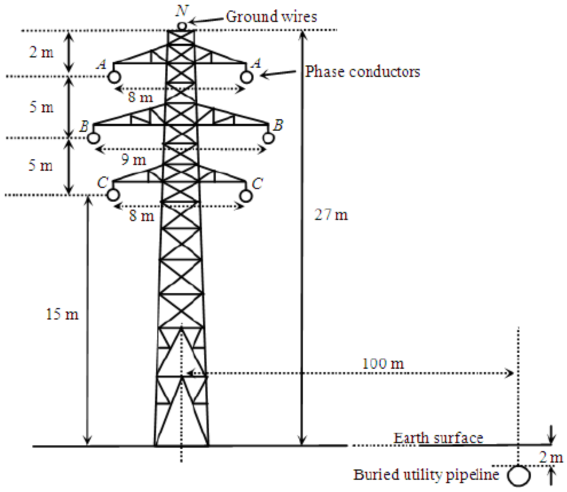

Figure 1: Outline of standard circuit 132 kV steel lattice transmission high voltage suspension towers (not to scale).

the bottom conductors was 15 m. The overhead ground wire was located at the top of the tower. In this case, the height to the earth surface is 27 m. The phase conductors for the bottom, middle and top were collocated horizontally with a separation of 4.0 m, 4.5 m and 4.0 m respectively between two adjacent conductors. The three phase steel lattice transmission high voltage suspension tower was designed with 6 cables. These cables were used as the source signal which propagates inside the problem space. Each of the 2 cables carries the same phase of the AC current. The simulation was carried out using the quasi-static FDTD at the transformed intermediate frequency of 460 kHz and the overall model was then transformed back to the proposed lower frequency of 50 Hz. Quasi-static approximation was obtained by using the expression [9–11]:

$$\vec{E}(f) = \left(\frac{\omega}{\omega'}\right)\left[\frac{\sigma'(f') + j\omega'\varepsilon(f')}{\sigma(f) + j\omega\varepsilon(f)}\right]\vec{E}'(f') \tag{1}$$

where $\vec{E}(f)$ is the resultant internal electric field (V/m), $\vec{E}'(f')$ is the scaling internal electric field (V/m), f is the frequency of interest (Hz), f' is the scaling frequency (Hz), ω is the angular frequency of interest (s^{-1}), ω' is the scaling angular frequency (s^{-1}), σ is the conductivity of the object (S/m), and σ' is the scaling conductivity of the object (S/m). By assuming $\omega\varepsilon(f) \ll \sigma(f)$ and $\omega'\varepsilon'(f' \ll \sigma'(f')$, then Equation (1) can be approximated as follows [9–11]:

$$\vec{E}(f) \cong \left[\frac{f\sigma'(f')}{f'\sigma(f)}\right]\vec{E}'(f') \tag{2}$$

Sinusoidal wave excitation of 460 kHz ($\lambda = 652.17$ m) was applied at each of the power transmission line cables. The pipeline was separated at a distance of 100 m from the steel lattice suspension towers and buried 2 m beneath the surface of the earth. The soil in the common corridor was designed to be inhomogeneous. The computational region at the coarse grids was discretised at a spatial resolution of 2,609 cells per wavelength ($\Delta y = \Delta z = 25$ cm). Subgridding involves local mesh refinement in the pipeline and some part of the ground in order to determine the propagation of the waves inside that area while observing the change in the fields. The computational space for the main region was 521 cells ×145 cells (130.25 m×36.25 m). The computational space for subgrid area was 10 cells ×10 cells. The ratio of the coarse to the fine grids was 4 : 1.

3. SIMULATION RESULTS

Subgrid technique was validated by illustrating example in Fig. 2. The problem space was excited by sinusoidal wave source at 1800 MHz. The fields at the same point without subgrid (Fig. 2(a)) and with subgrid (Fig. 2(b)) were observed and compared. In addition, they were found to be identical to each other as depicted in Fig. 3.

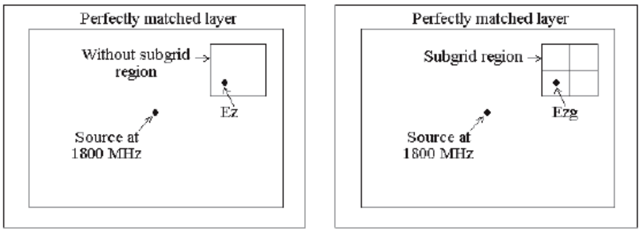

(a) (b)

Figure 2: Problem space: (a) without subgrid, (b) with subgrid.

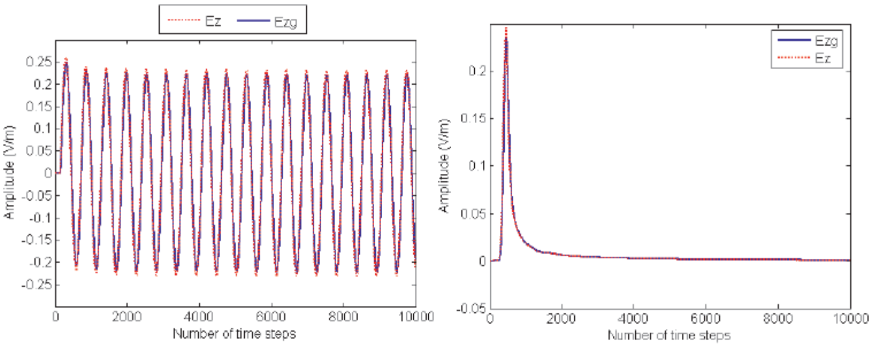

(a) (b)

Figure 3: The electric field at one point without subgrid (E_z) and with subgrid (E_{zg}): (a) when sinusoidal wave was excited, (b) when gaussian pulse was excited.

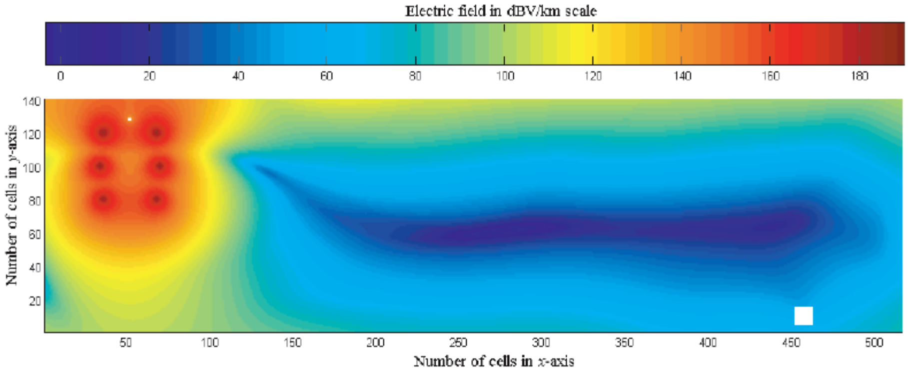

Figure 4: The electric field E_z distribution in the main FDTD grid.

The computation efforts can be reduced using quasi-static method due to the largest computational size was less than 0.2λ. The simulation was carried out by assuming normal condition of OHTL. Fig. 4 illustrates the electric field distribution in the main FDTD grid. The EM wave propagates from the 6 cables of the suspension tower to the surrounding area of air, ground and the pipeline. It varies from $1.0\,\mathrm{V/km}$ ($0\,\mathrm{dBV/km}$) to $1.78 \times 10^9\,\mathrm{V/km}$ ($185\,\mathrm{dBV/km}$). The fields inside the metallic pipeline were found to be zero as depicted in Fig. 5(a) due to the excess electrons at the surface of the metal preventing any incoming propagating waves from penetrating the pipeline. The electric field distribution surrounding the pipeline alters from $3.16\,\mathrm{V/km}$ ($10\,\mathrm{dBV/km}$) to $1.0 \times 10^3\,\mathrm{V/km}$ ($60\,\mathrm{dBV/km}$). Some of the waves were reflected back to the surface of the ground thus producing induced EM fields as shown in Fig. 5(b). The results were verified by comparing them with [12] which shows good agreements. Phase imbalance in the line may be produced due to the difference in the relative distance of each phase from the nearby pipeline. Under fault condition, the currents on the faulty phases of transmission lines were high. This in turn will induce AC voltage on the pipeline and create shock hazard rather than corrosion.

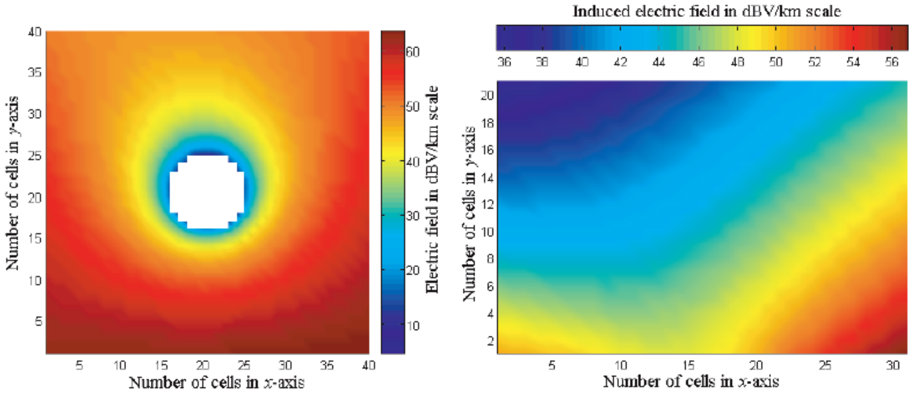

(a) (b)

Figure 5: (a) The electric field E_{zg} distribution in the subgrid section. (b) The induced electric field E_z at 1.75 m above pipeline.

4. CONCLUSIONS

An approach to model the interaction between overhead transmission lines and buried utility pipeline at power-line frequency has been presented. This uses the FDTD technique for the whole structure of the problem combined with subgridding method at the object of interest. The computational burden due to huge number of time steps in the order of tens of millions has been eased to tens of thousands by employing the method called quasi-static approach. The use of inhomogeneous soil in the common corridor permits a non-trivial proximity region of authentic ground properties to be simulated. Profound investigation of the interaction between electromagnetic fields and natural or utility arrangement with different electrical characteristics at different level of spatial resolution can be assisted by such tools. The combination of frequency scaling FDTD subgridding approach with arbitrary inhomogeneous soil element model paves the way in the development of new approach of EM fields interaction modelling.

ACKNOWLEDGMENT

The financial support from Ministry of Higher Education Malaysia and Universiti Tun Hussein Onn Malaysia (UTHM) is gratefully acknowledged.

REFERENCES

1. Taflove, A. and S. C. Hagness, *Computational Electrodynamics: The Finite-Difference Time-Domain Method*, 3rd Edition, Artech House, Boston, 2005.
2. Shreim, A. M. and M. F. Hadi, "Integral PML absorbing boundary conditions for the high-order M24 FDTD algorithm," *Progress In Electromagnetics Research*, Vol. 76, 141–152, 2007.
3. Ramli, K. N. and R. A. Abd-Alhameed, "Modelling of complex electromagnetic problems using FDTD subgridding methods," *9th Informatics Workshop for Research Students*, 200–201, University of Bradford, UK, 2008.
4. Wang, S. M., F. L. Teixeira, R. Lee, and J. F. Lee, "Optimization of subgridding schemes for FDTD," *IEEE Microwave and Wireless Components Letters*, Vol. 12, 223–225, 2002.
5. Dedkova, J. and T. Kritz, "FDTD analysis of a nonlinear transmission line," *Proceedings of Progress In Electromagnetics Research Symposium*, 282–285, Beijing, China, 2009.
6. Tang, J., X. Cui, L. Qi, T. Lu, L. Li, P. Zhu, G. Yang, and W. Zhang, "Analysis of transient inductive interference in underground pipelines due to faults on nearby power lines," *COMPEL: The International Journal for Computation and Mathematics in Electrical and Electronic Engineering*, Vol. 26, 1346–1363, 2007.
7. Lu, T. and X. Cui, "Transient analysis of wave processes for multi-conductor transmission lines with branches using FDTD," *IEEE International Symposium on Electromagnetic Compatibility*, Vol. 2, 699–703, 2000.
8. Lu, T., L. Qi, J. Li, and X. Cui, "Application of multi-conductor transmission lines on the transient analysis in power substation," *Asia-Pacific Conference on Environmental Electromagnetics*, 198–201, 2003.

9. Guy, A. W., S. Davidow, G. Y. Yang, and C. K. Chou, “Determination of electric current distributions in animals and humans exposed to a uniform 60-Hz high-intensity electric field,” *Bioelectromagnetics*, Vol. 3, 47–71, 1982.
10. Golestani-Rad, L., B. Elahi, and J. Rashed-Mohassel, “Investigating the effects of external fields polarization on the coupling of pure magnetic waves in the human body in very low frequencies,” *BioMagnetic Research and Technology*, Vol. 5, 1–5, 2007.
11. Gandhi, O. P. and J. Chen, “Numerical dosimetry at power-line frequencies using anatomically based model,” *Bioelectromagnetics*, Vol. 13, 43–60, 1992.
12. Amer, G. M., “Novel technique to calculate the effect of electromagnetic field of H.V.T.L. on the metallic pipelines by using EMTP program,” *18th International Conference and Exhibition on Electricity Distribution (CIRED)*, 1–5, Turin, Italy, 2005.

Asia-Pacific Microwave Conference (APMC), Singapore, 7–10 December 2009

Precise Computation of the Induced Fields Inside Biological Cell Tissue Using Floquet Boundary and Subgridding Quasi-Static FDTD Method

K.N. Ramli [#1], R.A. Abd-Alhameed [#1], C.H. See [#1], D. Zhou [#1], E.A. Elkhazmi [#2] and P.S. Excell [#3]

[#] *Mobile and Satellite Communications Research Centre, University of Bradford*
Richmond Road, Bradford, West Yorkshire, BD7 1DP, UK
[1] `r.a.a.abd@bradford.ac.uk`
[#] *The Higher Institute of Electronics, Bani Walid, Libya*
[2] `eaelkhazmi@hotmail.com`
[#] *School of Computing and Communications Technology, North East Wales Institute of Higher Education*
Wrexham, LL11 2AW, UK
[3] `p.excell@newi.ac.uk`

***ABSTRACT* —This paper demonstrates the detailed electromagnetic modelling of biological cell structures by using modified subgridding FDTD techniques. This is done by incorporating a quasi-static FDTD solution, Floquet periodic boundary conditions and modified PML boundary conditions to achieve microdosimetric modelling of bioelectromagnetic interactions at cellular level. Particular attention is paid to exploration of the field distribution over the membrane layer of the biological cells. The method enables the analysis of a large structure of cells in a more computationally efficient way than the modelling of the entire structure. An example is given to prove the stability of the proposed subgridding FDTD. The total fields of the simulated structures are shown to give reasonable and stable results at 2450MHz.**

***INDEX TERMS* —Finite Difference Time Domain (FDTD), Floquet periodic boundary conditions, Quasi-Static method, Subgridding.**

I. INTRODUCTION

With the massive growing of electronic, information, communication technologies, it motivates the explosive usage of mobile handsets over last decade. The possible mechanism of biological effect on human cells that could contribute to complex cellular process that leads to cancer, by using mobile phone, has increased the public concerned over recent years. As a result, it leads to a high demand on modelling a precious structure used to clarify the uncertainty of the electromagnetic (EM) behaviour of cells exposed to these fields. In this research area, finite-difference time-domain (FDTD) method has been dominating over the other numerical methods, due to its simplicity and its ability to treat highly nonhomogeneous structures.

Research on the interaction mechanism of electromagnetic field with the biological tissue at mobile communication frequencies have been performed by [1-2] by adapting modified FDTD technique. But, the accuracy of the model is questionable, due to the thickness of the cell membrane in the model is too thick (1 micro meter) and a minimum of one FDTD cell is used to represent the membrane. Cell membrane has been identified as the primary target for the study of possible actions of EM fields on biological structures. In order to facilitate deeper investigation of the field distribution inside the membrane, where the previous proposed models in [1-2] cannot be clarified, a modified subgridding FDTD scheme is used to model a high definition biological tissue model is presented.

II. SUMMARY OF METHODS

The traditional FDTD is not capable to model extremely small object which is much smaller than a wavelength. This is due to unaffordable computational resource is required to perform the calculation. By adapting the frequency scaled FDTD method [1-3], this problem can be easily overcome. Many structures of electromagnetic interest are extremely large and periodic in one or more dimensions. In order to perform the EM analysis of these types of structure with reasonable computational time, the structures are assumed to be an infinite grid and subsequently reducing the problem into a unit-cell analysis by using floquet boundary condition [4]. This will enable the numerical solution to simulate the effect of the periodic replication. In order to include the membrane effect on the biological tissue model, lumped-element membrane model [1-2] is used as a working hypothesis to develop the modelling technique.

A. Subgridding FDTD method

Standard FDTD suffers from staircase error due to cartesian grids everywhere in the computational grid and this error makes it less favour to use for complex geometry and small object modelling. Many researchers such as in [5-6] have extended FDTD to handle multi-resolution problems by using finer grids near structures with small geometrical features abutted to coarse grids in regions of empty space. It is well-known that the subgridding scheme in FDTD always encounters the late time instability problems due to the interpolation and extrapolation of neighbouring field values in the FDTD computation domain. However, this is a challenge

978-1-4244-2802-1/09/$25.00 ©2009 IEEE

Asia-Pacific Microwave Conference (APMC), Singapore, 7–10 December 2009

to implement this technique to establish a novel sophisticated biological tissue model.

The FDTD updating equation for the electric field E_x and magnetic field H_y components of 3-D FDTD can be derived as [7]:

$$E_x\Big|_{i,j,k}^{n+1} = C_{a,E_x}\Big|_{i,j,k} E_x\Big|_{i,j,k}^{n} + C_{b,E_x}\Big|_{i,j,k}\begin{pmatrix} H_z\big|_{i,j+1/2,k}^{n+1/2} - H_z\big|_{i,j-1/2,k}^{n+1/2} \\ + H_y\big|_{i,j,k-1/2}^{n+1/2} - H_y\big|_{i,j,k+1/2}^{n+1/2} \end{pmatrix} \quad (1)$$

$$H_y\Big|_{i,j,k}^{n+1/2} = D_{a,H_y}\Big|_{i,j,k} H_y\Big|_{i,j,k}^{n-1/2} + D_{b,H_y}\Big|_{i,j,k}\begin{pmatrix} E_z\big|_{i+1/2,j,k}^{n} - E_z\big|_{i-1/2,j,k}^{n} \\ + E_x\big|_{i,j,k-1/2}^{n} - E_x\big|_{i,j,k+1/2}^{n} \end{pmatrix} \quad (2)$$

A computer program was written in Fortran to implement the analysis. A cubical FDTD cells was implemented in which the cell size was set with Δx = Δy = Δz = 20μm. It was chosen such that the length of the grid remained at a fraction of a wavelength only. The time step was set at 1.5ps to satisfy the Courant stability condition that was given by [8]:

$$\sqrt{(\Delta x)^2 + (\Delta y)^2 + (\Delta z)^2} > c\Delta t = \sqrt{\frac{1}{\varepsilon\mu}}\Delta t \quad (3)$$

where c, ε and μ are the speed of light, electric permittivity and magnetic permeability respectively. Equation (3) relates the spatial and temporal resolution inside the FDTD computational domain. An interpolation algorithm was required to predict the missing fields between the coarse and fine region of the FDTD lattice. There were many articles published in the literature with different updating field methods at the unknown cell of the boundary by means of both interpolation and extrapolation techniques. In general, some of them were based on separated time and space interpolation interfaces [9], spatial field interpolation algorithm [10], dielectric transverse capability [11], interpolation of current density [12], time interpolation subgridding algorithm [13], finite element formulation [14-15] and quadratic interpolation [16]. In this work, the magnetic field in the fine region was interpolated by the six neighbouring magnetic field in the coarse region. The magnetic field basis in 2-D domain can be written as:

$$H_x = H(x,y) = a + b(x) + c(y) + d(xy) + e\left(x^2\right) + f\left(y^2\right) \quad (4)$$

where a is the constant, b, c, d, e and f are the coefficient of the equation. It can be deduced in matrix form as:

$$\begin{bmatrix} H_{x_1} \\ H_{x_2} \\ H_{x_3} \\ H_{x_4} \\ H_{x_5} \\ H_{x_6} \end{bmatrix} = \begin{bmatrix} 1 & x_1 & y_1 & x_1y_1 & x_1^2 & y_1^2 \\ 1 & x_2 & y_2 & x_2y_2 & x_2^2 & y_2^2 \\ 1 & x_3 & y_3 & x_3y_3 & x_3^2 & y_3^2 \\ 1 & x_4 & y_4 & x_4y_4 & x_4^2 & y_4^2 \\ 1 & x_5 & y_5 & x_5y_5 & x_5^2 & y_5^2 \\ 1 & x_6 & y_6 & x_6y_6 & x_6^2 & y_6^2 \end{bmatrix} \begin{bmatrix} a \\ b \\ c \\ d \\ e \\ f \end{bmatrix} \quad (5)$$

The coefficients can be obtained by:

$$\begin{bmatrix} a \\ b \\ c \\ d \\ e \\ f \end{bmatrix} = \begin{bmatrix} 1 & x_1 & y_1 & x_1y_1 & x_1^2 & y_1^2 \\ 1 & x_2 & y_2 & x_2y_2 & x_2^2 & y_2^2 \\ 1 & x_3 & y_3 & x_3y_3 & x_3^2 & y_3^2 \\ 1 & x_4 & y_4 & x_4y_4 & x_4^2 & y_4^2 \\ 1 & x_5 & y_5 & x_5y_5 & x_5^2 & y_5^2 \\ 1 & x_6 & y_6 & x_6y_6 & x_6^2 & y_6^2 \end{bmatrix}^{-1} \begin{bmatrix} H_{x_1} \\ H_{x_2} \\ H_{x_3} \\ H_{x_4} \\ H_{x_5} \\ H_{x_6} \end{bmatrix} \quad (6)$$

Hence, the magnetic field in the fine region can be calculated by:

$$H_x = a + b(x_0) + c(y_0) + d(x_0y_0) + e\left(x_0^2\right) + f\left(y_0^2\right) \quad (7)$$

where x_0 and y_0 are the reference point at the interpolation region.

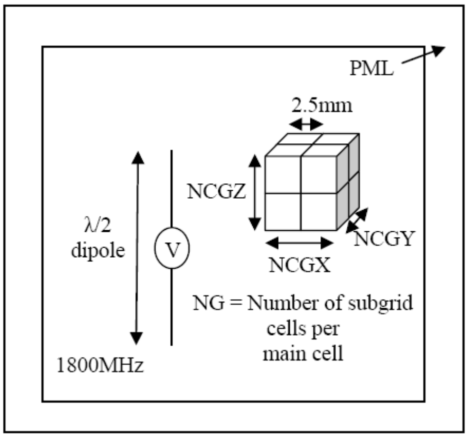

Fig.1: A half-wavelength dipole antenna was used as current source excitation to the subgrid cells. NCGX, NCGY and NCGZ are the number of cells to be subgridded in the direction of x-axis, y-axis and z-axis respectively.

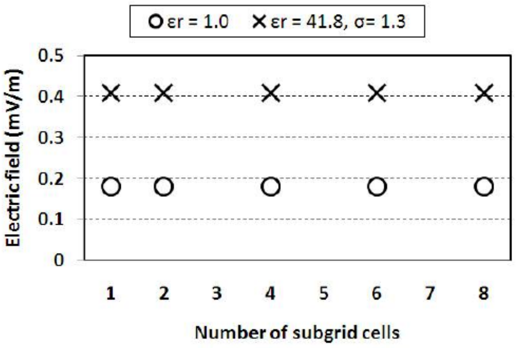

Fig.2: Stability analysis for different number of subgrid cells in one main FDTD cell.

Asia-Pacific Microwave Conference (APMC), Singapore, 7–10 December 2009

Fig. 1 depicts the configuration of the simulation environment inside the FDTD computational domain. A half-wavelength dipole was used to excite a sinusoidal voltage source at 1800MHz. The subgrid cells can be represented by free space or by a dielectric with different electrical characteristics. They were located near the voltage source as a scatterer. The interpolation scheme discussed earlier can be extended to the other mesh ratios. Two separate simulations was done for free space ($\varepsilon_r = 1.0$) and a dielectric with $\varepsilon_r = 41.8$ and $\sigma = 1.3$ for different number of subgrid cells. The results in Fig. 2 illustrate the stability of the simulation inside the problem space. The electric field remained at 0.18mV/m when using different values of subgrid cells for free space. Furthermore, it remained at 0.41mV/m when a dielectric was inserted inside the subgrid area.

III. SIMULATION AND RESULTS

Fig. 3 shows a stack of ten cubical cells tissue model. The side length of each cell was 20μm in which the thickness of the membrane was 1μm. The problem space was 220 × 20 × 20 cells of which the cell size was 1μm. A plane wave of 100V/m propagating in the z-direction and polarized in x-direction was used as excitation. Six FDTD cells were used for PML model. The floquet boundary condition was imposed along the x and y axes to effectively extend the grid structure to infinity. The detailed description and electrical properties of the structure can be found in [2].

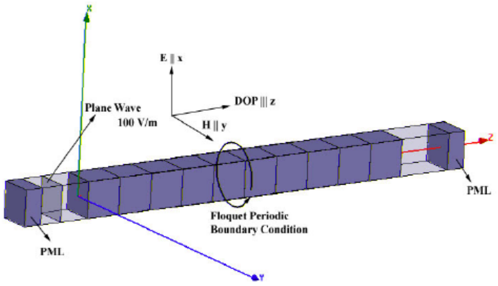

Fig.3: 3-D view of the basic simulated cubical structures in FDTD computational domain.

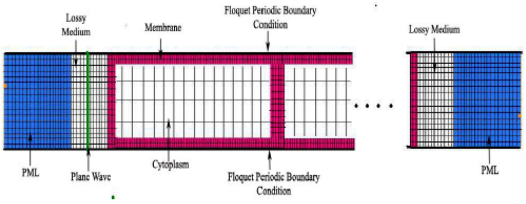

Fig.4: New proposed high definition biological tissue model by using modified subgridding FDTD model.

Applying the subgridding approach into the similar model of Fig. 3, a new high definition biological tissue model can be considered as shown in Fig. 4. The subgridding was imposed on membrane cells in which a cell size of 0.333μm was used i.e. 3 cells. The cell size used for cell cytoplasm was 1μm. Since the cell cytoplasm dominant the entire volume of the model then the entire problem space was descretised with membrane cell size except the cytoplasm volume was kept at 1μm. The proposed subgridding approach was shown in Fig. 5. The distributions of the electric field through the centre of the simulated structure, along the incident wave propagation direction at 2450MHz, were given in Fig. 6 to verify the proof of concept.

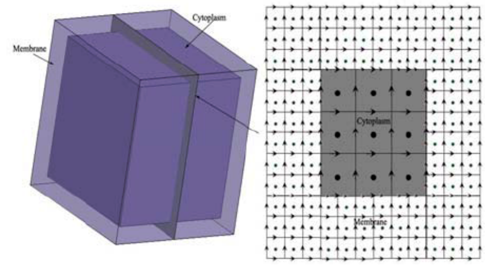

Fig.5: 2-D view of subgridding on a face of a single biological cell (not to scale).

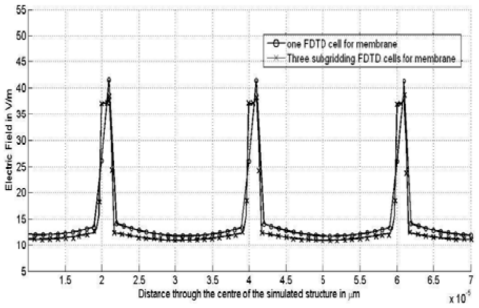

Fig.6: Electric field distribution along z-axis through the centre of the simulated structure in Fig.1.

IV. CONCLUSIONS

A new approach to microdosimetric modelling of bioelectromagnetic interactions at the higher definition cellular level by using modified subgridding FDTD has been presented. The utility of the method has been demonstrated, in which the subgridding FDTD method applied to model detailed biological cell structure, shown as a good candidate model for complex geometries.

Asia-Pacific Microwave Conference (APMC), Singapore, 7–10 December 2009

REFERENCES

[1] G. Emili, A. Schiavoni, F. L. Roselli, and R. Sorrentino, "Computation of electromagnetic field inside a tissue at mobile communications frequencies," *IEEE Trans on MTT*, 51, 2003, pp. 178-186.

[2] C. H. See, R. A. Abd-Alhameed, and P. S. Excell, "Computation of electromagnetic fields in assemblages of biological cells using a modified finite difference time domain scheme", *IEEE Trans on MTT*, 55, Sept 2007, pp. 1986-1994.

[3] O. P. Gandhi and J. Chen, "Numerical dosimetry at power-line frequencies using anatomically based models," *Bioelectromagnetics*, 13, 1992, pp. 43-60.

[4] A. Alexanian, N. J. Kolias, R. C. Compton, and R. A. York, "Three-dimensional FDTD analysis of quasi-optical arrays using Floquet boundary conditions and Berenger's PML," *IEEE Microwave and Guided Wave Letters*, 6,1996, pp. 138-140.

[5] A. Vaccari, R. Pontalti, C. Malacarne, and L. Cristoforetti, "A robust and efficient subgridding for finite-difference time-domain simulations of Maxwell's equations," *Journal of Computational Physics*, 194, 2004, pp. 117-139.

[6] C. H. See, R. A. Abd-Alhameed, R. S. Zadeh and P. S. Excell. "FDTD subgridding scheme for bioelectromagnetics application", *URSI Symposium at University of Portsmouth, UK*, pp.11, 2-3 July 2007,

[7] A. Taflove and S. C. Hagness, Computational Electrodynamics: The Finite-Difference Time-Domain Method, 3rd ed. Boston, MA: Artech House, 2005.

[8] K. S. Yee, "Numerical solution of initial boundary value problems involving Maxwell's equations in isotropic media," *IEEE Transactions on Antennas and Propagation*, vol. AP-14, pp. 302-307, 1966.

[9] P. Chow, T. Kubota, and T. Namiki, "A stable FDTD subgridding method for both spatial and temporal spaces," *IEEE Antennas and Propagation Society International Symposium*, pp. 1-4, 2008.

[10] K. Xiao, D. J. Pommerenke, and J. L. Drewniak, "A three-dimensional FDTD subgridding algorithm with separated temporal and spatial interfaces and related stability analysis," *IEEE Transactions on Antennas and Propagation*, vol. 55, pp. 1981-1990, 2007.

[11] M. J. White, Z. Q. Yun, and M. F. Iskander, "A new 3-D FDTD multigrid technique with dielectric traverse capabilities," *IEEE Transactions on Microwave Theory and Techniques*, vol. 49, pp. 422-430, 2001.

[12] K. Xiao, D. J. Pommerenke, and J. L. Drewniak, "A three-dimensional FDTD subgridding algorithm based on interpolation of current density," *IEEE International Symposium on Electromagnetic Compatibility*, vol. 1, pp. 118-123, 2004.

[13] T. Ohtani, K. Taguchi, and T. Kashiwa, "A subgridding technique for the complex nonstandard FDTD method," *Electronics and Communications in Japan Part 2 - Electronics*, vol. 87, pp. 1-9, 2004.

[14] M. Bonilla, M. F. Wong, and V. F. Hanna, "A finite-element formulation for FDTD subgridding," *Microwave and Optical Technology Letters*, vol. 32, pp. 104-108, 2002.

[15] N. V. Venkatarayalu, R. Lee, Y. B. Gan, and L. W. Li, "A stable FDTD subgridding method based on finite element formulation with hanging variables," *IEEE Transactions on Antennas and Propagation*, vol. 55, pp. 907-915, 2007.

[16] S. S. Zivanovic, K. S. Yee, and K. K. Mei, "A subgridding method for the time-domain finite-difference method to solve Maxwell's equations," *IEEE Transactions on Microwave Theory and Techniques*, vol. 39, pp. 471-479, 1991.

Ninth Informatics Workshop for Research Students Bradford UK ISBN 978 1 85143 251 6 1

Accurate Hybrid Computational Electromagnetics Techniques

K.N. Ramli, R.A. Abd-Alhameed, D. Zhou, P.S. Excell, C.H. See, Z. Zainal Abidin, M.S. Alkhambashi, M.M. Abusitta and H. Xu

***Abstract*—An approach to hybridization, linking the Method of Moments, the Finite Difference Time Domain method and subgridded FDTD regions is presented. This hybrid method is capable of analysing a system of multiple discrete regions by employing the Principle of Equivalent Sources to excite the coupling surfaces and then using a linear field-interpolation method. The method is developed to suit RFID model analysis for both near- and far-field applications.**

***Index Terms*—FDTD, MoM, Hybrid Method, RFID, Equivalent Surface.**

I. INTRODUCTION

The demand for efficient and accurate field modelling tools for electromagnetic (EM) problems is constantly growing. The various numerical methods can be divided into several categories. One possible division can be made, based on the domain in which the procedure is applied: time domain methods and frequency domain methods [1, 2].

The applications of these two classes of methods mainly depend on the type of problems to be solved and on the form of the required solution, e.g. impulse response or harmonic solution. It is clear that results can be moved from one domain approach to the other by applying a direct or inverse Fourier transform, applying the proper care to avoid aliasing and to ensure causality. However, there are deeper issues of stability which may also influence the decision on which method to use. A second possible classification for numerical methods is based on the type of formulation used: differential formulation and integral formulation.

This paper focuses on one differential method and one integral method, as shown in Fig. 1. The former is the Finite-Difference Time-Domain (FDTD) method which is a discrete time-domain differential formulation of Maxwell's equations that includes another embedded subgridding FDTD method (SGFDTD) to model small complex structures inside a normal FDTD method. The integral method is the 'Method of Moments' (MoM), most widely used in the frequency domain. The objective of this work is to explore subgridding inside the hybrid combinations between these two methods and apply the combined method to different EM scattering applications such as those found in RFID communication systems.

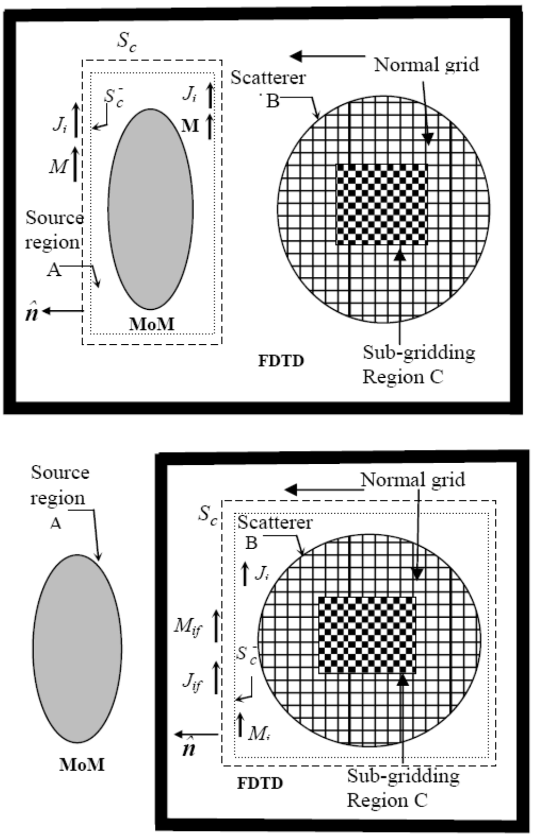

Fig. 1 Hybrid MoM/FDTD/SGFDTD configuration for the single source and scatterer geometries; (top) Near field application, (bottom) Far field application.

II. METHOD IMPLEMENTATION AND RESULTS

A computer program was written to implement the analysis method given in previous section. The new code was a modified version of the authors' work presented in [3], in which the subgridding technique is included [4]. The following example was chosen to validate the method accuracy.

A 900 MHz centre-fed half-wavelength dipole was considered as a transmitter source that represents as example of the RFID reader, whereas the RFID tag was considered as a small half-wavelength meander antenna, as shown in Fig. 2.

Manuscript received May 9, 2008.

The authors are with the Mobile and Satellite Communication Research Centre, University of Bradford, Bradford BD7 1DP, U.K. (e-mail: k.n.b.ramli@bradford.ac.uk; r.a.a.abd@bradford.ac.uk).

Two different distances between the source and the tag were studied and discussed. Two separate simulations were undertaken for each case, one with the far field application and other with near field application as shown in Fig. 1. The parameters used are summarized in Table 1.

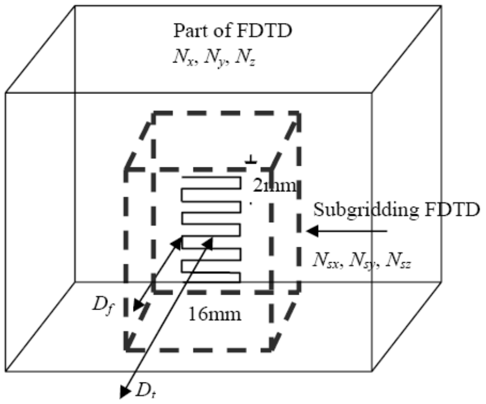

Fig. 2 FDTD/SGFDTD basic geometry.

TABLE I
INPUT PARAMETERS TO THE HYBRID METHOD

Formulation	Far Fields	Near Fields
FDTD problem space	20 × 20 × 30	20 × 40 × 30
Huygens surface	16 × 16 × 26	4 × 4 × 30
FDTD volume (cm^3)	24 × 24 × 36	24 × 48 × 36
FDTD cell size and time step	12 mm, 16.8 ps	12 mm, 16.8 ps
No. of the FDTD PML cells	8	8
Subgridding cells	5 × 5 × 15	5 × 5 × 15
Subgridding FDTD cell size and time step	2 mm, 2.8 ps	2 mm, 2.8 ps
The operating frequency	900 MHz	900 MHz
D_t: distance between the centres of transmitter and the sensor	33 cm	6 cm
D_f: distance between the centre of the sensor to the subgridding FDTD boundary	8 mm	8 mm

The transmitter is a dipole of half wavelength and radius 0.0025 wavelength.

The field distribution over an xz plane 2 cm distant from the sensor (scatterer) for near field and far field techniques is shown in Fig. 3. The plane size considered here was 20 cm × 16 cm for x and z axes respectively. The far field and near field techniques were checked for comparisons of one antenna geometry i.e. D_t was fixed to 6 cm for both techniques, the fields were found identical to the one shown in Fig. 3. Both methods show a good stability and the results were convergent within four iterations. However, the total field components was found ±2% when compared to results computed using NEC2 software.

III. CONCLUSIONS

Multiple-region hybrid techniques with frequency-domain Method of Moments, Finite-Difference Time-Domain and subgridding were proposed and investigated. The method was validated for far field and near field applications. The present computational electromagnetics technique gave stable and accurate results which is a step towards validation of complex hybrid theory problems such as are found in RFID applications in which the tag sensors are placed or mounted on dielectric or conducting materials.

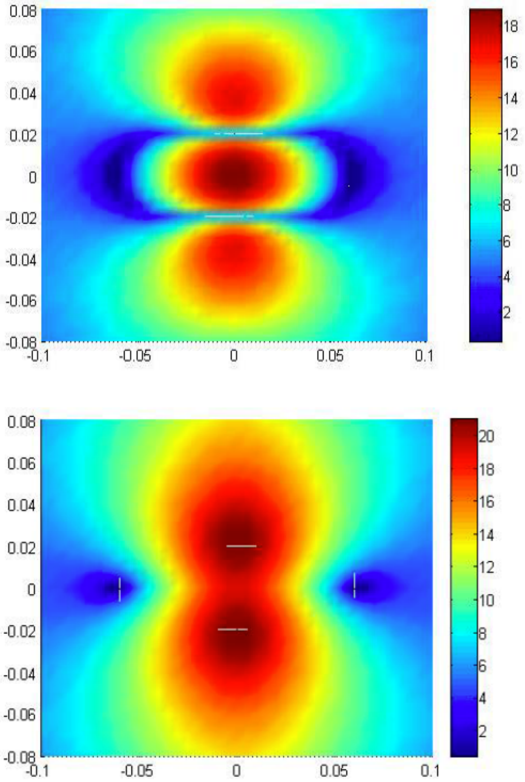

Fig. 3 The distribution of the E_z and E_{total} field components in dB at 2 cm away from the sensor, using near field technique; (top): E_z, (bottom): E_{total}.

REFERENCES

[1] A. Taflove and S. C. Hagness, Computational Electrodynamics: The Finite-Difference Time-Domain Method, 3rd ed. Boston, MA: Artech House, 2005.

[2] K. S. Yee, "Numerical solution of initial boundary value problems involving Maxwell's equations in isotropic media," IEEE Transactions on Antennas and Propagation, vol. AP-14, pp. 302-307, 1966.

[3] Abd-Alhameed, R.A., Excell, P.S and Mangoud, M.A.: 'Broadband antenna response using hybrid technique of frequency domain of MoM and FDTD', ACES Journal on Computational of Electromagnetics', vol. 20, No. 1, March 2005, pp. 70-77.

[4] C.H. See, R.A. Abd-Alhameed, R.S. Zadeh and P.S. Excell, 'FDTD Subgridding Scheme for Bioelectromagnetics Application', URSI Symposium, University of Portsmouth, Commission B, 2-3 July, 2007, UK, pp. 11.

Ninth Informatics Workshop for Research Students Bradford UK ISBN 978 1 85143 251 6

Modelling of Complex Electromagnetic Problems Using FDTD Subgridding Methods

K.N. Ramli, and R.A. Abd-Alhameed

Abstract—**A new FDTD subgridding scheme is proposed in one-dimension Cartesian coordinate. The accuracy of the scheme is validated by computing the source of the signal that propagates through the subgridding problem space and the reflection at the boundary of the PML is observed. The proposed scheme is found to be stable and presents 20 dB less reflective than the conventional FDTD subgridding method.**

Index Terms—**FDTD, subgridding method, Perfectly Matched Layer (PML).**

I. INTRODUCTION

THE development of robust finite-difference time-domain (FDTD) method has been widely used in electromagnetic scattering problems due to its easiness and potentiality to treat complex geometry structures in the huge calculation region [1]. This method of solving Maxwell's differential equations was first proposed in two-dimensional problems [2] and then utilized in three-dimensional applications [3]. However, the standard FDTD method is incompetent if the details of the geometry need to be modelled due to a global fine mesh. As a result, the total number of cells increases dramatically. The time step must be reduced to fulfill the Courant stability condition causing the computational time to increase significantly.

A few methods can be used to improve the efficiency of the FDTD method, such as non-uniform meshing [4], sub-cellular technique [5], non-orthogonal meshing [6] and subgridding method [7-10]. A stable subgridding algorithm can refine the mesh locally and improve the accuracy of the result without increasing the computational efforts significantly. It is hence very useful for FDTD code. Both the numerical dispersion and memory usage must be reduced but there is a trade-off between them. The accuracy of the solution can be improved by using finer grids since numerical dispersion is controlled by the size of the grid in the computational domain. However, the memory and computation requirement are increased accordingly.

An alternative approach to reduce the memory usage in the computational domain is to use FDTD subgridding scheme by controlling the distribution of the degrees-of-freedom. In FDTD subgridding method, the smaller size components in a structure is discretized by fine grids and the residual of the space is filled with coarse grids. The fields on the boundary between coarse and fine grids are coupled using spatial and temporal interpolations. The regions of the coarse and fine grids are computed by the FDTD method and are kept in time step. Many articles are published with different updating field methods at the unknown cell of the boundary by means of both interpolation and extrapolation techniques. In general, some of them are based on dielectric transverse capability [11], interpolation of current density [7], time interpolation subgridding algorithm [9] and finite element formulation [12, 13].

To overcome the shortcoming, a new FDTD subgridding scheme is proposed in one-dimension Cartesian coordinate. The accuracy of the scheme is validated by computing the source of the signal which propagates through the subgridding area while observing the reflection from the subgridding surface boundary. The results are compared with the numerical solutions for conventional FDTD mesh method.

II. METHOD IMPLEMENTATION AND RESULTS

Assuming cubical FDTD cells, the FDTD updating equation for the electric field E_x and magnetic field H_y components of 1D FDTD can be derived as [1]:

$$E_x\Big|_{i,j,k}^{n+1} = C_{a,E_x}\Big|_{i,j,k} E_x\Big|_{i,j,k}^{n} + C_{b,E_x}\Big|_{i,j,k}\begin{pmatrix} H_z\Big|_{i,j+1/2,k}^{n+1/2} - H_z\Big|_{i,j-1/2,k}^{n+1/2} \\ + H_y\Big|_{i,j,k-1/2}^{n+1/2} - H_y\Big|_{i,j,k+1/2}^{n+1/2} \end{pmatrix} \quad (1)$$

$$H_y\Big|_{i,j,k}^{n+1/2} = D_{a,H_y}\Big|_{i,j,k} H_y\Big|_{i,j,k}^{n-1/2} + D_{b,H_y}\Big|_{i,j,k}\begin{pmatrix} E_z\Big|_{i+1/2,j,k}^{n} - E_z\Big|_{i-1/2,j,k}^{n} \\ + E_x\Big|_{i,j,k-1/2}^{n} - E_x\Big|_{i,j,k+1/2}^{n} \end{pmatrix} \quad (2)$$

Numerical computation was done for TM waves. A computer program was written to implement the analysis. Fig. 1 shows the flow chart of the simulation. It was done for both the conventional and the new FDTD subgridding schemes. The cell size was set with $\Delta x = \Delta y = \Delta z = 1$ cm. It was chosen such that the length of the grid remained at a fraction of a wavelength only. The time step was set at 20 ps to satisfy the Courant stability condition that is given by [2]:

$$\sqrt{(\Delta x)^2 + (\Delta y)^2 + (\Delta z)^2} > c\Delta t = \sqrt{\frac{1}{\varepsilon\mu}}\Delta t \quad (3)$$

where c, ε and μ are the speed of light, electric permittivity and magnetic permeability respectively. The number of time step was 1000. A Gaussian pulse was used as the source signal which propagates inside the problem space area.

Manuscript received May 9, 2008.

The authors are with the Mobile and Satellite Communication Research Centre, University of Bradford, Bradford BD7 1DP, U.K. (e-mail: k.n.b.ramli@bradford.ac.uk; r.a.a.abd@bradford.ac.uk).

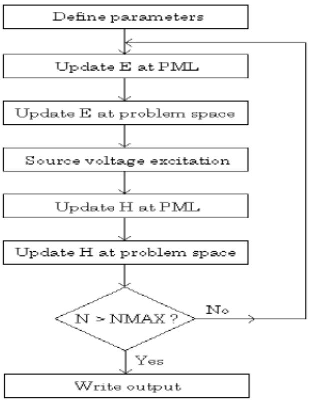

Fig. 1. Basic flow chart model.

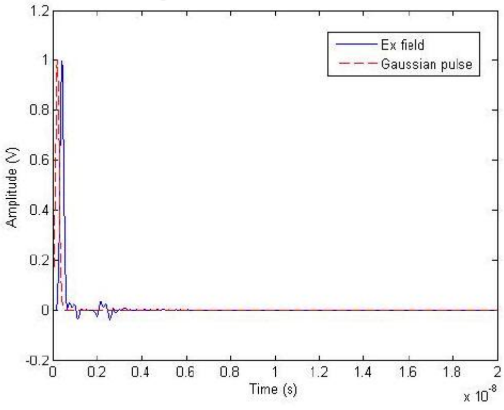

Fig. 2. The electric field variation for the conventional FDTD subgridding scheme.

Numerical results were presented here for the TM waves discussed above. Fig. 2 shows the E_x field component as a function of time for the conventional FDTD subgridding technique. In addition, the Gaussian pulse was shown as a reference signal. It can be clearly seen that -20 dB reflections occurred at the boundary of the subgridding surface that is observed between 1 and 3 ns. The field also stays stable after several reflections. Fig. 3 shows the E_x field component as a function of time for the proposed FDTD subgridding scheme in which the time step was advanced by half time step next to the surface boundary of the subgridding. It can be observed that -40 dB reflections occurred at the boundary of the subgridding surface that appears between 1 and 3 ns. The field continues with a minimum reflection of -60 dB for late response.

III. CONCLUSIONS

Overall, the proposed FDTD scheme was observed to be stable after late time response. The scheme was found to be 20 dB less reflective than the conventional FDTD subgridding method. The proposed scheme can be easily extended to 2D and 3D subgridding problems that will be used as part of the hybrids methods for future work.

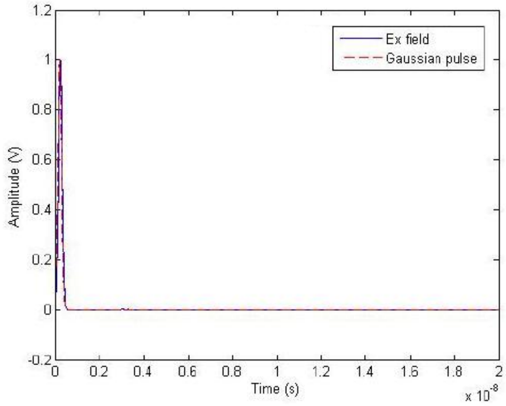

Fig. 3. The electric field variation for the proposed FDTD subgridding scheme.

REFERENCES

[1] A. Taflove and S. C. Hagness, Computational Electrodynamics: The Finite-Difference Time-Domain Method, 3rd ed. Boston, MA: Artech House, 2005.

[2] K. S. Yee, "Numerical solution of initial boundary value problems involving Maxwell's equations in isotropic media," IEEE Transactions on Antennas and Propagation, vol. AP-14, pp. 302-307, 1966.

[3] G. Mur, "Absorbing boundary conditions for the finite-difference approximation of the time-domain electromagnetic-field equations," IEEE Transactions on Electromagnetic Compatibility, vol. EMC-23, pp. 377-382, 1981.

[4] R. Wu, G. Benqing, and Y. Shiming, "An improved method in FDTD simulation to reduce reflection from non-uniform mesh," 3rd International Conference on Microwave and Millimeter Wave Technology Proceedings, pp. 646-649, 2002.

[5] S. Kapoor, "Sub-cellular technique for finite-difference time-domain method," IEEE Transactions on Microwave Theory and Techniques, vol. 45, pp. 673-677, 1997.

[6] P. Thoma and T. Weiland, "Numerical stability of finite difference time domain methods," IEEE Transactions on Magnetics, vol. 34, pp. 2740-2743, 1998.

[7] K. Xiao, D. J. Pommerenke, and J. L. Drewniak, "A three-dimensional FDTD subgridding algorithm based on interpolation of current density," IEEE International Symposium on Electromagnetic Compatibility, vol. 1, pp. 118-123, 2004.

[8] K. M. Krishnaiah and C. J. Railton, "A stable subgridding algorithm and its application to eigenvalue problems," IEEE Transactions on Microwave Theory and Techniques, vol. 47, pp. 620-628, 1999.

[9] T. Ohtani, K. Taguchi, and T. Kashiwa, "A subgridding technique for the complex nonstandard FDTD method," Electronics and Communications in Japan Part 2 - Electronics, vol. 87, pp. 1-9, 2004.

[10] K. Xiao, D. J. Pommerenke, and J. L. Drewniak, "A three-dimensional FDTD subgridding algorithm with separated temporal and spatial interfaces and related stability analysis," IEEE Transactions on Antennas and Propagation, vol. 55, pp. 1981-1990, 2007.

[11] M. J. White, Z. Q. Yun, and M. F. Iskander, "A new 3-D FDTD multigrid technique with dielectric traverse capabilities," IEEE Transactions on Microwave Theory and Techniques, vol. 49, pp. 422-430, 2001.

[12] M. Bonilla, M. F. Wong, and V. F. Hanna, "A finite-element formulation for FDTD subgridding," Microwave and Optical Technology Letters, vol. 32, pp. 104-108, 2002.

[13] N. V. Venkatarayalu, R. Lee, Y. B. Gan, and L. W. Li, "A stable FDTD subgridding method based on finite element formulation with hanging variables," IEEE Transactions on Antennas and Propagation, vol. 55, pp. 907-915, 2007.